CHARACTERIZATION OF UNBOUND AND STABILIZED MATERIALS AND IMPROVED CONSIDERATION OF THEIR EFFECTS ON PAVEMENT PERFORMANCE

A Dissertation

by

SAJIB SAHA

Submitted to the Office of Graduate and Professional Studies of
Texas A&M University
in partial fulfillment of the requirements for the degree of

DOCTOR OF PHILOSOPHY

Chair of Committee,	Robert L. Lytton
Committee Members,	Dallas Little
	Marcelo Sanchez
	Anastasia Muliana
Head of Department,	Robin Autenrieth

May 2019

Major Subject: Civil Engineering

ABSTRACT

The United States has more than 2.7 million miles of paved roads and highways that require approximately $165 billion spending each year. Pavement design, construction, maintenance, and management techniques are critical factors for optimizing this massive budget that are constantly being evolved. To control the design and maintenance of new and existing pavements, the American Association of Transportation Officials' (AASHTO) currently follow a design guide named AASHTOWare Pavement Mechanistic-Empirical (ME) Design. The design guide provides a methodology for the analysis and performance prediction of pavements and overlays. Although the performance of pavements is known to be closely related to properties of the subgrade and underlying layers (i.e., base and/or subbase), some recent research studies indicate that the performance predicted by this methodology shows a low sensitivity to the properties of underlying layers and does not always reflect the extent of the anticipated effect. To overcome these limitations, this study proposes several enhancements, as needed, to the Pavement ME Design procedures to better reflect the influence of subgrade and unbound layers (properties and thicknesses) on the performance of pavements. These enhancements include several modifications of the models contained in Pavement ME Design such as (a) development of an artificial neural network (ANN) based soil water characteristics curve (SWCC) prediction model of base and subgrade; (b) development of a mechanistic-empirical equilibrium suction (u_e) model for subgrade; (c) development of a ANN based resilient modulus (M_R) model of base ; (d) development of a new shear strength (τ) and permanent deformation (ε_p) prediction model; (d) development of a modified modulus of subgrade reaction (k) model. The sensitivity of base and

subgrade layers are evaluated on the basis of both flexible and rigid pavements performance using the developed models and compared with the predicted performance from Pavement ME design models. The results clearly show that the developed models have better sensitivity to moisture and interface bonding on both rutting and fatigue cracking performance compared to the Pavement ME design models.

Attaining uniform construction of the required specification quality is another key factor to ensure the performance of pavement. To develop more efficient quality control (QC) evaluation methods, this study develops a quick and accurate, non-destructive method for determining reliable values of the in-place as compacted base course modulus. Simple laboratory test methods are incorporated with the ground penetrating radar (GPR) scans to determine the resilient modulus of the base layer through a mechanistic-based approach. Research efforts have also been undertaken to develop and calibrate the mechanistic-based models for predicting the construction quality of stabilized base materials. A mechanistic-empirical model is developed to predict the percentage of stabilizer in the base layer from electrical conductivity readings in the laboratory and further incorporated with GPR scans to estimate the stabilizer content of the base layer in the field.

DEDICATION

To my parents and family members

ACKNOWLEDGEMENTS

I would like to express my deepest gratitude to my advisor and committee chair, Dr. Robert L. Lytton, for his guidance, encouragement and support throughout my graduate studies at Texas A&M University. I have been fortunate to work with Dr. Lytton on so many research projects. He is such a knowledgeable professor, who is always willing to share his experience and ideas with his students. I shall always remember those days discussing with Dr. Lytton about the research problems I encountered.

I also would like to appreciate my committee members, Dr. Dallas Little, Dr. Marcelo Sanchez, and Dr. Anastasia Muliana, for their guidance, support and valuable comments on my research work. Special thanks go to Dr. Xue Luo and Stephen Sebesta for providing me the opportunities to work on their research projects. These research experiences provide me a sound basis to explore my dissertation research. I am sincerely grateful to Dr. Xue Luo and Dr. Fan Gu, for their encouragement and help on my studies.

Many thanks go to all of my friends and colleagues at Texas A&M University. Their friendship is one of the most valuable gifts I have received in my study. I would like to specifically acknowledge my friend Md. Tauhidul Islam for his continuous support and motivation in my hard times. Last but not least, I would like to thank my wife, my parents, my brother and other family members for being understanding and supportive throughout my graduate study.

CONTRIBUTORS AND FUNDING SOURCES

Contributors

This work was supervised by a dissertation committee consisting of Professor Robert L. Lytton (advisor) and Dr. Dallas Little and Dr. Marcelo Sanchez of the Department of Civil Engineering and Dr. Anastasia Muliana of the Department of Mechanical Engineering.

The principle of Ground Penetrating Radar (GPR) operating system and the mechanistic approach to determine base modulus, described in Chapter 8 and Chapter 9 respectively, were provided by Dr. Hakan Sahin and published in 2014 (Sahin, 2014). The GPR signal processing analyses, depicted in Chapter 9, was conducted in part by Arvind Devadas of the Texas A&M Transportation Institute (TTI).

All other work conducted for the dissertation was completed by the student independently.

Funding Sources

Graduate study was financially supported by the National Cooperative Highway Research Program (NCHRP) [Grant Number: 01-53].

This work was also made possible in part by Texas Department of Transportation (TxDOT) under Grant Number 0-6874. Its contents are solely the responsibility of the author and do not necessarily represent the official views of the Texas A&M University.

TABLE OF CONTENTS

Page

LIST OF FIGURES

Page

LIST OF TABLES

Page

1. INTRODUCTION

1.1. Background

A pavement is a composite structure consisting of an asphalt concrete (AC) or, Portland cement concrete (PCC) surface layer, unbound or treated base layer and subgrade. Base and Subgrade layers act as a foundation of the pavement structure which provides support to the surface layer. It has been recognized that the performance of flexible and rigid pavements is closely related to the characteristics of unbound layers and subgrade. However, recent studies indicate that the performance predicted by the current pavement design guide named AASHTOWare Pavement ME Design shows low or no sensitivity to these underlying layers (Schwartz et al., 2011).
In particular, the following cases have been identified as major problems in performance predictions (Luo et al., 2017):

- Total rutting in flexible pavements is marginally sensitive to resilient modulus (M_R) and soil water characteristics curve (SWCC) and shear strength of unbound layers and subgrade;
- Load-related cracking in flexible pavements is non-sensitive to soil-water characteristics curve (SWCC) of unbound base layers, and marginally sensitive to the SWCC of subgrade;
- Faulting in jointed plain concrete pavement (JPCP) is marginally sensitive to resilient modulus, slab-base interface bonding and erodibility;

- Transverse cracking in JPCP is marginally sensitive to resilient modulus, thickness and erodibility of unbound layers

The sensitivity of the predicted performance from Pavement ME Design on base/subgrade layer can be improved by using modified performance prediction models and proper design inputs. Hence, a new set of mechanistic-empirical models have been proposed by Gu et al. (2015) and Chen et al. (2019) for permanent deformation and faulting respectively.

$$\varepsilon_p = \varepsilon_0 e^{-(\frac{\rho}{N})^{\beta}} (\frac{\sqrt{J_2}}{P_a})^m (\frac{\alpha I_1 + K}{P_a})^n \quad (1.1)$$

where, $\alpha = \frac{2\sin\phi}{\sqrt{3}(3-\sin\phi)}$

$$K = \frac{c.6\cos\phi}{\sqrt{3}(3-\sin\phi)}$$

where, ε_p is the permanent strain of the granular material; ε_0 is the maximum permanent strain; N is the number of load cycles; P_a is the atmospheric pressure; J_2 is the second invariant of the deviatoric stress tensor; I_1 is the first invariant of the stress tensor; ε_0, ρ, β, m, and n are model coefficients; c and ϕ are cohesion and friction angle, respectively.

$$f = \rho_e [\ln(\frac{N_\infty}{N - N_0})]^{-\frac{1}{\beta_e}} \quad (1.2)$$

where, f is the faulting depth; N is the number of days after pavement construction date; N_0 is the number of days after which faulting initiates; N_∞ is the number of days to failure due to erosion; and ρ_e and β_e are model coefficients.

However, the prediction accuracy of these models heavily relies on the accuracy of design inputs such as SWCC, equilibrium suction, resilient modulus (M_R), shear strength and modulus of subgrade reaction (k). Therefore, improved models are necessary to accurately predict these design inputs and get a better performance prediction of the pavement.

Quality control and quality assurance are the two significant challenges in pavement construction. To assure the construction quality of base and subgrade layer, the modulus values that are compacted should match as closely as possible the modulus values that are used in design. For stabilized pavement, the percentage of stabilizer is another significant measure of the strength of the base and subgrade layers and must also meet the design criteria. Quality assurance of the compacted base course must be conducted in a timely and efficient manner so as not to retard the pace of construction. Therefore, it is necessary to develop an efficient nondestructive testing (NDT) approach to measure the resilient modulus and stabilizer content of the compacted base and subgrade.

1.2. Problem Statement

1.2.1. Moisture Insensitive Resilient Modulus Model

The resilient modulus model incorporated by the AASHTOWare Pavement ME Design show very low or no sensitivity to soil moisture. But the resilient modulus has an increasing linear relationship with the matric suction on a semi-logarithmic coordinate (Edil et al., 2006). A number of studies recommended the use of soil suction in modeling resilient modulus and improving related mechanistic pavement design (Oloo and Fredlund, 1998; Wolfe and Butalia, 2004; Khoury and Zaman, 2004; Edil et al., 2006; Gupta et al., 2007). As a summary of these studies, the NCHRP Synthesis 382 (Puppala, 2007) points out that the concept of soil suction

plays a vital role in the better understanding of resilient properties of unsaturated soils, and this will help in better mechanistic design of pavements.

1.2.2. Inaccurate Assumption of Moisture Availability in Base/Subgrade Layer

The available moisture to the supporting layers of pavement is a key factor in prediction accuracy of the M_R and other performance models. At present, the Pavement ME Design software requires the input of the depth to a water table as the sole input to the moisture availability. It has been recognized that many pavements are built in areas where there is no water table within 40 feet of the pavement surface and recommended adding the depth below the pavement to the equilibrium suction level and also inputting that suction level. So, a comprehensive approach is needed to determine the equilibrium suction level underneath the pavement surface.

1.2.3. Lack of Shear Strength Consideration in Permanent Deformation Model

The Pavement ME Design paid little attention to the shear strength properties of unbound base and subgrade. This needs to be improved because the shear strength of underlying layer materials has significant influence on accumulation of permanent deformation in flexible pavements. Maree, (1978); Brown, (1996); Theyse et al., (1996); Núñez et al., (2004); and Fernando et al., (2008) showed that the shear strength directly affects the amount of total rutting. The ratio of the shear strength to shear stress performs well in limiting the permanent deformation of granular materials against shear failure (Maree, 1978; Theyse et al., 1996).

1.2.4. Lack of Slab-Base Interface Bonding Sensitivity in Effective Dynamic *k*-Value

Modulus of subgrade reaction (k) is the primary input for rigid pavement design which estimates

the reaction pressure sustained by the subgrade layer. In the Pavement ME Design, the modulus of subgrade reaction is characterized by a dense liquid or Winkler model, which has no consideration of the interface bond between slab and base. The researchers in the past have shown that the slab-base interface bonding has a significant impact on performance prediction of rigid pavements (Croney, 1977; Tarr et al., 1999; Delatte et al., 2000; Bari et al., 2013). Therefore, the inclusion of the degree of bonding effect on the effective dynamic k-value model is necessary to improve the influence of unbound layers on rigid pavement performance.

1.2.5. Lack of Efficient Non-Destructive Testing Methodology to Quality Assurance of Base Layer

During construction, the measured properties of flexible base for current quality control (QC) and quality assurance (QA) are M_R value. Due to the need to maintain the pace of construction, it is necessary to develop a quick, accurate, and simple nondestructive testing (NDT) approach for determining reliable values of the in-place-as-compacted base course modulus value and also the stabilizer content for stabilized base material. Falling weight deflectometer (FWD) and a ground-penetrating radar (GPR) are two NDT devices commonly used for QC purpose in pavement construction. But both these approaches are in need of mechanistic characterization model and comprehensive evaluation process.

1.3. Research Objective

In light of these problems, this study focused on developing enhanced prediction models to improve the current pavement design and construction process. The implementation of these models in the AASHTOWare Pavement ME Design will improve considerations of the influence of subgrade and unbound layers on the performance of flexible and rigid pavements.

The main objectives of this study are as follows

- Develop an improved SWCC prediction model based on Fredlund-Xing approach
- Develop an improved equilibrium suction model based on Thornthwaite Moisture Index
- Develop a moisture sensitive resilient modulus prediction model
- Develop moisture sensitive shear strength prediction model
- Develop a modified modulus of subgrade reaction model
- Develop a mechanistic based approach for rapid determination of percentage of stabilizer from electrical conductivity
- Develop an efficient NDT approach to determine on-site modulus value

1.4. Dissertation Outline

This dissertation is organized as follows:

Section 1 is an introduction which contains background, problem statement, research objectives and dissertation outline.

Section 2 presents the development of prediction models for the coefficients of Fredlund-Xing equation based soil-water characteristics curve, which include two separate three layer artificial neural network models for plastic and non-plastic soils respectively.

Section 3 presents a new mechanistic-empirical approach to predict equilibrium suction in subgrade soil, which allows the development of an equilibrium suction contour map in a geographic information system (GIS) platform.

Section 4 presents the development of new prediction models for the coefficients of a suction dependent resilient modulus (M_R) model. Two three layered artificial neural network architectures are constructed: one for plastic base and another for non-plastic base materials.

Both of these models are validated against the measured database collected from the Long Term Pavement Performance (LTPP) data base and other literature sources.

Section 5 presents the development of prediction models for permanent deformation model coefficients ($\epsilon 0$, ρ, β, m and n) and shear strength model coefficients (c' and φ'). In this study repeated and monotonic load triaxial test data are collected from the literature and the coefficients of the permeant deformation and shear strength model are calculated respectively.

Section 6 presents the detailed description of the development of a cross-anisotropic base modulus and slab-base interface bond sensitive modified *k*-value model. An ANN model is also developed in this section to predict the k-value for a wide range of pavement layer moduli, layer thicknesses and interface bonding ratios.

Section 7 presents the sensitivity analysis of moisture, interface bonding and tire speed on the predicted performance of flexible and rigid pavements. The developed models are also compared with the corresponding models in the Pavement ME design and shows the resulting differences.

Section 8 presents the development of a mechanistic-empirical model to predict the percentage of stabilizer in base material from electrical conductivity.

Section 9 presents the use of ground penetrating radar based non-destructive technology to determine in-situ resilient modulus of base material. The proposed methodology is validated with real time GPR scans and FWD backcalculated modulus values.

Section 10 presents overall summaries and conclusions of the dissertation. Recommendations for future studies are also suggested in this section.

2. DEVELOPMENT OF A SOIL-WATER CHARACTERISTICS CURVE PREDICTION MODEL FOR UNBOUND MATERIAL*

2.1. Introduction

The soil-water characteristics curve (SWCC) represents a relationship between soil suction and water content (or degree of saturation). The soil suction due to the presence of water between soil particles is an important indicator, which is directly related to the strength, volume change and fluid flow characteristics of unsaturated soil material (Fredlund and Rahardjo 1993). The unbound material is usually in an unsaturated condition when it is exposed in the field. The existing studies found that the degree of saturation or matric suction has a significant impact on the resilient modulus of the unbound material, which indicates that the resilient behavior of unbound material is stress-dependent and moisture-dependent. (Han and Vanapalli 2015; Gu et al. 2014, 2016, Islam et al. 2018). These studies recommended to incorporate the matric suction term to the stress-dependent resilient modulus model to reflect the moisture-dependent characteristic of unbound material. At various saturation levels, the matric suction values of unbound material are determined by the SWCC.

Currently, there are two common ways to determine the SWCC of unbound material. One way is by conducting laboratory tests (e.g., filter paper test and pressure plate test) to measure the matric suction at different water contents. This experimental method is usually time-consuming, and requires special test equipment and test expertise. An alternative way is to

* Reprinted with permission from "Prediction of soil-water Characteristic Curve for unbound material using Fredlund–xing Equation-based ANN approach" by Sajib Saha, Fan Gu, Xue Luo and Robert Lytton, 2018. Journal of Materials in Civil Engineering, 30(5), 06018002, Copyright [2018] by ASCE.

correlate the suction-water relationship to other unbound material indicators, such as grain size distribution (*GSD*), particle diameter, porosity, liquid limit (*LL*) and plasticity index (*PI*), mean annual air temperature (*MAAT*) etc. There are many prediction methods available, which can be classified into three categories (Zapata et al. 2003).

- Category 1: Direct prediction of SWCC, which is a curve-fitting method to correlate the soil properties (e.g., *GSD* and porosity) to the matric suction at the different tested water contents (Gupta and Larson 1979, Huston and Cass 1987, Reddi and Poduri 1997, and Zapata et al. 1999).
- Category 2: Prediction of SWCC model parameters, which is a statistical method to correlate the soil properties (e.g., *GSD*, *LL*, *PI* and *MAAT*) to the parameters of existing SWCC models (e.g., Fredlund-Xing equation). These estimated model parameters are further used to generate the SWCC of unbound material (Williams et al. 1983, Zapata et al. 2003, Perera et al. 2005, Torres-Hernandez 2011, and Sahin et al. 2015).
- Category 3: Development of a micromechanics-based SWCC model, which utilizes the microstructure of unbound material (e.g., porosity distribution) and the water-particle contact (or capillary rise) model to determine the matric suction (Mishra et al. 1989, Basile and D'Urso 1997, and Fredlund et al. 1997).

Among these approaches, Category 1 usually has a low prediction accuracy, since it ignores the existing relationship between matric suction and water content. Category 2 recognizes the existing SWCC models, and uses an indirect method to predict the SWCC via soil properties. The prediction accuracy of Category 2 relies on the selected statistical method and the quantity of the database used in the analysis. However, most of the aforementioned models were

developed based on either a simple regression analysis or a limited number of test results (Torres-Hernandez 2011). Compared to Categories 1 and 2, Category 3 is still in a state-of-development status, which is limited to the soils with large pores (Zapata et al. 2003). Therefore, approaches in Category 2 are more accurate and feasible to predict the SWCC of unbound material, as long as the issues of statistical method and quantity of database are solved.

Nowadays, the artificial neural network (ANN) approach becomes a more and more popular tool for the development of prediction models. Compared to regression models, the main advantage of the ANN approach is that it is capable of capturing nonlinear and complex scattered relationships between input and output parameters. In the past, several studies attempted to utilize the ANN approach to predict the SWCC of soil, which mainly focused on the Category 1-based method (i.e., direct prediction of SWCC). For example, Pachepsky et al. (1996) predicted the water retention curve using the particle size distribution and bulk density of soil. Similarly, Johari et al. (2010) utilized five input variables (i.e., initial void ratio, initial gravimetric water content, logarithm of suction normalized with respect to atmospheric pressure, clay fraction and silt content) to predict the gravimetric water content of soil. Haghverdi et al. (2012) developed a pseudo-continuous ANN approach to predict the water retention curve using the bulk density, porosity, organic matter, and percentage of clay, silt and sand. As it is mentioned previously, the direct prediction of SWCC does not need a specific equation between matric suction and water content, which usually results in a lower prediction accuracy than the equation-based prediction method (i.e., Category 2 method) (Jain et al. 2004). However, there is no Category 2-based ANN model currently available to predict the SWCC of soil. The main reason is that the development of Category 2-based ANN model requires a much larger database of SWCC results. In addition,

most of these existing ANN models dealt with subgrade soils (Pachepsky et al. 1996, Schaap and Bouten 1996, Koekkoek and Booltink 1999, Jain et al. 2004, Johari et al. 2010, Haghverdi et al. 2012), but none of these ANN models were capable of predicting the SWCCs of unbound granular materials (or unbound aggregates) that are commonly used in pavement base.

To overcome the aforementioned problems, a Category 2-based ANN approach is recommended for estimating the SWCC of unbound material. In this study, a large database collected from the NCHRP 9-23A project is used to develop the ANN models. The Fredlund-Xing equation is used to estimate the relationship between matric suction and water content, as shown in Equations 2.1 and 2.2 (Fredlund and Xing 1994).

$$S = C(\mathrm{h})\,\mathrm{x}\left[\frac{1}{\{\ln[\mathrm{e}+(\frac{h}{a_f})^{b_f}]\}^{c_f}}\right] \tag{2.1}$$

where $C(h)$ is a correction factor defined as

$$\mathrm{C}(h) = 1 - \frac{\ln(1+\frac{h}{h_r})}{\ln[1+(\frac{1.45x10^5}{h_r})]} \tag{2.2}$$

where S is the degree of saturation (unit: %); h is the soil matric suction (unit: psi); and a_f, b_f , c_f are h_r soil fitting parameters. The four fitting parameters are the outputs of ANN models and are predicted by the input variables.

The section is organized as follows. The next subsection presents the development of ANN models in detail. Subsequently, the ANN models are used to predict the fitting parameters in the Fredlund-Xing equation. After that, the developed ANN models are compared with other existing regression models in terms of prediction accuracy. A two-step validation process is

presented in the following section, which compares the ANN model-predicted SWCCs with those measured from the laboratory tests. The final subsection summarizes the major findings of this study.

2.2. Development of Artificial Neural Network Models

The ANN approach is a computer-based information processing technique, which allows to establish the correlations between the input variables X_i and the output variables Y_j through the inter-connected neurons (i.e., weight factor, w_{ji}). Note that the input variables X_i and the output variables Y_j are usually normalized to x_i and y_j, respectively. The correlations developed by the ANN models between the normalized input parameters x_i and the normalized output variables y_j are shown in Equation 2.3.

$$y_j = f\left(\sum_{i=1}^{n} w_{ji} x_i\right) \tag{2.3}$$

where f is a transfer function, which normally uses a sigmoidal, Gaussian, or threshold functional form, and w_{ji} are the unknown weight factors. Developing a neural network model specifically refers to the determination of the weight factors w_{ji} in Equation 2.3. In this study, the output variables Y_j represent the four fitting parameters in the Fredlund-Xing equation (i.e., a_f, b_f, c_f and h_r). The input variables X_i are selected from the SWCC-related material indicators, which will be elaborated in the following sub-section. In general, the development of ANN models include two critical steps: 1) data collection; and 2) construction of ANN architecture.

2.2.1. Data Collection

The database used in this study is collected from the NCHRP 9-23A project entitled “A national catalog for subgrade SWCC default inputs and selected soil properties for use with the ME-

PDG" carried out at Arizona State University in 2010 (Zapata 2010). In addition to the measured SWCC fitting parameters, the database includes material size distribution, soil *LL*, *PI* and saturated volumetric water content. To better evaluate the influence of soil plasticity, the collected database is separated into two groups: plastic soil dataset (*PI*>0), and non-plastic soil dataset (*PI*=0).

2.2.2. Construction of ANN Architecture

As shown in Figures 2.1a and 2.1b, two three-layered neural network architectures consisting of one input layer, one hidden layer and one output layer are constructed for plastic soil and non-plastic soil, respectively. The input variables in the ANN models are selected based on previous studies and the mechanics of unsaturated soil. The SWCC of a soil is greatly dependent on its pore structure (Fredlund and Xing 1994; Sillers et al. 2001; Rahardjo et al. 2012). The pore size is related to the height of each capillary tube using the Young–Laplace equation, which is equivalent to a suction value (Fredlund and Rahardjo 1993**)**. The capillary height of the corresponding pore can be expressed in terms of the radius of that pore. Thus, soil grain size distribution (i.e., percent passing No. 4 sieve and percent passing No. 200 sieve) and gradation scale parameter, Θ and shape parameter, Ψ, and saturated volumetric content are selected as input parameters. Saturated volumetric water content is a measure of the total porosity in soil structure. The equilibrium soil suction of plastic soil is proportional to its specific surface area (Zapata et al., 2000). The plasticity index (PI) is a simple indicator that reflects the specific surface area of soil. The relationship between soil surface area and plasticity index changes, particularly when the liquid limit (LL) is above 30% to 40% (Aubertin et al., 2003). Hence, LL is also selected as an input parameter in the ANN models. Previous studies investigated the effects

of temperature on soil suction-water retention relationship (Liu and Dane 1993, Wu et al. 2014, El-Keshky 2011). Soil water is composed of continuous water and isolated pockets of water. When the temperature increases, water flows from isolated pockets to the continuous phase, which results in a shift in SWCC. In this study, the MAAT is identified as one of inputs for ANN models and is collected from Natural Resources Conservation Services (NRCS) soil data mart.

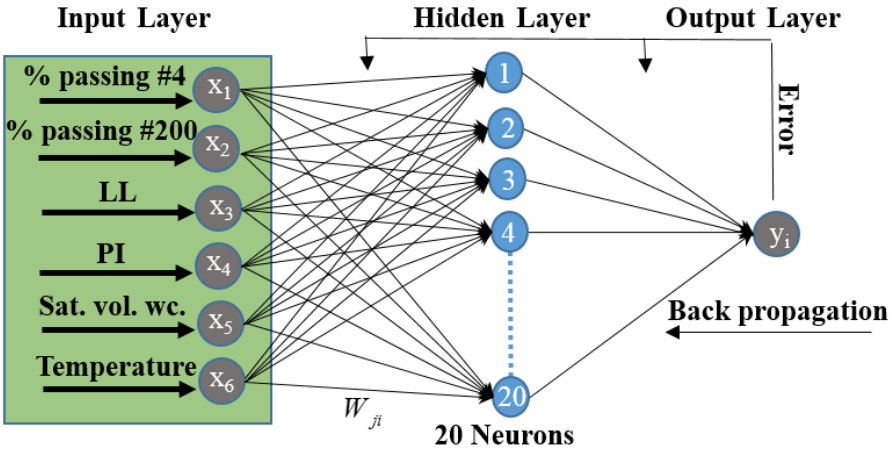

(a) Plastic soil

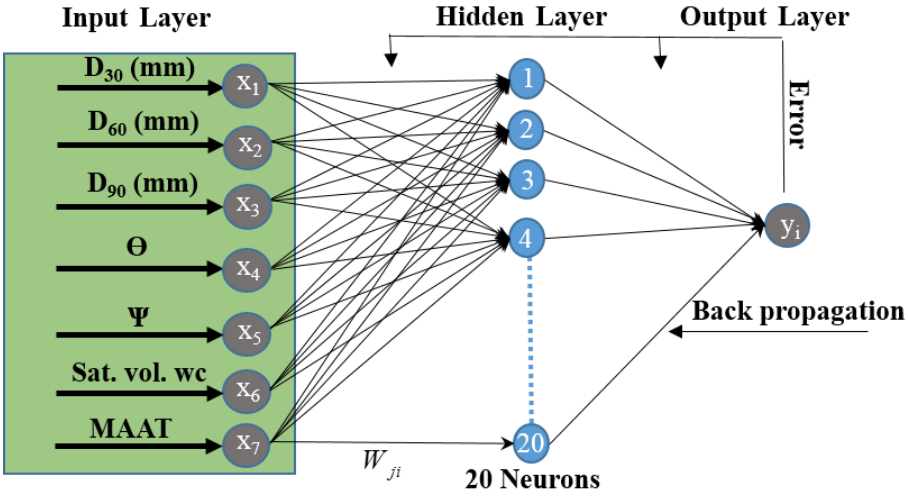

(b) Non-plastic soil

Figure 2.1 Illustration of three-layered neural network architecture

In Figure 2.1a, the input variables for plastic soil include percent passing No.4 sieve, percent passing No.200 sieve, *LL*, *PI*, saturated volumetric water content (Sat. vol. wc.) and local *MAAT* (Unit:^{0}C). Figure 2.1b shows that the input variables for non-plastic soil are D_{30}, D_{60}, D_{90}, scale parameter (Θ), shape parameter (Ψ), saturated volumetric water content and local *MAAT* (Unit:^{0}C). Herein, scale parameter Θ and shape parameter Ψ are estimated by fitting a power law model (Θx^{Ψ}) to the curve of the cumulative percent passing versus sieve size in mm. The hidden layer assigns 20 neurons to establish the connection between the output layer and the input layer.

Both the non-plastic and plastic soil models utilize the sigmoidal transfer function, as shown in Equation 2.4 (Gu et al. 2017, Saha et al. 2017).

$$f\left(I_i\right)=\frac{1}{1+\exp\left(-\varphi I_i\right)} \tag{2.4}$$

where I_i is the input quantity; φ is a positive scaling constant, which controls the steepness between the two asymptotic values 0 and 1. The ANN model determines these weight factors w_{ji} through the two major functions: training and validating.

The training data set is used to determine the trial weight factors, w_{ji} and the validating data set is employed to examine the accuracy of the model prediction. In this study, 80 percent dataset is used for training and 20 percent dataset for validation. The training algorithm uses the Levenberg-Marquardt back propagation method to minimize the mean squared error (MSE). The gradient descent weight function is employed as a learning algorithm to adjust the weight factors w_{ji}.

2.3. Prediction of SWCC Fitting Parameters Using ANN Model

The development of ANN models is to predict the SWCC parameters (i.e., a_f, b_f, c_f and h_r) in

Fredlund-Xing equation. These parameters are correlated to the soil physical properties. In this study, the ANN models are programmed using the Matlab software. The database used for training of ANN models consists of 3600 samples of plastic soil and 250 samples of non-plastic soil.

A statistical analysis was performed to determine the root mean squared error (*RMSE*) and coefficient of determination (R^2) associated with the predicted SWCC fitting parameters. The *RMSE* and R^2 are computed by using Equations 2.5 and 2.8.

Root mean squared error: $$RMSE = \sqrt{\frac{\sum (x-y)^2}{n}} \quad (2.5)$$

Residual sum of squares: $$SS_{res} = \sum (x-y)^2 \quad (2.6)$$

Total sum of squares: $$SS_{tot} = \sum (x-\bar{x})^2 \quad (2.7)$$

Coefficient of determination: $$R^2 = 1 - \frac{SS_{res}}{SS_{tot}} \quad (2.8)$$

where x is the measured SWCC fitting parameter; y is the predicted SWCC fitting parameter; and n is the number of data points. Figure 2.2 and Figure 2.3 compare the predicted SWCC parameters of plastic and non-plastic soils respectively against the measured ones using the training datasets. As shown in Figure 2.2 and Figure 2.3, the predicted a_f, b_f, c_f and h_r parameters are well coincident with the measured results. This indicates that the developed ANN models have desirable accuracy to predict the SWCC for plastic and non-plastic soils. The next section will compare these ANN models against the existing regression models in terms of model prediction accuracy.

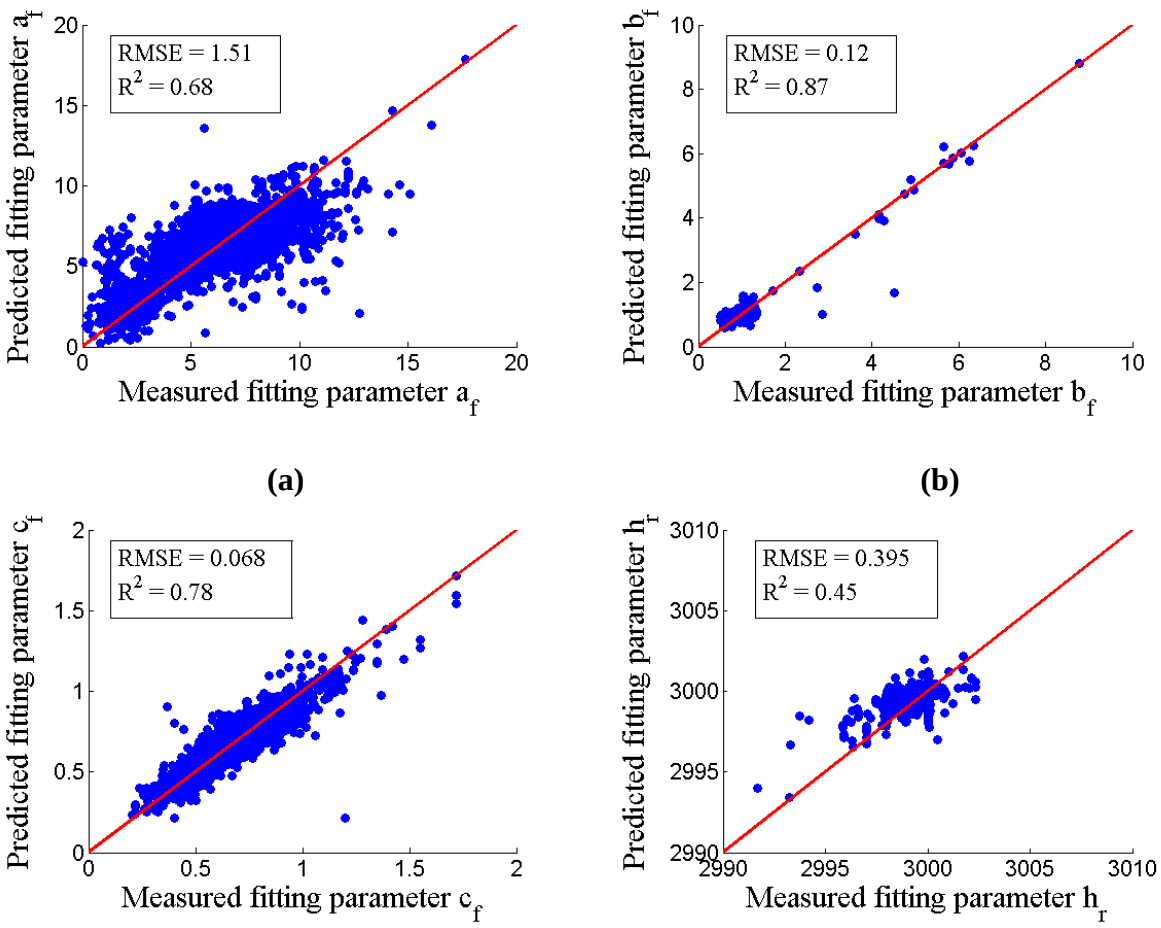

Figure 2.2 Comparison of measured versus predicted SWCC fitting parameters using ANN model for plastic soils: (a) a_f; (b) b_f; (c) c_f; and (d) h_r

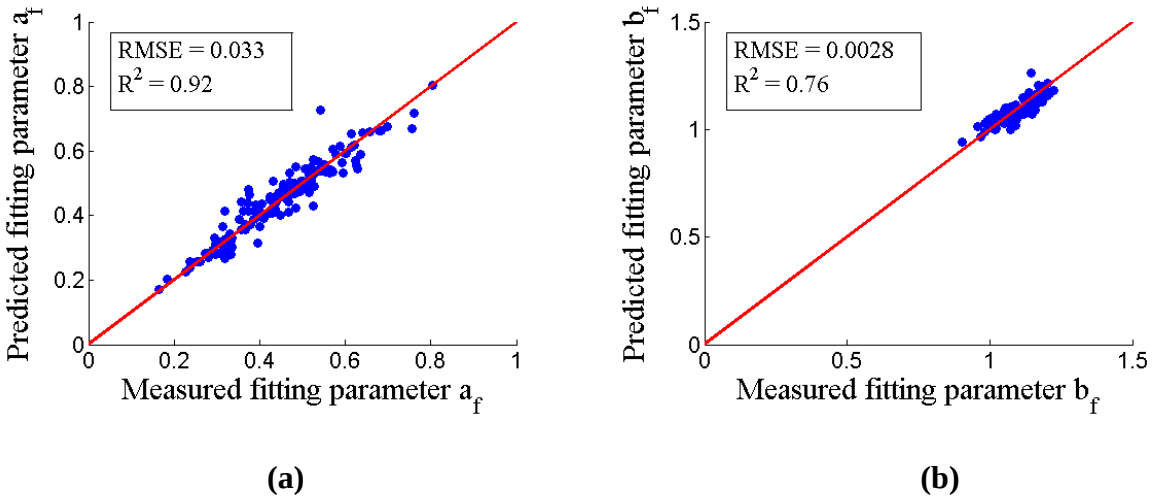

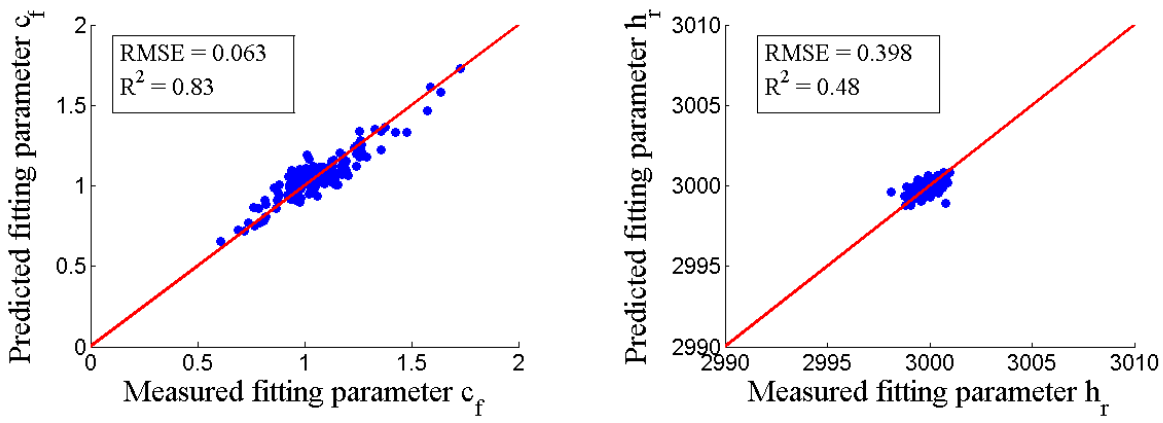

(c) **(d)**

Figure 2.3 Comparison of measured versus predicted SWCC fitting parameters using ANN model for non-plastic soils: (a) a_f; (b) b_f; (c) c_f; and (d) h_r

2.4. Comparison of ANN Model With Other Regression Models

A number of regression models have been developed to predict the SWCC fitting parameters. In this study, a comparison analysis is performed between the developed ANN models and those of the existing prediction models, including the Zapata model (Zapata et al. 2003) and Perera model (Perera et al. 2005). Table 2.1 lists the equations of these regression models.

Table 2.1 List of existing SWCC fitting parameter prediction models

Plastic Soil	Non-plastic soil
Zapata Model	
$a_f = 0.00364(wPI)^{3.35} + 4(wPI) + 11$ $\frac{b_f}{c_f} = -2.313(wPI)^{0.14} + 5$ $c_f = 0.0514(wPI)^{0.465} + 0.5$ $\frac{h_r}{a_f} = 32.44e^{0.0186(wPI)}$	$a_f = 0.8627(D_{60})^{-0.751}$ $\bar{b}_f = 7.5$ $c_f = 0.1772\ln(D_{60}) + 0.7734$ $\frac{h_r}{a_f} = \frac{1}{D_{60} + 9.7e^{-4}}$
where: w = percent of material passing No.200 sieve PI = Plasticity Index D_{60} = material diameter corresponding to 60% passing by weight of material	
Perera Model	
$a_f = 32.835\{\ln(wPI)\} + 32.438$ $b_f = 1.421(wPI)^{-0.3185}$ $c_f = -0.2154\{\ln(wPI)\} + 0.7145$ $h_r = 500$	$a_f = 1.14a - 0.5$ $a = -2.79 - 14.11\log(D_{20}) - 1.9x10^{-6} P_{200}^{4.34} + 7\log(D_{30}) + 0.055D_{100}$ $b_f = 0.936b - 3.8$ $b = \{5.39 - 0.29\ln[P_{200}(\frac{D_{90}}{D_{10}})] + 3D_0^{0.57} + 0.021P_{200}^{1.19}\}m_1^{0.1}$ $m_1 = \frac{30}{[\log(D_{90}) - \log(D_{60})]}, m_2 = \frac{20}{[\log(D_{30}) - \log(D_{10})]}$ $c_f = 0.26e^{0.758c} + 1.4D_{10}$ $c = \log(m_2^{1.15}) - (1 - \frac{1}{b_f})$ $h_r = 100$
where: D_{10}, D_{20}, D_{30}, D_{60}, D_{90}, D_{100} = material diameter corresponding to 10%, 20%,30%, 60%, 90% and 100% passing by weight of material, respectively	

The predictability of SWCC fitting parameters using the regression models above are analyzed in this study. Tables 2.2a and 2.2b list the computed *RMSE* and R^2 values for each model. The values of R^2 and *RMSE* indicate the model prediction accuracy. The higher R^2 value and the smaller *RMSE* value represent a higher prediction accuracy for the develop model (Gu et

al. 2016, Saha et al. 2018c). As presented in Tables 2.2a and 2.2b, the *RMSE* values associated with all the existing SWCC parameter prediction models are very high, meanwhile the corresponding R^2 values are extremely low. This indicates that the Zapata and Perera models have low prediction accuracy of the SWCC fitting parameters for both plastic and non-plastic soils. Among these two models, the computed *RMSE* and R^2 values are comparable with each other. This demonstrates that these models have the same level of prediction accuracy. Compared to these existing models, the developed ANN models have much higher R^2 values and smaller *RMSE* values. This indicates that the developed ANN models outperform these existing regression models in terms of prediction accuracy.

Table 2.2 Prediction accuracy of SWCC fitting parameter models

(a) Plastic Soil

Model	*RMSE*				R^2			
	a_f	b_f	c_f	h_r	a_f	b_f	c_f	h_r
Zapata	4.86	0.46	0.21	2798	0.0078	0.059	0.29	0.003
Perera	7.86	0.51	0.33	2544	0.0033	0.04	0.21	0.008
ANN	1.51	0.12	0.068	0.395	0.68	0.87	0.78	0.45

(b) Non-plastic Soil

Model	*RMSE*				R^2			
	a_f	b_f	c_f	h_r	a_f	b_f	c_f	h_r
Zapata	5.76	5.34	0.33	3000	0.009	0.00	0.018	0.01
Perera	7.95	2.19	0.68	2899	0.14	0.12	2.42E-04	0.00
ANN	0.033	0.028	0.063	0.398	0.92	0.76	0.83	0.48

Although the developed ANN models can accurately predict the SWCC fitting parameters, it is still necessary to examine the prediction accuracy of the SWCC. In the laboratory, these fitting parameters (i.e., a_f, b_f, c_f and h_r) in the Fredlund-Xing equation are calculated by fitting the SWCC with experimentally available suction-saturation data points. A

nonlinear least squared regression analysis is performed to determine the best fit parameters. In this study, the predicted SWCC fitting parameters are input into the Fredlund-Xing equation to estimate the soil suction at various water contents. The estimated soil suction values are then compared against the measured ones to investigate the model prediction accuracy.

To evaluate the suction predictability over the full range of saturation level, the matric suction values are calculated at three different degrees of saturation (i.e., 10%, 40% and 80%). The predicted matric suction values using different models were compared with experimental data at the same saturation level. Figure 2.4 shows the plots of measured versus predicted matric suction for plastic soils. Figures 2.4a, 2.4b, and 2.4c correspond to comparisons made by experimental data with the Zapata model, Perera model, and ANN model respectively. Compared to the two existing models, the developed ANN model has the least *RMSE* value and the highest R^2 value. This indicates that the developed ANN model outperforms other models to accurately estimate the matric suction of plastic soils at various degrees of saturation.

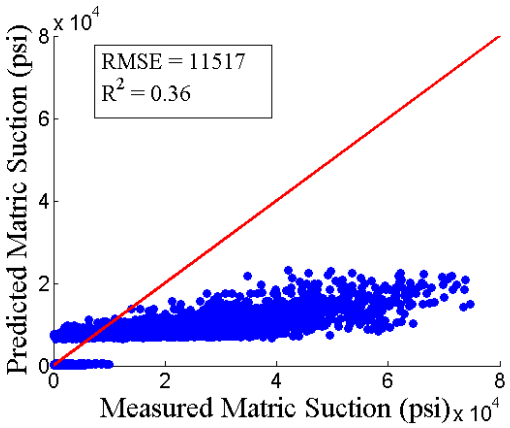

(a)

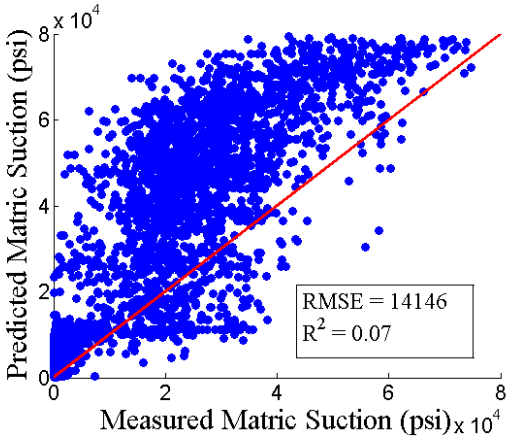

(b)

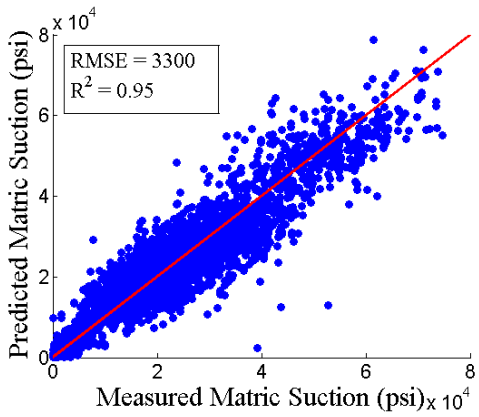

(c)

Figure 2.4 Comparison of measured versus predicted suction at various saturation levels for plastic soils: (a) Zapata model; (b) Perera model; and (c) ANN model

The obtained R2 value of 0.95 demonstrates that the developed ANN model can accurately predict the SWCC of plastic soil.

Figure 2.5 presents the measured versus predicted suction for non-plastic soils. As seen from Figures 2.5a and 2.5b, the predicted matric suction values using the existing models deviate significantly from the measured values. This indicates that the existing models yield inaccurate matric suction of non-plastic soils. As shown in Figure 2.5c, the developed ANN model has a R^2 value of 0.91, which significantly improves the prediction accuracy of the matric suction for the non-plastic soils. It is clearly concluded from Figures 2.4 and 2.5 that the developed ANN models are capable of accurately predicting the SWCC of both plastic and non-plastic soils.

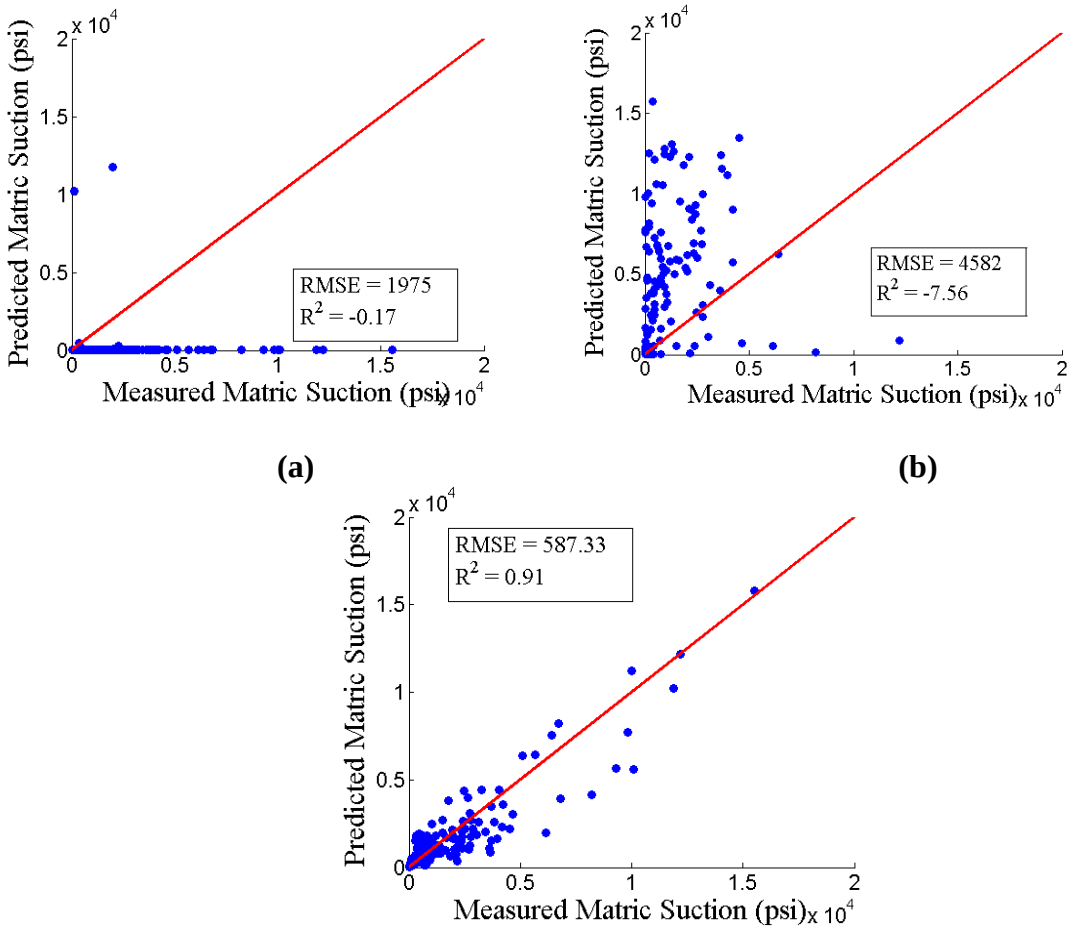

Figure 2.5 Comparison of measured versus predicted suction at various saturation levels for non-plastic soils: (a) Zapata model; (b) Perera model; and (c) ANN model

2.5. Validation of the Developed ANN Models

The validation of the prediction accuracy of the developed ANN models involves two steps, including: 1) the validation through the collected data from NCHRP 9-23A database and 2) the validation via the independent data from other literature sources.

At first, a new dataset of 500 plastic soils and 33 non-plastic soils are selected from the

NCHRP 9-23A database. The selected soil physical and climatic properties were input into the developed ANN models. Figures 2.6 and 2.7 compare the measured SWCC fitting parameters to those predicted by the ANN models for the selected plastic and non-plastic soils, respectively. It is seen that ANN model predictions have relatively small *RMSE* and high R^2 values for both cases. The determined R^2 values for plastic soils are in the range from 0.44 to 0.87, non-plastic soils show R^2 ranging from 0.49 to 0.87. This indicates that the model predicted SWCC fitting parameters match well with the measured results. The model predicted fitting parameters are then input into the Fredlund-Xing equation to estimate the matric suction values at the selected degrees of saturation.

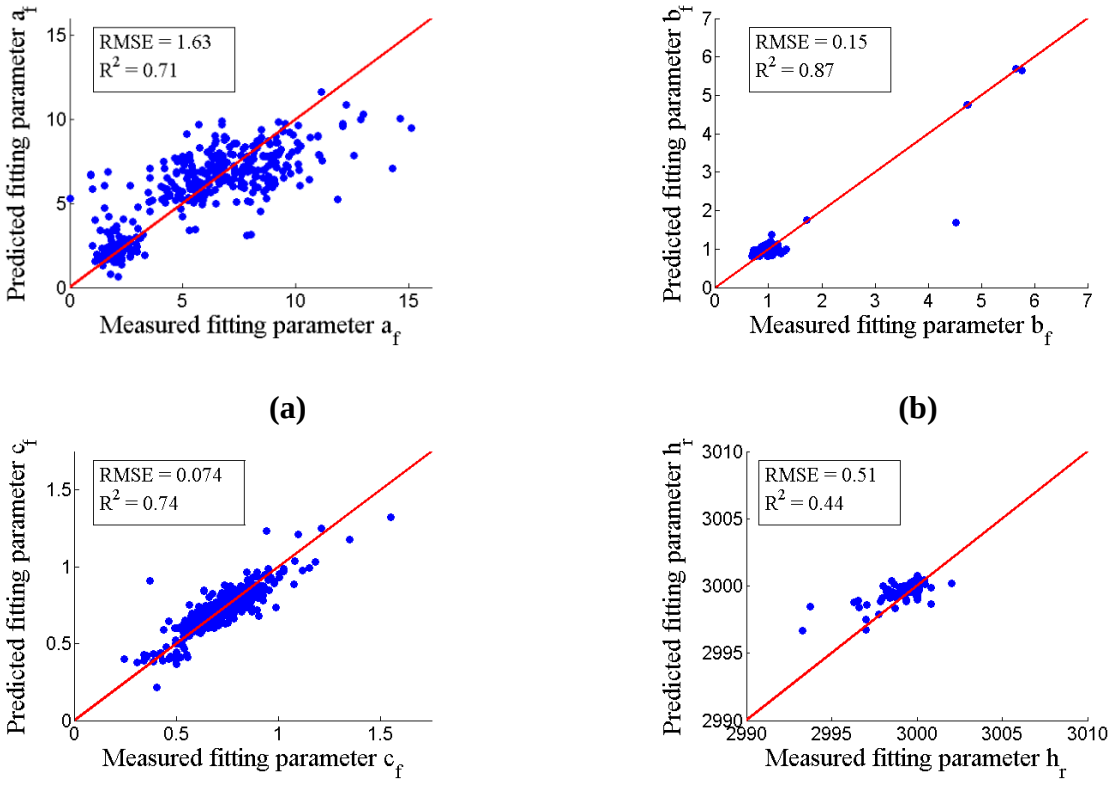

Figure 2.6 Validation of measured versus predicted SWCC fitting parameters using ANN model for plastic soils: (a) a_f; (b) b_f; (c) c_f; and (d) h_r

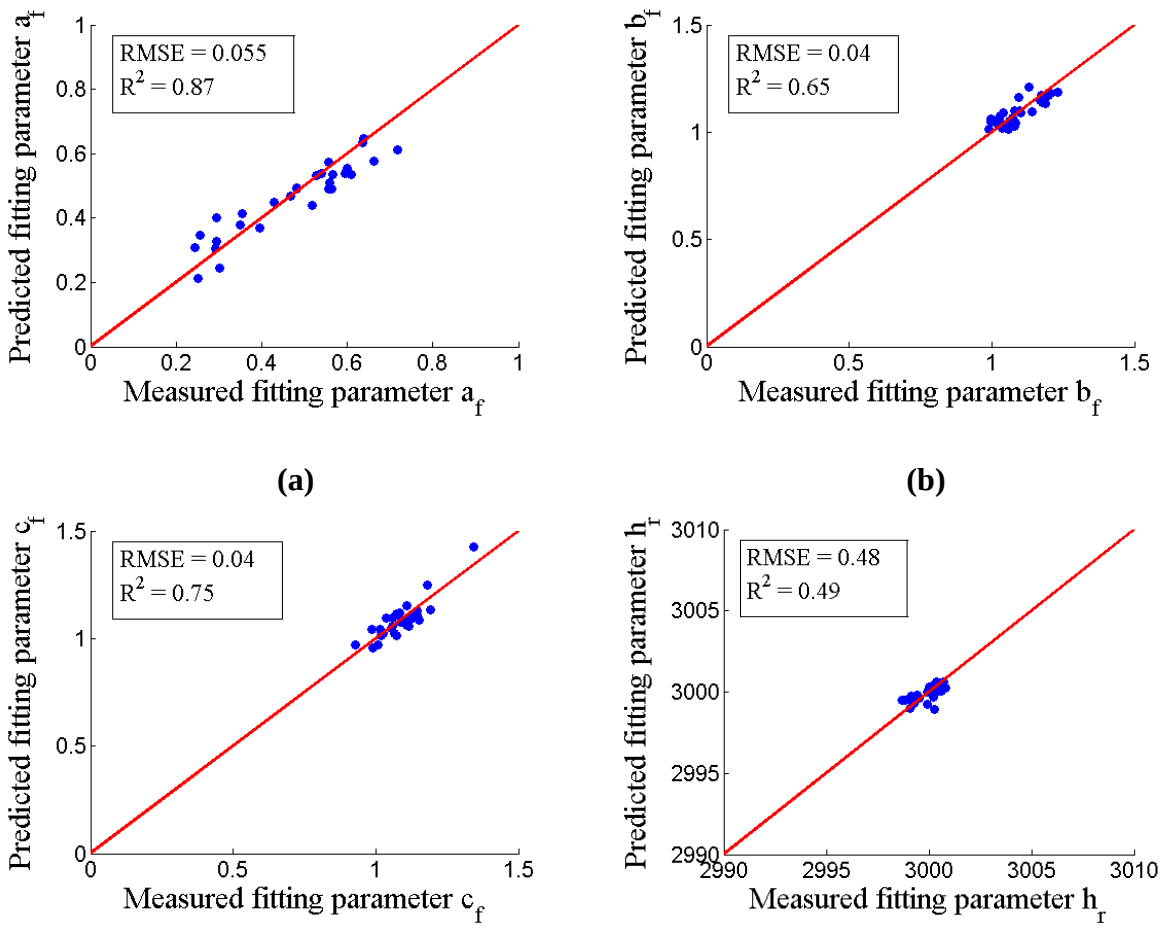

Figure 2.7 Validation of measured versus predicted SWCC fitting parameters using ANN model for non-plastic soils: (a) a_f; (b) b_f; (c) c_f; and (d) h_r

Figures 2.8a and 2.8b plot the measured versus predicted matric suction values at 10%, 40% and 80% saturation level for plastic and non-plastic soils, respectively. Results show that the predicted suction values fit well with the measured ones. Both plastic and non-plastic soil dataset show a R^2 value greater than 0.90. This validates that the developed ANN models provide desirable prediction accuracy of the SWCC.

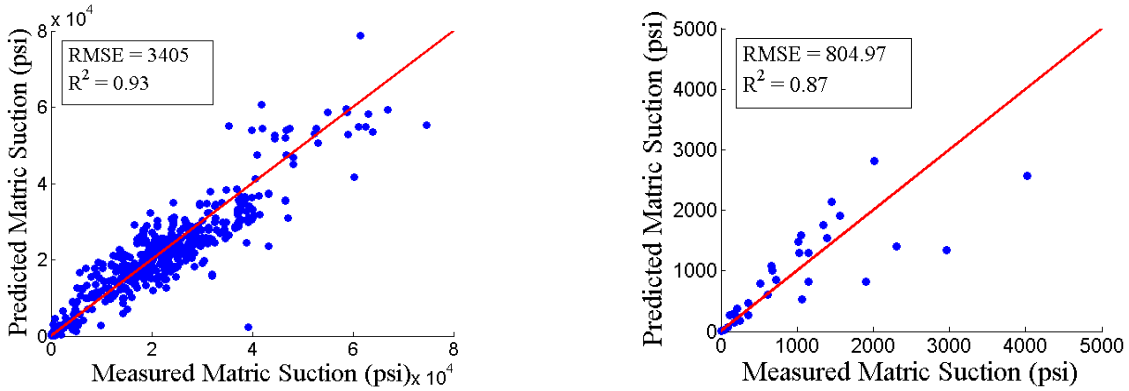

(a) **(b)**

Figure 2.8 Validation of measured vs ANN predicted suction at various saturation levels for unbound materials: (a) plastic soil; (b) non-plastic soil

To further validate the prediction accuracy of the developed ANN models, the independent data sources (i.e., 2 plastic and 2 non-plastic soil data) are collected from the literature (Salour et al. 2013; Ruttanaporamakul 2012; and Gupta et al. 2007) . All of these soil physical and climatic properties are shown in Tables 2.3a and 2.3b, which are used as inputs of the developed ANN models.

Table 2.3 Input parameters collected from literature for model validation

(a) Plastic soil

Reference	Soil source	#4 sieve	#200 sieve	*LL*	*PI*	Sat. vol. wc*	*MAAT(^{0}C)*
Ruttanaporamakul et al (2012)	Louisiana	100	45	23	12	5.4	18.5
Gupta et al. (2007)	Red Lake Falls	100	93.9	29	10	8.17	3.9

Note: *Sat.vol.wc = Saturated volumetric water content

(b) Non-plastic soil

Reference	Soil source	D_{30}	D_{60}	D_{90}	Sat. vol. wc	*MAAT(^{0}C)*
Ruttanaporamakul et al. (2012)	Mississippi	0.075	0.1021	1.41	18.76	17.9
Salour et al. (2013)	Torpsbruk	0.0911	0.6151	11.23	15.73	6.91

Figures 2.9a and 2.9b compare the measured and predicted SWCCs for plastic and non-plastic soils, respectively. As illustrated, the SWCC curves generated by using the predicted parameters from the predicted ANN model produce good fits with the experimental curves. In Figure 2.9a, the model predicted matric suction values of plastic soils (i.e., Red Lake Falls and Louisiana soils) are generally coincident with the experimental results. A small deviation is observed in the residual region for the Louisiana soil. This is due primarily to the effect of the c_f model which has a lower R^2 than a_f and b_f parameters. Similarly, Figure 2.9b presents that the predicted matric suction values of non-plastic soils (i.e., Torpsbruk and Mississippi soils) are in good agreement with the measured results. Considering the fact that the SWCC curve generated from experiment involves high level of variability, the difference between predicted and experimental curves are considered to be sufficiently accurate.

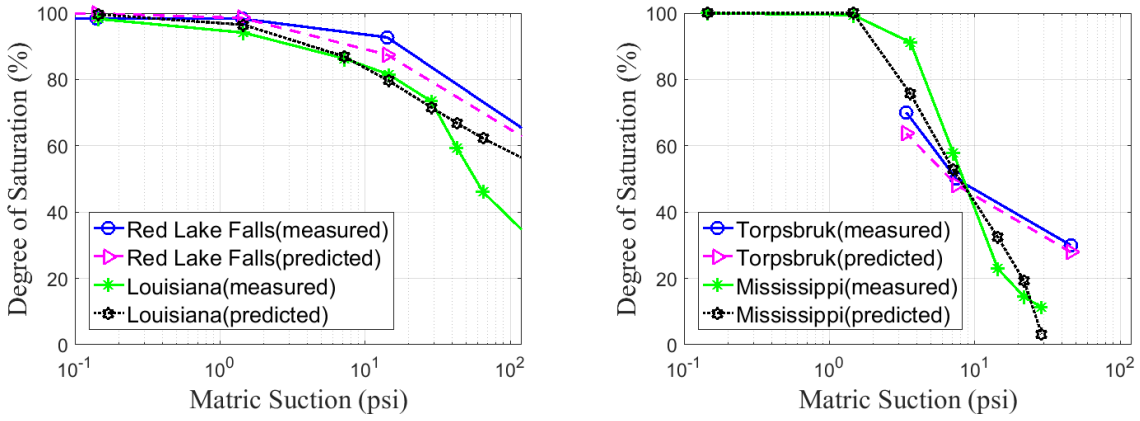

(a) Plastic Soil **(b) Non-plastic soil**

Figure 2.9 Comparison of measured versus predicted SWCC curves for unbound materials: (a) plastic soil; (b) non-plastic soil

2.6. Conclusions

This study proposes an artificial neural network (ANN) approach to predict the SWCC fitting parameters in the Fredlund-Xing equation by using the selected soil physical properties and climatic parameters. Two three layer ANN model are developed for plastic and non-plstic soils respectively and both models shows higher prediction accuracy compared to the existing regression models. The predicted fitting parameters are then input into the Fredlund-Xing equation to estimate the SWCC for unbound materials.

3. USE OF A MECHANISTIC-EMPIRICAL APPROACH TO PREDICT EQUILIBRIUM SUCTION IN SUBGRADE SOIL

3.1. Introduction

The pavement subgrade moisture condition is critical because it directly affects the strength and stiffness of the pavement structure (Perera et al., 2004). Subgrade soils are usually unsaturated and the resilient modulus of the subgrade soil is highly dependent on the degree of saturation and the corresponding matric suction (Liang et al., 2008; Oloo and Fredlund, 1998; Wolfe and Butalia, 2004; Khoury and Zaman, 2004; Gu et al., 2014; Luo et al., 2017; Saha et al., 2018b). Past studies have shown that matric suction in the subgrade layer reaches an equilibrium condition several years after construction (Aitchison and Richards, 1965; Basma and Ai-Suleiman, 1991). Hence, accurate approximation of equilibrium suction underneath pavement structures is required for accurate determination of long-term resilient modulus of the subgrade soil and thereby reliable prediction of pavement performance.

An Enhanced Integrated Climatic Model (EICM) is implemented in the current Pavement ME Design guide to incorporate the climatic design inputs. The EICM is a one dimensional heat and moisture flow program developed by the Federal Highway Administration (FHWA) for predicting the moisture condition in subgrade soils. The EICM uses the depth to ground water table to compute suction. However, this model will yield inaccurate suction values if the water table data is missing or the water table depth is greater than 7m. Current studies demonstrate that many other factors affect the suction profile in addition to ground water table. These include precipitation, evapotranspiration, field capacity etc. (Russam and Coleman, 1961 and Coleman,

1965). This study aims to develop an improved prediction model of equilibrium suction, which takes into account a variety of influence factors.

Matric suction in soil reaches an equilibrium condition at a certain depth of the moisture active zone (Z_m). There are primarily two different approaches available to determine the equilibrium suction: (1) correlation with a rational climatic index; and (2) statistical model based on climatic factors and soil index properties.

A climatic index that is related to the soil environment is based on a process in which the potential for soil moisture exchange is determined by the frequency analysis of precipitation and evapotranspiration. A number of climatic indices, e.g., Thornthwaite Moisture Index (TMI) (Thornthwaite, 1948) and Penman Index (Penman, 1963) were developed to correlate with various annual moisture balance indicators. TMI was correlated with depth of the moisture active zone and equilibrium suction (Carpenter et al., 1974; Edris and Lytton, 1976; Fityus and Buzzi, 2008; and Lytton et al., 2005). Gay (1994) developed a relationship between mean annual moisture depth and TMI. He used climatic data from 12 sites in Texas to establish a relationship between TMI values and mean moisture depth. The Post Tensioning Institute [PTI] (2004) and the Australian standard AS2870 (2011) developed a correlation between the subgrade equilibrium suction and TMI.

However, existing studies show that suction beneath covered areas depends on both climatic factors and soil index properties (Russam and Coleman, 1961; Fredlund and Rahardjo, 1993; and Zapata, 1999). Recently, Witzack et al. (2006) proposed a statistical model for predicting equilibrium suction of subgrade soil based on P_{200} and wPI parameters, where P_{200} is the percent of material passing No. 200 sieve and wPI is the product of P_{200} and plasticity index.

These correlation models were developed by using a limited number of data sets that are highly variable. To improve the prediction accuracy of equilibrium suction in a subgrade layer, a mechanistic-empirical approach was adopted in this study which involves the transient suction profile and soil water retention characteristics of soil as well as climatic factors.

The primary objective of this chapter is to introduce and support a method to predict equilibrium suction from TMI and soil plasticity index values. The following section describes the generation of the TMI contour map in a Geographic Information System (GIS) platform. This contour map provides the input required for determination of equilibrium suction of the subgrade soil using a mechanistic-empirical approach from which a contour map of the equilibrium suction values for the continental U.S is plotted. Following the description of the contour maps, a regression equation is presented that can be used to predict equilibrium suction using TMI and the plasticity index (PI). Subsequently a parametric study is described that was used to evaluate the effect of soil class and vegetation on equilibrium suction. The concluding section of this paper summarizes the paper's significant findings and addresses their utility.

3.2. Development of a GIS-Based Contour Map of Thornthwaite Moisture Index (TMI)

TMI is a moisture index that reflects climate and soil humidity (Thornthwaite, 1948). This index is calculated using soil moisture balance in terms of rainfall, potential evapotranspiration and the depth of available moisture balance stored in the rooting zone of vegetation at a particular site.

Figure 3.1 shows the TMI contour map of the United States originally developed by Thornthwaite (1948). Various improvements and simplifications have been proposed for calculating moisture balance since the development of original TMI map. TMI values primarily depend on adopted calculation methods and the time span over which the database was

developed (Sun et al., 2017). Olaiz et al. (2018) performed a comparison study of the four different TMI contour maps developed from 1948 to 2006, and concluded that the map developed by Witczak et al. (2006) matched closely with the original Thorthwaite map. In this study, Witczak's model is used to calculate the TMI value of the continental United States. A detailed description of the process used to develop the TMI map in the GIS platform is presented in the following paragraphs.

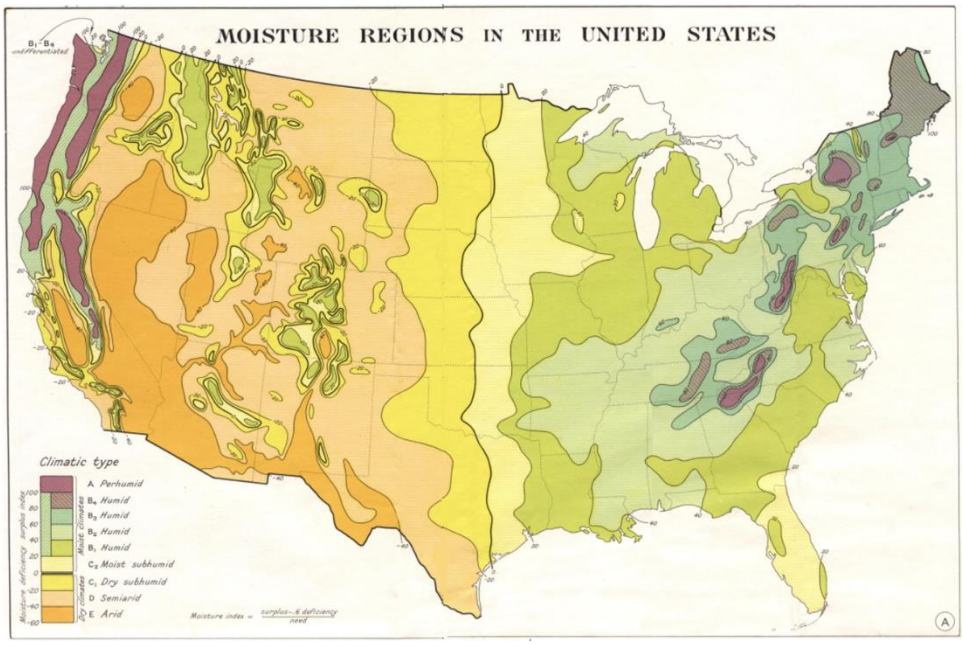

Figure 3.1 Thornthwaite moisture index distribution map of the United States (After Thornthwaite 1948)

A GIS-based TMI contour map was generated based on the precipitation and temperature metadata file. The spatial metadata files were collected from PRISM (Parameter-elevation Regressions on Independent Slopes Model) climate mapping system (Daly et al. 1994, 2002, 2008) at Oregon State University. The PRISM mapping system was developed based on the

National Oceanic and Atmospheric Administration (NOAA) climate database, which includes in situ measurements of temperature and precipitation from 5,852 weather stations across the continental United States. PRISM uses a weighted regression scheme to account for complex climate regimes associated with orography, rain shadows, temperature inversions, slope aspect, coastal proximity, and other factors and depicts climatological normal (from 1981 to 2010) at 30-arcsec (800 meters) resolution. Figure 3.2 shows the annual average precipitation (*P*) and temperature contour map of the United States in the GIS platform.

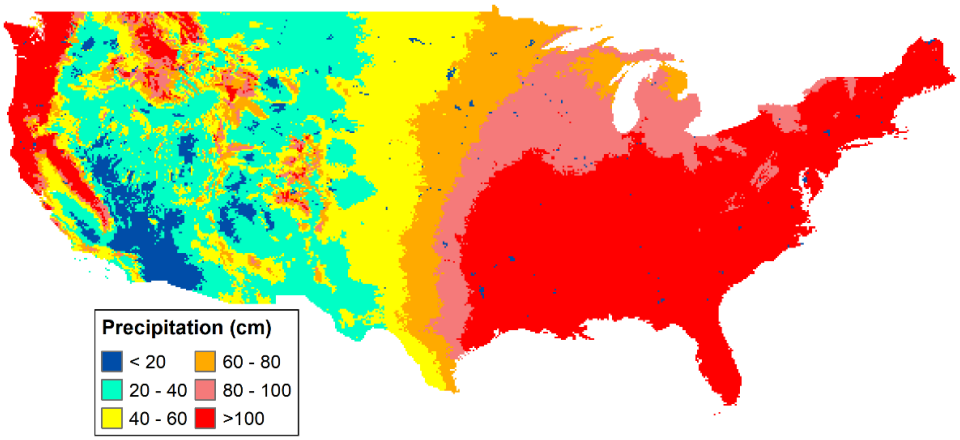

(a)

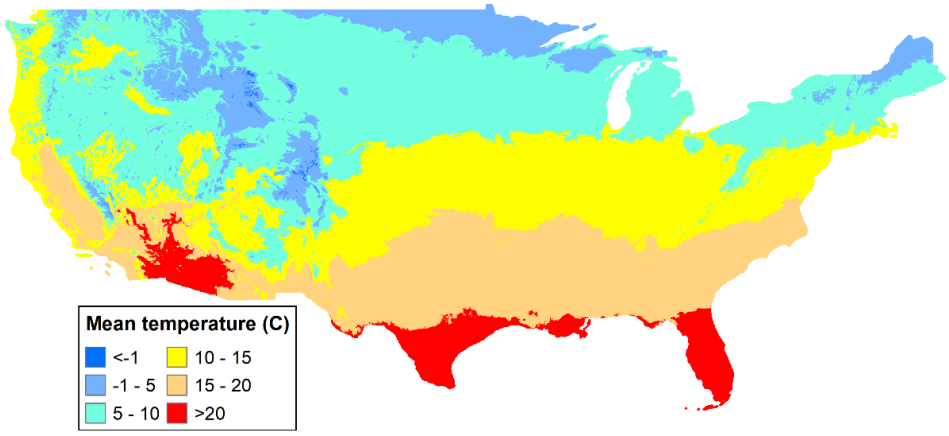

(b)

Figure 3.2 GIS map of the average annual (a) precipitation and (b) temperature (from 1981 to 2010)

Potential evapotranspiration was calculated using monthly average temperature (t_i) for the site in question (Wilm et al., 1944). An annual heat index (H_y) was determined using Equation 3.1.

$$H_y = \sum_{i=1}^{12} (0.2t_i)^{1.54} \quad (3.1)$$

Then, monthly potential evapotranspiration was quantified using Equation 3.2

$$pe_i = 1.6\left(\frac{10t_i}{H_y}\right)^a \quad (3.2)$$

where pe_i is the potential evapotranspiration in the ith month; and

$$a = 6.75x10^{-7} H_y^{\,3} - 7.71x10^{-5} H_y^{\,2} + 0.01792 H_y + 0.49239$$

The pe_i value represents potential evapotranspiration over a period of 30-days with 12 hour daylight duration. The effect of daily variations in daylight on monthly potential evapotranspiration were determined based on a correction factor, d_i introduced by Mckeen and Johnson (1990). The corrected potential evapotranspiration was calculated using Equation 3.3.

$$PE_i = pe_i\left(\frac{d_i n_i}{30}\right) \quad (3.3)$$

where PE_i is the monthly corrected potential evapotranspiration (unit: cm); d_i is the daylight correction factor for each month (unit: hrs); n_i is the number of days in the given month.

The average annual potential evapotranspiration (PE_y) was calculated by summing PE_i over a 12 month period (Equation 3.4).

$$PE_y = \sum_{i=1}^{12} PE_i \quad (3.4)$$

Figure 3.3 depicts the calculated PE_y map of continental United States on the GIS platform.

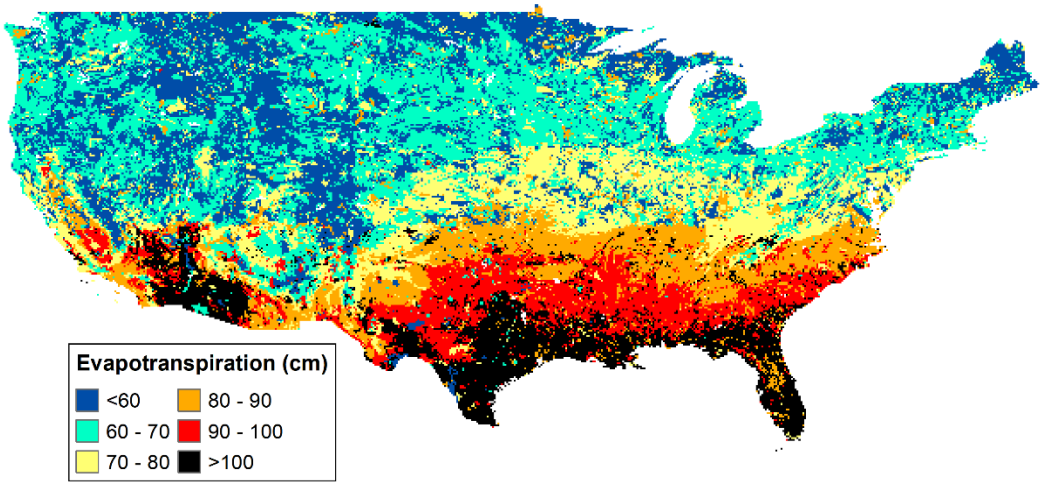

Figure 3.3 GIS map of the average annual potential evapotranspiration (from 1981 to 2010)

Finally, the TMI value is calculated using Equation 3.5 and plotted in Figure 3.4

$$TMI = 75(\frac{P}{PE_y} - 1) + 10 \quad (3.5)$$

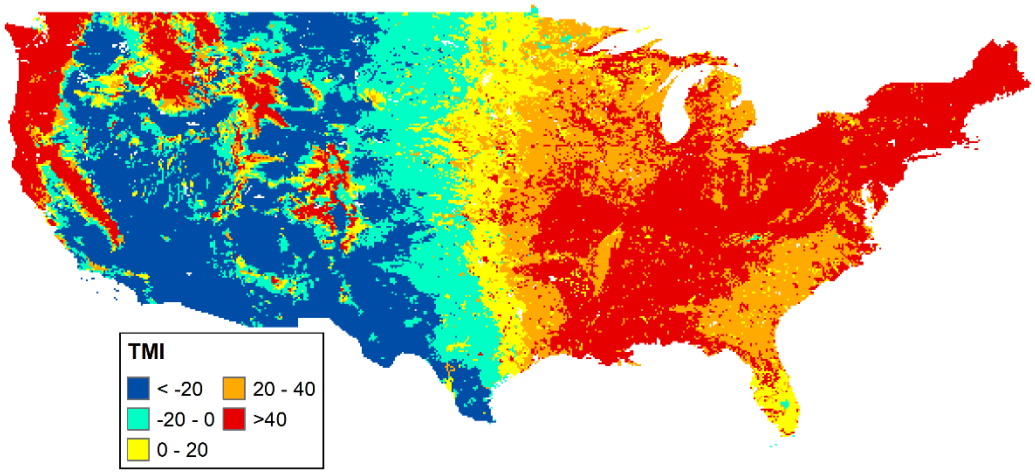

Figure 3.4 GIS map of Thornthwaite moisture index (from 1981 to 2010)

To validate the TMI contour map developed as described in the preceding approach, TMI values were compared with the original map at specific locations. Table 3.1 lists the collected

TMI values for specific locations from the original TMI map (Snethen et al., 1977, McKeen, 1981, Wray, 1989, and Jayatilaka et el., 1992). The corresponding geographic coordinates (latitude and longitude) of these locations are included in the Table 3.1.

Table 3.1 Collected TMI values for the validation of developed TMI contour map

Locations	Latitude	Longitude	TMI (original map)	Locations	Latitude	Longitude	TMI (original map)
Gallup, New Mexico	35.52	-108.74	-32	Port Arthur, Texas	29.88	-93.93	26.8
Synder, Texas	32.71	-100.91	-25	Lake Charles, Louisiana	30.22	-93.21	58.2
Durant, Oklahoma	33.99	-96.39	18.4	Reliance, South Dakota	43.87	-99.60	-12.9
Houston, Texas	29.76	-95.36	14.8	Ellsworth, Kansas	38.73	-98.22	9.1
San Antonio, Texas	29.42	-98.49	-21.3	Limon, Colorado	39.26	-103.69	-16.8
El Paso, Texas	31.76	-106.48	-46.5	Price, Utah	39.59	-110.81	-36.4
Monroe, Louisiana	32.51	-92.11	65.1				

Figure 3.5 compares the TMI values from the original map and the contour map developed in this study, shown in Figure 3.4. TMI values were extracted from the map developed in this research for selected geographic coordinates using ArcGIS software. A statistical analysis was performed to determine the coefficient of determination (R^2) associated with the TMI values from original and developed contour maps. This correlation resulted in a R^2 value of 0.93 indicating that the TMI contour map developed in this research is in good agreement with the original map.

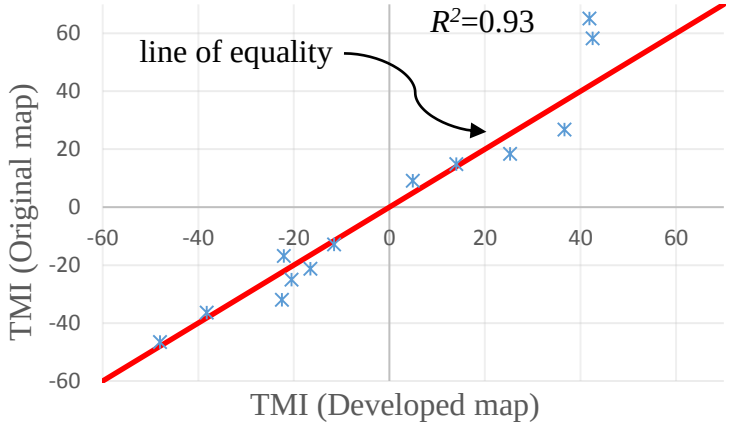

Figure 3.5 Comparison of TMI values from original map and the developed contour map

The next section of this chapter describes a mechanistic-empirical approach used to determine equilibrium suction within the soil using the TMI map developed in this section. To relate the TMI value with the soil properties for a specific location, the total map area of the continental United States was divided into 74,400 map units. The map units define the map areas identified in the Soil Survey Geographic (SSURGO) database that was developed by the National Cooperative Soil Survey. These areas are identified based on soil type and other components that have unique properties, interpretations, and productivity. The zonal distribution toolbar in ArcGIS software was used to calculate the average TMI value of each map unit.

3.3. Development of a Mechanistic-Empirical Model to Determine Equilibrium Suction

A fundamental method to determine equilibrium suction was developed in this study, which involves a steady state diffusion equation proposed by Mitchell (Mitchell, 1979) and a functional relationship between TMI and annual average moisture depth established by Gay (1994). Mitchell (1979) expressed matric suction at a depth *z* in the soil profile by solving a two

dimensional diffusion equation with surface boundaries subject to suction change, shown in Equation 3.6

$$u(z) = u_e \pm u_0 * e^{-\sqrt{\frac{\pi n}{\alpha}} z} \quad (3.6)$$

where $u(z)$ is the suction at depth *z* expressed on the pF scale; u_e is the equilibrium value of suction on the pF scale; u_0 is the suction profile amplitude; *n* is the number of suction cycles per second (1 year = 365 x 24 x 60 x 60 seconds); α is the unsaturated soil diffusion coefficient (unit: cm^2/sec); *z* is the depth below the surface (unit: cm).

Figure 3.6 illustrates a typical suction profile in unsaturated soil from the surface to the depth of the moisture active zone, Z_m. The terms u_{dry} and u_{wet} represent soil suction at the surface corresponding to an air dry state and soil field capacity, respectively. The terms $(u_{dry}')z_m$ and $(u_{wet}')z_m$ denote the suction in dry and wet profiles, respectively, at a depth of Z_m. The term u_{dry} is assumed to be 4.5 pF and 5.7 pF for vegetation and non-vegetation areas, respectively, whereas u_{wet} represents 3 pF suction level (FPA, 2017; Gay, 1994).

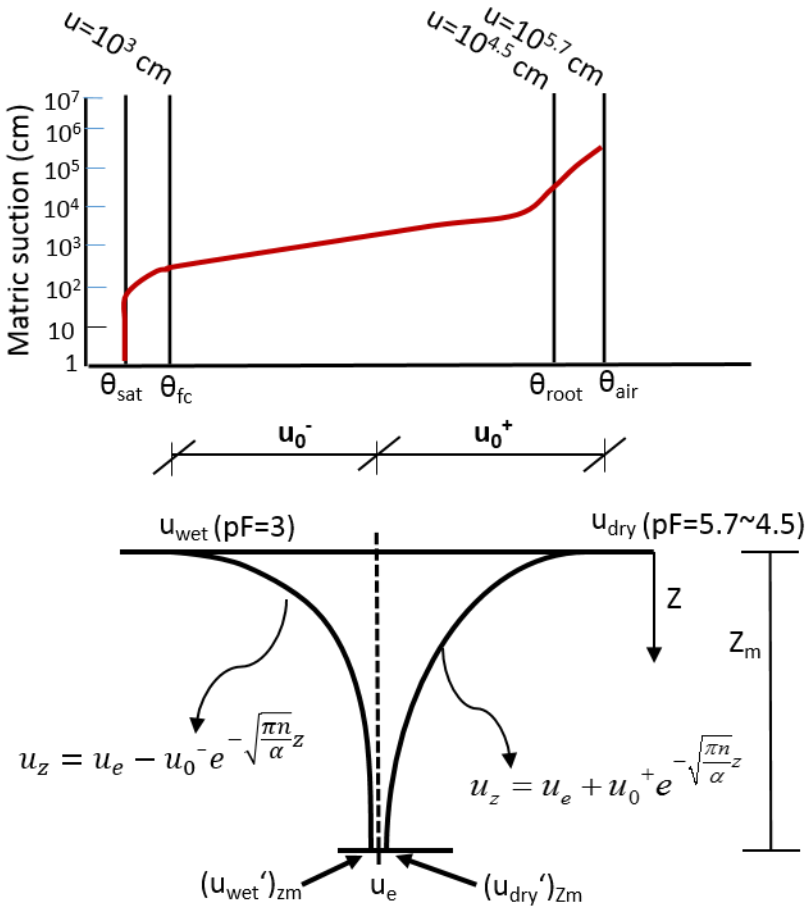

Figure 3.6 Typical suction profile in unsaturated soil between wet and dry state

The presence of vegetation significantly affects the depth of Z_m (Cameron, 2001). If the site has vegetation at the surface, Z_m is at least two feet deeper than the deepest vegetation root observed in the soil (FPA, 2017). However, when there is no vegetation in the surface, Z_m is the depth of desiccation. Several experimental studies were performed by FPA (2017) and Lytton et al. (1997) and the average depths of Z_m in non-vegetation and fully vegetation area were estimated to be 9.39 feet and 21 feet respectively. It is observed that the depth of Z_m is dependent on the amount of vegetation on the surface. To accurately determine the depth of Z_m, a vegetation cover map of continental United States is presented in the next section of this paper.

3.3.1. Calculation of the Fraction of Vegetation Cover

NOAA Climate Data Records (CDR) provide historical climate information using data from weather satellites. Normalized Difference Vegetation Index (NDVI) data were collected from this dataset, which was derived from surface reflectance data acquired by the Advanced Very High Resolution Radiometer (AVHRR) sensor. This long-term record spans from 1981 to 2013 and utilizes AVHRR data from six NOAA polar orbiting satellites. NDVI data were collected in Georeferenced Tagged Image File Format (GeoTIFF) with embedded geographic information for GIS applications.

The method proposed by Brunsell and Gillies (2003) was used in this study to obtain the fraction of vegetation cover from NDVI. The method scales the NDVI to obtain the fraction of vegetation cover (F_r) between bare soil and a full canopy and is expressed in Equations 3.7 and 3.8

$$N^* = \frac{NDVI - NDVI_0}{NDVI_{max} - NDVI_0} \tag{3.7}$$

$$F_r = (N^*)^2 \tag{3.8}$$

where $NDVI_0$ is the bare soil NDVI value set as 0.14; and $NDVI_{max}$ is the maximum NDVI corresponding to full cover dense vegetation set as 0.75.

Figure 3.7 shows the F_r map for the continental United States calculated using the raster calculator function in ArcGIS.

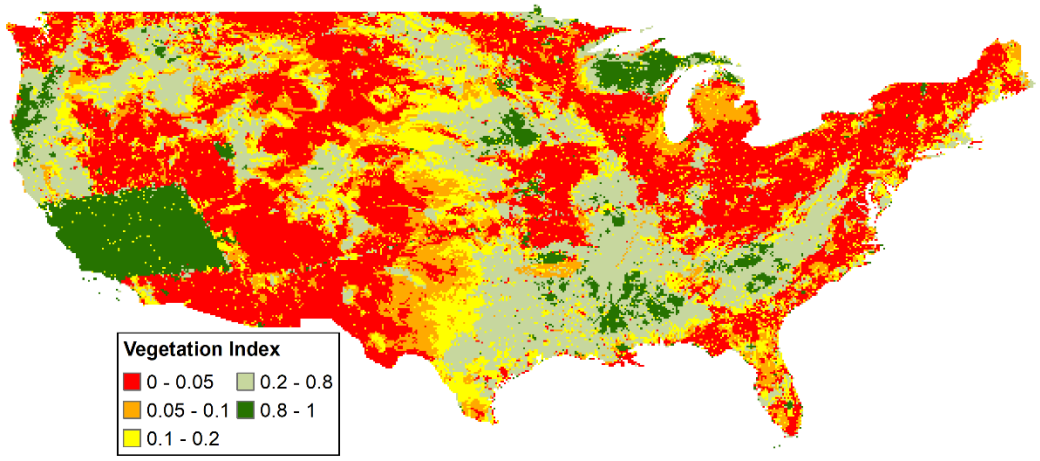

Figure 3.7 GIS map of vegetation cover

The Z_m value for specific sites were then determined by linearly interpolating F_r between the average Z_m of bare soil (9.39 feet) and full cover vegetation (21 feet). The calculated Z_m values were used to determine the maximum available moisture depth and subsequently establish a relationship between maximum available moisture depth and the mean moisture depth, which corresponds to the matric suction at equilibrium.

3.3.2. Calculation of Maximum Available Annual Moisture Depth (d_{am})

Maximum available annual moisture depth, d_{am} represents the maximum depth of moisture that is lost from soil during a transition from the wet state to the dry state at the root potential of resident vegetation. It is determined by the area of volumetric water content profile between dry and wet states. Figure 3.8 illustrates the volumetric water content (θ) profile where total moisture is stored between θ_{dry} and θ_{wet}. Herein, $(u_{dry}')z_m$ and $(u_{wet}')z_m$ are calculated using Equation 3.6 when u_e equals 3.0 pF.

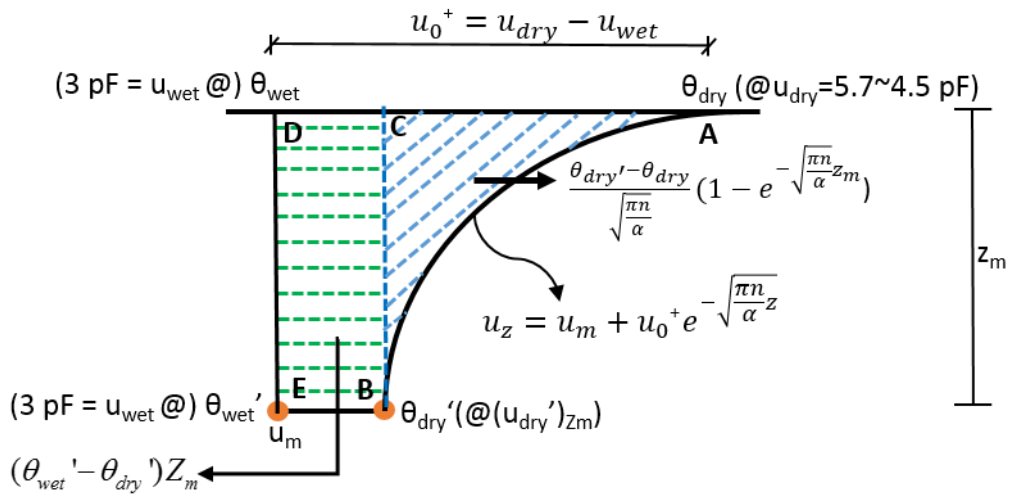

Figure 3.8 A schematic figure of maximum available annual moisture depth (d_{am})

The unsaturated diffusivity coefficient, α represents the slope of the suction profile. α was determined as a function of the slope of soil water-characteristics curve (SWCC), $\partial\theta_w / \log \partial h$ and saturated soil water permeability (van Genuchten, 1980).

$$\alpha = \frac{k_{sat}}{\partial\theta_w / \log \partial h} \tag{3.9}$$

Saturated soil water permeability, k_{sat}, was collected for all map units from the Natural Resource Conservation Service (NRCS) database. The value of *n* was assumed to be 1.0 cycle per year for all sites. The terms θ_{dry}, θ_{wet}, θ_{dry}' and θ_{wet}' were calculated using the SWCC for a particular site. The Fredlund-Xing equation was used to estimate the relationship between matric suction and volumetric water content, as shown in Equations 3.10 and 3.11 (Fredlund and Xing, 1994).

$$\theta_w = C(\mathrm{h})\ \mathrm{x}[\frac{\theta_{sat}}{\{\ln[\mathrm{e}+(\frac{h}{a_f})^{\mathrm{b_f}}]\}^{\mathrm{c_f}}}] \quad (3.10)$$

where h represents matric suction in units of cm of water and $C(h)$ is a correction factor defined as

$$\mathrm{C}(h) = 1 - \frac{\ln(1+\frac{h}{h_r})}{\ln[1+(\frac{1.021x10^7}{h_r})]} \quad (3.11)$$

The four fitting parameters i.e., a_f, b_f, c_f and h_r in Equations 3.10 and 3.11 were predicted using the artificial neural network (ANN) model developed by Saha et al. (2018a). Soil physical properties such as gradation, Atterberg limits, saturated volumetric water content (θ_{sat}) and mean annual air temperature (*MAAT*) were used as input parameters and the fitting parameters are obtained as output.

Finally, d_{am} can be expressed as the sum of areas **ABC** and **BCDE** in Figure 3.8 or according to Equations 3.12 and 3.13.

$$d_{am} = \int_0^{z_m} [\theta_{wet}(z) - \theta_{dry}(z)] \quad (3.12)$$

$$d_{am} = \frac{\theta_{dry}' - \theta_{dry}}{\sqrt{\frac{n\pi}{\alpha}}}(1 - e^{-\sqrt{\frac{n\pi}{\alpha}}z_m}) + (\theta_{wet}' - \theta_{dry}')z_m \quad (3.13)$$

In the moisture balance process, the moisture depth or soil moisture storage reaches an equilibrium condition, which is denoted as the mean annual moisture depth, d_m. The relationship between d_{am} and d_m will be described in the next section.

3.3.3. Relationship between Mean Annual Moisture Depth (d_m) and Maximum Available Annual Moisture Depth (d_{am})

The mean annual moisture depth (d_m) is not only dependent on water retention and diffusivity characteristics of soil, but is also affected by climatic factors. As discussed earlier, TMI is an indicator of annual moisture balance of a specified location based on precipitation, evaporation, deficit and runoff. In this study Gay's approach (Gay, 1994) was adopted to incorporate climatic factors in addition to soil characteristics to estimate moisture depth at equilibrium. He computed equilibrium moisture depth from the input of TMI (annual precipitation*; P*, potential evapotranspiration; *PE*), and the depth of maximum available moisture (d_{am}). When TMI (the difference between *P* and *PE*) is positive, water was added to the annual moisture storage up to a maximum value of d_{am}. If TMI is negative, soil moisture loss occurs and was subtracted from storage up to a minimum value of zero.

Gay (1994) collected climatic data from 12 sites and developed the relationship between d_m and TMI. In order to fit a rational function between TMI and d_m, it is necessary to establish the limits of the function. The dependent variable d_m logically has a maximum possible value of d_{am} and a minimum value of zero. In order to establish the limits of the assumed independent variable TMI, Equation 6 was examined. It was deduced from Equation 6 that the minimum value of TMI occurs if there is no precipitation for the entire year. Under this circumstance, the minimum value or lower bound of the TMI would be equal to -65, while the upper bound of TMI theoretically goes to infinity.

To establish the relationship between TMI and d_m, Juarez-Badillo's approach was applied in this study (Juarez-Badillo, 1975). The functional domains for the variables are shown in

Figure 3.9. The real domain for T (= TMI + 65) and moisture depth, *d* are $[0, \infty]$ and [0, d_{am}] respectively.

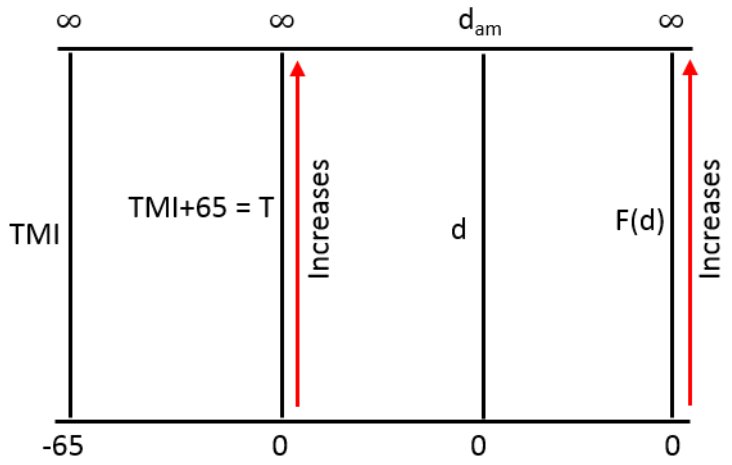

Figure 3.9 Functional domains of TMI, T, *d* and F*(d)*

The real domain for variable *d* is incomplete and therefore a function F(*d*) is needed that is similar and straight (i.e. increasing in the same direction) to the real domain of variable, T. The following function represents the simplified function form for *d* that satisfies these boundary conditions.

$$F(d) = [\frac{1}{d_{am} - d_m} - \frac{1}{d_{am}}] \tag{3.14}$$

Assuming a linear rate of change between *F(d)* and T, and integrating them within the limits of the domains shown in Figure 3.9, the final expression for d_m is obtained in Equation 3.17

$$\gamma \frac{dT}{T} = \frac{dF(d)}{F(d)} \tag{3.15}$$

$$\gamma \ln[\frac{T}{T_1}] = \ln[\frac{\frac{1}{d_{am} - d_m} - \frac{1}{d_{am}}}{\frac{1}{d_{am} - d_1} - \frac{1}{d_{am}}}] \quad (3.16)$$

$$d_m = \frac{d_{am}}{[1 + \frac{d_{am} - d_1}{d_1 (\frac{T}{T_1})^{\gamma}}]} \quad (3.17)$$

The parameters γ , T_1 and d_1 were regressed against the measured values of the depth of mean annual moisture, d_m for 17 locations (Snethen et al., 1977, McKeen, 1981, and Jayatilaka et el., 1992). The resulting expressions of γ , d_1 and T_1 are given by Equations 3.18 through 3.20

$$\gamma = 0.00547 * d_{am} \quad (3.18)$$

$$d_1 = 0.6388 * d_{am} \quad (3.19)$$

$$T_1 = 223.82 * d_{am} \quad (3.20)$$

Equilibrium suction was then calculated using the d_m value at each location, which included the regression parameters. Equation 3.21 was used to calculate equilibrium suction.

$$\frac{\theta_{dry}' - \theta_{dry}}{\sqrt{\frac{n\pi}{\alpha}}} (1 - e^{-\sqrt{\frac{n\pi}{\alpha}} Z_m}) + [(\theta_e - \theta_{dry}')] Z_m = d_m \quad (3.21)$$

To validate the prediction accuracy of the regression parameters, a new set of measured suction data at equilibrium were collected from the literature (Snethen et al., 1977, McKeen, 1981, and Jayatilaka et el., 1992). These were compared against the calculated equilibrium suction values and plotted in Figure 3.10

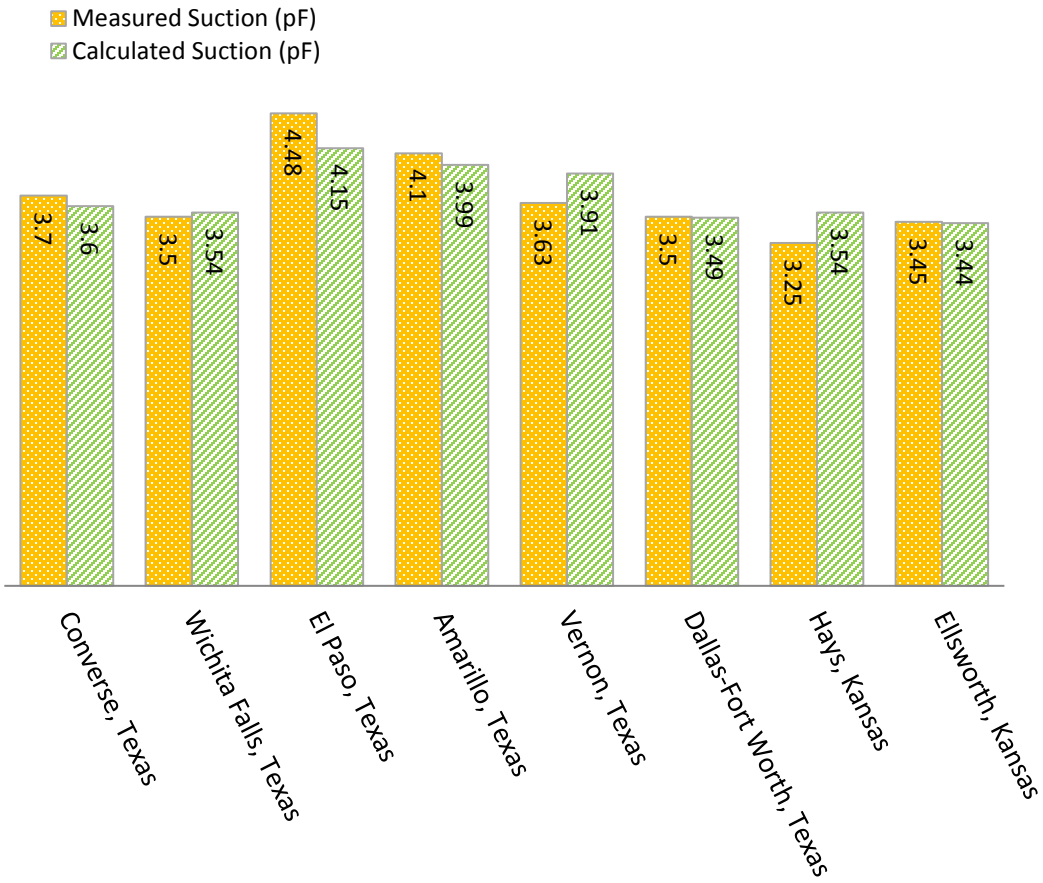

Figure 3.10 Comparison of measured and calculated equilibrium suction

The predicted suction values show good agreement with the measure values. Hence, these relationships facilitate the calculation of equilibrium suction for all map units in the United States. Equilibrium suction contour map of continental U.S. was generated in a GIS platform and is shown in Figure 3.11.

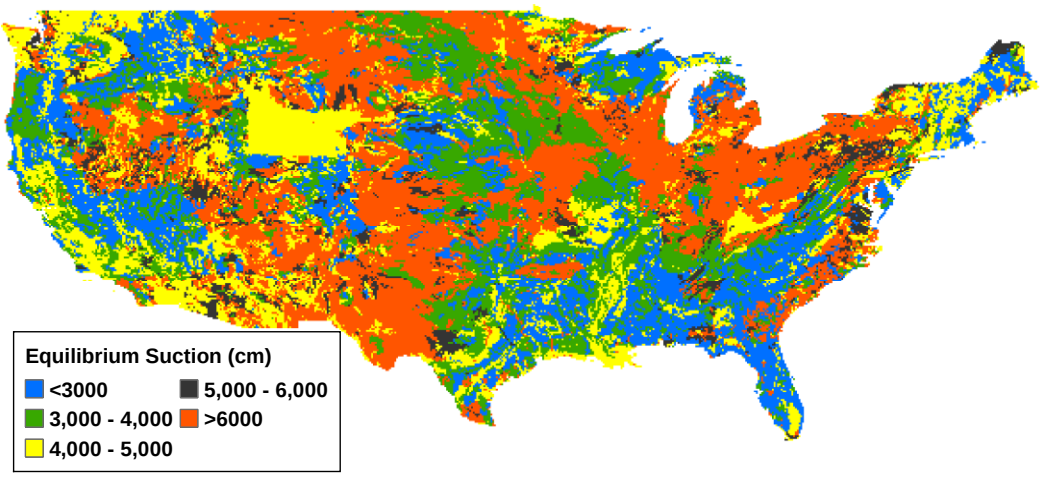

Figure 3.11 GIS based contour map of equilibrium suction

3.3.4. Example Calculation

The step by step calculation of equilibrium suction is elaborated using an example for a site located in Hattiesburg, Mississippi.

Step 1. Identify geographic coordinates (Latitude and Longitude) of the location

Hattiesburg, Mississippi: *Latitude: 31.327^0, Longitude: -89.29^0*

Step 2: Locate the corresponding map unit key (MUKEY) of this geographic coordinate from SSURGO metadata file in ArcGIS as shown in Figure 3.12.

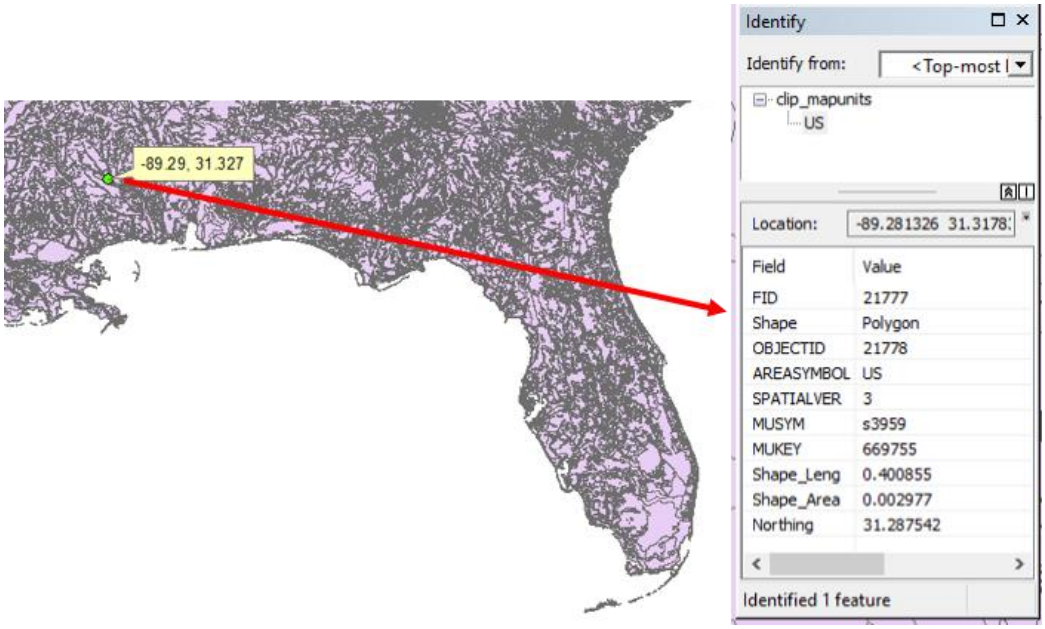

Figure 3.12 Identification of map unit using the geographic coordinates

Hattiesburg, Mississippi: mapunit 669755

Step 3: Determine the fitting parameters (a_f, b_f, c_f and h_r) of the SWCC for the map unit in question using the ANN model developed by Saha et al. (2018a). The inputs of the ANN model were collected from the NRCS soil database. Table 3.2 list the input and output parameters of the ANN model for map unit 669755.

Table 3.2 List of input parameters and the ANN predicted output parameters for map unit 669755

Input parameters						Output parameters			
Passing #4 sieve	Passing #200 sieve	LL	PI	θ_{sat}	MAAT (^{0}C)	a_f (psi)	b_f	c_f	h_r (psi)
95	41.5	17.5	1.5	40	18	2.49	0.99	0.87	3000

Step 4: Determine θ_{dry} (for a suction of 4.5 pF for full vegetation and for a suction of 5.7 pF for no vegetation) and θ_{wet} for a suction of 3.0 pF using the SWCC equation shown in Equations 3.10 and 3.11 and the predicted output parameters shown in Table 3.2

θ_{dry} @4.5 pF = 0.0915

θ_{dry} @5.7 pF = 0.045

@3 pF = 0.207

Step 5: Find the value of F_r for map unit 669755 from the vegetation cover map shown in Figure 7.

Map unit 669755: F_r = 0.67

Step 6: Since the value of F_r for this location is 0.67 (significant vegetation), θ_{dry} is considered to be at a suction level of 4.5 pF.

θ_{dry} (actual) = 0.0915

Step 7: Calculate the actual depth of the moisture active zone for F_r = 0.67 using a linear interpolation between 9.39 feet (F_r =0) and 21 feet (F_r = 1).

Z_m (actual) = 17.25 feet $\approx$ 526 cm

Step 8: Calculate the unsaturated diffusivity coefficient, α using Equation 3.10

Map unit: 669755; k_{sat} = 2.39 x10^{-05} cm/sec (NRCS database); $(\partial\theta / \log \partial h)_{5000\ cm}$= 0.07428 cm^{-1};

$$\alpha = \frac{2.39E-05}{0.07428} = 0.00032\ cm^2/sec$$

Step 9: Calculate $(u_{dry}')z_m$ using Equation 3.6 when $u_e = (u_{wet}')z_m$ = 3.0 pF

Map unit: 669755; $(u_{dry}')z_m$ = 3.0003 pF

Using Equation 3.10 and 3.11, determine θ_{dry}' and θ_{wet}'

$\theta_{dry}' = 0.206917$

$\theta_{wet}' = 0.206957$

Step 10: Calculate the available moisture depth, d_{am} using Equation 3.13

$d_{am} = 16.473\ cm$

Step 11: Find out the TMI of mapunit 669755 from the TMI contour map shown in Figure 3.4

Mapunit 669755: TMI = 49.7

Step 12: Calculate the mean annual moisture depth, d_m using Equation 3.16

$d_m = 9.274\ cm$

Step 13: Calculate the equilibrium suction, u_e using Equation 3.21.

$u_e = 3.439\ pF$

To simplify the calculation process, an empirical relationship was established to predict the equilibrium suction for various soil types from the TMI value. This relationship and its development is presented in the next section.

3.4. Development of Prediction Models for Equilibrium Suction

A stepwise multiple regression analysis was performed to identify the significant parameters that are correlated with equilibrium suction. The soil and climatic parameters used in the regression model were *TMI*, *PI*, u_{dry}, Z_m, F_r, $\sqrt{1/\alpha}$, θ_{sat}, a_f, b_f and c_f. The t ratio and the p-value obtained from the F-test were used to identify the significant variables in the regression model. If the p-value is less than 0.05, it indicates the variable is significant at the 95% confidence level. The t-

ratio is a ratio of the departure of an estimated parameter from its notional value and its standard error. A higher absolute value of the t-ratio corresponds to a smaller p-value (Saha et al. 2019c). Table 3.3 presents the results of the F-test, which were obtained from the commercially available Matlab software. The parameters TMI, PI, u_{dry} and $\sqrt{1/\alpha}$ have a p-value less than 0.05, and therefore are significant variables for the equilibrium suction prediction model. For the sake of simplicity, the parameter $\sqrt{1/\alpha}$ was not included and only *TMI, PI* and u_{dry} were used for model development.

Table 3.3 Results of the multiple regression analysis

Variables	Parameter estimate	Standard error	t Ratio	p-value
Intercept	1.26	0.41	3.11	0.002
TMI	-1.1E-03	5.9E-04	-1.93	0.045
PI	0.029	3.4E-03	8.59	4.41E-15
$\mathbf{u_{dry}}$	0.51	0.064	7.96	2.05E-13
Z_m	4.6E-04	3.1E-04	1.44	0.15
F_r	-0.11	0.18	-0.62	0.53
$\sqrt{1/\alpha}$	-4.2E-03	8.4E-04	-4.95	1.73E-06
θ_{sat}	-0.43	0.31	-1.36	0.17
a_f (pF)	-1.7E-03	0.026	-0.07	0.94
b_f	3.4E-03	6.1E-03	0.56	0.57
c_f	-0.17	0.11	-1.48	0.13

The developed regression equation for equilibrium suction is expressed in Equation 3.22

$$u_e(pF) = 1.95 - 0.00062 * TMI + 0.011 * PI + 0.324 * u_{dry} \quad (3.22)$$

It is observed from Equation 3.22 that equilibrium suction (pF) has a positive correlation with PI and u_{dry}, but follows a negative relationship with TMI. Figure 3.13 shows the plot of calculated versus predicted equilibrium suction using Equation 3.22. The R^2 value of 0.80

indicates that the developed regression model is capable of accurately predicting equilibrium suction.

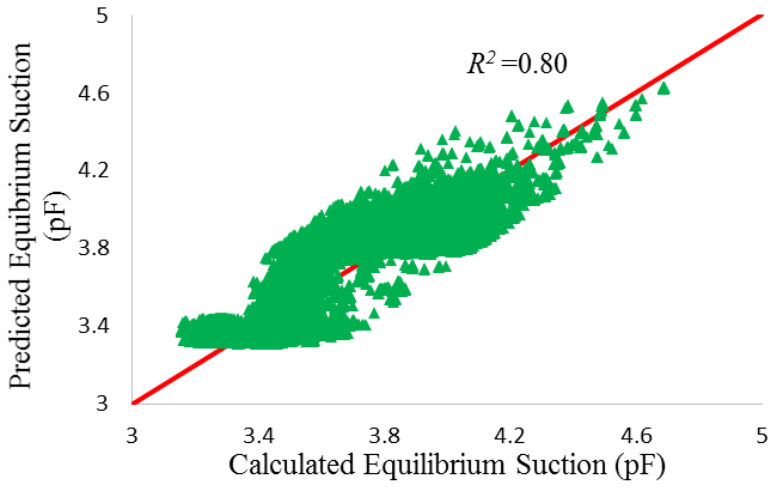

Figure 3.13 Calculated versus predicted equilibrium suction (pF)

3.4.1. Relationship between TMI and Equilibrium Suction

The calculated equilibrium suction values for all map units were categorized based on AASHTO soil classes. As the mechanistic approach of determining u_e depends on the availability of SWCC and diffusion characteristics of soil, a simple relationship to predict u_e for the various AASHTO soil types was established as a function of only the TMI value. An exponential trend line was fitted for each case to express the relationship between u_e and TMI.

The standard deviation (σ) of the scattered suction values from the trend line were also calculated and the results are presented in Figure 3.14.

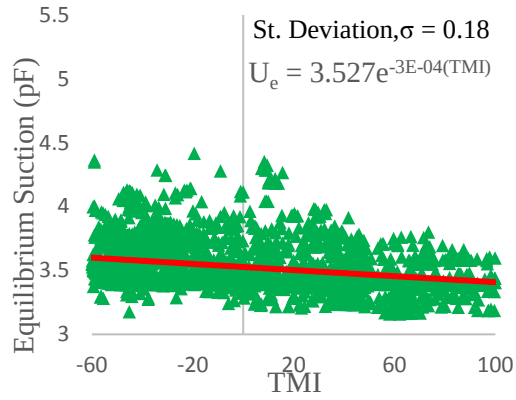

(a) AASHTO soil type: A-1

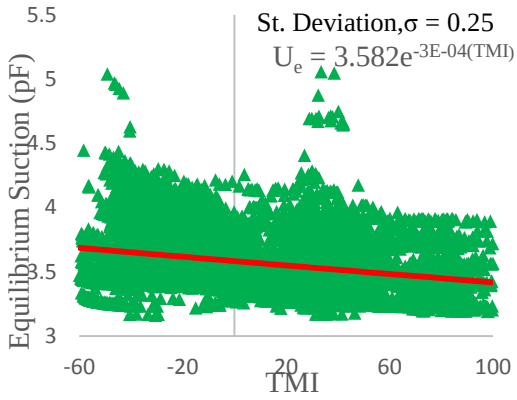

(b) AASHTO soil type: A-2

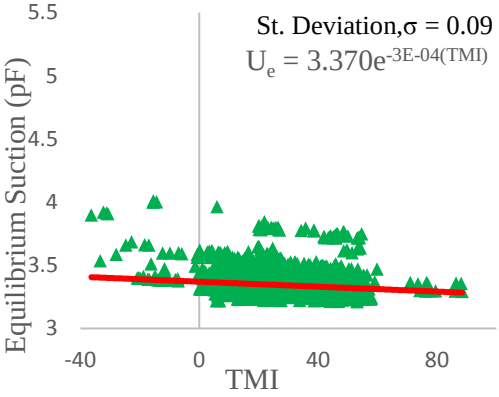

(c) AASHTO soil type: A-3

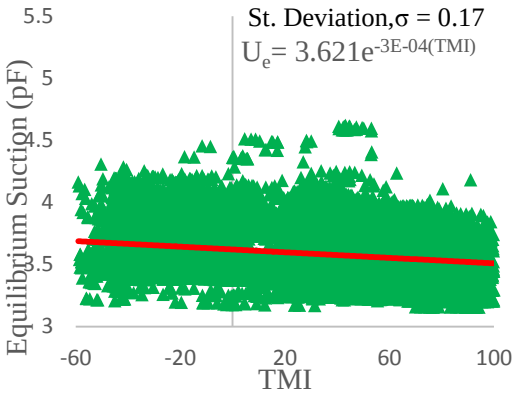

(d) AASHTO soil type: A-4

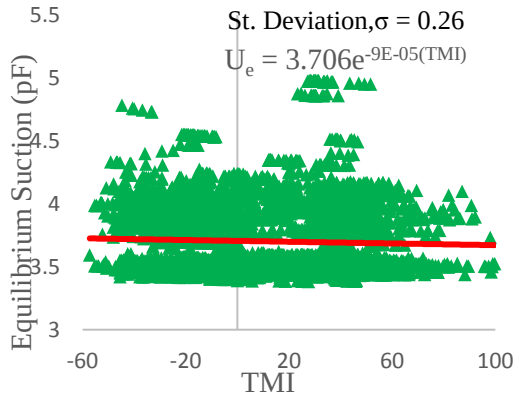

(e) AASHTO soil type: A-6

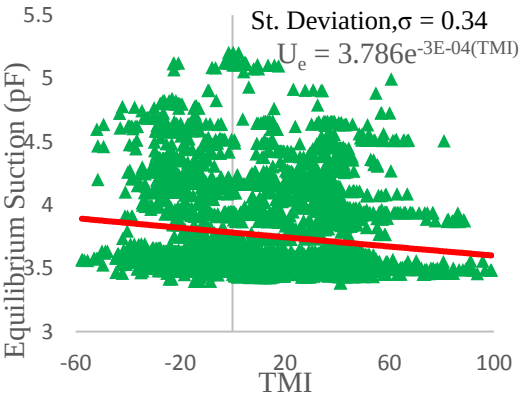

(f) AASHTO soil type: A-7-6

Figure 3.14 Thornthwaite moisture index (TMI) versus equilibrium suction (pF) plots for (a) A-1; (b) A-2; (c) A-3; (d) A-4; (e) A-6; and (f) A-7-6 soil types

It is evident from Figure 3.14 that the equilibrium suction (u_e) value decreases as TMI increases for all the soil types. This trend is in agreement with Equation 3.6 because a greater TMI value indicates a larger difference between precipitation (P) and evapotranspiration (PE) and therefore a larger amount of water being stored within the moisture active zone (larger θ_e) resulting in a smaller u_e value. Furthermore, the A-3 soil class has the shallowest slope while the A-7-6 soil class has the steepest slope in the TMI- u_e plots which is consistent with the fact that u_e increases with increasing percentage of fine material.

The σ values provide a measure of the dispersion of the data from the fitted trend line. In the TMI- u_e plots in Figure 3.14, σ values ranged from 0.09 to 0.34 which is well within the allowable limit compared to the total range of equilibrium suction values.

3.4.2. Relationship between Fraction of Vegetation Cover (F_r) and Equilibrium Suction

The amount of surface vegetation is a factor that is not typically considered in the calculation of equilibrium suction. However, FPA (2017) documented that vegetation has a major influence on soil moisture content within the root zone.

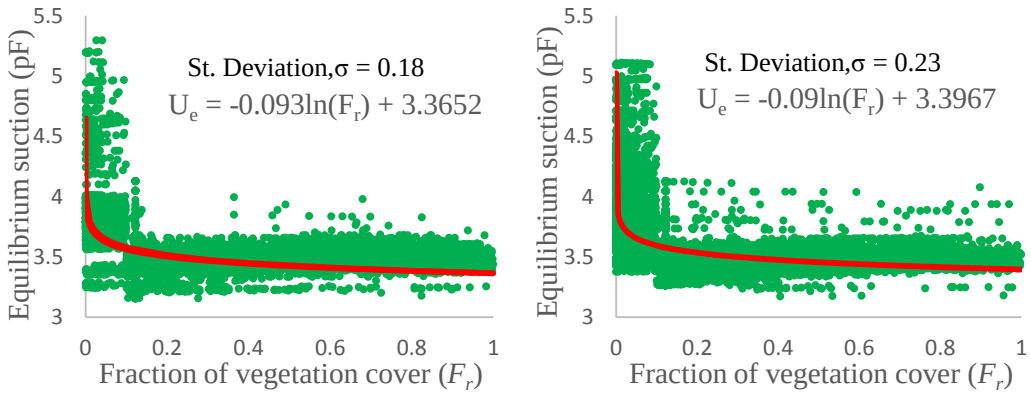

(a) TMI: >40 **(b) TMI: 40 to 11**

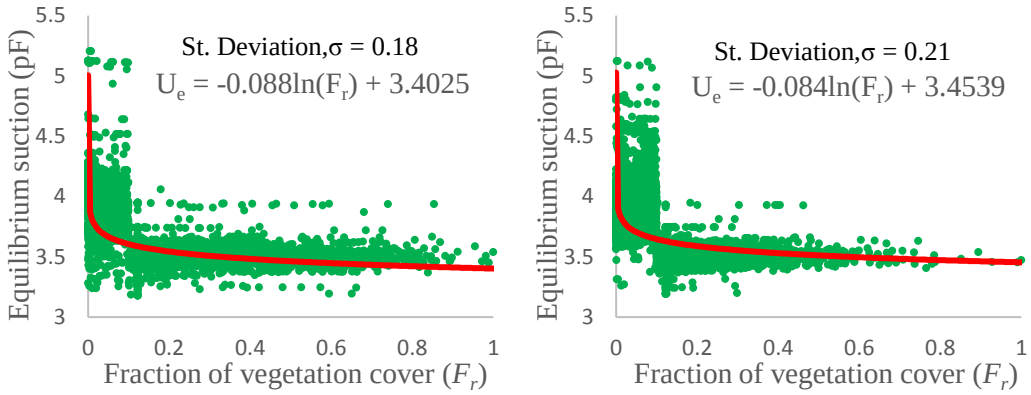

(c) TMI: 10 to -6

(d) TMI: -5 to -24

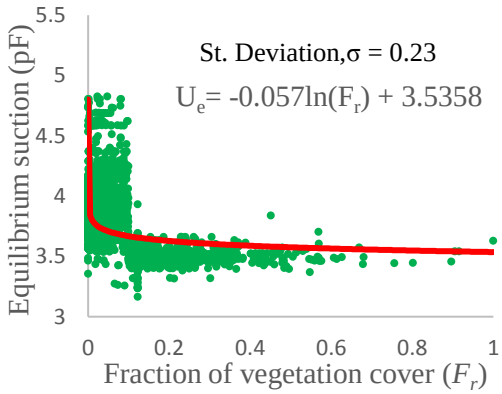

(e)TMI: -25 to -40

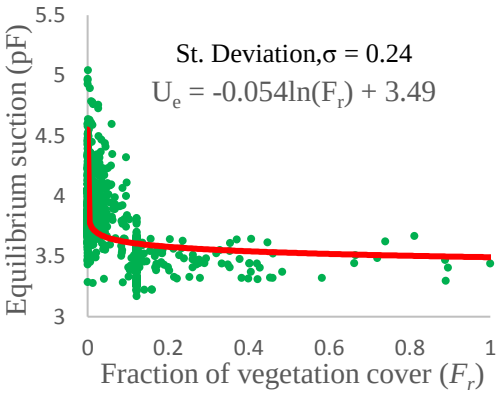

(f) TMI: < -40

Figure 3.15 Fraction of vegetation cover (F_r) versus equilibrium suction (pF) plots for TMI range (a) >40; (b) 40 to 11; (c) 10 to -6; (d) -5 to -24; (e) -25 to -40; and (f) <-40

To consider the effect of vegetation in the surface, a vegetation cover map was generated in this study for the continental United States in the GIS platform (Figure 3.7). The calculated equilibrium suction values for each map unit were plotted against the corresponding F_r value obtained from Figure 3.7. A logarithmic trend line was fitted for each TMI range to establish a relationship between u_e and F_r. The results are presented in Figure 3.15. The plots in Figure 3.15 clearly indicate that the magnitude of equilibrium suction (pF) decreases as the vegetation cover

increases. This is consistent with the fact that an increase of surface vegetation increases the depth of moisture active zone (Z_m), which attributes to higher volumetric water content at equilibrium and a smaller equilibrium suction value. Figure 3.15 also shows that the slope of the trend line is steepest for TMI>40 and shallowest for TMI<-40, which indicates that the impact of vegetation on u_e is likely to be greater in humid areas having higher TMI values (PTI, 2004; Bulut and Nevels, 2018). The range of σ values (0.18 to 0.24) indicate that the proposed model is sufficiently accurate for the range of equilibrium values predicted.

3.5. Conclusions

A mechanistic-empirical model was developed in this study for determining equilibrium suction of subgrade soils by considering the effects of physical properties of the soil and climatic factors. A parametric study was also conducted to evaluate the impact of TMI and vegetation on equilibrium suction for various soil classes and TMI ranges, respectively. Equilibrium suction values increased with increasing percentage of fine material and decreased as surface vegetation increased.

This study developed an improved prediction model of equilibrium suction for subgrade soils based on fundamental principles. The equilibrium suction contour map accompanying the model allows for a simple and accurate determination of a baseline equilibrium suction values at any given latitude and longitude within the continental United States. The incorporation of this model in an analysis approach will allow for a more reliable estimation of critical parameters such as subgrade resilient modulus and vertical movement due to swelling and shrinking of expansive clays thereby improving the prediction of pavement performance.

4. DEVELOPMENT OF A MOISTURE SENSITIVE RESILIENT MODULUS PREDICTION MODEL FOR UNBOUND BASE MATERIAL[†]

4.1. Introduction

Unbound base materials beneath the pavement surface are characterized by the resilient modulus (M_R) in the Pavement ME Design (AASHTO 2008, Rahman et al. 2019b, Islam et al. 2019), which directly affects the design and analysis of flexible pavement structures. The advantage of M_R over other material properties is that it represents the response to dynamic loading coming from vehicle movement. It is defined as the ratio of repeated cyclic loading (σ_{cyc}) divided by recoverable strain (ε_r) as shown in Equation 4.1.

$$M_R = \frac{\sigma_{cyc}}{\varepsilon_r} \tag{4.1}$$

The resilient modulus can be estimated in three different approaches: (1) conduct lab tests with compacted soil specimen e.g., repeated load triaxial test (RLT), (2) follow back calculation method from an in situ device e.g., falling weight deflectometer (FWD); and (3) predict M_R model coefficients from soil physical properties. The first and second approaches are expensive, time consuming and require expert labor. As a result, the third approach based M_R model is used in this study to characterize the unbound material under different conditions.

Various models have been developed to predict the resilient modulus of unbound base and subgrade materials. The most widely used generalized model developed in the National

[†] Reprinted with permission from "Use of an artificial neural network approach for the prediction of resilient modulus for unbound granular material" by Sajib Saha, Fan Gu, Xue Luo and Robert Lytton, 2018. Transportation Research Record, 0361198118756881, Copyright [2018] by SAGE Publications.

Cooperative Highway Research Program (NCHRP) project 1-28A, is shown in Equation 4.2 (Witczak 2003).

$$M_R = k_1 P_a \left(\frac{I_1}{P_a}\right)^{k_2} \left(\frac{\tau_{oct}}{P_a} + 1\right)^{k_3} \quad (4.2)$$

where I_1 is the first invariant of the stress tensor; τ_{oct} is the octahedral shear stress; P_a is the atmospheric pressure; and k_1, k_2 and k_3 are regression coefficients.

However, a number of studies showed that resilient modulus of unbound granular material is not only stress dependent but also moisture dependent (Lekarp et al. 2000). The AASHTO employed a moisture dependent M_R model which is later adopted by mechanistic-empirical pavement design guide (MEPDG) (AASHTO 2008).

$$\log \frac{M_R}{M_{Ropt}} = a + \frac{b-a}{1+\exp[\ln \frac{-b}{a} + k_m (S - S_{opt})]} \quad (4.3)$$

where M_R is resilient modulus at a given degree of saturation; M_{Ropt} is resilient modulus at a reference condition; a and b are minimum and maximum of $\log(M_R/M_{ROPT})$ respectively; k_m is the regression coefficient; and $(S - S_{opt})$ is variation of degree of saturation, expressed as a decimal.

Other researchers have also proposed different moisture dependent resilient modulus models for both unbound aggregates and subgrade (Heath et al., 2004, Liang et al., 2008, and Cary and Zapata, 2011). However, previous studies also demonstrated the importance of the matric suction in the resilient modulus model. There have been a number of other studies recommending the use of soil suction in modeling resilient modulus (Oloo and Fredlund, 1998,

Wolfe and Bulatia, 2004, Khoury and Zaman, 2004; Luo et al., 2017, Gu et al., 2016). It is shown that the matric suction can be different for the same variation of degree of saturation, i.e. (S-S_{opt}), from one material to another (ARA, Inc. 2004). Therefore, the degree of saturation and soil suction alone cannot accurately estimate the change of resilient modulus due to moisture. In order to consider the moisture and suction dependency of resilient modulus characteristics, a new model is proposed by Lytton (Lytton 1995).

$$E_y = k_1 P_a \left(\frac{I_1 - 3\theta f h_m}{P_a}\right)^{k_2} \left(\frac{\tau_{oct}}{P_a}\right)^{k_3} \tag{4.4}$$

where I_1 is the first invariant of the stress tensor; P_a is the atmospheric pressure; θ is the volumetric water content; h_m is the matric suction in the base matrix; f is the saturation factor, 1 < f < 1/ θ ; τ_{oct} is the octahedral shear stress; and k_1, k_2 and k_3 are regression coefficients.

In this model, I_1 and τ_{oct} vary with the stress state, and h_m is related to the moisture content of unbound aggregates. Three steps are followed to determine the coefficients k_1, k_2 and k_3 using Equation 4.4.

1. Matric suction h_m in Equation 4.4 is estimated first at tested specimen water content. A separate artificial neural network (ANN) model is used to predict the coefficients of the soil water characteristic curve (SWCC) parameters in the Fredlund-Xing equation described in later sections.

2. Volumetric water content, θ and saturation factor, f are calculated for each base material from the collected moisture content, maximum dry density and specific gravity data. The

saturation factor is an indicator of degree of saturation (Lytton 1995). It is multiplied with θ and h_m, to express the stress on soil mineral skeleton in the transition zone. The transition zone occurs between the air entry point suction value and the unsaturation point suction value. The saturation corresponding to the air entry point and the unsaturation point are considered as 100% and 85% respectively in this study. Equation 4.5 is followed to calculate the saturation factor, *f* in the transition zone.

$$f = 1 + \frac{S - 85}{15}\left(\frac{1}{\theta} - 1\right) \quad (4.5)$$

where S is the degree of saturation (unit: %); θ is the volumetric water content (unit: decimel); it is considered to be 2 pF and 3.5 pF at the air entry point and the unsaturation point respectively.

3. Coefficients k_1, k_2 and k_3 are calculated from collected M_R data at different combinations of confining pressure and deviator stresses. A matlab code was generated to fit the curve for each base material.

Researchers have developed many correlation models to predict k_1, k_2 *and* k_3 from soil gradation, index and strength properties (Yau and Quintus 2004, Nazzal and Mohammad 2010, Malla and Joshi 2007, Gu et al., 2014). However, most of these models are either confined to a limited number of datasets or have a poor prediction accuracy. As a result, an ANN model is developed in this study to predict the coefficients from soil properties. The main advantage of a neural network model over non-linear regression models are that it can capture complex non-linear scattered relationship between input and output parameters and train the model based on the evaluation of error function. The application of the ANN approach for predicting the resilient

modulus of subgrade soil has been studied by a few researchers (Coleri et al. 2010, Kim et al. 2014). Soil index properties (i.e., material percent passing No. 200 sieve, plasticity index (*PI*), optimum moisture content (OMC), maximum dry density (MDD), variation in compaction water content) and stress variables (i.e., confining pressure, bulk stress, deviator stress) were used as input variables to predict the resilient modulus (Coleri et al. 2010). A different neural network analysis was performed with nine different soil source in Georgia (Kim et al. 2014). A similar study has been performed for ln(k_1), k_2 and k_3 coefficients by Nazzal et al. (Nazzal and Tatari 2013). Input variables for the correlation models developed by Nazzal consisted of material percent passing No. 200 sieve, *LL*, *PI*, MDD, test dry density (TDD), OMC, test moisture content (TMC) and clay%. However, previous ANN approaches had some limitations. The resilient modulus values were predicted either as model output for a single stress combination or using only the locally available soil data as input. To overcome these limitations, an ANN model is developed in this study using a large database of unbound base materials collected from Long Term Pavement Performance (LTPP). Moreover, the resilient modulus equation coefficients (k_1, k_2, and k_3) were predicted as output to cover a wide range of stress combination.

The chapter is organized as follows. The next section describes the procedure to estimate suction at specific test specimen water content. Subsequently, ANN models are developed to predict the coefficients of the M_R model using the estimated suction. After that the M_R values using the predicted coefficients are compared against other existing regression models. Unbound base course data collected by the Texas A&M Transportation Institute (TTI) and University of Illinois at Urbana-Champaign (UIUC) were used to validate the developed ANN models and described in following section. The final section summarizes the major findings of this study.

4.2. Prediction of Suction at Test Specimen Water Content

Matric suction of unbound granular base material was required to accurately estimate the resilient modulus in unsaturated condition as shown in Equation 4.4. However, the quantity of available SWCC data of unbound base materials from the available literature was not sufficient to train an ANN model. Hence the Soil Survey Geographic Database (SSURGO) was used for data collection from the United States Department of Agriculture-Natural Resources Conservation Service (USDA-NRCS). The database included soil physical and climatic properties as well as water content at specific suction pressure. Collected suction-saturation data points for each soils were fitted in the Fredlund-Xing equation as shown in Equations 4.6 and 4.7 (Fredlund and Xing 1994).

$$S = C(h)\,\mathrm{x}\left[\frac{1}{\{\ln[\mathrm{e}+(\frac{h}{a_f})^{b_f}]\}^{c_f}}\right] \tag{4.6}$$

$$\mathrm{C}(h) = 1 - \frac{\ln(1+\frac{h}{h_r})}{\ln[1+(\frac{1.45x10^5}{h_r})]} \tag{4.7}$$

where h is the the soil matric suction (unit: psi); and a_f, b_f , c_f are h_r are soil fitting parameters.

A Matlab code was generated to fit the Fredlund-Xing equation with measured data points and calculate the SWCC fitting parameters. Out of a total 34,237 soil data collected from the NRCS, soils which satisfy gravel characteristics according to Unified Soil Classification System (more than 50 percent material retained on the No.200 sieve is defined as coarse grained material and more than 50 percent of the coarse grained material retained on the No.4 sieve)

were separated out to train and validate the ANN models for the SWCC fitting parameters. The 2598 plastic (PI>0) soil data and 311 non-plastic (PI=0) soil data were collected and used to train the neural network to predict the SWCC fitting parameters for unbound materials.

Following the architecture in Saha et al. (2018a), two three-layered ANN models consisting of one input layer, one hidden layer and one output layer were constructed for plastic and non-plastic soils respectively. The input variables for plastic soils included percent passing No.4 sieve, percent passing No.200 sieve, liquid limit (LL), plastic limit (PL), saturated volumetric water content and local mean annual air temperature (MAAT). Input variables for non-plastic soils were particle diameters corresponding to 30, 60 and 90 percent passing of material D_{30}, D_{60} *and* D_{90}, gradation scale parameter (Θ), and shape parameter (Ψ), saturated volumetric water content and local *MAAT*. The output of the developed ANN models were fitting parameters (i.e., a_f, b_f, c_f and h_r) of the SWCC in the Fredlund-Xing equation, as shown in Equations 4.6 and 4.7.

The hidden layer in the ANN model assigned 20 neurons to establish connection between input and output layers. The 80 percent of the total dataset was used for training and 20 percent for validation of ANN models. Water contents at 0.1, 0.33 and 15 bars (1 bar = 100 kPa) were available in the USDA-NRCS database. In this study, the predicted SWCC parameters were input into the Fredlund-Xing equation to estimate the water content at the same suction levels. The estimated water contents were compared against the measured values to investigate the prediction accuracy.

Figures 4.1a and 4.1b showed the plots of measured versus predicted degree of saturation for plastic and non-plastic soils, respectively. The developed ANN models had a very good

prediction accuracy generating a R^2 value of 0.91 for both plastic and non-plastic soils. Hence the same trained models were used to predict the SWCC fitting parameters for base materials collected from the LTPP database. Predicted af, bf, cf and hr parameters of the LTPP materials were input into the Fredlund-Xing equation to estimate matric suction of the specimen at the tested water content.

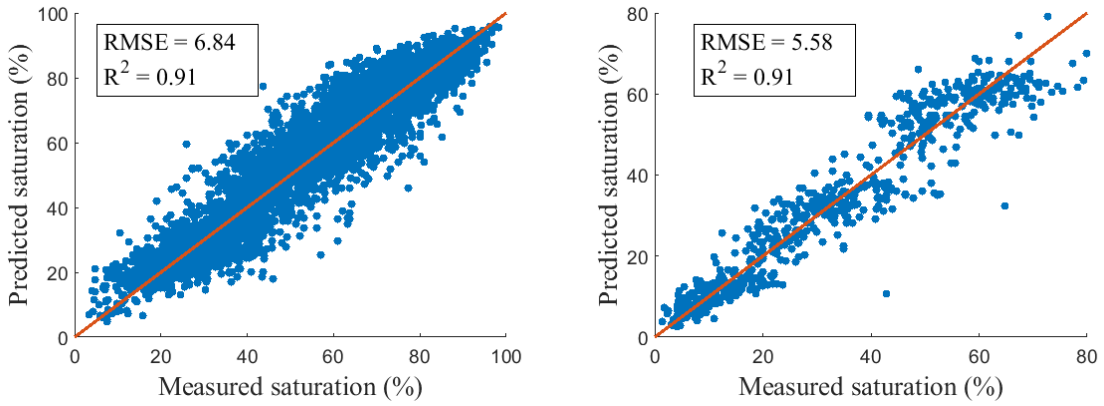

(a) Plastic soils **(b) Non-plastic soils**

Figure 4.1 Comparison of measured versus predicted saturation (%) at 0.1, 0.33 and 15 bars suction level for unbound granular base materials using ANN model

4.3. Development of Artificial Neural Network Models for M_R Model Coefficients

The ANN approach is an adaptive information processing technique, which allows to establish the correlations between the input variables X_i and the output variables Y_j through the inter-connected neurons (i.e., weight factor, w_{ji}). Note that the input variables X_i and the output variables Y_j are usually normalized to x_i and y_j, respectively. The correlations developed by the ANN models between the normalized input parameters x_i and the normalized output variables y_j are shown in Equation 4.8.

$$y_j = f\left(\sum_{i=1}^{n} w_{ji} x_i\right) + b_j \quad (4.8)$$

where f is a transfer function, which normally uses a sigmoidal, Gaussian, or threshold functional form; w_{ji} and b_j are the unknown weight factors and bias term respectively.

A neural network model specifically adjusts the weight factors w_{ji} and bias bj in Equation 4.8 based on the minimum error function. In pavement engineering, the ANN approach is usually used to develop prediction models on the basis of a large number of data collected from experiments and numerical analysis. ANN models have been successfully developed to predict the crack growth function (e.g., reflective cracking and top-down cracking) in asphalt concrete (Ceylan et al. 2011, Ling et al. 2017). The ANN approach was also utilized to predict the geogrid-reinforced flexible pavement performance (Gu et al. 2017). In general, the development of ANN models includes two critical steps: 1) data collection; and 2) construction of ANN architecture.

4.3.1. Data Collection

A large collection of unbound base materials was available in the LTPP database. Out of total 3010 unbound base materials 717 materials were selected which passes gravel specifications. 217 plastic (PI>0) and 500 non-plastic (PI=0) base materials were separated out to develop two different sets of ANN models for k_1, k_2 and k_3. Resilient modulus tests were conducted on 15 different combinations of confining pressure and nominal maximum axial stress level. In addition to the resilient modulus test data, physical properties of base materials such as gradation, Atterberg limits, moisture content, density and specific gravity were collected from the LTPP database.

4.3.2. Construction of ANN Architecture

Two three-layered ANN models, one for plastic and another for non-plastic soil were constructed as shown in Figure 4.2a and 4.2b respectively. Three layers of the ANN model consisted of a single input, a hidden and an output layer. Soil physical properties i.e., percent of material passing 3/8" sieve, percent of material passing no. 200 sieve, *PL*, *PI*, OMC, MDD and TMC were introduced as input parameters for plastic soils. Input parameters for non-plastic soils included the percent of material passing the 3/8" sieve, percent of material passing the No. 200 sieve, gradation scale parameter;Θ, and shape parameter; Ψ, OMC, MDD, and TMC. The hidden layer assigned 10 neurons to establish the connection between the output layer and the input layer. The number of neurons was selected based on the number of data points. Too many hidden neurons allow the network to memorize instead of generalizing the training set (Lawrence and Peterson 1993).

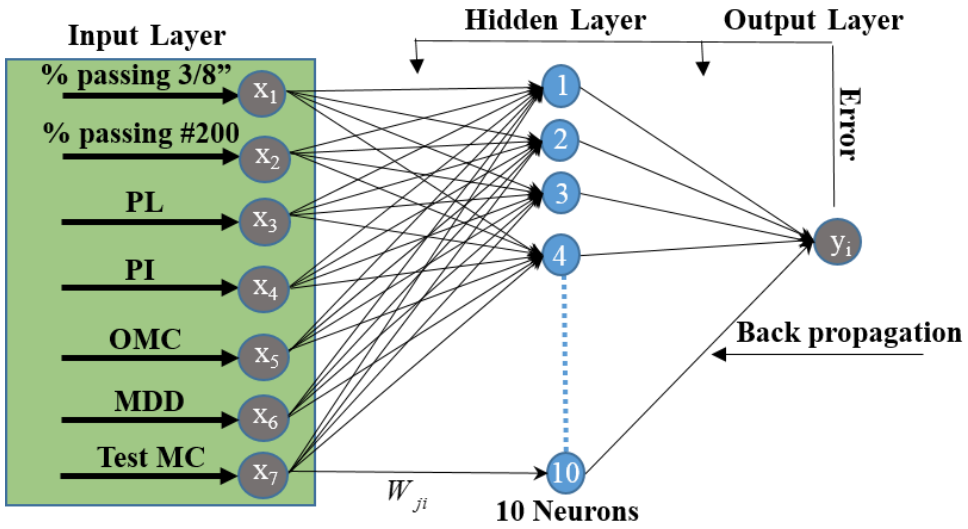

(a) Plastic soil

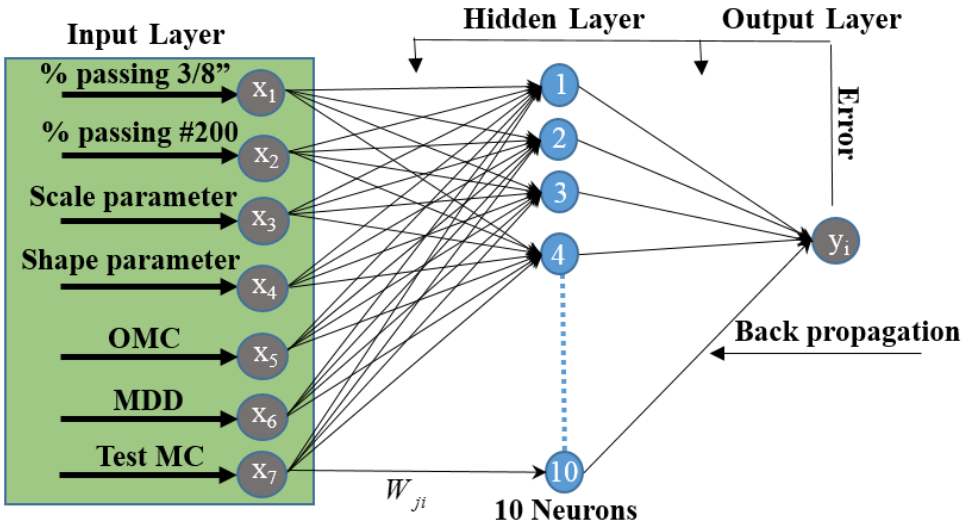

(b) Non-plastic soil

Figure 4.2 Illustration of three-layered neural network architecture (a) Plastic; (b) Non-plastic soil

Both the non-plastic and plastic soil models utilized the sigmoidal transfer function, as shown in Equation 4.9 (Gu et al. 2017).

$$f\left(I_i\right)=\frac{1}{1+\exp\left(-\varphi I_i\right)} \tag{4.9}$$

where I_i is the input quantity, and φ is a positive scaling constant.

The parameter φ controls the steepness between the two asymptotic values 0 and 1. The ANN model determines these weight factors w_{ji} through the two major functions: training and validating. The training data set is used to determine the trial weight factors, w_{ji} and bias term, b_j the validating data set is employed to examine the accuracy of the model prediction. In this study, 80 percent of the dataset was used for training and 20 percent of the dataset is for validation. The training algorithm used the Levenberg-Marquardt back propagation method to

minimize the mean squared error (MSE). The gradient descent weight function was employed as a learning algorithm to adjust the weight factors w_{ji}.

4.4. Prediction of M_R Model Coefficients Using ANN Model

In this study, the ANN model was developed to predict the M_R model coefficients (i.e., k_1, k_2 and k_3) from base physical properties. The coefficients of the M_R model were correlated with base material physical properties and used to estimate the resilient modulus. Figure 4.3 showed the comparison between measured and predicted M_R model coefficients for plastic soils. The predicted M_R coefficients showed high R^2 and low *RMSE*, which indicated a good prediction accuracy. The R^2 values for M_R coefficients were in the range of 0.66 to 0.73. Similarly, Figure 4.4 plotted the comparisons between measured and predicted M_R model coefficients for non-plastic soils. The R^2 value for k_1, k_2 and k_3 coefficients were 0.78, 0.74 and 0.58 respectively.

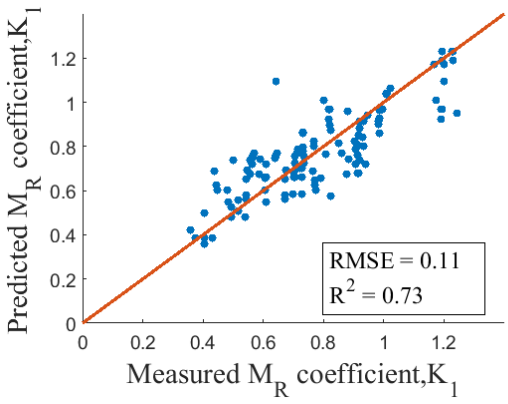

(a) k_1

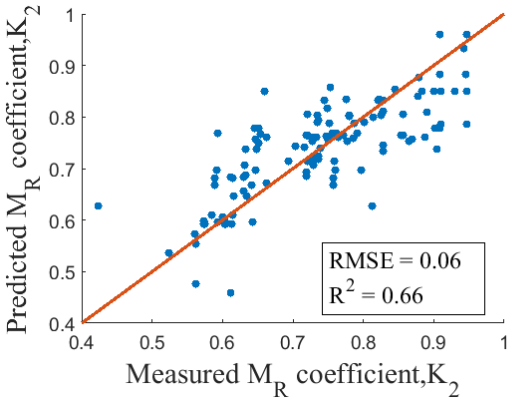

(b) k_2

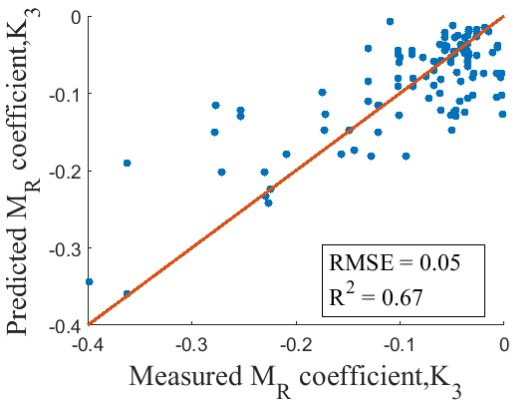

(c) k_3

Figure 4.3 Predicted M_R model coefficients of plastic base materials from physical properties using ANN approach

Note that a high level of variability was involved in estimated coefficients due to variations in cyclic load triaxial test results and seasonal changes in selected physical properties (Ji et al. 2014). Hence, the predicted k_1, k_2 and k_3 values need to be scrutinized in the validation process. If the validation dataset provides comparable results, then the predicted coefficients can be considered to be sufficiently accurate to use in M_R model equation.

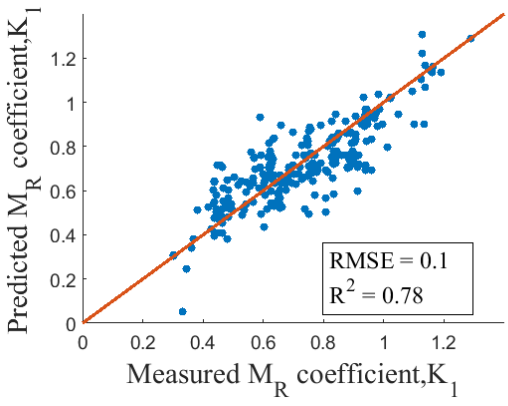

(a) k_1

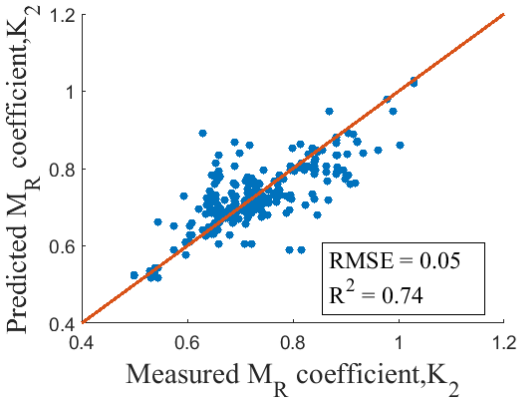

(b) k_2

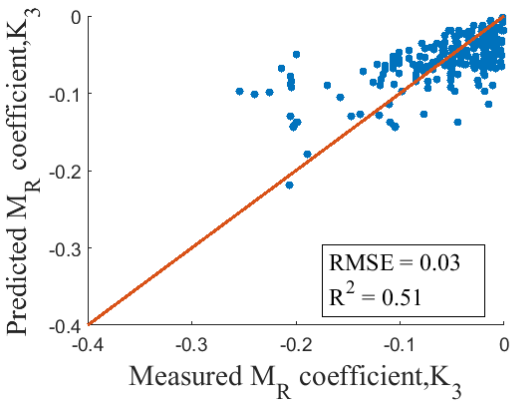

(c) k_3

Figure 4.4 Predicted M_R model coefficients for Non-Plastic base materials from physical properties using ANN approach

4.5. Comparison of ANN Model with Other Regression Models

A number of regression models have been developed to correlate the soil physical properties with M_R model coefficients. In this study the correlation models (Nazzal et al. 2010, Gu et al. 2014, and Soliman et al. 2016) were selected and compared against measured values to investigate the accuracy of the M_R coefficients. They were named as Yau model (Yau and Quintus 2004), Malla model (Malla and Joshi 2007), and Soliman model (Soliman and Shalaby 2016), respectively. All of these three regression models used the generalized M_R constitutive equation shown in Equation 4.2.

Seven different sets of regression equations were proposed by Yau and von Quintus for crushed stone materials, crushed gravel,uncrushed gravel, sand, coarse grained soil-aggregate mixture, fine grained soil-aggregate mixture and fine grained soil, respectively. The physical properties used to correlate with the generalized M_R model coefficients were material percent passing No. 3/8" sieve, No. 4 sieve, No. 40 sieve, No. 200 sieve, percentage of silt (% silt),

percentage of clay (% clay), *LL*, *PI*, OMC, MDD, TMC and test dry density (TDD).

Malla and Joshi studied the correlation between the M_R model coefficients and the gradation and compaction parameters of base materials. Regression analysis was performed on M_R model coefficients for uncrushed gravel and crushed limestone. The variables were selected on the basis of the literature and the logical influence of gradation, compaction and moisture content parameters on the regression constants (k_1, k_2 and k_3). These variables included: OMC, TMC, MDD, material percent passing No. 4 sieve, material percent passing No. 40 sieve, material percent passing No. 200 sieve.

Soliman and Shalaby presented regression equations of the generalized M_R model coefficients for six AASHTO soil types (A-1-b, A-3, A-2-4, A-4, A-6 and A-7-6). Data used in the regression analysis was collected from 19 states in New England and the nearby regions in the United States and two provinces in Canada. The soil properties that were considered in the regression analysis include: OMC, TMC, MDD, LL, PI, TDD, percentage of coarse sand (% CSAND), percentage of fine sand (% FSAND), percentage of silt (% silt), percentage of clay (% clay), material percent passing 3" sieve, 2" sieve, 1 ½" sieve,1" sieve, ¾" sieve, 1/2" sieve, 3/8" sieve, No. 4 sieve, No. 10 sieve, No. 40 sieve, No. 80 sieve and No. 200 sieve.

The accuracy of the prediciton of the M_R model coefficients by the existing correlation models were analyzed in this study. Table 4.1 listed all the predicted M_R coefficients using Yau, Soliman, Malla and ANN models. Compared to the ANN model, the estimated *RMSE* values from the three regression models were high and the R^2 values were extremly low.

Table 4.1 Prediction Accuracy of SWCC Fitting Parameter Models

Model	R^2			*RMSE*		
	k_1	k_2	k_3	k_1	k_2	k_3
Yau	-4.51	-2.15	-3.06	0.31	0.25	0.54
Soliman	-2.27	-0.16	-1.42	0.43	0.59	0.89
Malla	-0.023	-0.03	-1.86	28.82	0.94	0.61
ANN	0.76	0.72	0.63	0.10	0.05	0.04

High *RMSE* and low R^2 values indicated a poor prediction accuracy. The R^2 values for k_1, k_2 and k_3 from all the three regression models were less than zero, while R^2 values from ANN model were in the range of 0.63 to 0.76. The negative R^2-values indicated the slope of the best fit line relating the predicted to the measured coefficients was negative. Therefore, the developed ANN models had a significant improvement in predicting the M_R model coefficients from base physical and compaction properties.

The accuracy of M_R values using the predicted coefficients were examined in the next section. Predicted coefficients from the three regression models were input into Equation 4.2 and the ANN model coefficients were input into Equation 4.4 to calcualte M_R values, which were compared to the measured values. Figure 4.5 showed the comparisons between measured and estimated M_R values using the ANN predicted coefficients.

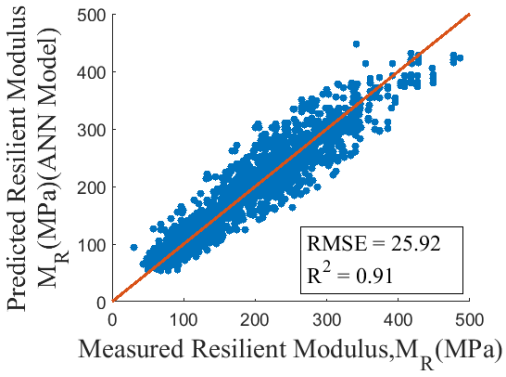

(a) Plastic base materials

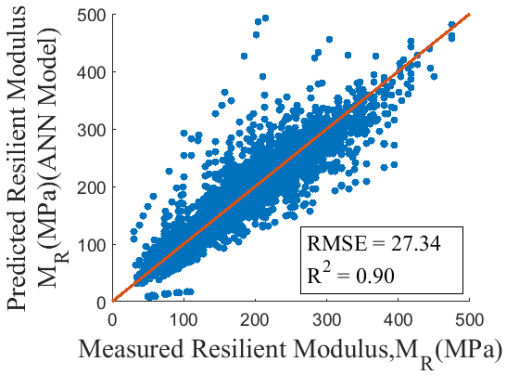

(b) Non-plastic base materials

Figure 4.5 Comparison of ANN model predicted resilient moduli against measured values

Clearly the M_R values estimated using the ANN coefficients matched well with the test data. The R^2 value estimated for both plastic and non-plastic base materials were 0.91, which demonstrated a high accuracy. Figures 4.6a, 4.6b and 4.6c presented the results from Yau, Soliman and Malla models respectively. The R^2 value estimated from Yau, Soliman and Malla models were 0.32, -1.53 and -1.62e^{06} respectively, which indicated the regression models failed to predict the coefficients. The negative R^2 value from Soilman and Malla model indicated that the best fit line relating the predicted to the measured values had a negative slope.

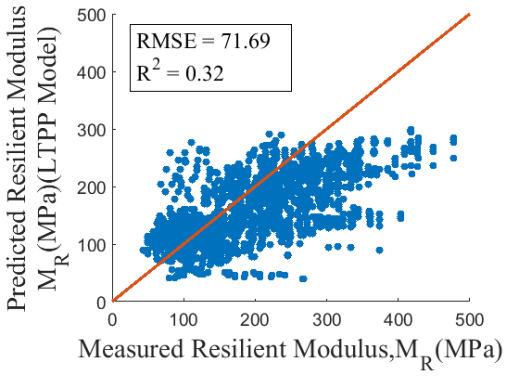

(a) Yau model

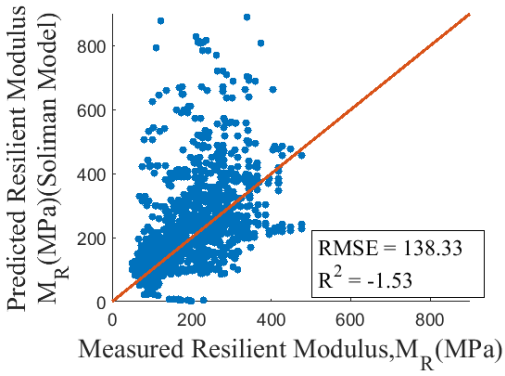

(b) Soliman model

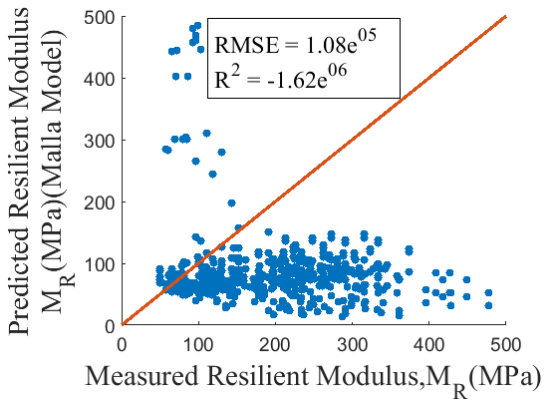

(c) Malla model

Figure 4.6 Comparison of measured versus predicted resilient moduli using regression mdoels

4.6. Validation of the Developed ANN Models

To validate the developed ANN models for the M_R model coefficients, test data were collected from the TTI (Epps et al. 2014, and Titus-Glover and Fernando 1995) and UIUC (Tutumluer et al. 2009). Epps et al. (2014) conducted triaxial repeated load tests to evaluate the laboratory performance of unbound granular materials. In addition to the M_R test results at different combinations of confining pressure and deviator stresses, aggregate physical, strength and moisture properties were also collected. Titus-Glover and Fernando performed the compressive creep and recovery tests for collected unbound base materials in the TTI laboratory. Tutumluer et al. conducted resilient modulus tests at the 15 various stress states. Since no suction values were provided by the UIUC research team, the suction is estimated using the developed ANN models from the base physical properties. Table 4.2 listed all the collected physical properties used as the ANN inputs for the validation dataset.

Table 4.2 Input Parameters Collected From Literature for Model Validation

Data Souces	Soil source	#3/8 sieve	#200 sieve	*PL*	*PI*	MDD	OMC	TMC
Epps et al.	E-02-2-3-2	45.9	12.36	10	5	136.2	7.2	7.2
	E-08-2-1-6	49.2	6.3	9	5	140.4	6.5	6.5
Titus-Glover and Fernando	Limestone (-2% OMC)	64.71	17.61	12.8	7.9	127.4	9.045	7.045
	Limestone (OMC)	64.71	17.61	12.8	7.9	127.4	9.045	9.045
Tutumluer et al.	Dolomite FC 4% (OMC)	69.9	4	N/A	N/A	133	10.5	10.5
	Dolomite FC 8% (OMC)	71.1	8	N/A	N/A	133	8.48	8.48

The collected base properties were input into the trained ANN model to predict k_1, k_2 *and* k_3. Resilient modulus values were calculated using the predicted coefficients from the ANN models and compared with the test results. Figure 4.7 showed the comparison between measured and estimated M_R values using the ANN predicted coefficients.

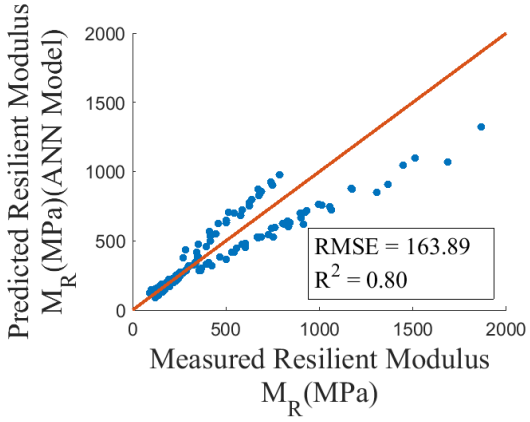

Figure 4.7 Validation of measured versus ANN predicted M_R at various stress levels for collected unbound materials

The data points plotted above the line of equality were from the UIUC dataset and those plotted below were from the TTI. The TTI data were all plastic base whereas UIUC base

materials were non-plastic. The over predictions in estimated suction for non-plastic base materials contributed to the over predicted M_R values for UIUC dataset. Overall, the M_R values estimated using the predicted coefficients from the ANN models produced a good fit with the test results. Figure 4.7 depicted a R^2 value of 0.8 between measured and predicted dataset. Hence, the developed ANN model can be used as a prediction tool to accurately estimate the M_R model coefficients that are used in pavement design and analysis.

4.7. Conclusions

This study developed ANN models to predict the coefficients of a stress and moisture dependent resilient modulus model. Two three layered ANN models were developed for plastic and non-plastic base materials respectively where base physical and index properties were selected as input. A good prediction accuracy of the developed models indicate better estimation of the resilient modulus of base materials.

5. PREDICTION MODEL FOR SHEAR STRENGTH AND PERMANENT DEFORMATION MODEL COEFFICIENTS

5.1. Introduction

The Pavement ME design mainly considers the elastic behavior of unbound base and subgrade materials but little attention has been paid to their shear strength. Previous studies have presented that the shear strength of underlying layer materials is related to the pavement performance through the following aspects:

- Influence on accumulation of permanent deformation in flexible pavements
- Influence on extent of erosion in rigid pavements
- Influence on degree of bonding between the concrete slab and the base course in rigid pavements

In flexible pavements, the shear strength directly affects the amount of total rutting (Theyse et al. 1996, Fernando et al. 2008, Maree 1978). For example, it was suggested that the dominant factor in determining permanent deformation is the relationship between the shear strength of the soil and the applied shear stress. The ratio of the shear strength to shear stress performs well in limiting the permanent deformation of granular materials against shear failure (Theyse et al. 1996, Maree 1978).

Shear strength effects the extent of erosion in the base course of rigid pavements, which is the key factor in the development of faulting in JPCP and punchouts in CRCP. “Soil Erodibility”, (2014) depicted that a small change in the shear strength has a considerable effect of the degree of erosion in the lower range of shear strength. Furthermore, in rigid pavements,

the shear strength is directly related to the degree of bonding between the concrete slab and base course and the degree of bonding has a significant impact on the performance of rigid pavements (Tarr et al. 1999, Bari et al. 2013, Croney 1977, Delatte et al. 2000).

5.2. Prediction Model for Shear Strength of Base and Subgrade

In light of the critical role of shear strength in performance prediction, it is incorporated by the research team in the model formulation of both flexible and rigid pavements. The general shear strength model is defined according to the Mohr-Coulomb failure envelope, which is determined from triaxial tests on laboratory molded specimens.

$$\tau = c + \sigma_n \tan\phi \qquad (5.1)$$

where τ is the shear stress; c is the total cohesion; σ_n is the normal stress on the failure plane; ϕ is the angle of internal friction

Furthermore, the impact of moisture variations on the shear strength is taken into account in this study. As the water content increases by a small amount, the shear strength decreases significantly depending on the magnitude of normal stress (Oloo, 1994). Such a reduction accelerates shear failure and intensifies rutting in flexible pavements and erosion in rigid pavements. The research team has developed a moisture-sensitive shear strength model for unbound base materials (Lytton 1995).

$$\tau = c' + (\sigma_n - \theta f h_m)\tan\phi' \qquad (5.2)$$

where c' is the effective cohesion; ϕ' is the effective friction angle; θ is the volumetric water content; f is the saturation factor; and h_m is the matric suction;

Figure 5.1 illustrates the Equation 5.2 which represents the dependence of the shear strength of unbound materials on the matric suction.

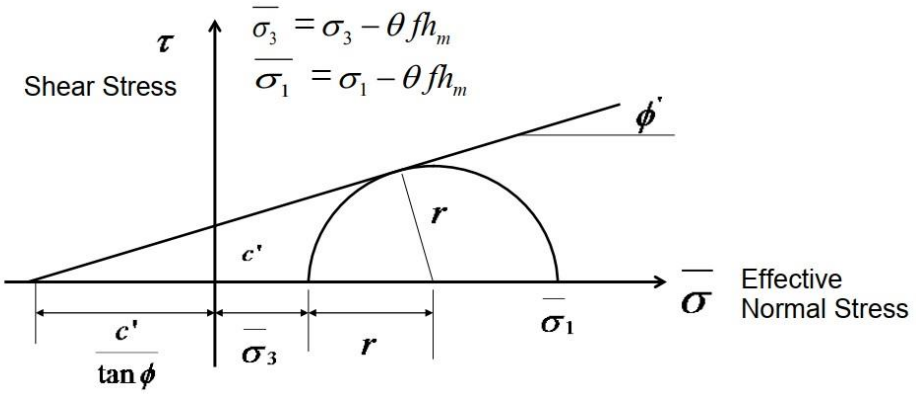

Figure 5.1 Schematic plot of Mohr's circle showing dependence of shear strength on matric suction

To make the moisture-sensitive shear strength model more applicable in the pavement design, prediction models have been developed for the shear strength parameters c′ and ϕ'. In this way, the shear strength of unbound layers and subgrade can be estimated using common soil properties in the absence of triaxial test data.

5.2.1. Prediction Model for Unbound Base

To develop the prediction models for unbound base materials, the measured shear strength parameters of different types of base materials were collected from literature sources (Epps et al. 2014, Tutumluer et al. 2009, and Chow et al. 2014). Additional data were collected to obtain soil physical properties such as gradation, Atterberg limit, optimum and saturated moisture content and the soil water characteristic curve of the various materials tested. Finally, regression analysis was conducted to determine the relationships between the shear strength parameters (c′ and ϕ') and the collected physical properties.

$$c' = -0.221 * PI + 4.6 * \theta_{sat}(\%) + 455.62 * G_s - 1262.75 \quad (5.3)$$

$$\phi' = 0.0272 * PI - 0.638 * MC_{opt}(\%) - 1.487 * \theta_{sat}(\%) + 69.92 \quad (5.4)$$

The goodness of fitting by the developed regression equations is shown in Figure 5.2 for the collected base materials. R^2 value of 0.81 and 0.87 for c′ and ϕ' parameters respectively indicate that the regression equations have a good prediction accuracy.

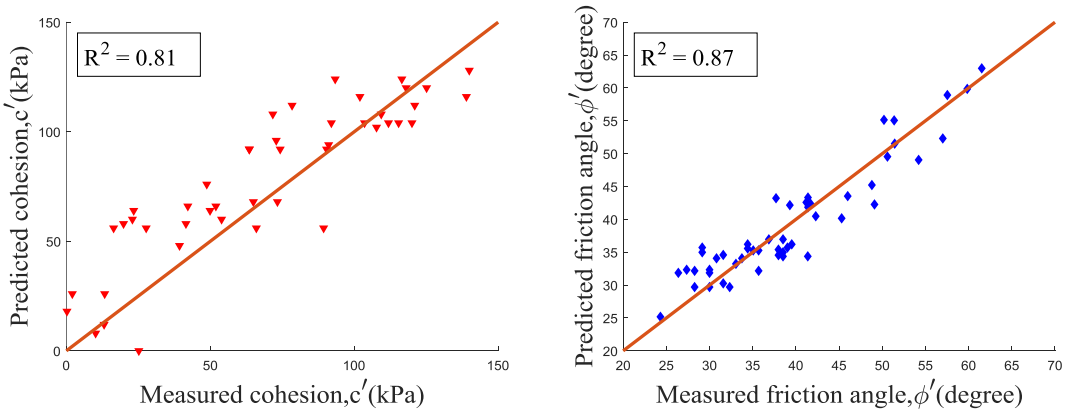

(a) **(b)**

Figure 5.2 Comparison of predicted and measured shear strength model parameters (a) c′ and (b) ϕ'

5.2.2. Prediction Model for Subgrade

Similar prediction models have been developed for the shear strength parameters of subgrade. The friction angle is dependent on the Plasticity Index (Holtz and Kovacs 1981). Based on the experimental test data, an empirical correlation is developed between ϕ' and PI for normally consolidated soils as shown in Equation 5.5.

$$\phi' = 0.0014 * PI^2 - 0.28 * PI + 35.87 \quad (5.5)$$

It is obvious that the matric suction, friction angle, porosity, and gradation of the subgrade material have an effect on the cohesive shear strength, and this is confirmed with subsequent studies in the mechanics of unsaturated soils (Lytton 1995, Epps et al. 2014). Due to insufficient triaxial test data for subgrade, unconfined compressive strength test data were

collected form LTPP database and used to develop the prediction model for cohesive strength. In this study, an ANN model has been developed to predict the cohesion parameter from subgrade physical and strength properties. The architecture of the ANN model is shown in Figure 5.3. A three layered network was constructed with one input, one hidden and a single output layer. Maximum dry density, soil porosity, effective friction angle and suction value at optimum moisture content are selected as input parameters. The hidden layer is consisted of 10 neurons and the c′ parameter is the output of the developed model. 432 unconfined compressive strength test data were collected from LTPP and used in training and validating the ANN model.

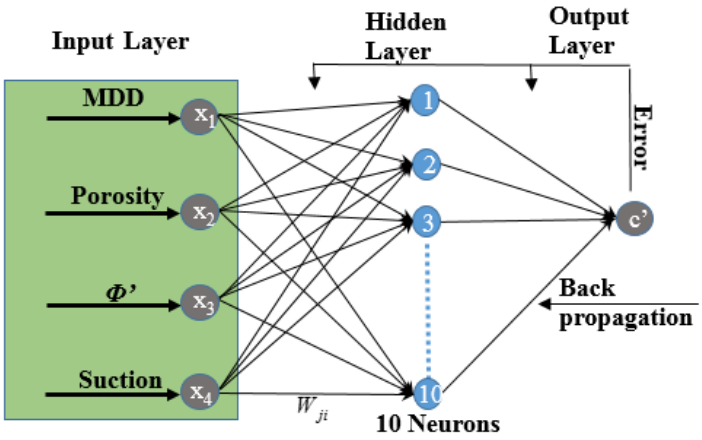

Figure 5.3 Illustration of three-layer neural network archtictute to predict c′ parameter

Figure 5.4 shows the prediction accuracy of the developed ANN model for training and validation datasets. The obtained R^2 value of 0.98 and 0.97 for training and validation dataset demonstrate that the developed ANN model can accurately predict the c′ parameter.

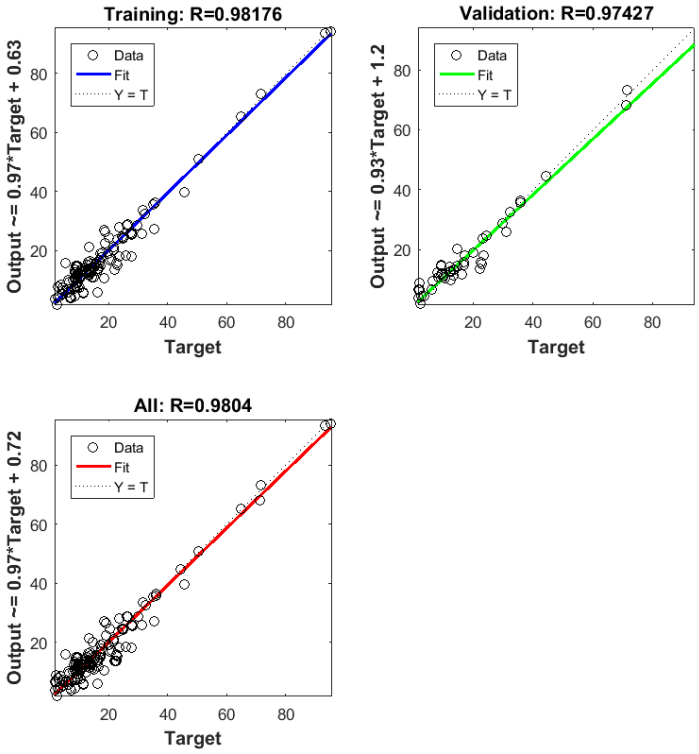

Figure 5.4 Target and output c´ values for training, validation and overall datasets

5.3. Prediction Model for Permanent Deformation of Unbound Material

Permanent deformation is a major form of distress in flexible and rigid pavement. In the pavement ME design, the total permanent deformation is the sum of the individual layer permanent deformations, i.e., surface layer, unbound layers and subgrade layer. The permanent deformation model for unbound base and subgrade layers used in the Pavement ME design is shown in Equation 5.6.

$$\delta = \beta_s \left(\frac{\varepsilon_0}{\varepsilon_r}\right) e^{-\left(\frac{\rho}{N}\right)^{\beta}} \varepsilon_v h \qquad (5.6)$$

where δ is the permanent deformation for the layer; ϵ_r is the resilient strain imposed in the laboratory test; ϵ_v is the average vertical resilient strain in the layer; *h* is the thickness of the

layer; N is the number of traffic repetitions; $\epsilon 0$, ρ, β are the model coefficients; βs is the gloabal calibration coefficient (1.673 for granular materials and 1.35 for subgrade soils).

However, the rutting model used in the pavement ME design is less sensitive to the modulus and the thickness of the unbound layers (Masad and Little 2004). As a result, a different permanent deformation model is proposed by Tseng and Lytton (Tseng and Lytton 1989), shown in Equation 5.7.

$$\delta = \varepsilon_0 e^{-(\frac{\rho}{N})^{\beta}} h \tag{5.7}$$

Later on, the Tseng-Lytton model was improved and a new mechanistic-empirical permanent deformation model for unbound materials was proposed, which is capable of predicting the permanent deformation behavior at different stress states using the single-stage test protocol (Gu et al. 2015). The formulation of the model is given as follows:

$$\varepsilon_p(N) = \varepsilon_0 e^{-(\rho/N)^{\beta}} (\frac{\sqrt{J_2}}{p_a})^m (\frac{\alpha I_1 + K}{p_a})^n \tag{5.8}$$

$$\alpha = \frac{2\sin\phi'}{\sqrt{3}(3-\sin\phi')} \tag{5.9}$$

$$K = \frac{c'.6\cos\phi'}{\sqrt{3}(3-\sin\phi')} \tag{5.10}$$

where J_2 is the second invariant of the deviatoric stress tensor; I_1 is the first invariant of the stress tensor; ε_0 , ρ , β , m , and n are model coefficients; c′ and ϕ' are effective cohesion and friction angle, respectively.

In this model, the two terms, J_2 and ($\alpha I_1 + K$) are incorporated into the Tseng-Lytton model, which is used to reflect the influence of a stress state on the permanent deformation of unbound materials.

Many laboratory tests were conducted by the same research team and validated the accuracy of the model proposed in Equation 5.8. They concluded that the proposed model matches well with the measured permanent deformation curves. The sensitivity of the proposed model was also studied and demonstrated that it improved the sensitivity of unbound layer significantly (Gu et al. 2017). Hence the model proposed by Gu et al. (2015) is adopted is this study to predict permanent deformation of base and subgrade soils.

The model coefficients (ϵ_0, ρ, β, m and n) in Equation 5.8 can be determined by two approaches.

1. By fitting the model to the permanent strain measured in the repeated load permanent deformation test
2. Using prediction models developed from a set of physical properties such as the maximum dry density, percent fines content, and aggregate gradation etc.

From these two approaches, approach 1 is time consuming, requires an extensive laboratory setup and expert personnel to conduct the test. In this study a regression model is developed to predict the permanent deformation of unbound materials.

5.3.1. Prediction Models for Permanent Deformation Coefficients of Unbound Base

In order to develop the prediction models of the coefficients of Equation 5.8, the research team utilized the measurements from the repeated load triaxial test on 108 different types of base materials collected from literature sources (Epps et al. 2014, Tutumluer et al. 2009, Chow et al. 2014, Cetin et al. 2014a, Soliman and Shalaby 2015). In addition to triaxial test data, soil physical properties such as gradation, Atterberg limit, maximum dry density and optimum moisture content data were also collected for the base samples. Finally, regression analysis was

conducted to determine the relationships between the permanent deformation model coefficients (ϵ_0, ρ, β, m and n) and the collected physical properties.

$$\log \varepsilon_0 = 0.017 * P_4 - 0.00967 * MDD + 0.99 \quad (5.11)$$

$$\log(\rho) = 0.0574 * P_4 - 0.0937 * MC + 5.0756 \quad (5.12)$$

$$\beta = -0.01483 * P_4 + 0.00813 * MDD - 0.00136 * sat(\%) \quad (5.13)$$

$$m = 0.2153 * \varepsilon_0 + 0.396 \quad (5.14)$$

$$n = -0.22993 * m - 0.746 \quad (5.15)$$

where P_4 is the percent of material passing No. 4 sieve (unit: %); *MDD* is the maximum dry density (unit: lb/ft^3); *MC* is the test moisture content (unit: %); *sat(%)* is the degree of saturation (unit: %)

The goodness of fitting by the developed regression equations is shown in Figure 5.5 for the collected base materials. The predicted coefficients showed a good match with the measured values.

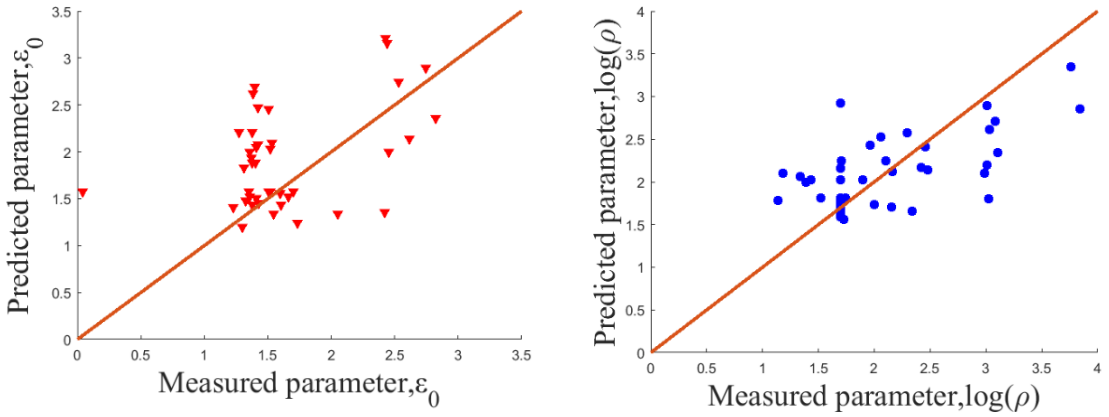

(a) **(b)**

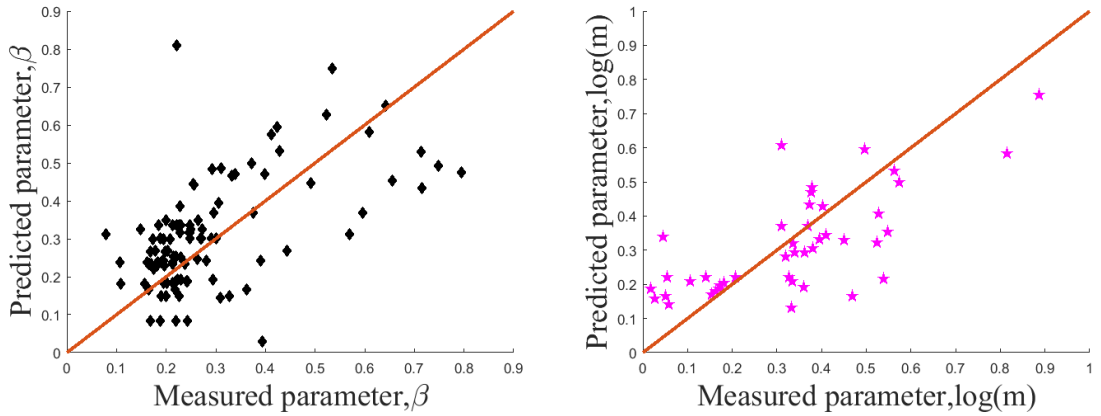

(c) **(d)**

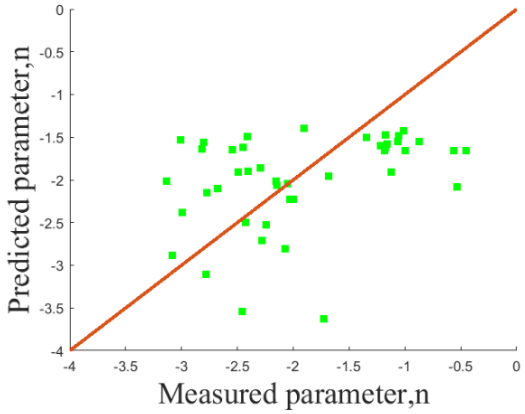

(e)

Figure 5.5 Comparison of predicted and measured permanent deformation model parameters (a) ε_0 (b) ρ (c) β (d) m and (e) n

6. DEVELOPMENT OF A MODULUS OF SUBGRADE REACTION MODEL TO IMPROVE SLAB-BASE INTERFACE BOND SENSITIVITY[‡]

6.1. Introduction

Subgrade acts as a supporting layer in pavement structure. Proper characterization of subgrade strength is necessary for pavement design and construction. Modulus of subgrade reaction (*k*-value) is widely used to evaluate subgrade strength and soil structure interaction, and design the rigid pavements. It is represented as the reaction pressure (P) sustained by the soil under a rigid plate per unit settlement (Δ). The *k*-value can be measured from a field plate load test conducted on top of subgrade (Rao, 2000; MnDOT 2007) or estimated from correlations with other load bearing capacity tests e.g., consolidation test, triaxial test and California Bearing Ratio (CBR) test (Ziaie-Moayed and Janbaz, 2009).

The *k*-value from the plate load test is calculated using the Winkler model, which assumes an elastic plate resting on a liquid foundation (Winkler, 1867). This model considers the soil behavior as a series of linear elastic springs, as shown in Figure 6.1a. Many researchers have utilized the model to characterize soil-foundation interaction (Biot, 1922; Terzaghi, 1955; Vesic, 1961; Horvath, 1983; Vallabhan and Das, 1988). In the Winkler model, the submodel of elastic plate is well established, but the submodel of foundation needs modification. It was attempted to improve the Winkler model by adding other forms of interaction among the spring elements (Filonenko-Borodich, 1940; Hetényi, 1971; Pasternak, 1954; Vlasov and Leont'ev, 1966;

‡ Reprinted with permission from "Development of a modulus of subgrade reaction model to improve slab-base interface bond sensitivity" by Sajib Saha, Fan Gu, Xue Luo and Robert Lytton, 2019. International Journal of Pavement Engineering, 1-12, Copyright [2019] by Taylor & Francis.

Vallabhan and Das, 1989). The Pasternak model shown in Figure 6.1b allows the transverse connection in the supporting media and introduces shear interaction on slab-base interface (Shi et al., 1993&1994). Later on, Iancu-Bogdan and Vasile, (2010) and Farouk (2014) investigated the problem of beam on foundations using the finite element method. They considered more complex factors such as the realistic contact stresses between slab and foundation, and the nonlinear stress-dependent elastoplastic behavior of soil foundation.

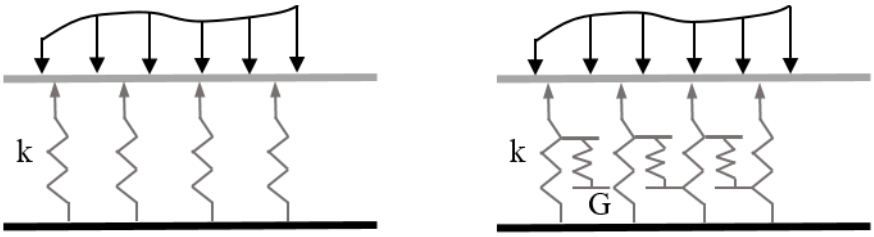

(a) **(b)**

Figure 6.1 Foundation models for rigid pavement (a) Winkler model; (b) Pasternak model

Recently, the concept of modulus backcalculation was proposed using the deflection basin generated from a falling weight deflectometer (FWD) (Hoffman and Thompson 1981). Hall et al. (1991) derived the solution of the dynamic *k*-value of subgrade from the FWD deflection basin. Subsequently, the "backcalculated best-fit approach (BBF)" was adopted by the Long Term Pavement Performance (LTPP) program to determine *k*-values for rigid pavements (FHWA, 2001).

For the rigid pavement analysis in the Pavement ME Design, the load bearing capacity of subgrade foundation is characterized by an effective dynamic *k*-value. The actual rigid pavement structure is transformed into an equivalent structure with a *k*-value, which represents the compressibility of all layers underneath the concrete slab. The subbase and subgrade materials in

the design guide have been characterized by the Winkler model, which is easy for implementation but neglects the shear interaction with the supporting media. In the BBF approach, the degree of bonding on the slab-base interface is assumed to be either 1 for fully rough interface or 0 for frictionless slip interface. However, it is recognized that none of these assumptions are realistic for base courses (Tarr et al. 1999, Saha et al. 2019a). Shear restraints exist between the slab and base layer because of rough interfaces. This causes an interlocking of the slab and base, which has a significant effect on the structural performance of pavement (Jeong and Zollinger, 2001; Jung and Zollinger, 2011; Bari et al., 2013).

In addition, the nature of cross anisotropy of base material is not considered in the Pavement ME Design while calculating the *k*-value. Recent studies have shown that granular base materials exhibit stress dependent and cross anisotropic behavior (Gu et al., 2016; Zhang et al., 2018a&b). The triaxial testing protocols were developed by Adu-Osei et al. (2001) and Tutumluer and Seyhan (1999) for determining anisotropic resilient properties of granular materials in the laboratory. Tutumluer et al. (2003) and Park and Lytton (2004) found that the use of nonlinear anisotropic base modulus significantly affects the stress distribution in the base layer and diminishes the horizontal tensile stresses in the bottom half of the base layer. The performance of pavement was predicted by Masad et al. (2006) and Oh et al. (2006) using the nonlinear cross-anisotropic model and showed good agreement with the field measurements. Hence, there was a need to develop a modified *k*-value model, which involves both corrected base modulus due to cross anisotropy and the slab-base interface bond.

This chapter is organized as follows. The next section presents the detailed description of the development of the modified *k*-value model. Subsequently, the modified *k*-value is calculated

for the LTPP sections. In the following, an artificial neural network (ANN) model is developed to predict the modified *k*-value for a wide range of pavement layer moduli, layer thicknesses and slab-base bonding ratios. The development of an ANN model involves two steps: 1) estimation of pavement structural response using the commercial finite element (FE) software ABAQUS; and 2) construction of ANN architecture based on the FE simulation results. After that, the developed ANN models are compared with the calculated *k*-values for selected pavement sections in terms of prediction accuracy. The final section summarizes the major findings of this study.

6.2. Development of Modified *k*-Value Model

The development of modified *k*-value model is elaborated as below, which contains four submodels:

- Cross anisotropic modulus submodel for the base layer
- Slab-base equivalent thickness submodel
- Slab-base interface shear bonding submodel
- Modified *k*-value submodel

6.2.1. Cross Anisotropic Modulus Submodel for Base Layer

The cross-anisotropic behavior of base material is characterized by the generalized Hooke's Law, which is shown in Equation 6.1.

$$\begin{bmatrix} \frac{1}{E_x} & \frac{-\nu_{xy}}{E_y} & \frac{-\nu_{xx}}{E_x} \\ \frac{-\nu_{xy}}{E_x} & \frac{1}{E_y} & \frac{-\nu_{xy}}{E_x} \end{bmatrix} \begin{bmatrix} \sigma_x \\ \sigma_y \\ \sigma_x \end{bmatrix} = \begin{bmatrix} \varepsilon_x \\ \varepsilon_y \end{bmatrix} \tag{6.1}$$

where E_x is the horizontal modulus; E_y is the vertical modulus; v_{xy} is the Poisson's ratio to characterize the effect of vertical strain on horizontal strain; v_{xx} is the Poisson's ratio to characterize the effect of horizontal strain on the perpendicular horizontal strain.

A layered elastic program, WinJULEA, is used in this submodel to determine the stress states in the middle of base layer. The computed stresses are then input into the generalized resilient modulus model shown in Equation 6.2 to calculate the vertical modulus of base layer (NCHRP, 2003). In general, the resilient moduli in the vertical and horizontal directions follow a constant ratio, *n* (Tutumluer et al. 1999, Masad et al. 2006), which is shown in Equation 6.3. It is known that the current Pavement ME Design does not allow inputting both horizontal and vertical moduli of base materials. To consider the effect of cross anisotropy, the base modulus is corrected as the golden mean of the vertical and horizontal modulus, as shown in Equation 6.4.

$$M_R{}^{v} = k_1 P_a \left(\frac{\theta}{P_a}\right)^{k_2} \left(\frac{\tau_{oct}}{P_a} + 1\right)^{k_3} \tag{6.2}$$

$$n = \frac{M_R{}^{H}}{M_R{}^{V}} \tag{6.3}$$

$$M_R = (M_R{}^{V} \times M_R{}^{H})^{1/2} = M_R{}^{V} (n)^{1/2} \tag{6.4}$$

where $M_R{}^{V}$ is the resilient modulus in the vertical direction; $M_R{}^{H}$ is the resilient modulus in the horizontal direction; *n* is the modulus ratio.

An iterative model is developed within this submodel to determine the cross anisotropic resilient modulus of base material. Figure 6.2 is a schematic flowchart for the iterative method.

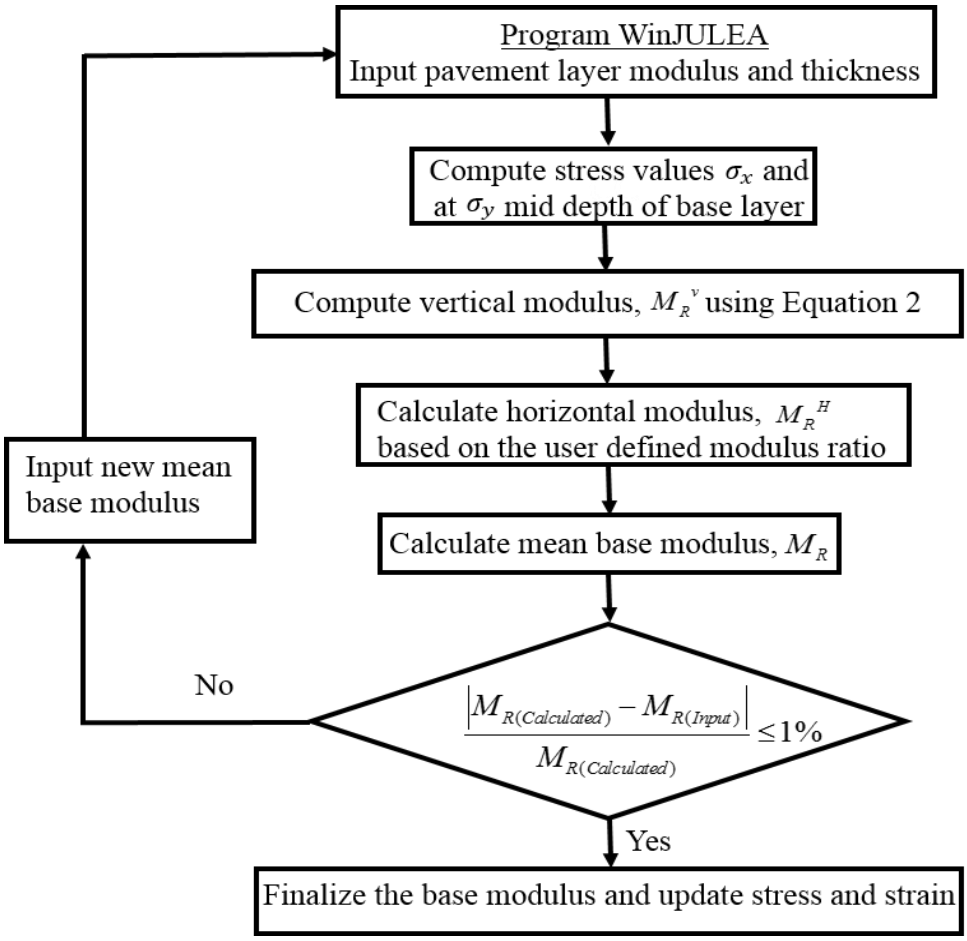

Figure 6.2 Flowchart of corrected base modulus due to cross anisotropy

The input parameters include the pavement layer thicknesses and initial moduli in the WinJULEA program. Initial values of the vertical and horizontal stresses are computed from the analysis. The computed initial stresses are then used to calculate the resilient moduli using Equations 6.2-6.4. Equation 6.5 presents the convergence criterion for the iteration, which indicates that the base modulus is finalized whenever the difference between the input and calculated moduli is less than 1 percent of the calculated modulus. If the difference is greater

than 1 percent of calculated modulus, the calculated modulus will be input again in the WinJULEA program, and the iteration process is continued until the desired criterion is reached.

$$\frac{\left|M_{R(Calculated)} - M_{R(Input)}\right|}{M_{R(Calculated)}} \leq 1\% \tag{6.5}$$

6.2.2. Slab-Base Equivalent Thickness Submodel

The formulation of the equivalent thickness submodel includes two steps. First, a cooperating slab and base system is introduced using the transformed-section method, as shown in Figure 6.3.

The moment of inertia of the pavement cross section is calculated based on the transformed section as follows:

$$I_{tr} = I_{slab} + I_{base} + \delta \sum A_i \bar{d}_i^2 \tag{6.6}$$

where I_{tr} is the moment of inertia of the transformed pavement section; I_{slab} is the moment of inertia of the slab; I_{base} is the moment of inertia of the transformed base; A_i is the area of the slab and the transformed area of the base course; d_i is centroidal distance to each of the areas; and δ is the interface shear bonding.

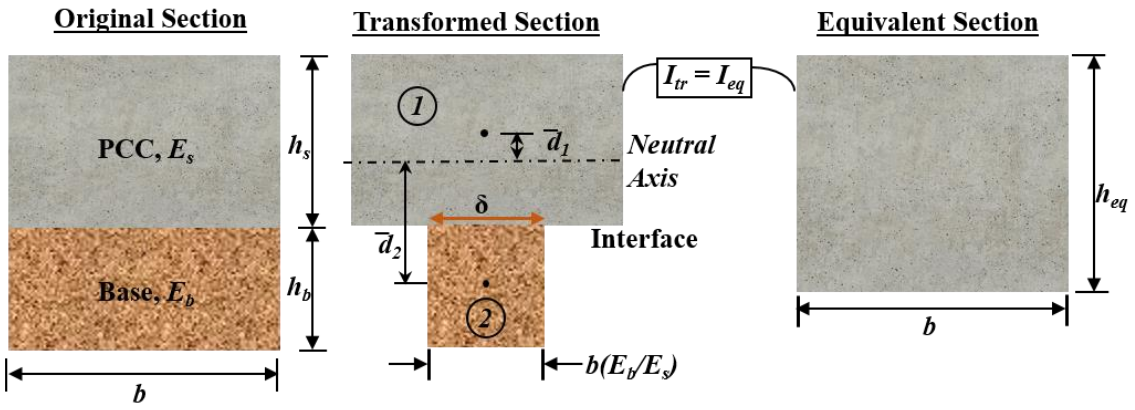

Figure 6.3 Illustration of transformed-section method for a cooperated concrete slab and base course system

The calculation steps of the moment of inertia for a typical cooperated slab and base system is shown in Table 6.1.

Table 6.1 Steps of moment of inertia calculation for a cooperated slab and base system

Body	Area(A)	$\bar{y}$	$A\bar{y}$	$\bar{z}$	$I_{C.G.}$	$\bar{d}$	$I_{N.A.}$
(1)	bh_s	$h_s/2$	$bh_s^2/2$	$\frac{\sum A_i\bar{y}_i}{\sum A_i}$	$\frac{1}{12}bh_s^3$	$\bar{z}-\frac{h_s}{2}$	$I_{C.G._1}+A_1\bar{d}_1^2$
(2)	$b(\frac{E_b}{E_s})h_b$	$h_s+h_b/2$	$(h_s+h_b/2)b(\frac{E_b}{E_s})h_b$		$\frac{1}{12}b(\frac{E_b}{E_s})h_b^3$	$h_s+\frac{h_b}{2}-\bar{z}$	$I_{C.G._2}+A_2\bar{d}_2^2$
	$\sum A_i = A_1+A_2$		$\sum A_i\bar{y}_i = A_1\bar{y}_1+A_2\bar{y}_2$				

Second, the thickness of the equivalent section is calculated using the moment of inertia of the transformed section. The transformed section that consists of concrete and base is converted into an equivalent cross section of concrete. The thickness of the equivalent section is estimated by considering the same moment of inertia for both sections. For a plate, the thickness of equivalent section is expressed as,

$$h_{eq} = \sqrt[3]{\frac{I_{tr} * 12}{b}(1-\nu^2)} \quad (6.7)$$

where h_{eq} is the thickness of the equivalent section; b is the width of the equivalent section; and ν is the Poisson's ratio of concrete

As shown in Equations 6.6 and 6.7, the thickness of the equivalent cross section depends on the degree of bonding, δ in the slab-base interface. A formulation of slab-base interface shear bonding is presented in the next section.

6.2.3. Slab-Base interface shear bonding model

The interface shear bonding, δ in Equation 6.6 is expressed by the ratio of in-situ shear stress $(\tau_{zx})_{2\theta_f}$ and the shear stress v_2 on the slab-base interface when shear stress is fully transferred.

$$\delta = \frac{(\tau_{zx})_{2\theta_f}}{v_2}, \quad (\tau_{zx})_{2\theta_f} \le s_f \quad (6.8)$$

where s_f is the shear strength of the base course;

Figure 6.4 shows a schematic of the shear stress in the PCC-base interface. The parameters v_1 and v_2 are shear stresses on the interface in the slab and base layer, respectively when shear stress is fully transferred. The parameter $(\tau_{zx})_{2\theta_f}$ is the shear stress in the base course on the interface for in situ conditions, which is limited by the shear strength, s_f of base course.

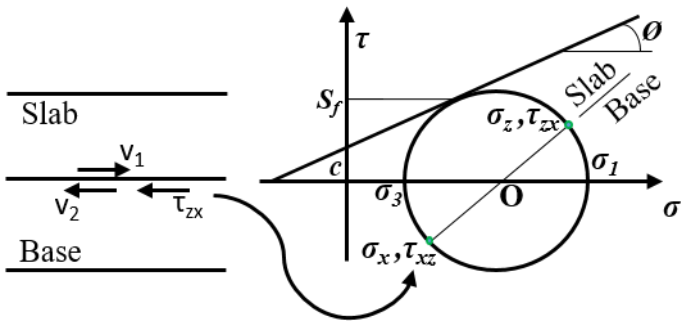

Figure 6.4 Illustration of in-situ shear stress in the base course on the PCC-base interface using a Mohr-Coulomb failure envelope

When $(\tau_{zx})_{2\theta_f}$ is greater than v_2, the interface is considered as fully bonded. Depending on the ratio of the $(\tau_{zx})_{2\theta_f}$ and v_2, the partial bonding condition is defined on the PCC-base interface. The following subsections derive the expressions of v_2 and $(\tau_{zx})_{2\theta_f}$.

Formulation of v_2

The shear stress acting on the two faces of PCC-base interface can be expressed using the theorem of elastic beam shear stress on the transformed section. It is assumed that shear stress is fully transferred through the interface of the transformed section.

$$v_1 = \frac{VQ_1}{Ib}; \tag{6.9}$$

$$v_2 = \frac{VQ_2}{Ib(\frac{E_b}{E_s})} \tag{6.10}$$

where V is the shear force acting on the cross section; E_s is the slab modulus; E_b is the base modulus.

The parameter Q is the first moment of area from the neutral axis of the transformed section; herein $Q_1 = A_1\bar{d}_1$ and $Q_2 = A_2\bar{d}_2$.

Substituting Equation 6.9 into Equation 6.10 yields,

$$v_2 = v_1 * \frac{Q_2}{Q_1(E_b / E_s)} \tag{6.11}$$

Note that v_1 is determined using the Boussinesq point load solution (Boussinesq, 1885), as shown in Equation 6.14. Figure 6.5 illustrates the shear stress acting on the PCC-base interface.

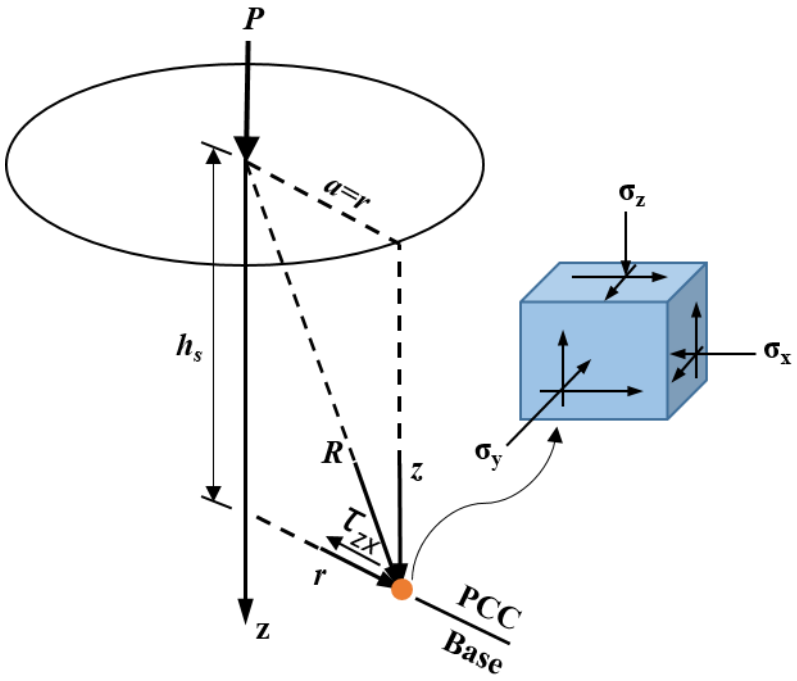

Figure 6.5 Stresses in slab-base interface caused by a point load

$$\sigma_x = \frac{P}{2\pi}\left[\frac{3h_s a^2}{(h_s^2 + a^2)^{5/2}} - \frac{(1-2\nu)}{(h_s^2 + a^2)^{1/2}[(h_s^2 + a^2)^{1/2} + h_s]}\right] \quad (6.12)$$

$$\sigma_z = \frac{3P}{2\pi}\frac{h_s^3}{(h_s^2 + a^2)^{5/2}} \quad (6.13)$$

$$v_1 = \tau_{zx} = \frac{3P}{2\pi}\left[\frac{ah_s^2}{(h_s^2 + a^2)^{5/2}}\right] \quad (6.14)$$

where P is the surface point load; h_s is the thickness of the slab; a is the horizontal distance of target point from P; ν is the Poisson's ratio

Substituting Equation 6.14 into Equation 6.11 yields,

$$v_2 = \frac{3P}{2\pi}\left[\frac{ah_s^2}{(h_s^2 + a^2)^{5/2}}\right]\frac{h_b(h_s + \frac{h_b}{2} - \bar{z})}{h_s(\bar{z} - \frac{h_s}{2})} \quad (6.15)$$

where h_b is the thickness of the base; $\bar{z}$ is the distance of neutral axis from point of interest;

Formulation of $(\tau_{zx})_{2\theta f}$

The expression of in-situ shear stress in the base course on PCC-base interface is derived using the Mohr-Coulomb failure envelope, as shown in Figure 6.6. The failure envelope is defined by the shear strength parameters, i.e., cohesion, c and friction angle, ϕ.

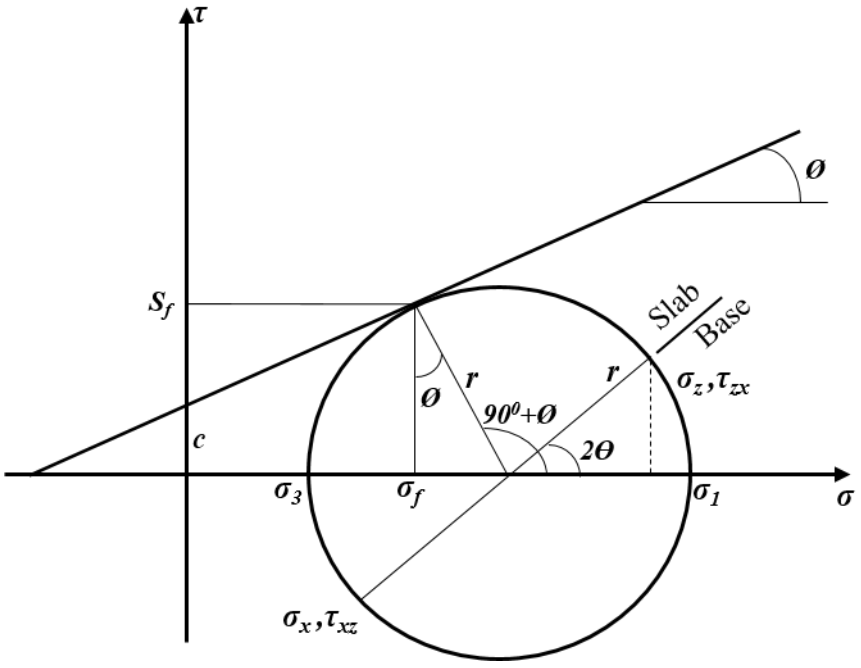

Figure 6.6 Maximum shear strength of base course in Mohr Coulomb failure envelope

$$(\tau_{zx})_{2\theta_f} = r\sin 2\theta \tag{6.16}$$

where r is the radius of the Mohr's circle;

Herein, the state of plane stress on the slab-base interface is defined by σ_x, σ_z and τ_{zx}, which is rotated by an angle of 2θ from principal plane of stress. The angle of rotation, 2θ is expressed in Equation 6.17.

$$\tan 2\theta = \frac{\tau_{zx}}{\frac{\sigma_z - \sigma_x}{2}} = \frac{3\left[\frac{ah_s^2}{(h_s^2 + a^2)^2}\right]}{\frac{1}{2}\left[\frac{3(h_s^3 - h_s a^2)}{(h_s^2 + a^2)^2} + \frac{(1-2\nu)}{\left[\left(h_s^2 + a^2\right)^{1/2} + h_s\right]}\right]}$$

$$\Rightarrow 2\theta = \tan^{-1}\left(\frac{3\left[\frac{ah_s^{\,2}}{(h_s^{\,2}+a^2)^2}\right]}{\frac{1}{2}\left[\frac{3(h_s^{\,3}-h_s a^2)}{(h_s^{\,2}+a^2)^2}+\frac{(1-2\nu)}{\left[\left(h_s^{\,2}+a^2\right)^{1/2}+h_s\right]}\right]}\right) \tag{6.17}$$

As illustrated by Figure 6.6, the shear strength of the base course is calculated by Equations 6.18 and 6.19.

$$s_f = r\cos\phi \tag{6.18}$$

$$s_f = c+\sigma_f \tan\phi = c+[\bar{\sigma}-r\sin\phi]\tan\phi \tag{6.19}$$

where σ_f is the normal stress on the failure plane;

Therefore,

$$r = (c+\bar{\sigma}\tan\phi)\cos\phi \tag{6.20}$$

Herein,

$$\bar{\sigma} = \frac{\sigma_z+\sigma_x}{2} = \frac{P}{4\pi}\left[\frac{3(h_s^{\,3}+h_s a^2)}{(h_s^{\,2}+a^2)^{5/2}} - \frac{(1-2\nu)}{(h_s^{\,2}+a^2)^{1/2}[(h_s^{\,2}+a^2)^{1/2}+h_s]}\right] \tag{6.21}$$

According to Equations 6.16, 6.17 and 6.20, it is obtained that

$$(\tau_{zx})_{2\theta_f} = (c+\bar{\sigma}\tan\phi)\cos\phi\sin\left[\tan^{-1}\left(\frac{3\left[\frac{ah_s^{\,2}}{(h_s^{\,2}+a^2)^2}\right]}{\frac{1}{2}\left[\frac{3(h_s^{\,3}-h_s a^2)}{(h_s^{\,2}+a^2)^2}+\frac{(1-2\nu)}{\left[\left(h_s^{\,2}+a^2\right)^{1/2}+h_s\right]}\right]}\right)\right] \tag{6.22}$$

The expression of interface shear bonding, δ is derived from Equations 6.8, 6.15 and 6.22,

$$\delta = \frac{(c+\bar{\sigma}\tan\phi)\cos\phi\sin[\tan^{-1}(\frac{3\left[\frac{ah_s^{\,2}}{(h_s^{\,2}+a^2)^2}\right]}{\frac{1}{2}[\frac{3(h_s^{\,3}-h_s a^2)}{(h_s^{\,2}+a^2)^2}+\frac{(1-2\upsilon)}{\left[\left(h_s^{\,2}+a^2\right)^{1/2}+h_s\right]}]})]}{\frac{3P}{2\pi}\left[\frac{ah_s^{\,2}}{(h_s^{\,2}+a^2)^{5/2}}\right]\frac{h_b(h_s+\frac{h_b}{2}-\bar{z})}{h_s(\bar{z}-\frac{h_s}{2})}} \quad (6.23)$$

6.2.4. Modified Subgrade k-Value Submodel

The modified *k*-value submodel is developed using the calculated h_{eq} and δ values from the previous submodels. The determination of the modified *k*-value is divided into the following steps (Saha et al. 2019b):

- The deflection patterns generated by FWD are used to determine the modified *k*-values. The FWD sensor deflections (0 cm, 30.48 cm [12 inch], 60.96 cm [24 inch], and 91.44 cm [36 inch] away from the loading point) are obtained, and the basin area, BA, is calculated as:

$$BA = \frac{SS}{2\times D_0}[D_0 + 2(D_1 + ... + D_{j-1}) + D_j] \quad (6.24)$$

  where *SS* is the FWD sensor spacing (30.48 cm ≈ 12 inch); and D_j is the sensor deflection (*j*=0 to 3).

- The effective relative stiffness length is calculated as follows:

$$l_e = [\frac{\ln(\frac{k_1 - BA}{k_2})}{-k_3}]^{1/k_4} \quad (6.25)$$

where k_1, k_2, k_3 and k_4 are the coefficients obtained from the field correlation, k_1=36, k_2=1812.597, k_3=2.559, and 1/k_4=4.387 (Smith et al., 2017)

- Finally the subgrade *k*-value is formulated in Equation 6.26. The concept of equivalent slab thickness is applied from Equation 6.7 to consider the effects of both the slab and base layer on the pavement subgrade *k*-value

$$k = \frac{E_s {h_{eq}}^3}{12(1-\nu^2){l_e}^4} \tag{6.26}$$

where E_s is the elastic modulus of the PCC; and ν is the Poisson's ratio of PCC.

6.3. Estimation of Modified *k*-value for LTPP Pavement Sections

The pavement data used in this study to estimate the modified *k*-value is collected from the LTPP database. A total of 505 sets of rigid pavement section data are collected, including both Jointed Plain Concrete Pavement (JPCP) and Continuously Reinforced Concrete Pavement (CRCP). In addition to the backcalculated layer moduli, the database includes layer thicknesses and FWD deflection patterns. In the LTPP, the FWD test uses four loading sequences with a target load of 27 kN (6000 lbs), 40 kN (9000 lbs), 53.38 kN (12000 lbs) and 71.17 kN (16000 lbs) respectively. In this study, only the deflection basins generated from 40 kN load are selected for analysis. To avoid the discrepancy in measured deflection patterns, the deflection basin tests that were performed along the mid-lane path are selected for the analysis. The mid-lane test locations are designated as J1 and C1 for JPCP and CRCP pavements, respectively.

6.3.1. Correction of Base Modulus

As shown in Equation 6.3, the resilient moduli of base material in the horizontal and vertical directions follow a constant ratio. Based on the existing laboratory results (Adu-Osei et al., 2001;

Kim, 2004), the *n* value is in the range of 0.3-0.5. In this study, the n value is assumed as 0.4 for all base materials collected from the LTPP pavement sections. Following the flowchart in Figure 6.2, the modulus of base materials are corrected for all pavement sections.

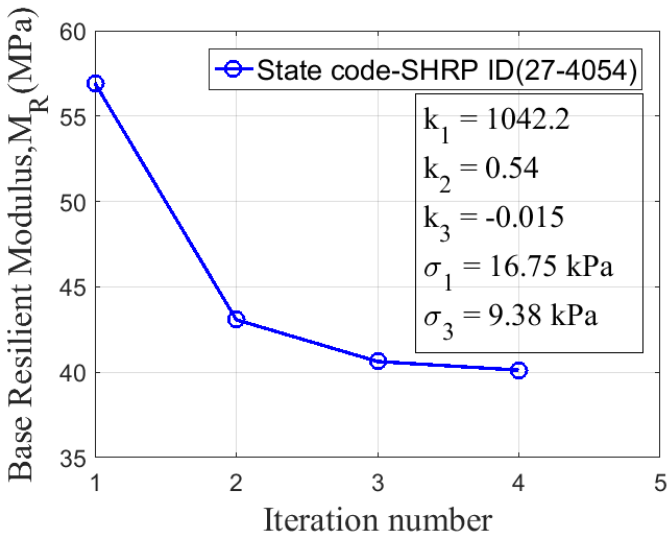

Figure 6.7 Base resilient modulus convergence with iteration number

The procedure to determine the corrected base modulus is illustrated for an example LTPP section 27-4054 (State code-SHRP ID). The pavement section 27-4054 consists of a 0.24 m (9.4-in.) PCC layer, a 0.15 m (6-in.) unbound base layer, and a semi-infinite silty clay subgrade layer. Herein, the backcalculated modulus value is collected from the LTPP database and used as the initial input at each layer. Figure 6.7 shows the plot of golden mean base modulus against iteration number. The value of collected M_R coefficients k_1, k_2 and k_3 for the base layer and the determined vertical and horizontal stress values after first iteration are also included in Figure 6.7. The final M_R value is achieved after four iterations when it meets the convergence criteria shown in Equation 6.5.

6.3.2. Estimation of Slab-Base Interface Bonding Ratio

The interface shear bonding ratio is calculated for the collected LTPP pavement sections. From the collected 505 pavement sections, 267 sections have the treated base layer underneath the PCC surface layer and 238 pavements section are constructed using unbound base course.

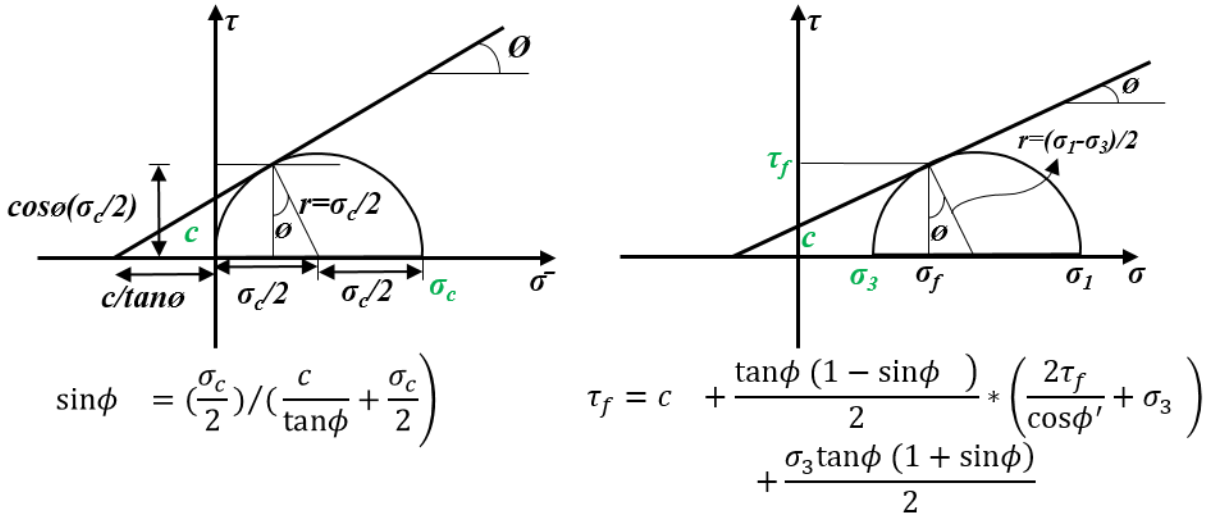

$$\sin\phi = \left(\frac{\sigma_c}{2}\right)/\left(\frac{c}{\tan\phi}+\frac{\sigma_c}{2}\right)$$

$$\tau_f = c + \frac{\tan\phi\,(1-\sin\phi)}{2} * \left(\frac{2\tau_f}{\cos\phi'}+\sigma_3\right) + \frac{\sigma_3\tan\phi\,(1+\sin\phi)}{2}$$

(a) **(b)**

Figure 6.8 Formulation of friction angle from Mohr Coulomb failure envelope for (a) treated base; (b) unbound base

As shown in Equation 6.23, the expression for the degree of bonding δ is based on the shear strength parameters c and ϕ. In the LTPP database, the available experimental data are not sufficient to determine these shear strength parameters. The unconfined compressive strength test data are available for cement and lime treated base materials, whereas triaxial shear strength tests are conducted for unbound base materials only at a confining pressure of 34.47 kPa (5psi). Hence, empirical models are used in this study to estimate the *c* and ϕ parameters from base strength and saturation properties.

Stabilized base layer

Existing studies have investigated the relationship between the cohesion parameter, *c* and the physical and strength properties of stabilized base materials. Balmer (1958) and Clough et al. (1981) reported that cement treatment increases cohesion while internal friction angle remains constant. Thompson (1966) stated that addition of lime to unbound material yields a substantial increase in cohesion and minor improvement in internal friction angle. The relationship suggested by Thompson (1966) is used in this study to determine the cohesion of treated soils based on unconfined compressive strength.

$$c = 64.12 + 0.292\sigma_c \tag{6.27}$$

where, σ_c is the unconfined compressive strength, unit: kPa;

Then the friction angle, ϕ, is determined from *c* and the collected unconfined compressive strength test data, as shown in Figure 6.8a. The unconfined compressive strength test data are collected for 55 treated base materials from the LTPP database. The degree of bonding, δ on the slab-base interfaces is calculated from Equation 6.23 using the estimated shear strength parameters.

Unbound base layer

Similarly, many researchers had investigated the shear strength test data and identified the influence of several physical properties on the shear strength parameters of unbound granular materials. The relative density and degree of saturation are the two most important parameters affecting the shear strength parameters of unbound base (Maree, 1978). Theyse (2000) evaluated the effects of relative density and degree of saturation on the shear strength parameters, and

proposed the following relationship for cohesion.

$$c = 0.0107e^{12.12RD}e^{-2.30S} \tag{6.28}$$

where *RD* is the relative density, unit: %; *S* is the degree of saturation, unit: %; and, c is the cohesion, unit: kPa.

Herein, RD is the ratio of the compacted density of a material to the maximum dry density (MDD). The density and water content data are collected from the LTPP database to calculate the *RD* and *S* in Equation 6.28. Figure 6.8b presents the equation to calculate the friction angle ϕ. Shear strength and compressive strength test data are collected from 88 granular unbound base courses, which are then used to calculate δ.

The black and green bars in Figure 6.9a denote the degree of bonding on slab-base interface using the proposed shear bonding submodel and BBF approach respectively.

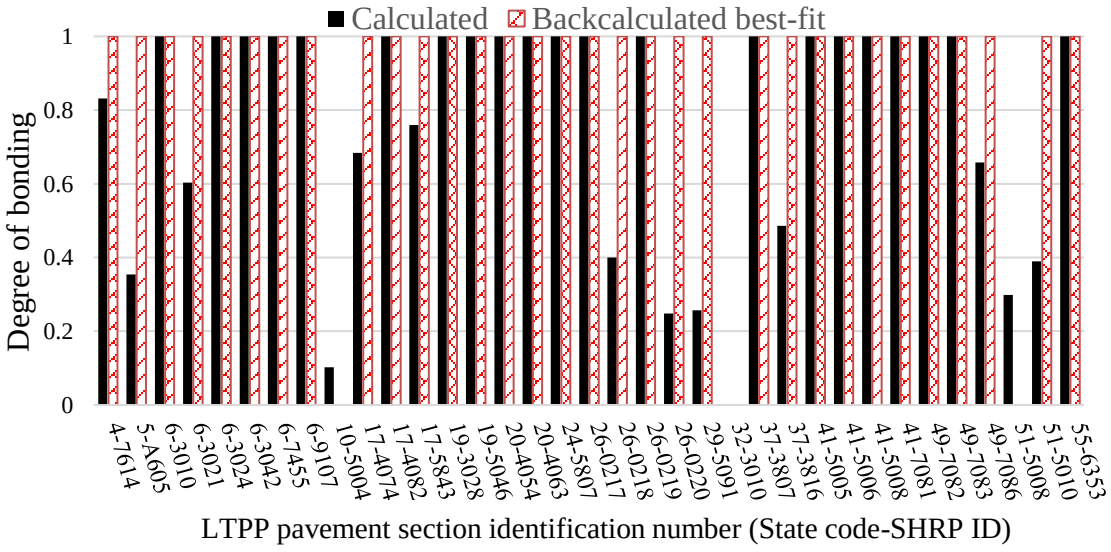

(a)

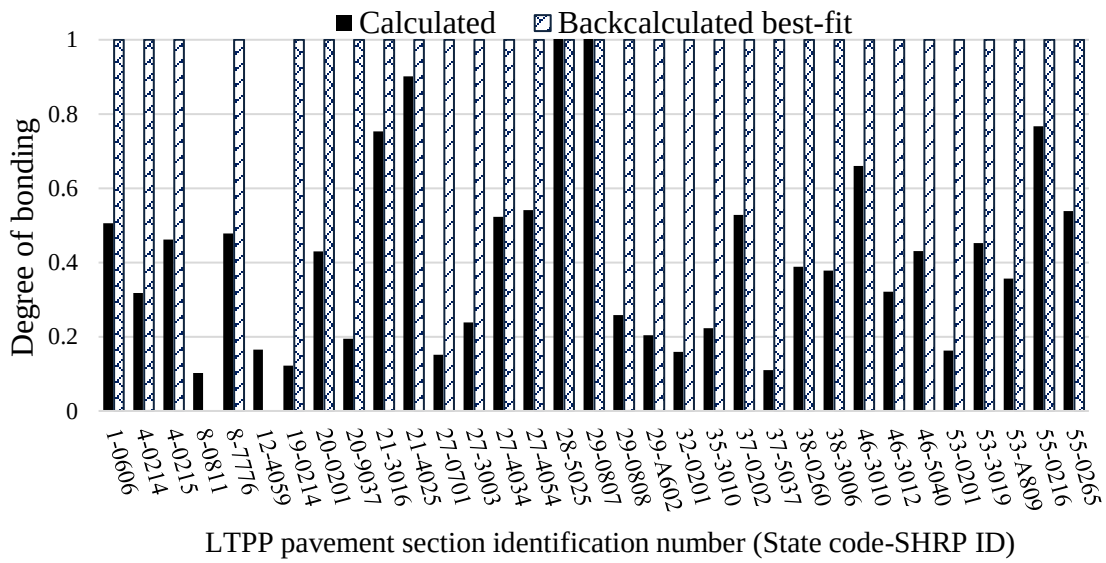

(b)

Figure 6.9 Comparison of calculated slab-base interface degree of bonding ratio with the backcalculated best-fit appraoch for (a) treated base; and (b) unbound base layer

Using the proposed bonding submodel, approximately a half of the pavement sections with treated base material are fully bonded (δ =1) with the PCC slab layer and the rest of the pavements have partially bonded slab-base interface. However, no partial bonding condition exists in the BBF approach. Note that the BBF approach assumes the bonding condition based on the PCC modulus (FHWA, 2001). The slab-base interface is considered as fully bonded if the PCC modulus is greater than 26890 MPa (3900 ksi) whereas a frictionless slip interface is applied for lower PCC modulus values. Figure 6.9b compares the calculated degree of bonding using the proposed bonding submodel and the BBF approach. It is observed that most pavement sections are partially bonded with the PCC layer using the proposed submodel, while all pavement sections are fully bonded using the BBF approach.

Comparison with wheelpath faulting

The degree of interface bonding has a significant impact on erodibility prediction of rigid pavements (Tarr et al., 1999; Bari et al., 2013; Croney, 1977; Delatte et al., 2000). In the process of erosion, the concrete slab deforms under repeated traffic loading, which yields shear stress between the slab and base. As a result, adequate interface bonding can significantly reduce erosion. Erosion is addressed through the faulting distress model (ARA, 2004). A better interfacial bonding model can infer better sensitivity to measured faulting. The correlation between the measured wheelpath faulting and the calculated degree of bonding is presented in Figure 6.10. The wheelpath fauling data are collected for JPCP pavement sections from the LTPP database.

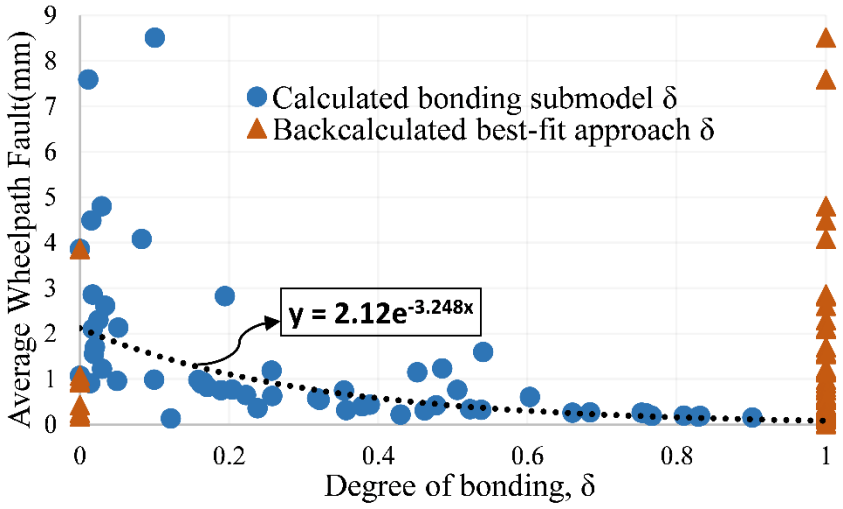

Figure 6.10 Sensitivity of slab-base degree of bonding on wheelpath fault (mm)

The calculated degree of bonding shows a better sensitivity to the observed faulting data. It is obvious that the faulting value decreases with the increasing degree of bonding in the slab-base interface. However, the assigned interface bonding in the BBF approach shows no sensitivity to

observed faulting. It is concluded that the developed interface bonding model can better predict the interface condition for rigid pavements.

6.3.3. Estimation of Modified k-Value

In this section, the modified *k*-values are calculated by following the previously presented approach. Figure 6.11 plots the modified *k*-values versus BBF *k*-values for the same pavement structure collected from the LTPP database. As presented, the BBF approach has higher *k*-values than the modified *k*-value model. This discrepancy has occurred due to the different interface bonding ratios. The interface between the slab and base is considered as fully bonded in the BBF approach for most of the pavement sections, while most of them are partially bonded in the modified *k*-value model.

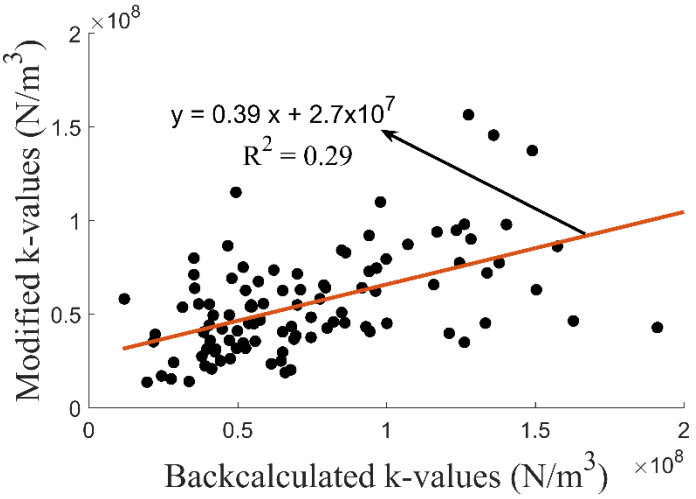

Figure 6.11 Comparison of modified versus LTPP k-values

An ANN model will be developed in the next section to predict the modified *k*-values for various combinations of pavement structure and layer moduli. A wide range of pavement structural properties, including layer thicknesses and material strength properties, resilient

moduli and slab-base interface bonding ratios, will be input in the ANN model. The deflection basin (BA) which is generated due to FWD loading is determined using FE analysis of pavement structure and used in the calculation of modified k-value. Application of ANN model eliminate the use of FE simulation for each pavement structure. Moreover, the AASHTOWare Pavement ME design software facilitate the incorporation of ANN model and therefore it is the most convenient way of implement modified k-value model in that software. The development of the ANN model is elaborated as follows.

6.4. Development of Artificial Neural Network Model

The ANN approach is an adaptive information processing technique, which allows to establish the correlations between the input variables X_i and the output variables Y_j through the inter-connected neurons (i.e., weight factor, w_{ji}). The input variables X_i and the output variables Y_j are usually normalized to x_i and y_j, respectively. The correlations developed by the ANN models between the normalized input parameters x_i and the normalized output variables y_j are shown in Equation 6.29.

$$y_j = f\left(\sum_{i=1}^{n} w_{ji} x_i\right) + b_j \tag{6.29}$$

where f is a transfer function, which normally uses a sigmoidal, Gaussian, or threshold functional form; w_{ji} and b_j are the unknown weight factors and bias term respectively.

The ANN model specifically adjusts the weight factors w_{ji} and bias bj in Equation 6.29 based on the minimum error function. In pavement engineering, the ANN approach is usually used to develop prediction models on the basis of a large number of data collected from experiments and numerical analysis (Gu et al., 2017; Saha et al., 2018a&b). In general, the

development of ANN models includes two critical steps: 1) calculation of deflection basin; and 2) construction of ANN architecture, which are described as below.

6.4.1. Calculation of Deflection Basin

The deflection basin of a specific pavement structure for FWD loading is estimated using FE program Abaqus. A total of 1296 simulation cases are developed with different combinations of pavement layer thicknesses, layer modulus and PCC-base interface bond. Pavement structural responses are calculated under falling weight deflectometer (FWD) loading using the finite element software ABAQUS. A typical rigid pavement structure and the corresponding finite element model is shown in Figure 6.12. In this study a large variety of pavement structures are modeled with different combinations of PCC and base thickness and PCC, base and subgrade modulus. In order to properly represent the effect of the strength of the base course and its level of erosion on the interface, it is necessary to accurately characterize the slab-base interface. A Coloumb interface model is placed between the bottom of the concrete and the top of the base course. The interface model has a normal and a tangential load transfer behavior at each nodal point. By adjusting the friction coefficient and the elastic slip distance, it is possible to represent a variety of shear strength levels of the base course on the interface, including zero strength. Varying the strength of the base course interface will generate different deflection patterns. These deflection patterns are used to generate the different levels of the subgrade *k*-values that are needed to represent the effect of lowered shear strength and erosion of the surface of the base course on the foundational support. The FWD sensor deflections (0 cm, 30.48 cm, 60.96 cm, and 91.44 cm away from the loading point) are obtained from the FEM analysis, and the modified *k*-value is calculated using Equations 6.24, 6.25 and 6.26.

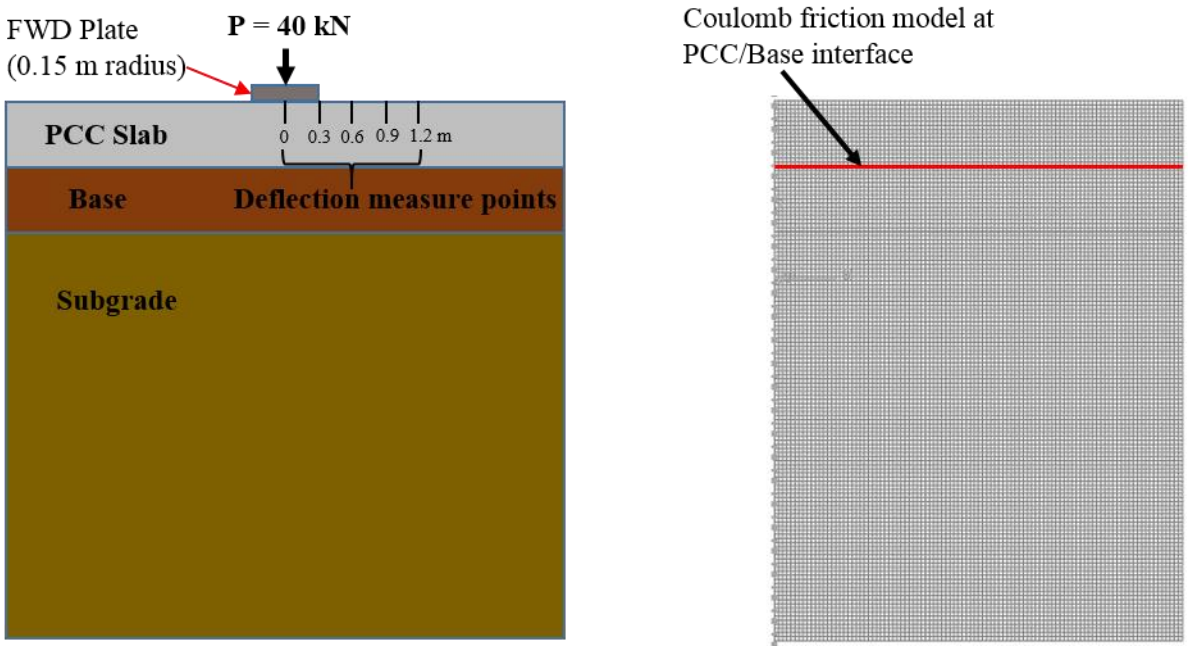

(a) (b)

Figure 6.12 (a) Schematic plot of a typical pavement structure; (b) Axisymmetric model of pavement in ABAQUS

6.4.2. Construction of ANN Architecture

A three-layered ANN model is constructed in this study as shown in Figure 6.13. Three layers of the ANN model consists of one input, one hidden and one output layer. Pavement structural properties (i.e., PCC slab and base thicknesses), strength properties (i.e.; PCC, base and subgrade moduli), and PCC-base interface bonding ratio are introduced as input parameters. Table 6.2 summarizes the range of the input parameters in the ANN model. A total of 20 neurons are assigned in the hidden layer (Lawrence and Petterson, 1993). The developed ANN model utilizes the sigmoidal transfer function, as shown in Equation 6.30 (Gu et al., 2017).

$$f\left(I_i\right)=\frac{1}{1+\exp\left(-\varphi I_i\right)} \tag{6.30}$$

where I_i is the input quantity; φ is a positive scaling constant,

The parameter φ controls the steepness between the two asymptotic values 0 and 1. The ANN model determines these weight factors w_{ji} through the two major functions: training and validating. The training data set is used to determine the trial weight factors, w_{ji} and bias term, $b_{j.}$ and the validating data set is employed to examine the accuracy of the model prediction.

Table 6.2 Selected range of input parameters in ANN training dataset

Input parameters	Level	Input values
PCC thickness (mm)	3	178, 254 and 348
Base thickness (mm)	3	101.6, 203.2 and 254
PCC modulus (MPa)	3	14420, 41400, and 82737
Base modulus (MPa)	4	69, 690, 6894 and 25000
Subgrade modulus (MPa)	3	34.5, 282 and 551
PCC-base interface bonding	4	0, 0.3, 0.6, and 1

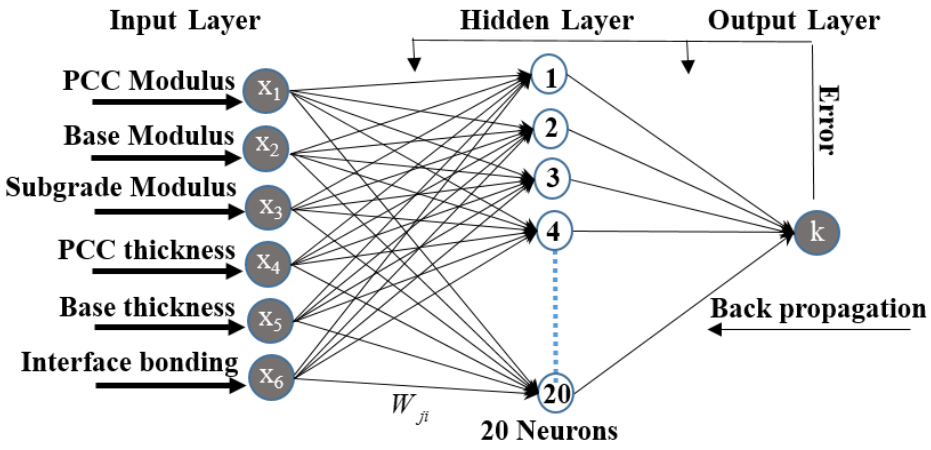

Figure 6.13 Illustration of Three-Layered Neural Network Architecture for *k*-values

In this study, 80 percent of the dataset is used for training and 20 percent of the dataset is for validation. The training algorithm uses the Levenberg-Marquardt back propagation method to

minimize the mean squared error (MSE). The gradient descent weight function is employed as a learning algorithm to adjust the weight factors w_{ji}. Figure 6.14 shows the comparison between targeted and predicted *k*-values from the ANN model. The high R^2 values for training and validation datasets indicate a good prediction accuracy of ANN model.

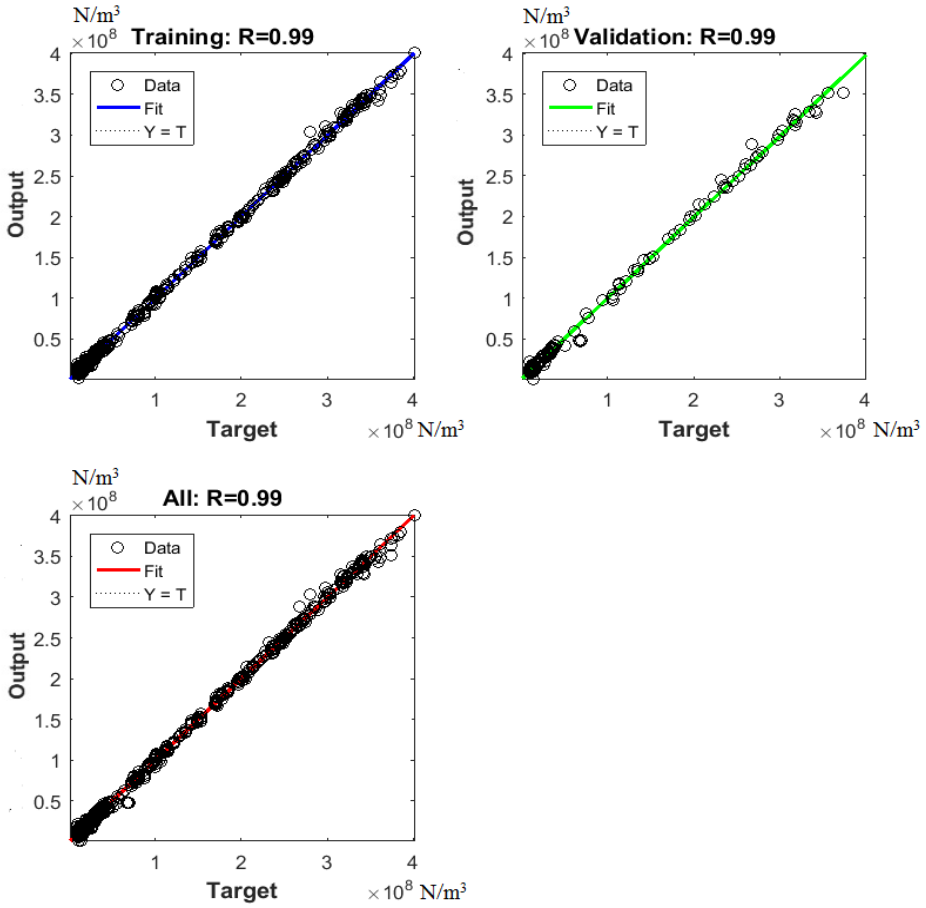

Figure 6.14 Target and output k-values for training, validation, and overall data sets for 1296 simulation cases

To further validate the prediction accuracy of ANN model, the k-values that are calculated using the modified subgrade reaction model are collected for 125 LTPP pavement sections. The slab-base interface degree of bonding in these pavement sections are calculated

using Equation 6.23. Figure 6.15 presents the comparison of calculated and ANN predicted *k*-values for the collected pavement sections at the calculated degree of bonding condition. The ANN model shows high prediction accuracy with a R^2 value of 0.92. This indicates that the developed ANN model is capable of accurately predicting the modified *k*-value at any given degree of bonding.

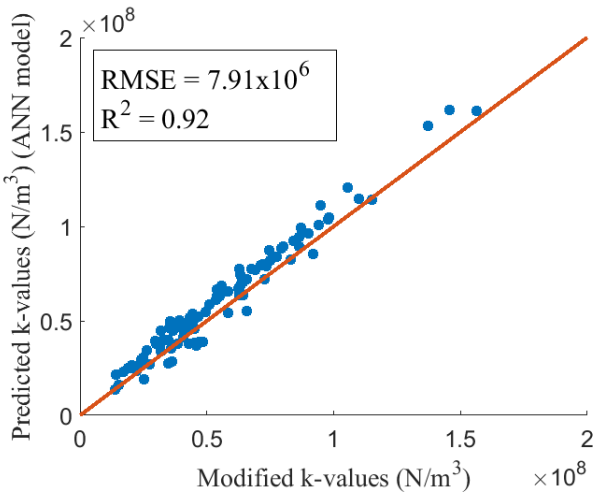

Figure 6.15 Comparison of calculated versus predicted modified k-values

A sensitivity analysis for the degree of bonding is performed for selected pavement sections and shown in Figure 6.16. As illustrated, the modified *k*-values increase with the increasing degree of bonding for most pavement sections. However, for pavement sections 8-0214 and 29-5000, *k*-values slightly decrease with the increasing degree of bonding ratio. The potential reason is that the increase of slab-base bonding ratio causes a higher thickness of equivalent transformed section and basin area. The *k*-value increases with the increase of equivalent thickness but it continues to decrease when basin area increases. In case of a relatively higher modulus ratio (E_{base}/E_{slab}) between slab and base, the degree of bonding has a greater

impact on the thickness of equivalent section compared to the basin area. Therefore, k-value increase with the increasing degree of bonding. But pavement section 8-0214 and 29-5000 have a slab-base modulus ratio of 0.001285 and 0.001049 respectively that is very low. Hence there is a negligible amount of increase in equivalent thickness with degree of bonding and it has a greater effect on basin area. As a result, k-value decreases with the increasing degree of bonding for these pavement sections.

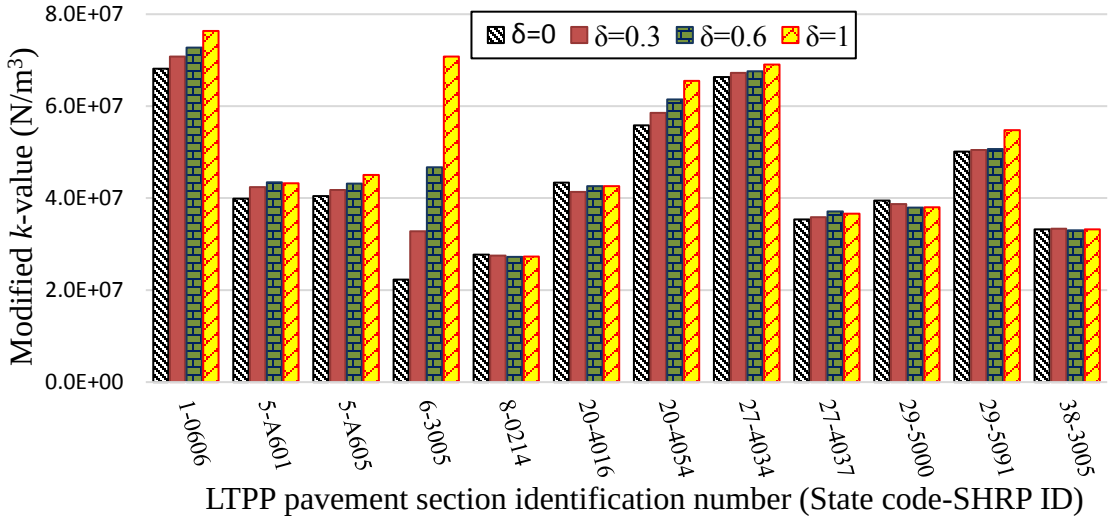

Figure 6.16 Modified *k*-values at 0, 0.3, 0.6 and 1 degree of bonding for selected LTPP pavement sections

6.5. Conclusions

This study proposed a modified modulus of subgrade reaction (*k*) model that considered the nature of cross anisotropy for base material and the shear interaction between PCC slab and base course. The modified k-values obtained from the proposed model were significantly different from the k-values from Pavement ME design. The new model could also determine the k-value

for partial interface bonding conditions accurately. An ANN model was developed to predict the modified k-value for a wide range of pavement layer thicknesses, moduli and bond ratios.

7. SENSITIVITY ANALYSIS

7.1. Introduction

Pavement structure is typically consist of the top surface layer, an intermediate base course layer and a bottommost subgrade layer. Currently, AASHTOWare Pavement ME Design software is used for the analysis and predict the performance of pavements and overlays. The performance of flexible and rigid pavement is known to be closely related to the properties of base and/or subbase as well as subgrade layer. However, recent studies indicated that the performance predicted by the software shows low sensitivity to the properties of base and subgrade layers (Schwartz et al. 2011), so the procedure contained in the Pavement ME Design need to be improved. The properties of base and subgrade layers that include in Pavement ME Design software are: resilient modulus (M_R), soil-water characteristics curve (SWCC), thickness, erodibility index, load transfer efficiency (LTE), slab-base interface bond, ground water depth from subgrade (Luo et al. 2017). It is required to enhance these property models and implement in Pavement ME Design software and therefore have the anticipated effect of base and subgrade layer properties on the performance of rigid pavement.

This study developed several models as described in previous chapters for unbound granular materials and subgrade, which are intended to enhance the sensitivity of predicted pavement performance to these underlying layers. The sensitivity of these enhanced models is evaluated in this chapter for both flexible and rigid pavements. The common performance indicators contained in the Pavement ME Design that will be evaluated here include: fatigue cracking and rutting for flexible pavements, and fatigue cracking and faulting for rigid

pavements. The sensitivity analysis will demonstrate whether the predicted performance changes with the change of traffic speed, moisture conditions, and interface degree of bonding of the structural layers. In addition, the proposed enhanced models are compared with the corresponding models in the Pavement ME Design, which shows the resulting difference in the prediction of pavement performance.

7.2. Improved Sensitivity of Base Layer on Flexible Pavement Performance

Unbound granular materials are generally applied in the bases and subbases to support pavement surfaces and transfer vehicle loads to the subgrades. The stiffness of the bases and subbases in the pavement design are described using resilient modulus which is the ratio of axial stress and recoverable axial strain (Kalcheff and Hicks 1973, Rahman et al. 2017). However, in most pavement designs, the bases and subbases are treated as linear elastic and isotropic materials using one resilient modulus and Poisson's ratio, which do not represent realistic properties of unbound granular materials. Researchers have shown that the modulus of unbound granular materials in the vertical direction is greater than that in the horizontal direction. The ignorance of this property will cause overestimation of tensile stresses in base layers, which affect further pavement performance models. Studies with the anisotropic base and subbase layers showed better predictions with field measurements compared with isotropic models (Wang and Al-Qadi 2012). In addition to the effects of anisotropy of materials, characterization of the resilient modulus is significantly dependent upon the moisture content and suction state (Lytton 1995, Luo et al. 2017).

Tire dimension and contact pressure is another important factor for accurate prediction of pavement performance. In Pavement ME design, uniform vertical contact pressure is used

resulting from standard inflation pressures of a stationary tire (ARA, Inc. 2004). However, it was recognized that the assumption of uniform contact stress distribution and static loading ignore the localized tire-pavement contact stresses which contribute to the development of pavement ruts and initiation of crack in the pavement (Wang et al. 2012; Al-Qadi et al. 2010). Past researchers have developed 3D FE models to investigate the influence of non-uniform tire pressure distribution and showed high horizontal strain compared to that obtained from uniform pressure distribution (Fang et al. 2007, Hernandez 2010, Khavassefat et al. 2012 and Wang, 2011). Moreover, field experiment from previous studies clearly shows that rolling tire induces not only vertical contact stress but also longitudinal and transverse contact stresses as well. Al-Qadi et al. 2010 investigated the surface tangential contact stress due to rolling tire effect and showed that the computed values, especially at shallow depth, matches well with the measured values. It is recognized that the developed longitudinal and transverse strains are related to the interaction behavior of tire-pavement contact surface (Wang et al. 2014; Gruber et al. 2012). Tire-pavement contact is a transient rolling contact and only a realistic tire-pavement contact interaction model can simulate the longitudinal and transverse strain conditions. In order to properly investigate the dynamic behavior of tire-pavement interaction under different rolling conditions, this paper developed a numerical model of rolling smooth tire and a tire-pavement interaction model, which is capable of accurately characterizing the contact and traction stress distribution at the tire-pavement interface.

The following subsection presents a tire-pavement interaction model with stress-dependent, moisture-sensitive, anisotropic base layer using the commercial finite element software ABAQUS. The responses of the pavement under different tire speed and the effects of

moisture content on base material properties will also be evaluated.

7.2.1. Finite Element Model of Pavement Structures

A pavement section with 5,000 mm length and 1122 mm width was used in this study. The width and the height of the pavement were selected from Al-Qadi et al. (2004) and LTPP pavement section database respectively. the predictability of this model were validated against experimental results (Saha, 2013). The length of the pavement was determined by conducting parametric study to reduce the boundary effect on the computed results. The 3D model of the pavement section is shown in Figures 7.1a. The transverse section shown in Figure 7.1b is collected from a typical LTPP section 13-4111 (State code-SHRP ID) with three different layers. The finite element mesh for 3D analysis was created using eight-node linear brick reduced integration elements (C3D8R).

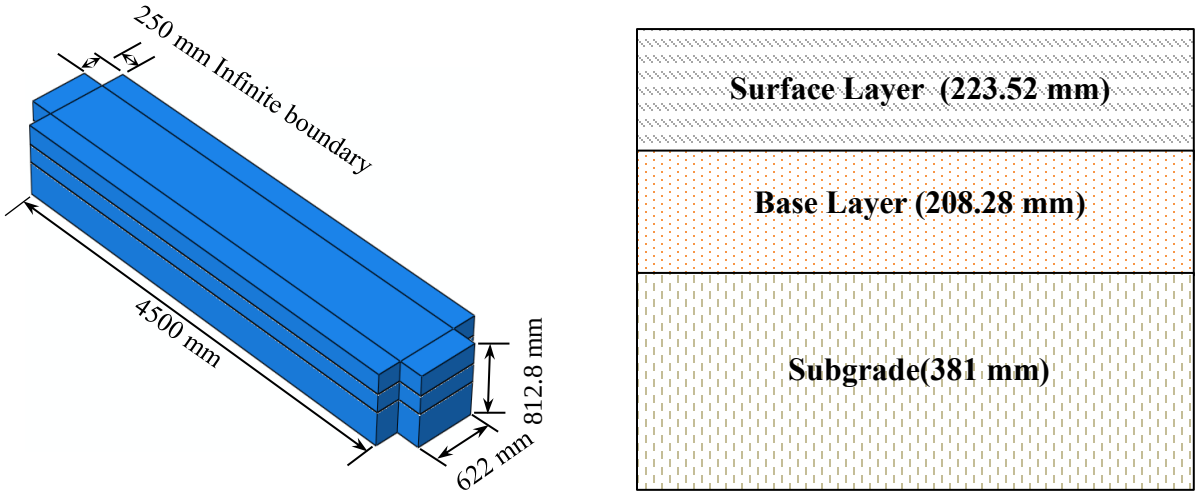

(a) **(b)**

Figure 7.1 (a) Dimensions of developed pavement model in 3D simulation domain; (b) Layer property and thickness of each pavement layer

Accurate representation of the inter layer characteristics is important for obtaining accurate pavement behavior under tire loading. Similar to Al-Qadi et al. (2004), the interaction between the layers was modeled using the Coulomb's friction law which involves the surface-to-surface contact feature in ABAQUS. A friction coefficient of 1.0 was used for each interface. In the pavement model, the bottom boundary was fixed in all directions and the tire load was applied at the top. The horizontal boundaries (back, front, left and right) were modeled using infinite elements (CIN3D8) to nullify the edge effect errors.

7.2.2. Finite Element Model of Tire Load

Physically, traffic load acts as a moving dynamic load in pavement. To simulate the movement of traffic load, a dynamic implicit (quasi-static application) approach was adopted in this study. The loading on the pavement was applied through simulating a rolling tire at design velocity. A wide base tire (455/55R22.5) was considered in this study for the application of traffic load.

Figure 7.2 illustrates the layout and dimensions of developed tire model. According to the tire designation code, the sidewall height was selected as 222.5 mm (445 X 0.50). Out of the total sidewall height, tire tread thickness was considered to be 18 mm (Wang et al 2012) and belt thickness as 20 mm. Because of simplicity and free rolling tire condition, no inflation pressure applicability was adopted and therefore, the tire model did not include any physical side wall and radial ply section. An inflated air zone was placed in between belt and tread material which facilitate the calibration of contact stress-length with pavement surface.

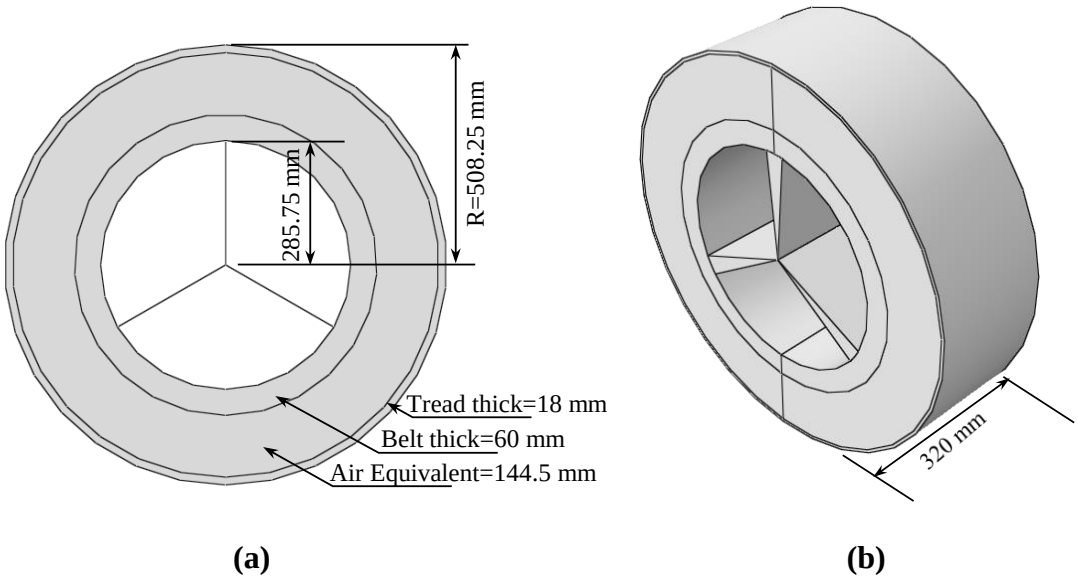

Figure 7.2 Layout and dimension of developed (a) 2D and (b) 3D tire model

The length of three tire rim as shown in Figure 7.2a was selected as 285.75 mm (22.5 X 25.4), which represent the decimal number of the designation code in inches. The 3D width of the tire was selected as 320 mm (Al-Qadi et al 2004, Saha et al. 2019e), shown in Figure 7.2b. The contact pressure at the tire-pavement interface was employed by applying a concentrated point load at the center of tire tire rim without any air inflation pressure. Angular velocity boundary condition was applied to the tire to maintain a linear velocity in the tire-pavement interaction path. At first the velocity was increased from 0 to the constant velocity for 1 sec and then maintained the same velocity throughout the path. The velocity incremental time period was allowed to avoid inconvergence in slip phenomena. As the realistic tire-pvement contact area-pressure distribution and simulation of realistic fictional effect was the main purpose of rolling tire technique, a tire-pavement interaction was applied at the interface followed by contact area-pressure calibration.

7.2.3. Material Properties of Pavement Layers

The surface material is modeled as viscoelastic and isotropic. For solid-like viscoelastic materials such as asphalt concrete, a generalized Maxwell model is applied to represent the relaxation modulus of the material in terms of Prony series as in Equation 7.2.

$$\sigma_{ij} = \lambda e_{kk}\delta_{ij} + 2\mu e_{ij} \tag{7.1}$$

where λ, μ is the Lame's constant; σ_{ij}, e_{ij} are stress and strain component, respectively; e_{kk} is the first invariant of stress tensor; δ_{ij} is Kronecker delta;

$$E(t) = E_{\infty} + \sum_{i=1}^{N} Ei \exp(-\frac{t}{\tau i}) \tag{7.2}$$

where $E(t)$ is the relaxation modulus of the material; E_{∞} is the long-term modulus of the material; N is the the number of Prony series terms (or Maxwell elements); τ_i is relaxation time;

The stress-dependent nonlinearity of unbound granular base materials can be characterized using Equation 7.3 from the Pavement ME Design Guide.

$$E_z = k_1 P_a (\frac{I_1}{P_a})^{k_2} (\frac{\tau_{oct}}{P_a} + 1)^{k_3} \tag{7.3}$$

Also, the research team proposed an improved model to characterize the resilient modulus of unbound granular materials which takes the moisture condition of the material into consideration. The formula is expressed as Equation 7.4.

$$E_z = k_1 P_a (\frac{I_1 - 3\theta f h_m}{P_a})^{k_2} (\frac{\tau_{oct}}{P_a})^{k_3} \tag{7.4}$$

where E_z is the vertical modulus of the material (assuming z axis is the vertical axis); k_1, k_2 and k_3 are regression coefficients determined from laboratory tests; P_a is the the atmosphere

pressure; I_1 is the first invariant of stress tensor; τ_{oct} is the octahedral shear stress; θ is the volumetric water content; f is the saturation factor; h_m is the matric suction; An example of the base information is given in the following Table 7.1.

Table 7.1 Example of Base Material Information

State: Georgia, State Code: 13, SHRP ID: 4111			
	Moisture	Volumetric Water Content, %	Matric Suction, kPa
Base	Dry	8.76	527
	Medium	9.73	309
	Wet	10.70	187
	a_f =27.44 , b_f =0.58, c_f =1.066, h_r =20684		
	Moisture	Volumetric Water Content, %	Matric Suction, kPa
Subgrade	Medium	23.34	308
	a_f =45.57 , b_f =0.88, c_f =0.56, h_r =20684		

$$E_y = k_1 P_a \left(\frac{I_1 - 3\theta f h_m}{P_a}\right)^{k_2} \left(\frac{\tau_{oct}}{P_a}\right)^{k_3}$$

$$S = C(h)\left[\frac{1}{\{\ln[e + (\frac{h}{a_f})^{b_f}]\}^{c_f}}\right]$$

$$C(h) = 1 - \frac{\ln(1 + \frac{h}{h_r})}{\ln[1 + (\frac{1x10^6}{h_r})]}$$

The anisotropy of the unbound granular base is modeled as cross-anisotropy which requires five independent parameters to characterize the materials as shown in Equation 7.5.

$$\begin{bmatrix}\sigma_{xx}\\ \sigma_{yy}\\ \sigma_{zz}\\ \sigma_{xy}\\ \sigma_{yz}\\ \sigma_{zx}\end{bmatrix}$$

$$= \frac{E_z}{\alpha_0\beta_0}\begin{bmatrix} n(1-n\upsilon_{zx}^2) & n(\upsilon_{xy}+n\upsilon_{zx}^2) & n\upsilon_{zx}\alpha_0 & 0 & 0 & 0 \\ n(\upsilon_{xy}+n\upsilon_{zx}^2) & n(1-n\upsilon_{zx}^2) & n\upsilon_{zx}\alpha_0 & 0 & 0 & 0 \\ n\upsilon_{zx}\alpha_0 & n\upsilon_{zx}\alpha_0 & 1-\upsilon_{xy}^2 & 0 & 0 & 0 \\ 0 & 0 & 0 & \frac{1}{2}n\beta_0 & 0 & 0 \\ 0 & 0 & 0 & 0 & m\alpha_0\beta_0 & 0 \\ 0 & 0 & 0 & 0 & 0 & m\alpha_0\beta_0 \end{bmatrix}\begin{bmatrix}\varepsilon_{xx}\\ \varepsilon_{yy}\\ \varepsilon_{zz}\\ 2\varepsilon_{xy}\\ 2\varepsilon_{yz}\\ 2\varepsilon_{zx}\end{bmatrix} \quad (7.5)$$

in which

$$n = E_x / E_z \quad (7.6)$$

$$m = G_{zx} / E_z \quad (7.7)$$

$$\alpha_0 = 1 + \upsilon_{xy} \quad (7.8)$$

$$\beta_0 = 1 - \upsilon_{xy} - 2n\upsilon^2{}_{zx} \quad (7.9)$$

where E_z is the vertical modulus of the material; E_x is the horizontal modulus of the material; G_{zx} is the shear modulus in the z-x plane; υ_{xy} is the Poisson's ratio in the x-y plane; υ_{zx} is the Poisson's ratio in the z-x plane. The material parameters applied in the models are presented in Table 7.2.

Table 7.2 Material Parameters of Pavement Layers

Surface	E_∞	42	E, MPa; τ, s	
	E_1	6564	τ_1	4.09E-06
	E_2	6582	τ_2	0.000256
	E_3	3200	τ_3	0.00771
	E_4	1342	τ_4	0.21
	E_5	299	τ_5	3.88
	E_6	103	τ_6	66.3
Base	k_1	1637	n	0.45
	k_2	0.42	m	0.35
	k_3	-0.20	υ_{zx}	0.38
	υ_{xy}	0.43		
Subgrade	k_1	1220	k_2	0.28
	k_3	-2.28		

7.2.4. Pavement Performance Model in Pavement ME Design

The performance of pavements is affected by the material properties of pavements including the stiffness and responses of pavements under traffic loading including strains at critical locations (Rahman et al. 2019a). In this chapter, the pavement performance predicted by the Pavement ME Design Guide distress models will be utilized to investigate how the pavement structure, material properties and the loading level influence the pavement performance. Additionally, the modulus models for unbound granular base proposed by the research team and Pavement ME Design Guide will be compared in terms of distresses such as fatigue cracking and rutting.

Fatigue cracking in asphalt mixtures

The approach explained in the Pavement ME Design Guide to predict fatigue life of the pavement is based on the calculation of damage at either the surface for top-down cracking or the bottom for bottom-up cracking (AASHTO, 2008). The final form to predict the number of load repetitions to the fatigue cracking is from the Asphalt Institute (AI) model (Asphalt Institute, 1981) with the national field calibrated model. Since the original form of AI model was proposed

to only predict load repetitions in the phase of crack initiation and the difference between national and local conditions, the available performance prediction model is limited in terms of its accuracy and variability (Wang and Al-Qadi, 2012). The performance of fatigue cracking in this section is evaluated using bottom-up fatigue cracking model in MEPDG. For top-down cracking, alternative models can be found in recent research (Ling et al., 2018, Roque et al., 2010).

$$N_f = 0.00432 k_1' C \left(\frac{1}{\varepsilon_t}\right)^{3.9492} \left(\frac{1}{E}\right)^{1.281} \tag{7.10}$$

in which, for the bottom-up cracking

$$k_1' = \frac{1}{0.000398 + \frac{0.003602}{1 + e^{(11.02 - 3.49 h_{ac})}}} \tag{7.11}$$

$$C = 10^M \tag{7.12}$$

$$M = 4.84\left(\frac{V_b}{V_a + V_b} - 0.69\right) \tag{7.13}$$

where N_f is the number of load repetitions to fatigue cracking; ε_t is the tensile strain at the critical location; E is the stiffness of the material; h_{ac} si the thickness of the asphalt layer; V_a, V_b are the content of the air voids and the effective binder content, respectively;

Permanent deformation in the base layer

To predict the permanent deformation of the pavement, the Pavement ME Design Guide applies models corresponding to the material type and computes the accumulated plastic strain at each sublayer. For the unbound granular materials, the proposed model (AASHTO, 2008) with the calibrated coefficient to predict the permanent deformation is presented as Equation 7.14.

$$\delta_a(N) = \beta_{GB}(\frac{\varepsilon_0}{\varepsilon_r})e^{(-\frac{\rho}{N})^\beta}\varepsilon_v h \quad (7.14)$$

in which

$$\log\beta = -0.61119 - 0.017638W_c \quad (7.15)$$

$$\frac{\varepsilon_0}{\varepsilon_r} = \frac{(e^{\rho^\beta}a_1 E_r^{b_1} + e^{(\rho/10^9)^\beta}a_9 E_r^{b_9})}{2} \quad (7.16)$$

$$C_0 = \ln\frac{a_1 E_r^{\ b_1}}{a_9 E_r^{\ b_9}} \quad (7.17)$$

$$\rho = 10^9(\frac{C_0}{(1-(10^9)^\beta)})^{\frac{1}{\beta}} \quad (7.18)$$

Where β_{GB} si the national calibration factor, 1.673; W_c is the water content (%); E_r is the resilient modulus of the layer/sublayer (psi); $\varepsilon_0, \beta, \rho$ are material properties; ε_r is the resilient strain imposed in laboratory test to obtain material properties; ε_v is the average vertical strain in the layer/sublayer as obtained from the primary response

model; a_1=0.15; a_9=20.0; b_1=0.0; b_9=0.0;

A new mechanistic-empirical rutting model has been developed to predict the rut depth in unbound granular materials with the load cycle. Compare with the Equation 7.14 in the Pavement ME Design Guide, the proposed model eliminates the term of the thickness of the unbound granular materials and are more involved with the stress states and material properties. The formula of the model is presented as the following equation.

$$\varepsilon_p(N) = \varepsilon_0 e^{-(\rho/N)^\beta}(\frac{\sqrt{J_2}}{p_a})^m(\frac{\alpha I_1 + K}{p_a})^n \quad (7.19)$$

in which

$$\alpha = \frac{2\sin\phi'}{\sqrt{3}(3-\sin\phi')} \tag{7.20}$$

$$K = \frac{c'.6\cos\phi'}{\sqrt{3}(3-\sin\phi')} \tag{7.21}$$

$$c' = -0.221*PI + 4.6*\theta_{sat}(\%) + 455.62*G_s - 1262.75 \tag{7.22}$$

$$\phi' = 0.0272*PI - 0.638*MC_{opt}(\%) - 1.487*\theta_{sat}(\%) + 69.92 \tag{7.23}$$

$$\log\varepsilon_0 = 0.017*P_4 - 0.00967*MDD + 0.99 \tag{7.24}$$

$$\log(\rho) = 0.0574*P_4 - 0.0937*MC + 5.0756 \tag{7.25}$$

$$\beta = -0.01483*P_4 + 0.00813*MDD - 0.00136*sat(\%) \tag{7.26}$$

$$m = 0.2153*\varepsilon_0 + 0.396 \tag{7.27}$$

$$n = -0.22993*m - 0.746 \tag{7.28}$$

where c' is the cohesion of the material; ϕ' is the friction angle of the material; PI is the plasticity index of the material; SG is the specific gravity of the material; P_{200} is the percent passing No. 200 sieve; θ_{opt} is the optimum volumetric water content; θ_{sat} is the saturated volumetric water content; γ_d is the dry density of the material; I_1 is the first invariant of the stress tensor; J_2 is the second invariant of the deviatoric stress tensor; P_a is the atmosphere pressure, 101.3 kPa;

7.2.5. Comparisons of Results from Proposed Models and Pavement ME Design Models

Comparison of rutting models in unbound granular base

Equations 7.14 and 7.19 present the rut depth which is the permanent deformation in the base layer under repeated loads. The material properties required in these two models are obtained from LTPP database and presented in Table 7.3.

Table 7.3 Base Material Information for Rut Depth Calculation

Information	Value
Volumetric Water Content in FE Model, %	9.73
P200 (Percent Passing No. 200 Sieve)	8.5
Maximum Dry Density, lb/ft^3	135
PI (Plasticity Index)	14
Optimum Water Content, %	9
Specific Gravity	2.687
Load Number	100,000

Figure 7.3 shows the rut depth in the base layer using two models when other factors such as the pavement structure, material properties, the loading level and the number of load repetitions are the same. It can be seen when using the model proposed by the research team, the rut depth is greater.

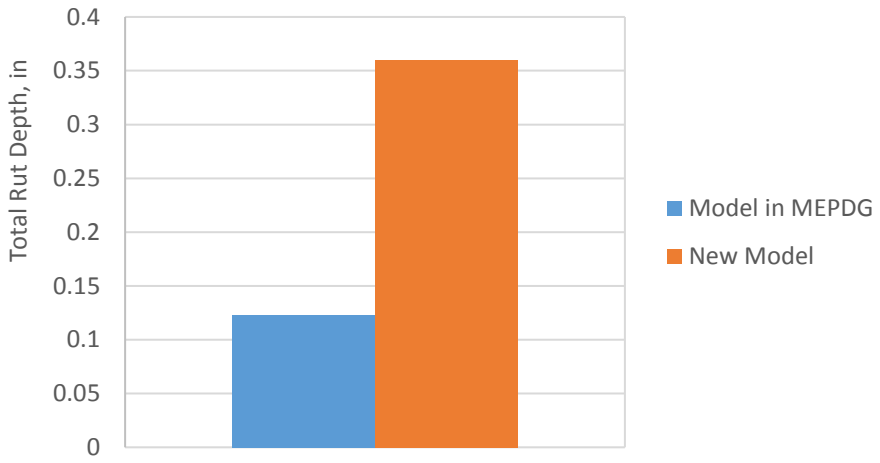

Figure 7.3 Rut Depth in the Base Layer Using Different Models

Sensitivity analysis

In the previous sections, the finite element models with new granular base and subgrade models were run to check the feasibility and effectiveness of the proposed models. Also, the proposed rutting model was compared with the one in the Pavement ME Design Guide. In this section,

sensitivity analysis will be performed on the finite element models with new based/ subgrade models to determine the effects of the load level, pavement structure, material properties and moisture conditions on the pavement performance, in which the rutting model is the proposed rutting model.

Different Loading Levels

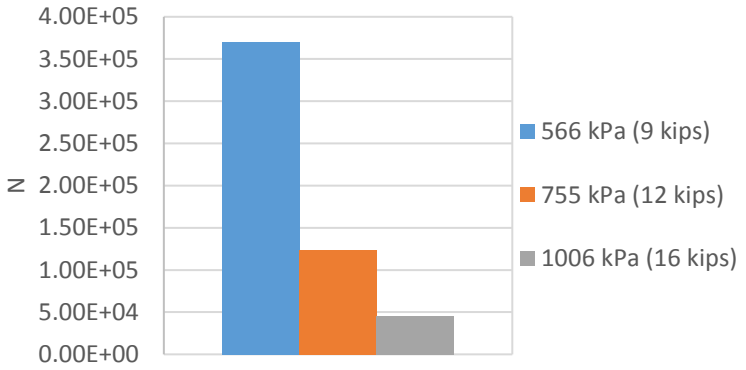

(a)

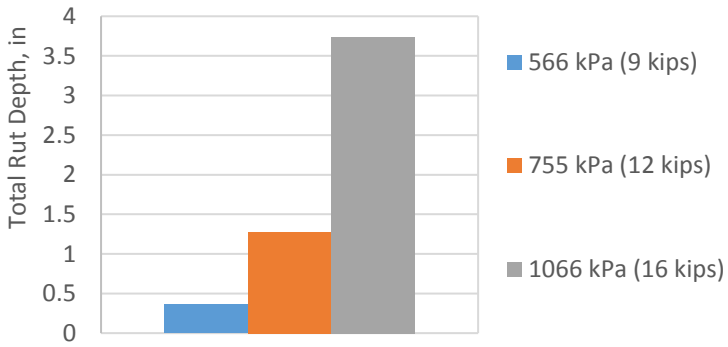

(b)

Figure 7.4 Pavement Performance Including (a) Load Repetitions to the Fatigue Cracking (b) Rut Depth in the Base at Different Loading Levels

Figure 7.4 presents the pavement performance under different loading levels as computed with the ABAQUS using models developed by this study. For the fatigue cracking, the loading

repetitions are calculated based on the Pavement ME Design Guide criteria. It can be seen that the number load repetitions decreases dramatically with the increase of the loading level. The total rut depth in the base layer is calculated using the permanent deformation model proposed by the research team when the loading repetition number is 100,000. The rut depth increases with the increase of the loading level.

Different Moisture Conditions of the Base Layer

Figure 7.5 presents the pavement performance when stresses and strains computed with ABAQUS and the material models developed by the research team and when the moisture of the base layer varies. As the moisture content of base layer increases, the modulus of the base decreases, which reduces the load repetitions to the fatigue cracking. For the rut depth, when the moisture content of the base layer changes from 8.76% to 10.70%, the total rut depth also increases.

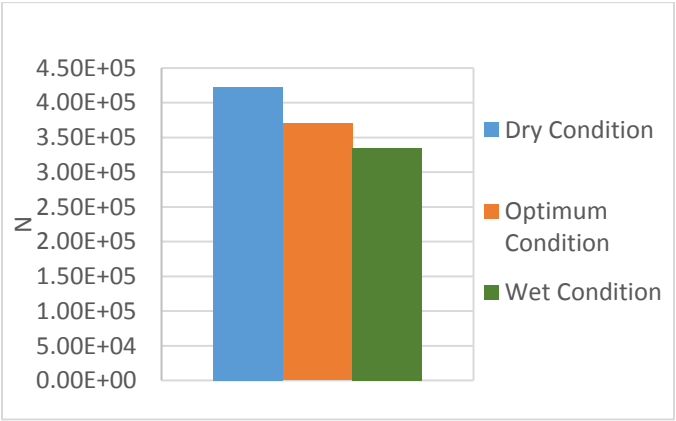

(a)

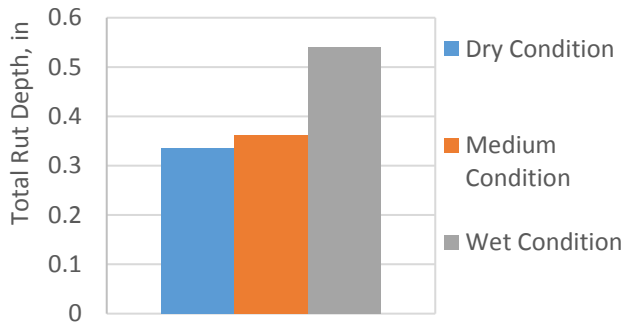

(b)

Figure 7.5 Pavement Performance Including (a) Load Repetitions to the Fatigue Cracking and (b) Rut Depth in the Base at Different Moisture Conditions of the Base Layer

7.3. Improved Sensitivity of Base Layer on Rigid Pavement Performance

A moisture and suction dependent resilient modulus (M_R) model is used in this subsection, as noted in Equation 4.20. Similarly, to improve the slab-base interface bond sensitivity in rigid pavement performance, an artificial neural network model is developed in Chapter 4.

Table 7.4 Selected LTPP pavement sections and FWD backcalculated modulus values for each layer

Climate zone	State	State Code	SHRP ID	Slab thickness (in)	Base thickness (in)	Backcalculated values			δ
						Slab modulus (psi)	Base modulus (psi)	Subgrade modulus (psi)	
Wet-Freeze	Minnesota	27	4034	10	3.6	5342000	98000	11000	0.52
	Kentucky	21	4025	9.8	6	5693000	195000	25000	0.9
Wet-Nonfreeze	Alabama	01	0606	10.3	6.3	7798000	195000	8000	0.5
	North Carolina	37	5037	7.8	15.1	4875000	20000	14000	0.11
Dry-Freeze	Colorado	08	7776	10.7	15.3	4147000	100000	27000	0.48
	North Dakota	38	3006	8.5	3.8	10000000	199000	50000	0.37
Dry-Nonfreeze	New Mexico	35	3010	7.9	6.9	7171000	64000	22000	0.22
	Arizona	04	0214	8.3	6.1	7087000	98000	25000	0.32

To examine the sensitivity of the moisture and degree of bonding on pavement performance, the proposed models were applied in eight LTPP pavement sections listed in Table 7.4. Each pavement section in Table 7.4 is consisted of one surface, one base and a subgrade layer. The modulus values for each layer are calculated using falling weight deflectometer backcalculation procedure. To illustrate the effect of moisture in subgrade *k*-value and therefore, pavement performance, M_R values were calculated first at three different moisture conditions. Table 7.5 lists the M_R values for each pavement structure at three selected moisture conditions: (1) equilibrium volumetric water content + 10%; (2) equilibrium volumetric water content; (3) equilibrium volumetric water content - 10%. Equilibrium suction and the corresponding volumetric water content were calculated using Equation 4.15 and the SWCC equation developed by Fredlund and Xing as shown in Equation 4.1 and 4.2. The four fitting parameters (a_f, b_f, c_f and h_r) of the SWCC equation were predicted from the ANN model developed in section 2.

Table 7.5 Calculated M_R values at the mid-depth of base layer at different moisture conditions

State Code	SHRP ID	δ	SWCC parameters				θ	-hm (kPa)	f	M_R parameters			M_R (MPa)
			a_f	b_f	c_f	h_r				k_1	k_2	k_3	
27	4034	0	4.91	2.62	1.65	3000	0.00306	2621	1	689.3	0.66	-0.03	37.2
		0.52					0.0034	1931	1				33.9
		1					0.00374	1635	1				32.8
21	4025	0	5.86	0.34	1.74	2999	0.0418	5976	1	945.55	0.67	-0.29	880.2
		0.9					0.0465	3845	1				707.5
		1					0.0511	2498	1				569.2
01	0606	0	6.71	1.01	0.07	2998	0.1265	9386	1	913.7	0.73	-0.03	1397.2
		0.5					0.1406	1750	2.74				930.3
		1					0.1546	41	5.81				115.8
37	5037	0	7.57	0.98	1.08	2999	0.0606	732	1	431.43	0.92	-0.23	126.3
		0.11					0.067	533	1				105.7
		1					0.0741	403	1				91.5

Table 7.5 Continued

State Code	SHRP ID	δ	SWCC parameters				θ	-hm (kPa)	f	M_R parameters			M_R (MPa)
			a_f	b_f	c_f	h_r				k_1	k_2	k_3	
08	7776	0	1.06	1.01	0.69	2999	0.072	3832	1	983.52	0.207	-0.03	167.2
		0.48					0.08	1858	1				147.6
		1					0.088	975	1				132.4
38	3006	0	1.00	1.01	0.79	2999	0.038	3778	1	544.43	0.65	-0.08	184.2
		0.37					0.042	1961	1				131.1
		1					0.046	1100	1				98.5
35	3010	0	5.30	3.35	1.05	2998	0.012	3189	1	859.5	0.73	-0.02	114.3
		0.22					0.013	2093	1				92.5
		1					0.015	1565	1				84.8
04	0214	0	5.05	0.12	2.18	2999	0.066	1995	1	900.14	0.509	0.047	162.9
		0.32					0.073	533	1				92.3
		1					0.08	124	1				54.7

The coefficients of the proposed M_R model were predicted using the ANN model shown in Figure 4.17. To compare the sensitivity of moisture on subgrade k-value, the M_R values were calculated at different moisture conditions using the proposed model and the Pavement ME design model. After that the subgrade k-values were calculated using the developed ANN model shown in Figure 6.13 and Pavement ME design approach. Table 7.5 also list three different bonding conditions for each pavement structure: (1) No bond; (2) partially bonded and (3) fully bonded. Each bonding condition was applied as an input in the developed ANN model and compared with the predicted k-values from Pavement ME design.

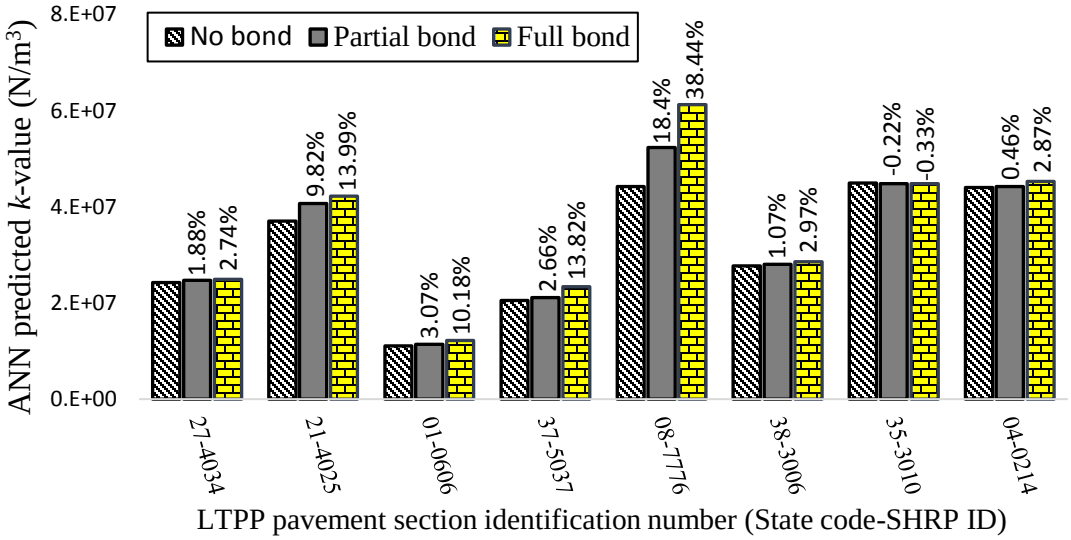

(a)

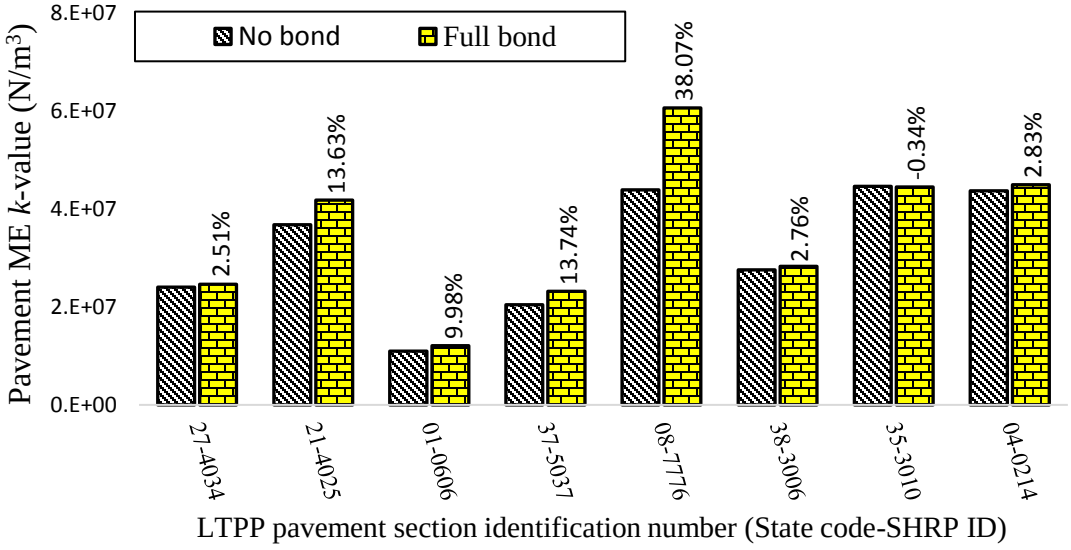

(b)

Figure 7.6 Sensitivity of degree of bonding on subgrade k-value using (a) ANN model; (b) Pavement ME design model

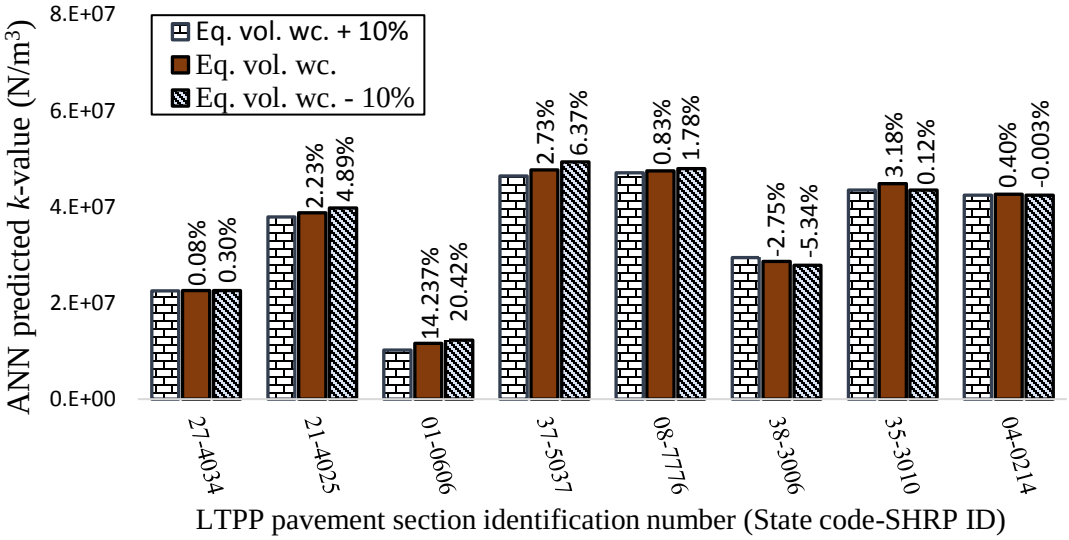

(a)

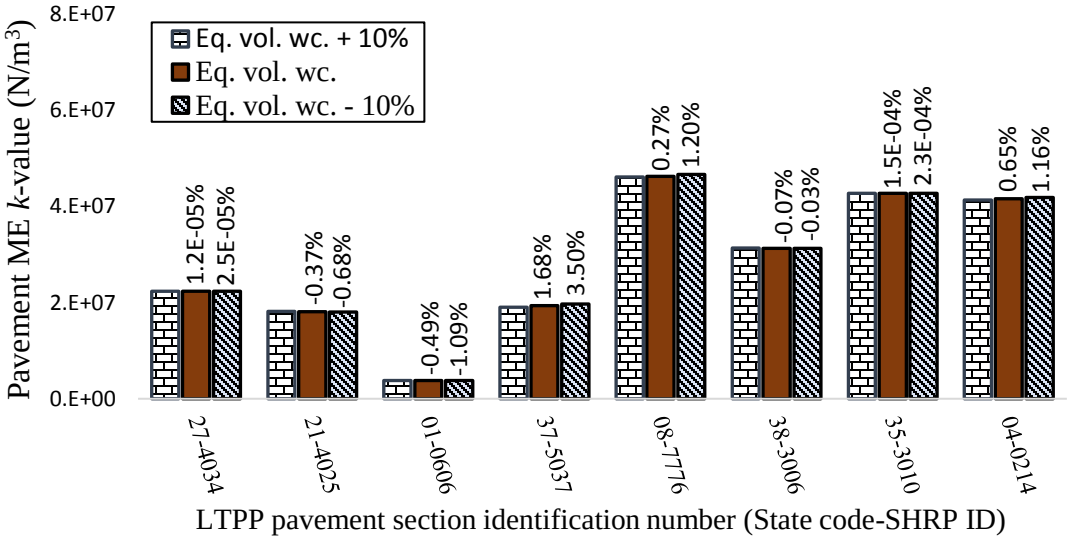

(b)

Figure 7.7 Sensitivity of moisture on subgrade *k*-value using (a) ANN model; (b) Pavement ME design model

Figure 7.6 presents the sensitivity of degree of bonding on subgrade *k*-value using the developed ANN model and the Pavement ME design model. The effect of moisture on subgrade *k*-value is illustrated in Figure 7.7. It is observed from Figure 7.6 that both ANN model and the Pavement ME design have similar sensitivity of degree of bonding on k-value. But, as shown in

Figure 7.6a, ME design model has no partial bonding condition whereas ANN model can predict k-value at any bonding conditions. In both cases, degree of bonding has higher sensitivity when the base-slab modulus ration is relatively higher. LTPP section 21-4025 and 08-7776 have a higher modulus ration compared to the other sections and therefore shows a significant change in k-value due to the change in degree of bonding.

Figure 7.7 compares the sensitivity of moisture on k-value using the ANN model and Pavement ME design model. Pavement ME design has almost no sensitivity of moisture on subgrade k-value. But the proposed ANN model shows relatively higher sensitivity. Although the combination of moisture sensitive M_R model and the developed ANN model show large sensitivity to moisture and slab-base degree of bonding on k-value, it is still necessary to evaluate the effect of moisture and degree of bonding on pavement performance. The next subsection describes the prediction of the fatigue cracking (top-down and bottom-up) and faulting performance for various bonding and moisture conditions and compares with the predicted performance using Pavement ME design model.

7.3.1. Effect of Moisture and Slab-base Interface Bonding on Rigid Pavement Performance

The Pavement ME design guide adopted an incremental distress calculation procedure which requires hundreds of thousands of stress and deflection calculation to compute monthly damage (i.e., different loads, load positions and temperature gradients) over a design period. ISLAB2000 finite element (FE) software is used in the design guide to accurately compute rigid pavement responses, such as stresses and deflections under the influence of traffic and environmental load.

The structural distress considered for JPCP design are fatigue related transverse cracking of PCC slabs and differential deflection related transverse joint faulting. Transverse cracking of

PCC slab initiate either at the top surface of the PCC slab and propagate downward (top-down cracking) or vice-versa (bottom-up cracking) depending on the loading and environmental conditions. Both types of fatigue cracking and the faulting performance are considered in this study for sensitivity analysis.

The fatigue damage at the top of the slab occurs due to repeated loading by heavy axles when the pavement is exposed to high negative temperature gradient (the top of the slab cooler than bottom of the slab). The critical loading condition for top-down cracking involves a combination of axles that loads the opposite ends of a slab simultaneously. In the presence of high negative temperature gradient, such load combinations cause a high tensile stress at the top of the slab near the critical edge (Saha et al. 2019d).

Similarly bottom-up transverse cracking initiate due to a critical tensile bending stress at the bottom of the slab. This bending stress is maximum when the truck axles are near the longitudinal edge of the slab, midway between the transverse joints. Moreover, this stress increases greatly when there is a high positive temperature gradient through the slab (the top of the slab is warmer than the bottom of the slab).

A difference in elevation across a joint or crack is classified as faulting distress. Repeated heavy axle loads crossing transverse joints creates the potential for joint faulting. In this study, to compute the critical stress for top-down cracking, two single axles load, weighing 22,000 lbs. each, were applied at opposite ends of the transverse joint in addition to a negative 3^0C temperature gradient. While for bottom-up cracking, one single axle load of 22,000 lb at midway between the transverse joints was exposed to a positive 3^0C temperature gradient. Lastly, one tendem axle load, weighing 57,000 lb near the edge of transverse joint was applied for the

computation of joint faulting. No temperature gradient was applied for faulting distress calculation.

Figure 7.8 shows the effect of degree of bonding on pavement performance i.e., tensile stress at surface, tensile stress at slab bottom and differential deflection across the transverse joint using the k-value predicted from ANN model and Pavement ME design model.

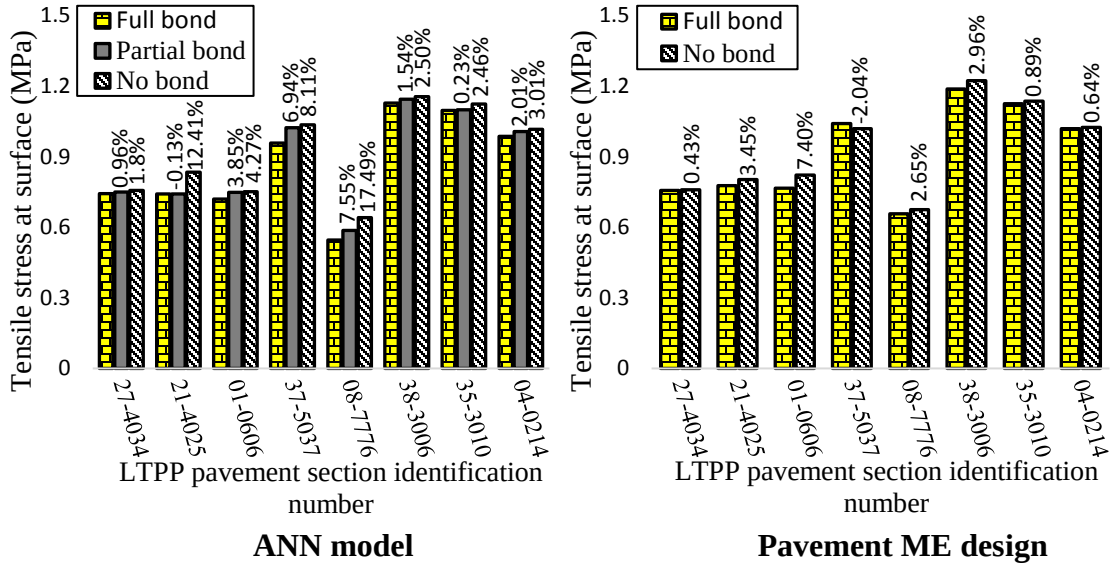

(a)

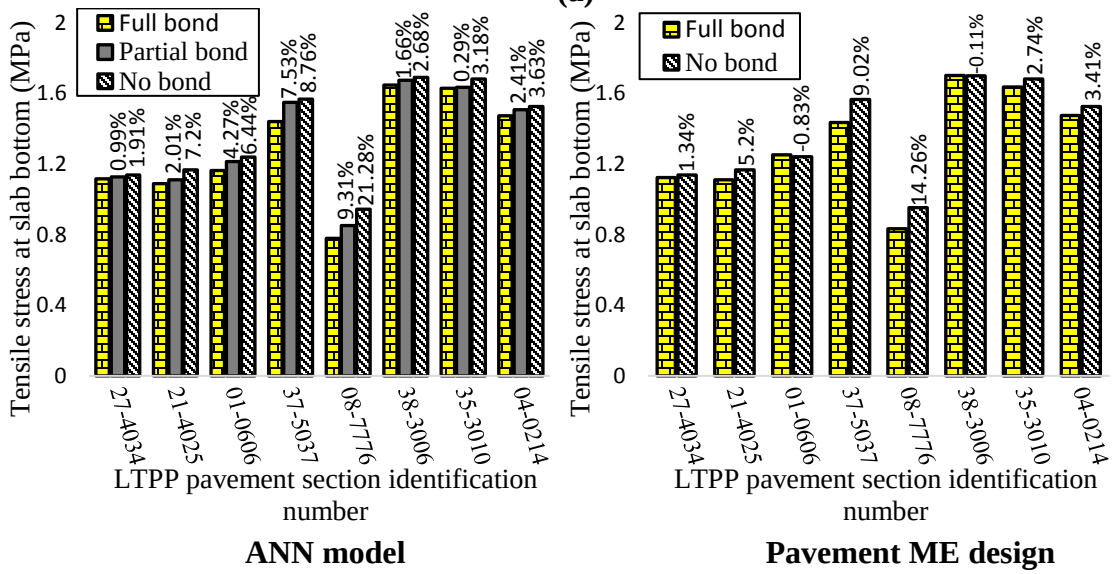

(b)

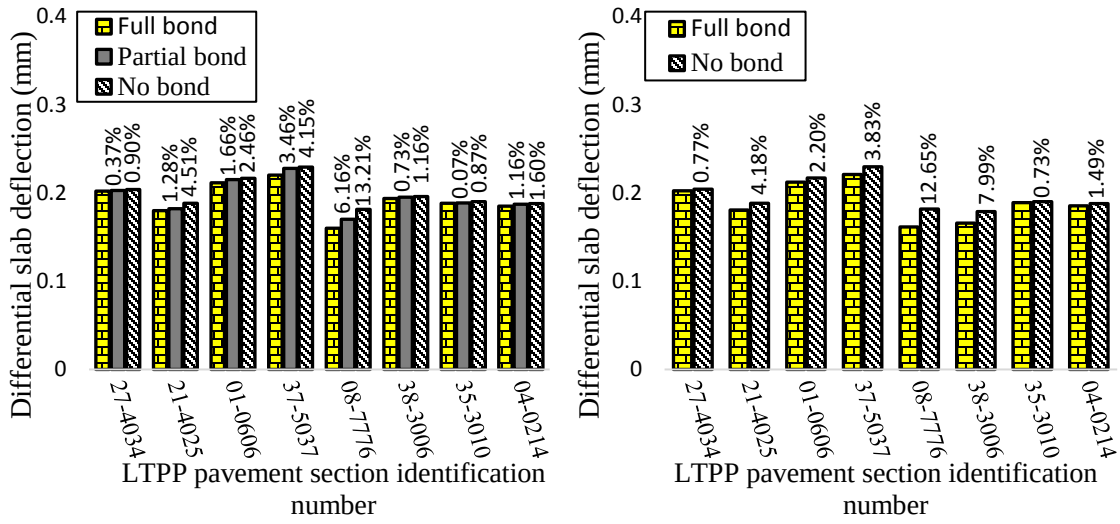

(c)

Figure 7.8 PCC slab-base interface bond sensitivity on (a) tensile stress at top of slab; (b) tensile stress at bottom of slab; and (c) deferential deflection on transverse joints

It is observed that the developed ANN model has larger sensitivity of tensile stress and differential deflection due to change in degree of bonding at slab-base interface. For both ANN model and Pavement ME design model, fully bonded condition shows the lowest tensile stress and differential deflection whereas no bonding between slab and base develop largest tensile stress and deflection. As it is seen, Pavement ME design model can only calculate tensile stress and deflection at two extreme bonding conditions but the developed ANN model has the capability of predict tensile stress and deflection at partially bonded condition as well.

Figure 7.9 shows the sensitivity of moisture on tensile stress and differential deflection using the proposed moisture and suction dependent MR model and Pavement ME design model.

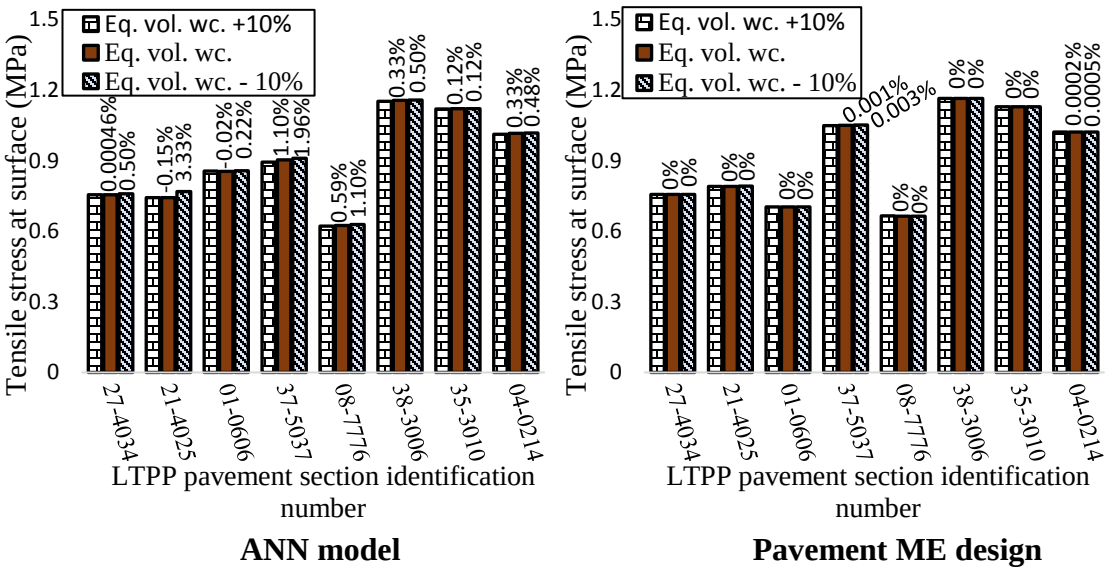
Eq. vol. wc. +10%
Eq. vol. wc.
Eq. vol. wc. - 10%
Tensile stress at surface (MPa)
1.5
1.2
0.9
0.6
0.3
0
0.00046%
0.50%
-0.15%
3.33%
-0.02%
0.22%
1.10%
1.96%
0.59%
1.10%
0.33%
0.50%
0.12%
0.12%
0.33%
0.48%
0%
0%
0%
0%
0%
0%
0.001%
0.003%
0%
0%
0%
0%
0.0002%
0.0005%
27-4034
21-4025
01-0606
37-5037
08-7776
38-3006
35-3010
04-0214
LTPP pavement section identification number
ANN model
Pavement ME design

(a)

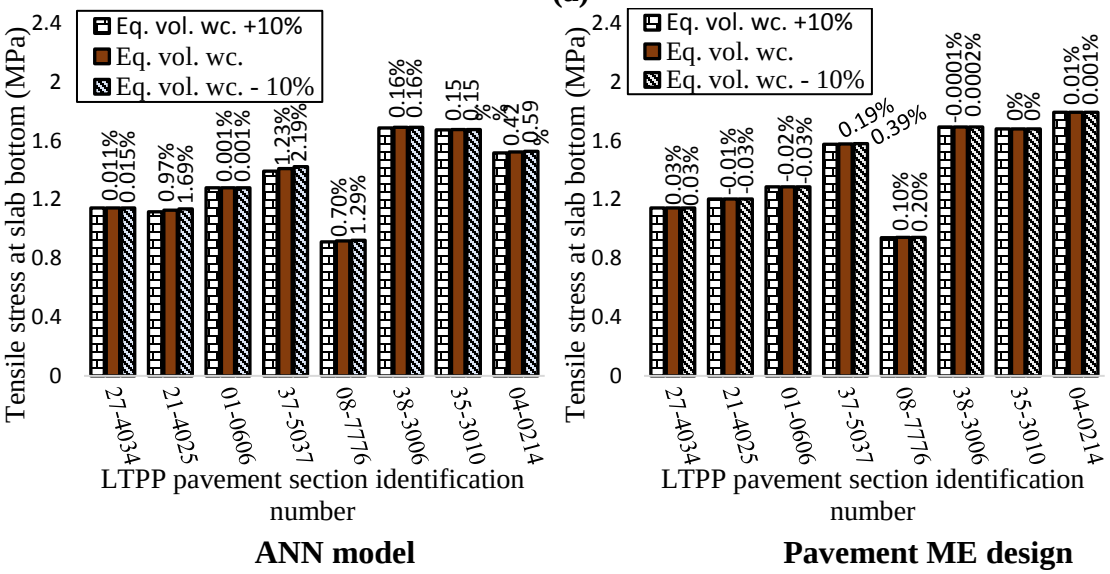
Eq. vol. wc. +10%
Eq. vol. wc.
Eq. vol. wc. - 10%
Tensile stress at slab bottom (MPa)
2.4
2
1.6
1.2
0.8
0.4
0
0.011%
0.015%
0.97%
1.69%
0.001%
0.001%
1.23%
2.19%
0.70%
1.29%
0.16%
0.16%
0.15
0.15
%
0.42
0.59
%
0.03%
0.03%
-0.01%
-0.03%
-0.02%
-0.03%
0.19%
0.39%
0.10%
0.20%
-0.0001%
-0.0002%
0%
0%
0.01%
0.01%
27-4034
21-4025
01-0606
37-5037
08-7776
38-3006
35-3010
04-0214
LTPP pavement section identification number
ANN model
Pavement ME design

(b)

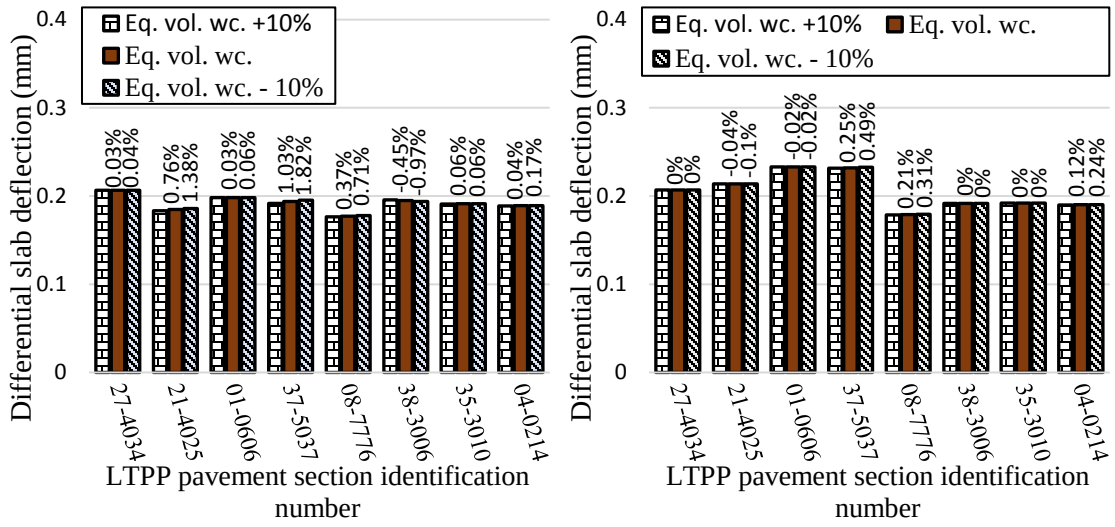

(c)

Figure 7.9 Base layer moisture sensitivity on (a) tensile stress at top of slab; (b) tensile stress at bottom of slab; and (c) deferential deflection on transverse joints

As shown in Figure 7.9, the Pavement ME design model shows very low sensitivity of tensile stress at slab top and bottom and differential deflection due to the change in moisture at middle of base layer. However, the proposed M_R model and the corresponding k value from ANN model shows higher sensitivity in tensile stress and differential deflection for change in moisture. Tensile stress at slab top and bottom increases with the increase of moisture in base layerIn summary, the models developed in this project are sensitive and capable of identifying various pavement responses including stress and strain at the bottom and top of asphalt layer and distress including cracking and rutting in asphalt pavement and faulting in concrete pavement with different base and subgrade properties with different environmental conditions including moisture and temperature, while in the Pavement ME Design such obvious differences cannot be observed.

8. DEVELOPMENT OF A MECHANISTIC-EMPIRICAL MODEL TO ESTIMATE PERCENTAGE OF STABILIZER FROM ELECTRICAL CONDUCTIVITY

8.1. Introduction

In this study, a mechanistic non-destructive approach is developed to predict the percentage of stabilizer in the base material based on electrical conductivity and water content readings. To do the laboratory test, unbound base material was collected from US 259 site. Detail description of the site location and laboratory test results are presented in following sub-sections.

8.2. US 259 Site

Unbound base materials were collected form a pavement section located in US259 site, as shown in Figure 8.1. Section 1 and 2 in Figure 8.1 are located in Texas and Oklahoma respectively, which have different layer structure. Figure 8.2 illustrates the cross-sectional view of both sections. The pavement layers that are same in both sections are consisted of a 3-inch hot mix asphalt (HMA) layer, a 10-inch base course, and subgrade soil. The only difference between the two pavement sections is the type of base material that has been used. A cement treated base layer is placed in pavement section 1, whereas flexible base is used for the pavement section 2. The following sub-section describe the laboratory tests that were performed using the base materials from US 259 pavement section.

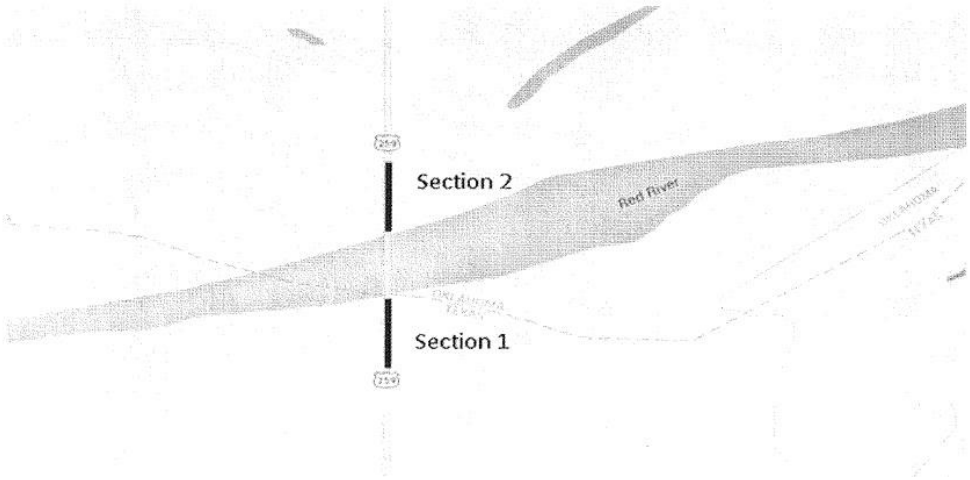

Figure 8.1 Location of Pavement Section 1 and Section 2 in US259

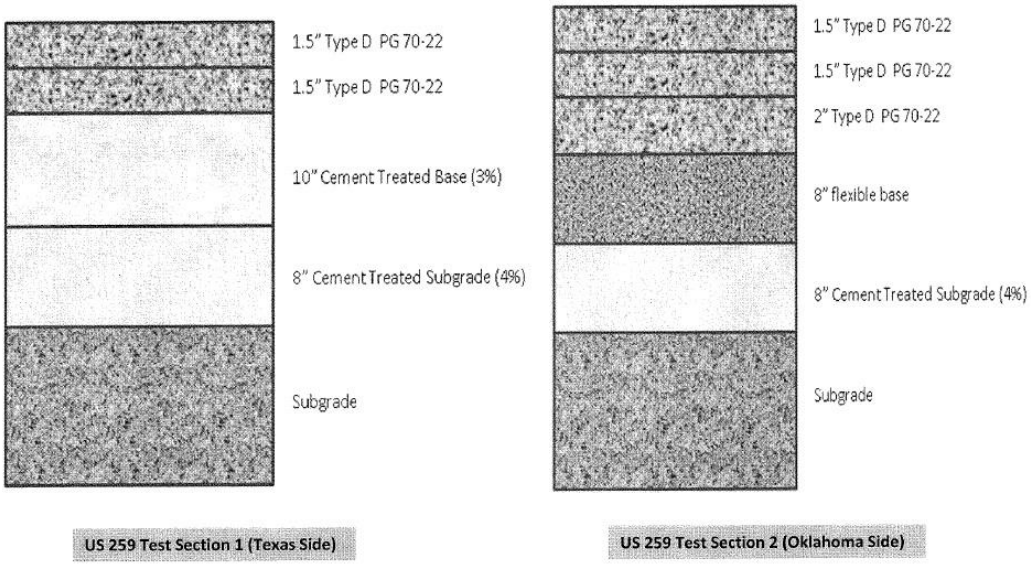

Figure 8.2 Structures of Identified Pavement Sections 1 and 2 in US 259

8.2.1. Moisture-Density Relationship

In this study, neat base materials were collected from US259 section 2 location. Maximum dry density (MDD) - optimum moisture content (OMC) tests were performed for neat base material

in the laboratory following the specification Tex-113-E. The specification documented in Tex-120-E was followed to determine the MDD-OMC relationship for cement treated base materials. MDD-OMC tests were performed only for 2% cement treated US259 base material. Then the OMC for 4% and 6% cement treated US259 materials were calculated using the relationship documented in Tex-120-E (Equation 8.1).

% molding water = % optimum moisture from M/D curve

+ 0.25 (% cement increase) (8.1)

where % cement increase is the difference in cement content between curve and other cement contents

Tables 8.1 and 8.2 present the results of the moisture content tests and the corresponding dry unit weight for neat and 2% cement treated US 259 materials respectively. The calculated dry densities at different moisture content are plotted in Figure 8.3. The optimum moisture content for neat US 259 material was calculated as 6.5% whereas it had increased to 7.75% for 2% cement treated material. Equation 8.1 was used to determine the OMC for 4% and 6% cement treated base material and the calculated OMC values were 8.28% and 8.75% respectively.

Table 8.1 Laboratory Dry Unit Weight Results for Neat US 259 Base Material

Compacted Soil-Sample no.	1	2	3	4
Water content (%)	5	6	7	8
Compacted soil + mold (g)	10341.89	10337.36	10527.87	10477.97
Mold (g)	1800.76	1714.58	1827.97	1700.97
Wet mass of soil (g)	8541.13	8622.78	8699.9	8777
Volume of specimen (cm^3)	3872.14	3808.51	3809.9	3812.69
Wet density (g/cm^3)	2.2057	2.264	2.283	2.302
Dry density (g/cm^3)	2.1	2.136	2.134	2.131

Table 8.2 Laboratory Dry Unit Weight Results for 2% Cement Treated US 259 Base Material

Compacted Soil-Sample no.	1	2	3
Water content (%)	6	8	10
Compacted soil + mold (g)	16980.6	17249.4	16987.7
Mold (g)	8125.3	8125.3	8250.6
Wet mass of soil (g)	8855.3	9124.1	8737.1
Volume of specimen (cm^3)	3892	3892	3892
Wet density (g/cm^3)	2.275	2.344	2.244
Dry density (g/cm^3)	2.146	2.170	2.040

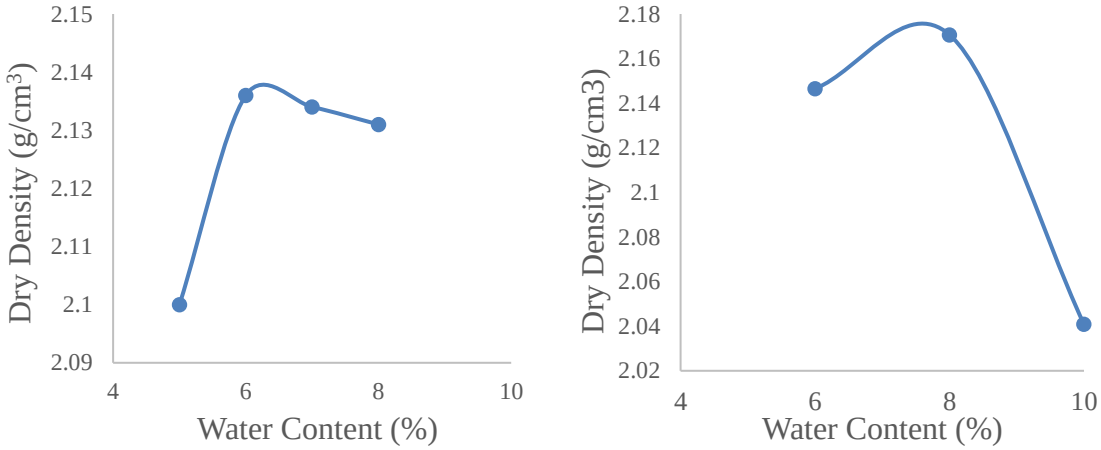

(a) **(b)**

Figure 8.3 Moisture-Density Results for (a) Neat; and (b) 2% Cement Treated US 259 Base Material

8.2.2. Percometer Test

The percometer test quickly measures the dielectric constant and electrical conductivity of materials (Saha et al. 2019f). The frequency of the percometer that has been used in this study is 50 kHz. Figure 8.4 shows a typical measurement of dielectric constant of flexible base using the percometer instrument. The dielectric constant of unbound and treated base was measured to directly relate to the moisture content and percentage of stabilizer in base material.

Figure 8.4 Measurement of Dielectric Constant of Base material Using Percometer (Reprinted from Sahin 2014)

8.2.3. Filter Paper Test

The filter paper test specified in ASTM D5298 was followed to measure matric suction for unbound and treated US259 base materials. Materials passing No. 4 sieve were collected and compacted at different moisture contents. Filter papers were placed in a sealed jar for seven days with the compacted unbound aggregate specimen. After seven days, the increasing mass of the filter papers were measured by a highly accurate scientific scale. Finally, the matric suction of the specimen was determined using the filter paper calibration curve (Bulut et al. 2001). Next section describes the test results and establish the empirical model to predict percentage of stabilizer from electrical conductivity and evaporable water content.

8.3. Development of a Prediction Model for Percentage of Stabilizer

8.3.1. Soil-Water Characteristics Curve for Neat and Cement Treated Samples

The suction at different degrees of saturations were measured using the filter paper test method described in previous section. Both matric and total suctions were determined by means of the

filter paper method. Figure 8.5 plots the soil water characteristics curves (SWCC) for neat US 259 and 2% cement treated US 259 soil samples. Similarly SWCC were generated for 4% and 6% cement treated soil samples.

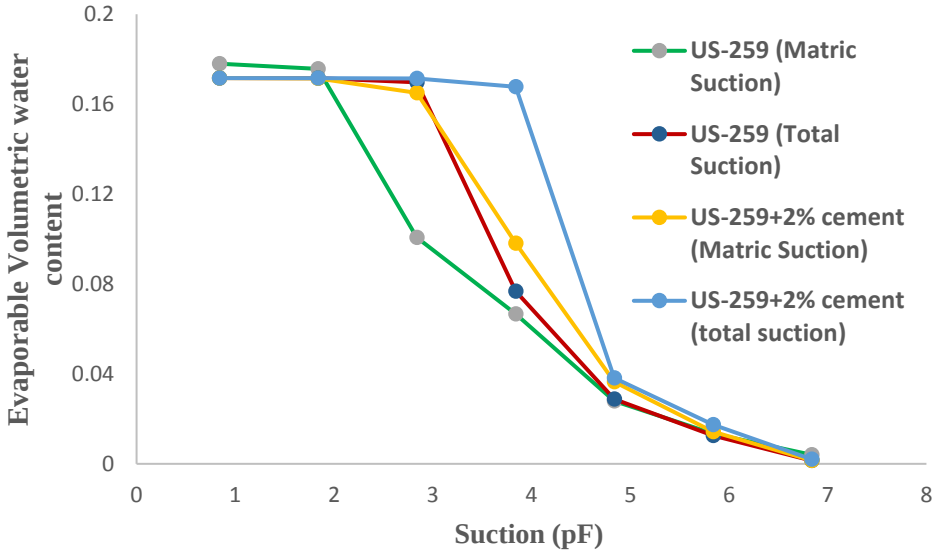

Figure 8.5 Soil water characteristics curve for Neat US 259 and 2% cement treated US 259 base materials

8.3.2. Determination of Evaporable Water Content from Electrical Conductivity Readings

The relation between the evaporable water content and the electrical conductivity in base material was investigated using the percometer and filter paper measurements. Figure 8.6a presents the plot of measured matric suction versus electrical conductivity data, whereas Figure 8.6b on the right hand side is plotted to present the variation of matric suction with evaporable volumetric water content. The curves were plotted for neat, 2%, 4% and 6% cement treated soil specimens. The evaporable water content in unbound base material can be easily estimated from the recorded electrical conductivity and suction readings. Figure 8.6 shows that the evaporable

volumetric water content in 6% cement treated US 259 base material is 0.085 for a corresponding electrical conductivity of 11 µs/cm.

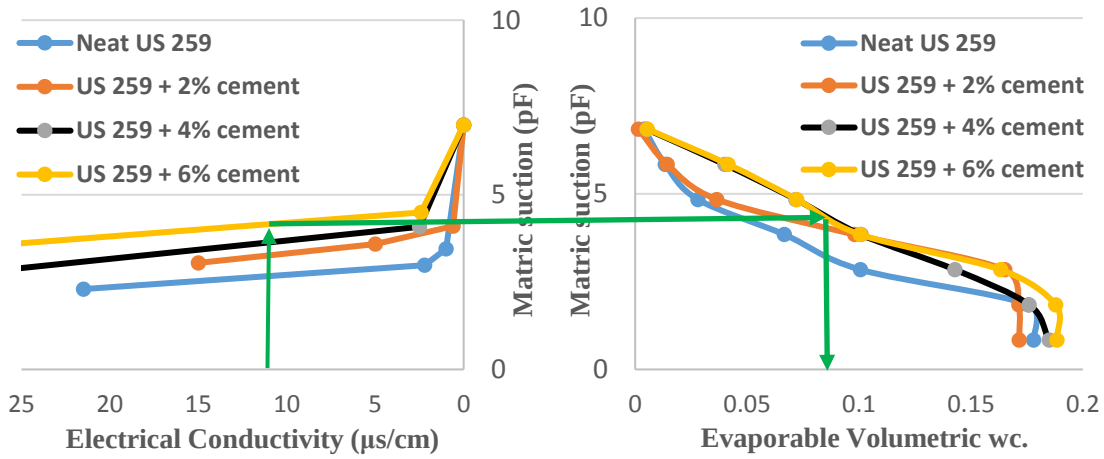

(a) **(b)**

Figure 8.6 Determination of volumetric water content from electrical conductivity

8.3.3. Prediction of Osmotic Suction from Electrical Conductivity and Volumetric Water Content

Osmotic suction is related to the amount of salts dissolved in the free pore-water (Fredlund et al. 1993). Past studies have proposed several procedures to measure the osmotic suction of soil. In this study, the osmotic suction was determined by subtracting the estimated matric suction from total suction.

Figure 8.7 plots the calculated osmotic suction against volumetric water content for US 259 base material. The curves were plotted for both neat and cement treated base materials.

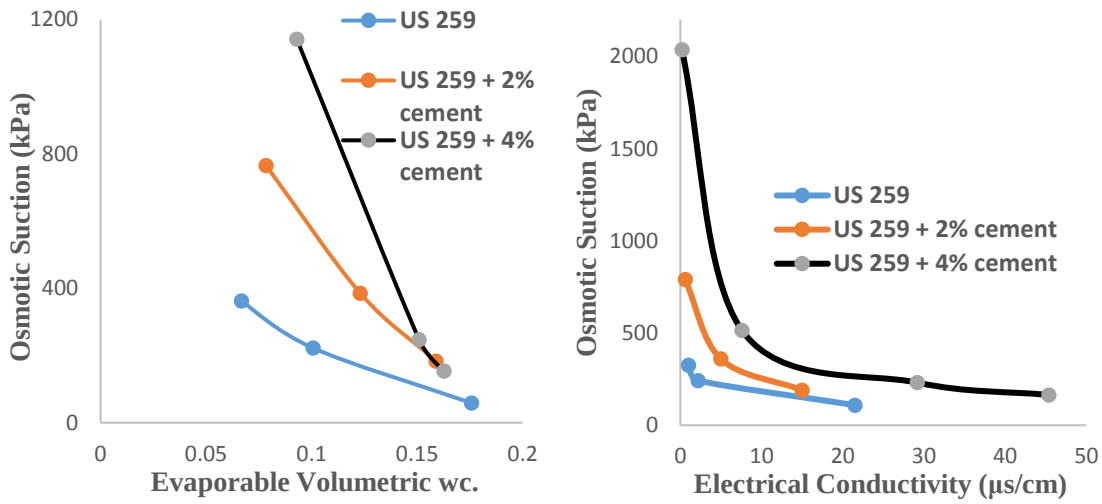

(a) **(b)**

Figure 8.7 (a) Osmotic Suction versus evaporable volumetric water content plot; (b) Osmotic Suction versus Electrical Conductivity plot, for neat, 2% and 4% cement treated US 259 base material

As it is seen, osmotic suction value increased with the increase of cement stabilizer in base material. The observed phenomena is obvious because the amount of dissolved salt increases with the higher percentage of cement. Similarly figure 8.7b depicts that osmotic suction has an inverse relationship with electrical conductivity.

Based on the observed relationship shown in Figure 8.7, an empirical equation was developed to predict the osmotic suction from measured evaporable volumetric water content and electrical conductivity.

$$O.S. = \frac{2.8}{(E.V.wc.)^3} * \frac{1}{\sqrt{E.C.}} \qquad (8.2)$$

where, O.S. is the osmotic suction, (unit: kPa); E.V. wc. Is the evaporable volumetric water content, and E.C. is the Electrical conductivity, (unit: µs/cm).

8.3.4. Molar Concentration of Cement Solute in Water

As stated earlier, osmotic suction is a soil property which arises from the salt content in the soil pore fluid. Therefore, in a stabilized base material osmotic suction is influenced by the percentage of stabilizer in the pore solution. Van't Hoff proposed a relationship between Molar concentration, $\nu C\phi$, and osmotic suction that is applicable for both treated and neat base material.

From Van't Hoff's equation,

$$\pi = -\nu RTC\phi \qquad (8.3)$$

where π is the osmotic Suction; ν is the number of ions from one molecule of solute; R is 8.314×10^{7} J mol/K; T is (273+ ^{0}C) K; C is the molar concentration (moles/1000g of solvent); and ϕ is the osmotic coefficient

Figure 8.8 plots the molar calculated concentration of 2% cement treated US 259 material at various water content.

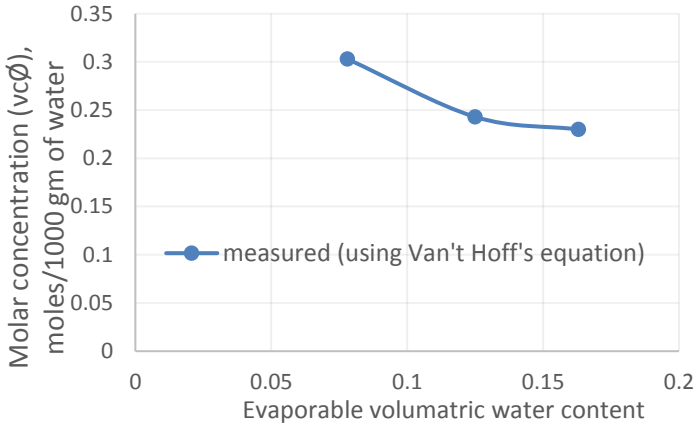

Figure 8.8 Molar concentration of cement solute for 2% cement treated US 259 material

8.3.5. Comparison of the Estimated Molar Concentration with Literature Data

Approximately 0.3 grams of water are required per gram anhydrous cement to form hydrated solid products and achieve normal plasticity (Glasser and Marr, 1984). Portland cement pastes are usually about 40 percent hydrated with one day at 15 to 25^{0}C, 70 percent hydrated within one month (Reardon, 1992). In this study, 2% cement (13.4 grams) was used to stabilize the base material. Considering a hydration rate of 70 percent, water required to form the hydration product is 0.7*13.4*0.3 = 2.814 gm.

Table 8.3 Concentration of ions in Pore Water

Ion	Concentration (mM)								
	Case-1	Case-2	Case-3	Case-4	Case-5	Case-6	Case-7	Average (Cement = 2000 gm)	Average (Cement = 13.4 gm)
OH-	743	590	440	477	546	689	651	591	3.96
Ca^{2+}	2	0.6		1	<1	<1	<1	1	0.01
Si^{4+}					0.9		1	1	0.01
K^{+}	639	420	490	376	442	547	519	490	3.28
Na^{+}	323	250	560	136	110	156	173	244	1.63
Al^{3+}							0.1	0.1	0.00
$SO4^{2-}$	27				4	3	19	13	0.09

Evap. v.w.c. = 0.078		Evap. v.w.c. = 0.123		Evap. v.w.c. = 0.159	
Concentration (per 49.11 gm of water)	Concentration (per 1000 gm of water)	Concentration (per 37.96 gm of water)	Concentration (per 1000 gm of water)	Concentration (per 24.18 gm of water)	Concentration (per 1000 gm of water)
3.96	80.63	3.95	104.3	3.95	163.75
0.01	0.14	0.006	0.176	0.0067	0.277
0.01	0.14	0.006	0.176	0.0067	0.277
3.28	66.85	3.28	86.48	3.283	135.773
1.63	33.29	1.63	43.06	1.63	67.609
0.00	0.01	0.0006	0.0176	0.00067	0.0277
0.09	1.77	0.087	2.294	0.0871	3.602
	Total = 182.83		Total = 236.52		Total = 371.32

*Evap. v.w.c. = Evaporable volumetric water content

However, the change of evaporable water content was measured after the addition of cement, and it was observed that the amount of evaporable water reduced was approximately 2.96 grams. In other words, 2.96 grams of water was used to form the hydration products. So, water available in the solution = (52.07 – 2.96) = 49.11 grams. Reardon (1992) listed the concentrations of major solute components in pore water expressed from ordinary Portland cement pastes with water/ cement ratios of approximately 0.5. Since all quantities are in milimoles per 1000gm of water, cement content for the listed amount is 2000 gm in Table 8.3.

Figure 8.9 shows the comparison of estimated molar concentration in 2% cement treated US 259 base material using Van't Hoff's equation and the molar concentration calculated from the typical cement ions concentration collected from the literature. A reasonable agreement is observed between the estimated concentration using Van't Hoff's equation and the concentration calculated from the literature.

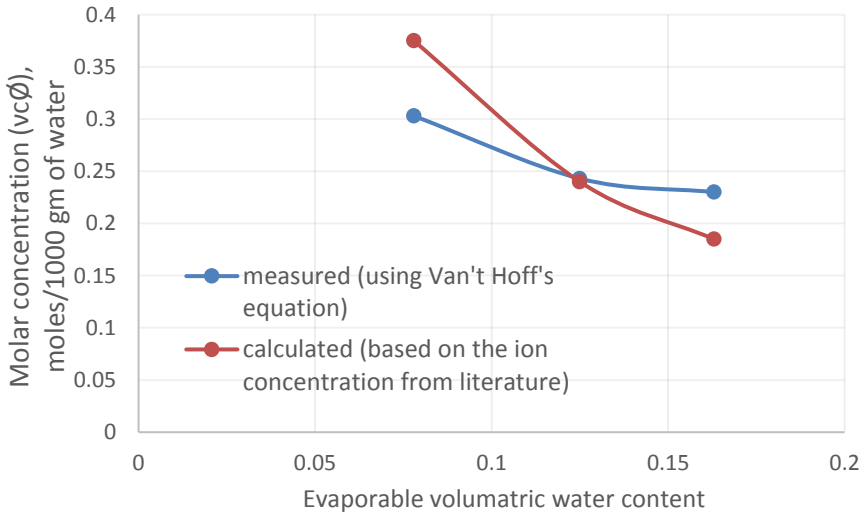

Figure 8.9 Comparison of Molar Concentration of Cement Solute calculated based on Van't Hoff's Equation and Ion Concentration from Literature

A nondestructive approach has been evaluated in the later sub-sections to incorporate the prediction model of percentage of stabilizer and determine in-situ stabilizer content in the base material. The ground penetrating radar is a nondestructive geophysical tool to detect the dielectric properties of each layer in pavement. The formulation of calculating electrical conductivity from radar waves with non-normal incidents have been developed by (Balanis, 2012) and discussed in the following subsections.

8.4. Determination of Electrical Conductivity from Ground Penetrating Radar Waves

The ground penetrating radar (GPR) is one of the nondestructive geophysical tools used to detect the underground layer properties and monitors the variations in the layer beneath the surface layer. It is has been adapted and was successfully applied to predict the pavement layer system characteristics by pavement engineers. The basic principle of the GPR operation system is that it emits the electromagnetic (EM) pulses and receives the reflected signals through an antenna and measures in the time of arrival of each wave. The magnitude of the signals amplitudes changes are based on the dielectric properties of each layer (Annan, 2003). The mechanics of the radar sending energy and the reflection from each layer interface is shown in Figure 8.10.

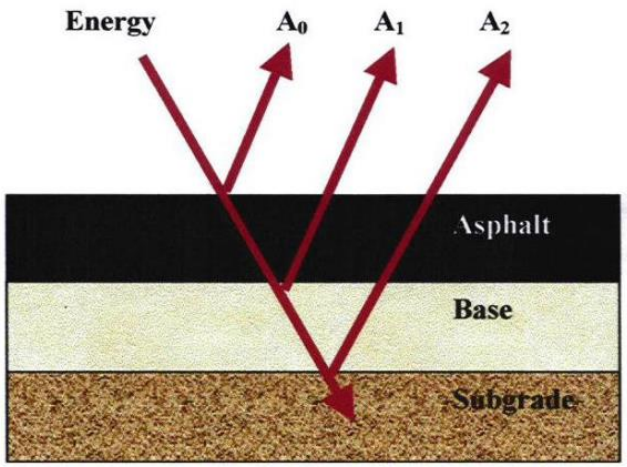

Figure 8.10 A Typical Received Radar Signal from a Pavement Structure (Reprinted from Sahin, 2014)

The GPR technology offers a high speed data collection and assessment of the continued dielectric profile. A transmitter antenna transmits a high-frequency monopulse electronic signal, which travel through each layer and reflects at the interface between the two layers of the materials with different dielectric properties. This high frequency signal is received by the antenna and transmitted to a signal acquisition unit to convert them to relatively lower signal pulses. A typical plot of a received radar signal versus time for one pulse is shown in Figure 8.11. The first amplitude A_o is the reflection from the lower end of the antenna and the second amplitude is reflected signal from the pavement surface.

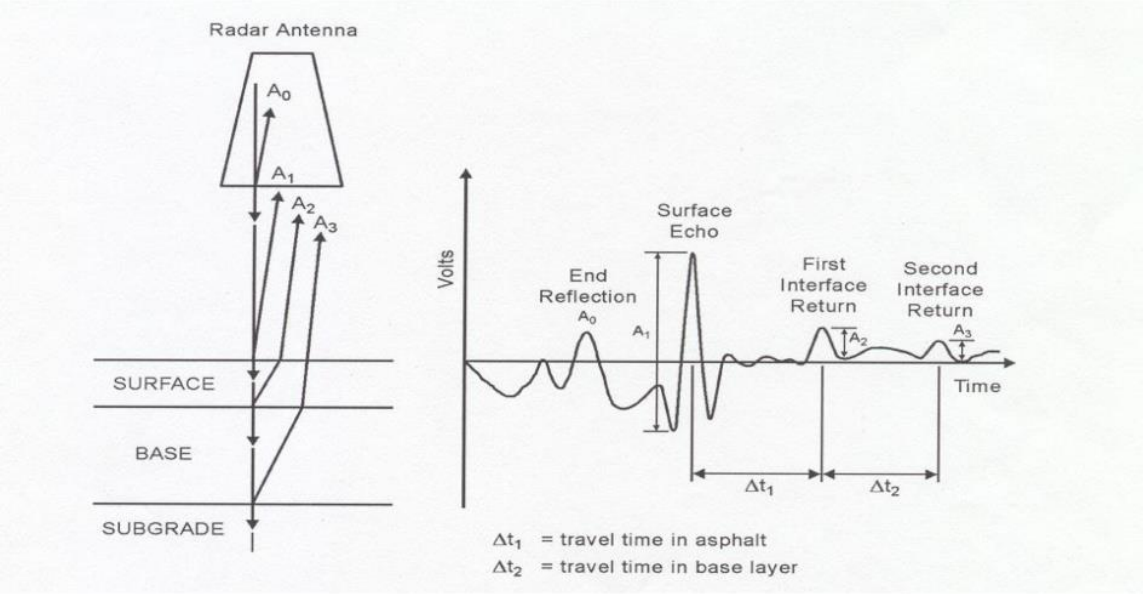

Figure 8.11 Radar Operation System Principals of a Typical Emitted and Received Radar Signal Schematic (Reprinted from Sahin, 2014)

Figure 8.11 shows that the incident wave is reflected at each layer interface and plotted as return voltage against time of arrival in nanoseconds. The amplitude A_1 represents the pulse energy from the surface of the pavement, amplitude A2 and A3 represent the reflection from the surface of the base and subgrade, respectively. These signals are received by a receiver and are converted in a low frequency and digitized by an A/D converter and then sent to a host computer to data process and display. A radar system moves along the survey location and received waves displayed in a 2-D pseudo color strip map by the host computer. A radar system is usually carried by a van, and the radar antenna is mounted on the front bumper. An air launched ground penetrating radar unit is shown in Figure 8.12a.

(a)

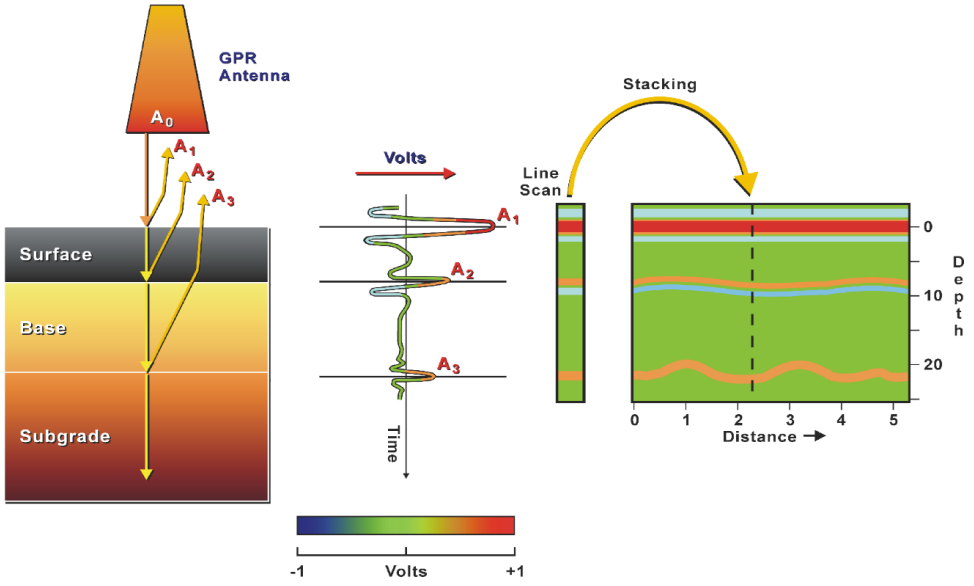

(b)

Figure 8.12 (a) A GPR Equipment and; (b) Mechanics of Signal Operation System (Reprinted from Sahin, 2014)

This particular GPR van operates at a highway speed of 60 mph and can effectively collect the data. This unit is capable of emitting and receiving 50 pulses per second in penetrating to a depth of 2 feet. In Figure 8.12 (b), A_o is the incident amplitude; A_1 is the amplitude of the GPR wave that is reflected from the surface; A_2 is reflected from the interface between the surface layer and the base course; A_3 is reflected from the interface between the base course and the subgrade. The GPR uses a very sophisticated system and most advanced technology. The main component of a GPR is a high speed pulse generator, high speed data acquisition, real time data processing, and wireless communication systems. Displaying data is a synchronized process in the GPR unit. This system was adapted by the state transportation departments and agencies: likewise, TxDOT and TTI have the GPR vans.

8.4.1. Principal of Ground Penetrating Radar System

The dielectric constant and the layer thickness can be calculated by using the measured amplitudes (volts) and time delays (ns). The general form of the equations are summarized below. The surface layer dielectric equation is given in Equation 8.4

$$\varepsilon_a = \left[\frac{1 + A_1 / A_m}{1 - A_1 / A_m} \right]^2 \tag{8.4}$$

where ε_a gives the dielectric of the surface layer, A_1 is the amplitude of surface reflection (volts), A_m is the amplitude of reflection from a large metal plate in volts (this represents the 100% reflection case).

The top layer thickness is presented in Equation 8.5

$$h_1 = \left[\frac{c\Delta t_1}{2\sqrt{\varepsilon_a}} \right] \tag{8.5}$$

where h_1 shows the thickness of the top layer, c is the speed of electromagnetic wave in air (5.9 ins/ns two way travel), Δt_1 is the time delay between peaks A_1 and A_2 (in ns).

The dielectric value of base course layer is presented in Equation 8.6

$$\sqrt{\varepsilon_b} = \sqrt{\varepsilon_a} \left[\frac{1 - (\frac{A_1}{A_m})^2 + (\frac{A_2}{A_m})}{1 - (\frac{A_1}{A_2})^2 + (\frac{A_2}{A_m})} \right] \tag{8.6}$$

where ε_b yields the dielectric value of the base course aggregate and A_2 is the amplitude of reflection (volts) from the top of the base course layer.

The thickness of the base course layer is estimated in Equation 8.7

$$h_{base} = \frac{c\Delta t_2}{2\sqrt{\varepsilon_b}} \tag{8.7}$$

where h_{base} yields the thickness of the base and Δt_2 is time delay (ns) between A_2 and A_3

The given equations from 8.4 to 8.7 provide a summary that are derived to calculate the pavement layer dielectric values and thickness. In this particular study, the base course thickness and dielectric constant will be utilized to calculate the electrical conductivity of base layer. This study is discussed in the following sub-section in detail.

8.4.2. Formulation of Electrical Conductivity

Figure 8.13 illustrate the incidence of a non-normal radar wave at the interface between two layers

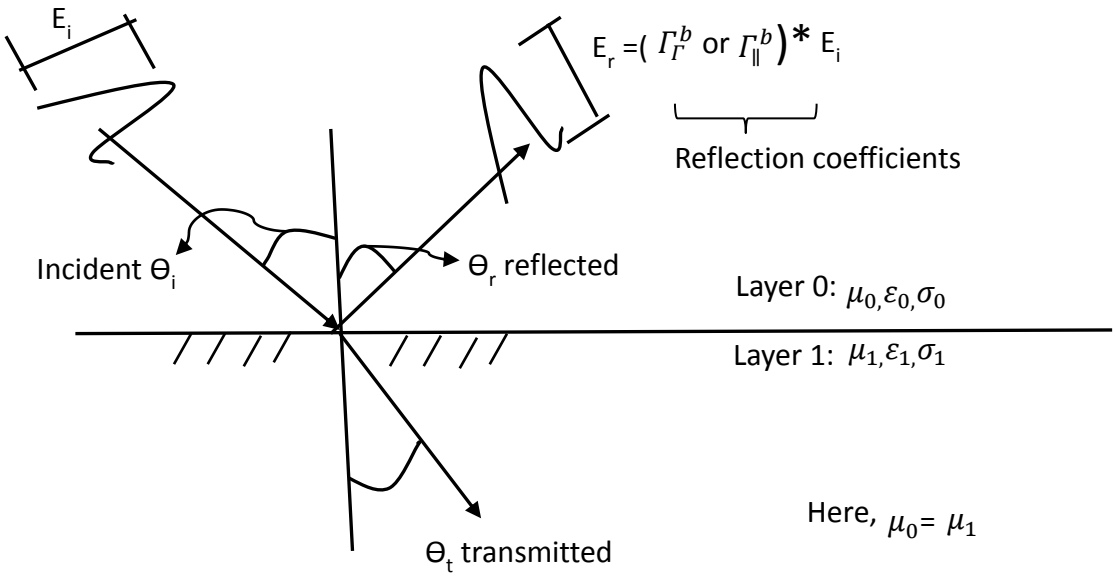

Figure 8.13 Illustration of Radar Waves with Non-normal Incidents

Here, $\perp$ is the perpendicular polarized GPR wave; and II is the parallel polarized GPR wave

The impotent properties of a free space wave signal are,

$\varepsilon_0 = \frac{1}{36\pi x10^{-9}}$ Farads /meter; $\mu_0 = 4\pi x10^{-7}$ Henry's/meter; and $c = \frac{1}{\sqrt{\mu_0\varepsilon_0}} = 3x10^8$ meter/sec

The reflection coefficients are expressed as,

$$\Gamma_{\perp}^{b} = \frac{\cos\theta_i - \frac{\eta_0}{\eta_1}}{\cos\theta_i + \frac{\eta_0}{\eta_1}} \tag{8.8}$$

$$\Gamma_{\square}^{b} = \frac{-\cos\theta_i + \frac{\eta_1}{\eta_0}}{\cos\theta_i + \frac{\eta_1}{\eta_0}} \tag{8.9}$$

Now,

$$\frac{\eta_0}{\eta_1} = \frac{\sqrt{\frac{\mu_0}{\varepsilon_0}}}{\sqrt{\frac{jw\mu_1}{\sigma_1 + jw\varepsilon_1}}} = (\frac{\varepsilon_1}{\varepsilon_0})^{1/2}\sqrt{1 - j(\frac{\sigma_1}{w\varepsilon_1})} \tag{8.10}$$

Here,

$$\frac{\eta_0}{\eta_1} = (\frac{\varepsilon_1}{\varepsilon_0})^{1/2}[\xi + j\phi] \tag{8.11}$$

$$\xi = \{\frac{1}{2}[1 + (\frac{\sigma_1}{w\varepsilon_1})^2]^{1/2} - 1\}^{1/2} \tag{8.12}$$

$$\phi = \{\frac{1}{2}[1 + (\frac{\sigma_1}{w\varepsilon_1})^2]^{1/2} + 1\}^{1/2} \tag{8.13}$$

Let $[1 + (\frac{\sigma_1}{w\varepsilon_1})^2]^{1/2} = r$

Then,

$$\xi + j\phi = (\frac{r}{2} - 1)^{1/2} + j(\frac{r}{2} + 1)^{1/2} \tag{8.14}$$

The real part of $[\xi + j\phi]$ is

$$\xi = (\frac{r}{2} - 1)^{1/2} \qquad \text{if } \frac{r}{2} > 1 \tag{8.15}$$

The imaginary part of $[\xi + j\phi]$is

$$\phi = [(1-\frac{r}{2})^{1/2} + (1+\frac{r}{2})^{1/2}] \qquad \text{if } \frac{r}{2} < 1 \tag{8.16}$$

The reflection coefficient for perpendicular polarization,

$$\Gamma_{\perp}^{b} = \rho_{01} = \mathrm{Re}(\frac{A_1}{A_0}) = \frac{\cos\theta_i - \sqrt{\frac{\varepsilon_1}{\varepsilon_0}}[\mathrm{Re}(\xi + j\phi)]}{\cos\theta_i + \sqrt{\frac{\varepsilon_1}{\varepsilon_0}}[\mathrm{Re}(\xi + j\phi)]} \tag{8.17}$$

If $\frac{r}{2} > 1$,

$$\rho_{01}\cos\theta_i + \rho_{01}\sqrt{\frac{\varepsilon_1}{\varepsilon_0}}[\frac{r}{2}-1]^{1/2} = \cos\theta_i - \sqrt{\frac{\varepsilon_1}{\varepsilon_0}}[\frac{r}{2}-1]$$

$$\rho_{01}\cos\theta_i - \cos\theta_i = \sqrt{\frac{\varepsilon_1}{\varepsilon_0}}[\frac{r}{2}-1]^{1/2}[-1-\rho_{01}]$$

$$\frac{\cos\theta_i(\rho_{01}-1)}{(-1-\rho_{01})} = \sqrt{\frac{\varepsilon_1}{\varepsilon_0}}[\frac{r}{2}-1]^{1/2} \tag{8.18}$$

If $\frac{r}{2} < 1$,

$$\frac{\cos\theta_i(1-\rho_{01})}{(1+\rho_{01})} = \sqrt{\frac{\varepsilon_1}{\varepsilon_0}}[\frac{r}{2}+1]^{1/2} \tag{8.19}$$

If Layer 1 is base (dielectric) material,

<u>Perpendicular Polarization:</u> $\varepsilon_1 \neq 0;\ \sigma_1 = 0;\ \mu_1 = \mu_0$

$$\frac{\eta_0}{\eta_1} = \frac{\sqrt{\frac{\mu_0}{\varepsilon_0}}}{\sqrt{\frac{jw\mu_1}{jw\varepsilon_1}}} = \sqrt{\frac{\varepsilon_1}{\varepsilon_0}}$$

$$\Gamma_{\perp}^{b} = \rho_{01} = \frac{\cos\theta_i - \sqrt{\frac{\varepsilon_1}{\varepsilon_0}}}{\cos\theta_i + \sqrt{\frac{\varepsilon_1}{\varepsilon_0}}}$$

$$\frac{\cos\theta_i(1-\rho_{01})}{(1+\rho_{01})} = \sqrt{\frac{\varepsilon_1}{\varepsilon_0}} \qquad (8.20)$$

Parallel Polarization: $\varepsilon_1 \neq 0$; σ_1=0; $\mu_1 = \mu_0$

$$\Gamma_{\square}^{b} = \rho_{01} = \frac{-\cos\theta_i + \sqrt{\frac{\varepsilon_0}{\varepsilon_1}}}{\cos\theta_i + \sqrt{\frac{\varepsilon_0}{\varepsilon_1}}}$$

$$\frac{(1-\rho_{01})}{\cos\theta_i(1+\rho_{01})} = \sqrt{\frac{\varepsilon_1}{\varepsilon_0}} \qquad (8.21)$$

Using the estimated electrical conductivity values from GPR signal waves expressed in Equation 8.8 to 8.21 and the laboratory prediction model of percentage of stabilizer based on conductivity readings, a non-destructive methodology of determining percentage of stabilizer in the base materials can be developed with further validation.

9. A GROUND PENETRATING RADAR BASED NON-DESTRUCTIVE METHODOLOGY TO DETERMINE M_R

9.1. Introduction

Flexible base layer is laid between asphalt concrete layer and subgrade in asphalt pavements. A flexible base with high quality can provide functional support to the pavement structures, and effectively dissipate the stresses induced by the traffic load to the underlying subgrade (Huang, 1993). During construction, the measured properties of flexible base for current quality control (QC) and quality assurance (QA) are the dry unit weight and water content. They are compared with the laboratory compaction curves of unbound aggregates specimens to assure that an adequate level of compaction has been achieved for flexible base. However, the current pavement design is not based upon the dry unit weight and moisture content of flexible base, but based upon the resilient modulus of base layer. The resilient modulus of each individual pavement layer significantly influences the performance and service life of pavement. To assure the construction quality of flexible base, the modulus values of the base course that were compacted should match as closely as possible the modulus values of base course that were used in design. Quality assurance of the compacted flexible base course must also be conducted in a timely and efficient manner so as not to retard the pace of construction. Therefore, it is necessary to develop an efficient nondestructive testing (NDT) approach to measure the resilient modulus of the compacted flexible base.

Falling weight deflectometer (FWD) and ground penetrating radar (GPR) are two nondestructive testing devices commonly used in pavement engineering. FWD is primarily used

to estimate the resilient modulus of each individual pavement layer by measuring the pavement surface deflections at the different load levels. The use of FWD normally requires a specific traffic control, which significantly increases the potential user time delay costs and the road safety problems. GPR is another nondestructive testing device used to measure the dielectric constant of paving materials, and to estimate the layer thickness of pavements. The measured dielectric constant profiles are related to the density of asphalt concrete, the density of base course, and the moisture content of base course. Compared to the FWD device, the GPR system can be operated at normal highway speed (e.g., 60 mph), thus it will not cause any traffic disruptions. According to the aforementioned task objectives, the GPR system-based NDT approach is selected for evaluating flexible base construction.

9.2. Estimation of Resilient Modulus of Flexible Base in the Field

In this section, the mechanistic-based NDT approach is employed to evaluate the quality of flexible base in terms of the determined resilient modulus profiles. Figure 9.1 illustrates the procedures of implementing the mechanistic-based NDT approach for field projects. The GPR outputs are analyzed by the software PaveSCM to obtain the dielectric constant profile of flexible base. The laboratory characterization results and the dielectric constant data are input into the software LayerMAPP to estimate the resilient modulus of the in-situ flexible base. The FWD test is also conducted on the field test sections. The FWD test data is analyzed by the software Modulus 6.0 to backcalculate the resilient modulus of the in-situ flexible base. To validate the mechanistic-based NDT approach, the predicted resilient moduli of flexible base are compared to those backcalculated from the FWD test data.

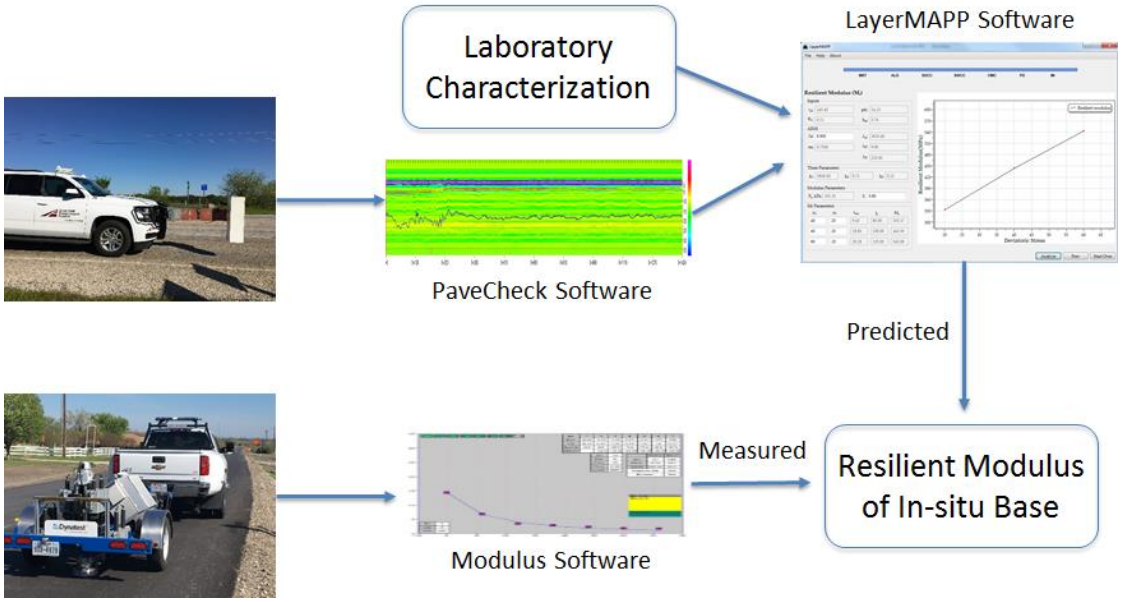

Figure 9.1 Validation of Mechanistic-Based NDT Approach Using Field Project Data

9.2.1. GPR Signal Processing

The successful deployment of the mechanics-based M_R determination models rely on collecting quality GPR data and suitably processing those data (Saha et al. 2019g). Before readings of dielectric constant, thickness or any other pavement properties are estimated from a GPR scan, the raw GPR scan needs to be pre-processed. Pre-processing of the raw GPR scans helps remove background noise in the signals, reduce the effects of the antenna height variation due to the bounce of the vehicle while driving, and enables more accurate identification of layer interfaces. The pre-processing of the raw GPR scan is performed using the following methods:

- Filtering of the radar signals
- Surface normalization
- Height variation correction of signal amplitude
- Thin-layer subtraction

Filtering of Radar Signals

The raw GPR scans can contain low and/or high frequency noise that would need to be removed. The low and high frequency noise can be removed by applying bandpass FIR or IIR filters. The frequency of the bandpass filter will depend on the frequency of the GPR antenna. The system currently in use by the research team does not usually encounter this noise, so no filtering is currently applied. However, for eventual implementation, it's possible that other currently available GPR systems may use or require filtering.

Surface Normalization

The height of the antenna(s) can change due to the bounce of the vehicle during a scan. This height change results in the surface reflection of the signal to vary along the length of the scan. This occurrence can be seen in the Figure 9.2, where the surface reflection is inside the highlighted box. The variation in the height of the antenna can be seen in the radar signal with the variation in the signal reflection of the surface.

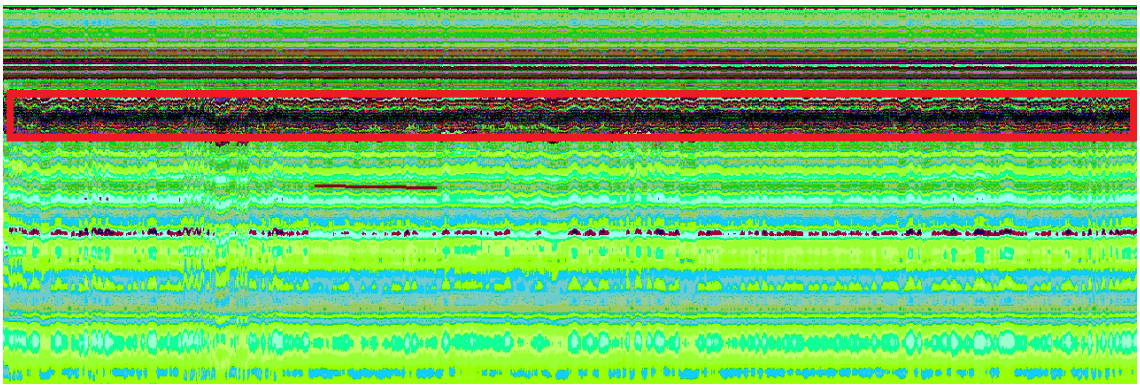

Figure 9.2 B-scan Plot Showing Variation in Surface Reflection Location

This variation in the signal reflection propagates through the entire signal. The small horizontal brown line highlights what could be mistaken for an interface. But when a *surface normalization* is applied, the surface reflection is repositioned so that all the signals in the scan have the surface reflection located at the same depth (i.e. time). As a result, the variation of the position of the signal due to the antenna height variation is removed. Figure 9.3 shows the same scan with the surface normalization applied.

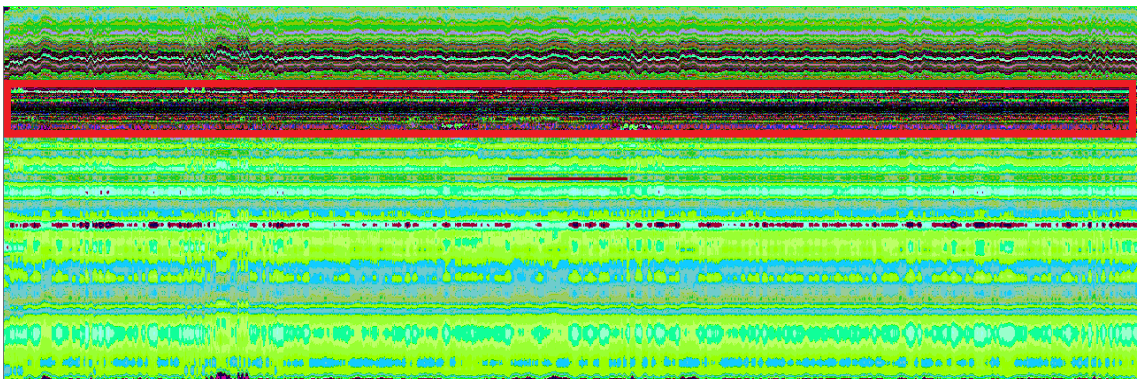

Figure 9.3 B-scan Plot Showing Surface Reflection at Same Depth

In Figure 9.3, the surface reflections of all the signals appear at the same depth. Also, what had appeared to be an interface in the original scan, highlighted by the brown line, is now a complete flat line, meaning that it is not an interface and instead is just noise in the signal. This example scan was performed on top of the lime-treated subgrade (LTS) layer at the RELLIS test site. In this example, applying the *surface normalization* eliminates the misidentification of the bottom of the LTS layer.

Height Variation Correction of Signal Amplitude

The variation in the height of the antenna caused by vehicle bounce during a scan also affects the amplitude of the signal. When the antenna gets closer to the pavement the signal amplitude

increases, and when the antenna is further away from the pavement the signal amplitude decreases. This variation in antenna height which in turn affects the signal amplitude is corrected by applying a bounce correction. Figure 9.4 illustrates how the time between the end reflection and surface reflection are used to determine the bounce correction.

$$B_k = -1.1907 \times \Delta t + 9.1617 \quad (9.1)$$

where B_k – Bounce correction factor, Δt – Time difference between End Reflection and Surface Reflection

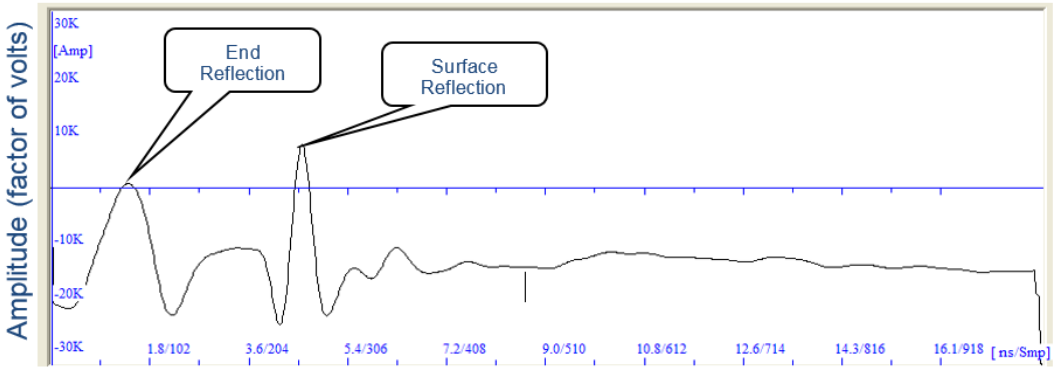

Figure 9.4 A-scan of Signal Showing End Reflection and Surface Reflection

An improvement on the above bounce correction equation could be to use a polynomial equation instead of the linear equation.

Thin-layer Subtraction

The thin-layer subtraction allows identifying top layer(s) whose thickness is under 2 or 3 inches and also reduces any back-ground noise in the raw GPR signal. The thin-layer subtraction is performed by subtracting the raw GPR signal by the signal recorded over a metal plate. The signal recorded over a metal plate will be almost identical to the signal sent from the antenna.

The amplitude of the metal plate signal is adjusted so that it has the same amplitude as the GPR signal recorded over the pavement. Then surface reflections from both the signals are lined up and the subtraction is performed for the entire signal. In order to improve this subtraction, the number of samples in the signal is increase by a factor of 100.

Figure 9.5 shows an A-scan that was recorded over the TOM-F layer at the RELLIS test site. From looking at the reflections, the interface of the TOM-F and the D Mix layers is not visible.

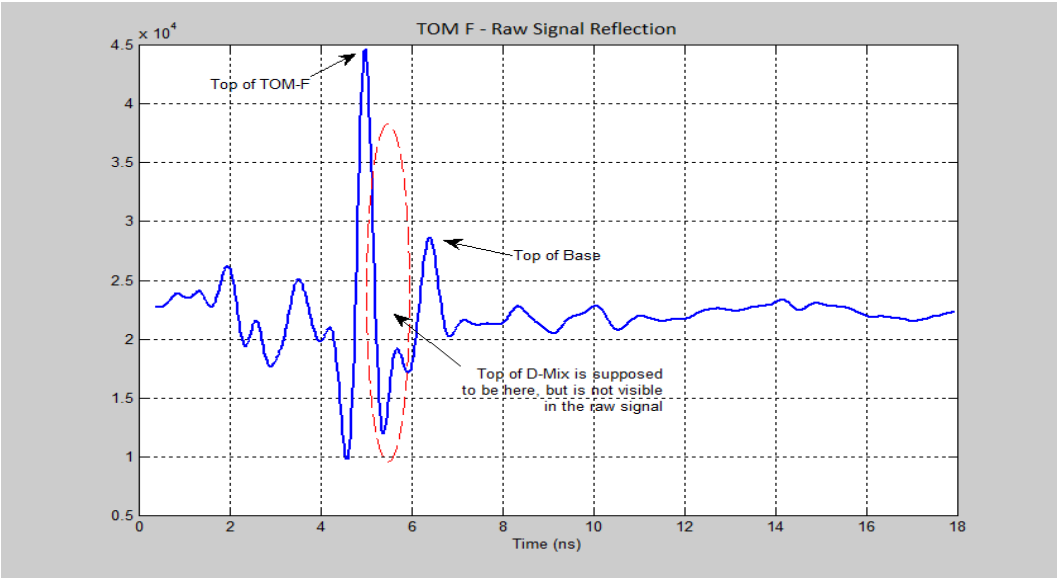

Figure 9.5 A-scan signal without Thin-Layer Subtraction

Figure 9.6 presents the signal after the thin-layer subtraction. From the plot the interface of the bottom of the TOM-F / top of the D Mix layers is visible.

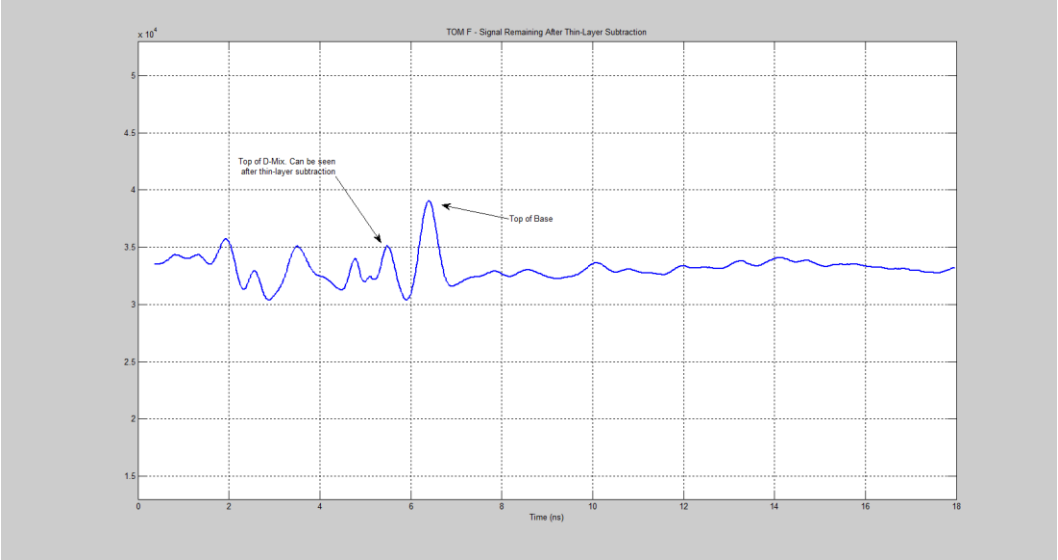

Figure 9.6 A-scan signal after Thin-layer Subtraction

To perform the signal analysis, a new signal is formed that combines the original signal and the thin-layer subtracted signal. The beginning part of the original signal is used up to the surface reflection, and then combined with the thin-layer subtracted signal after the surface reflection as shown in Figure 9.7.

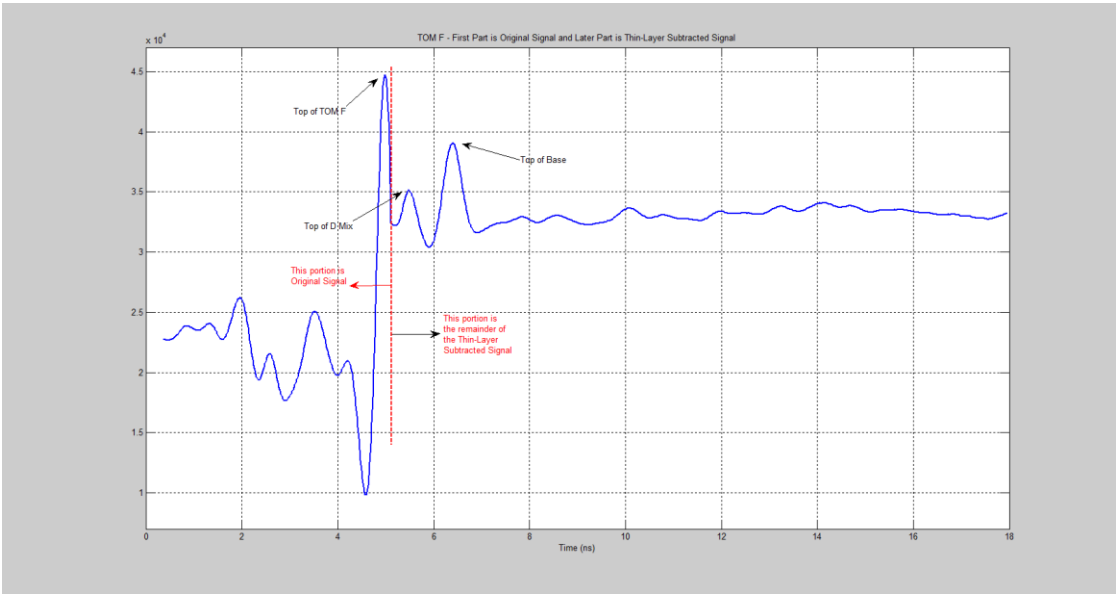

Figure 9.7 A-scan signal - Part of Surface Reflection and Thin-layer Subtracted Signal

Figure 9.7 contains both the surface reflection from the original signal and the remaining part of the signal from the thin-layer subtraction. From this signal the top of the TOM-F layer, the top of the D-Mix layer, and the top of the base layer are visible.

Thickness and Dielectric Constant Calculations

To calculate the thickness, the dielectric constant of each layer needs to be calculated first. The dielectric constant, ε, for a layer is calculated using these formulae,

$$\varepsilon_i = \varepsilon_{i-1} \times \left(\frac{1+\rho}{1-\rho}\right)^2 \tag{9.2}$$

where i – Layer number

when i = 0 the layer is air, the ε_0 = 1.0

$$\rho_i = \frac{k_a \times \frac{A_i}{IA}}{T_i} \tag{9.3}$$

where ρ_i – Reflection coefficient, k_a – Calibration amplitude correction factor, A_i – Layer amplitude, *IA* – Incident amplitude

$$T_i = T_{i-1} \times \frac{4 \times \sqrt{\varepsilon_{i-1} \times \varepsilon_i}}{\left(\sqrt{\varepsilon_{i-1}} + \sqrt{\varepsilon_i}\right)^2} \tag{9.4}$$

where T_i – Transmission coefficient

When i = 1, T_1 = 1.0, the thickness of the layers is calculated using this formula,

$$Thickness = 5.9 \times \frac{(\Delta t + k_t)}{\sqrt{\varepsilon_i}} \tag{9.5}$$

where, $Thickness$, in inches, Δt – Time delay, in nano-seconds, k_t – Calibration time correction factor

The correction factors k_t and k_a are calculated using a ground-truth thickness from a core, with the GPR signal having been recorded over the core location. The correction factor k_t

is usually needed to be used for pavements with thin surface layers. The reason for the correction factor is the overlapping of the signal reflections will affect time delay by a factor, which is caused by the variations in the slopes of the signal reflections.

9.2.2. Dielectric Constant Scans

Figures 9.8, 9.9, 9.10, 9.11 and 9.12 illustrate the dielectric constant results from each layer at the RELLIS site. With further processing in coordination with the mechanics-based models, these contour plots will be transformed into outputs of modulus or density.

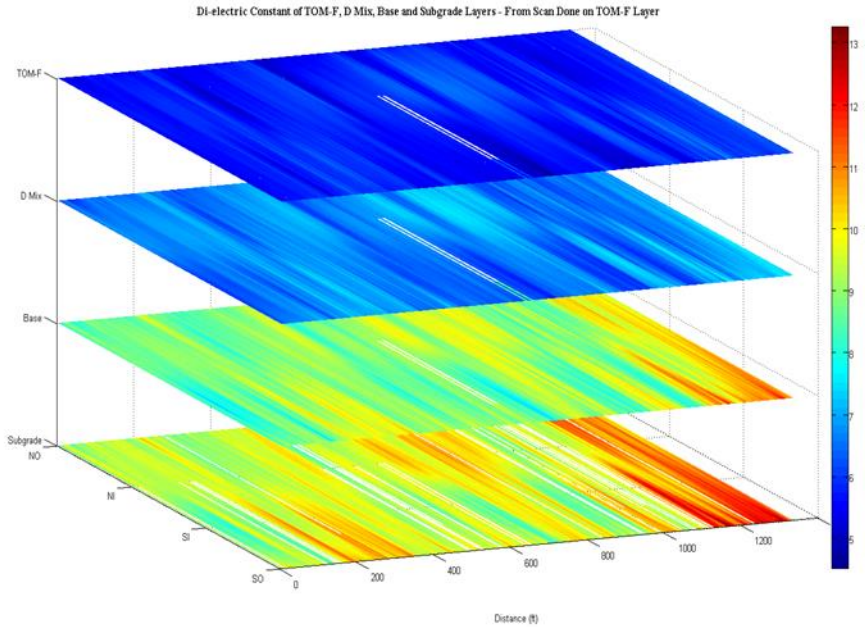

Figure 9.8 Dielectric Constants - TOM-F, D Mix, Base and Subgrade Layers – Flexible

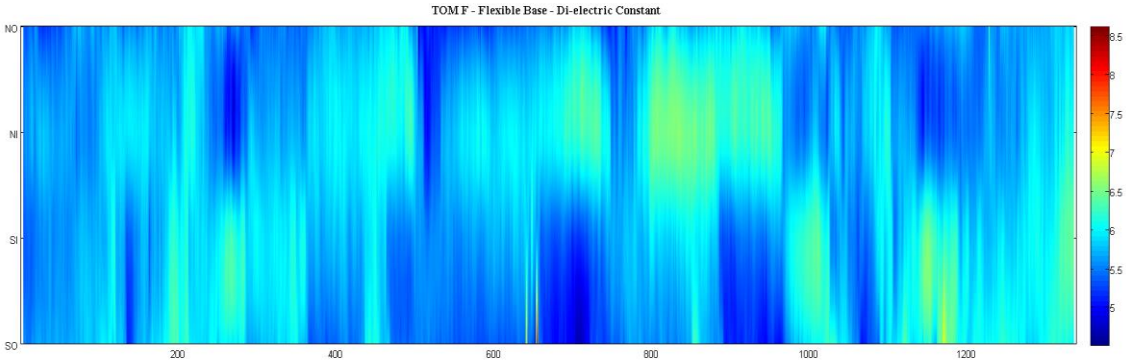

Figure 9.9 Dielectric Constant - TOM-F Layer – Flexible

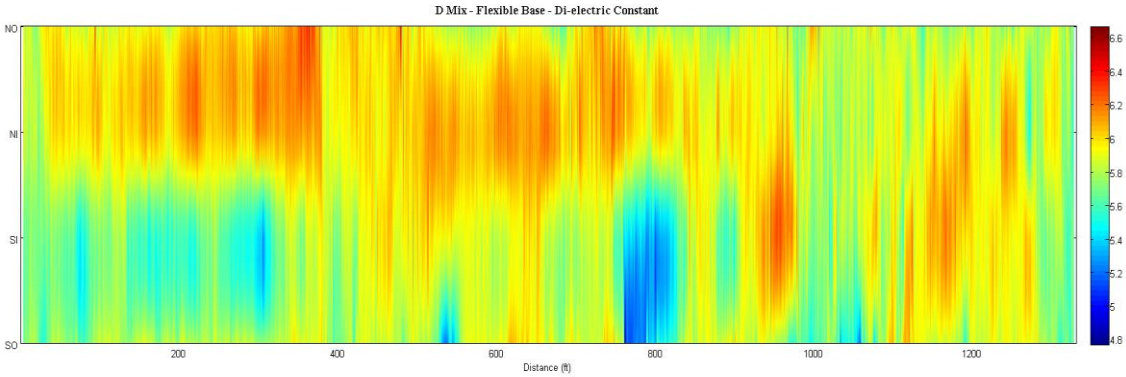

Figure 9.10 Dielectric Constant - D Mix Layer – Flexible

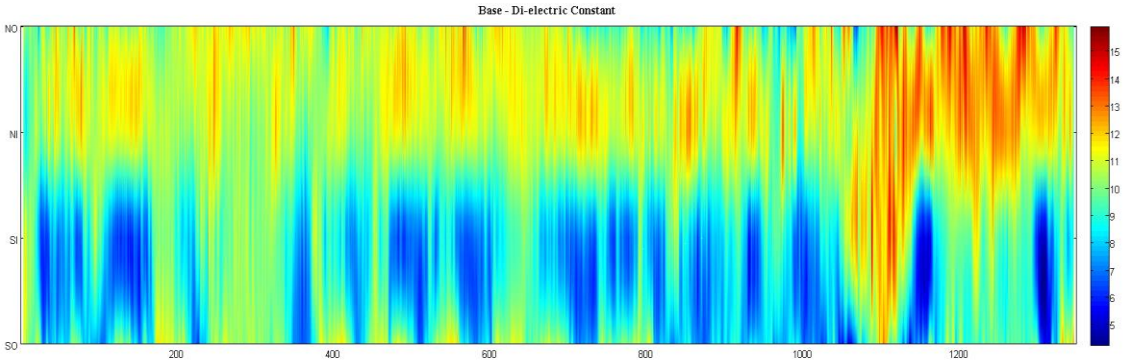

Figure 9.11 Dielectric Constant - Base Layer

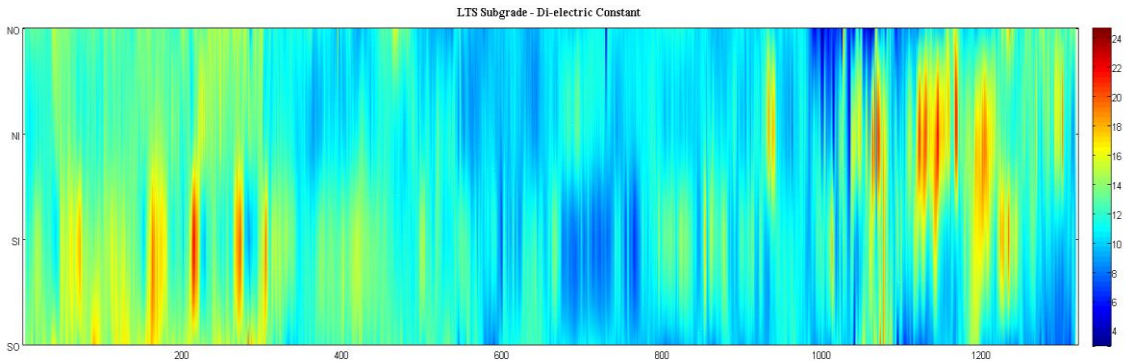

Figure 9.12 Dielectric Constant - Subgrade Layer

9.2.3. Thickness Calculations

Figures 9.13, 9.14, 9.15, and 9.16 present the thickness calculations from the GPR. These results illustrate how, if desired, GPR may also be able to provide near full-coverage assessment of constructed layer thickness for quality acceptance.

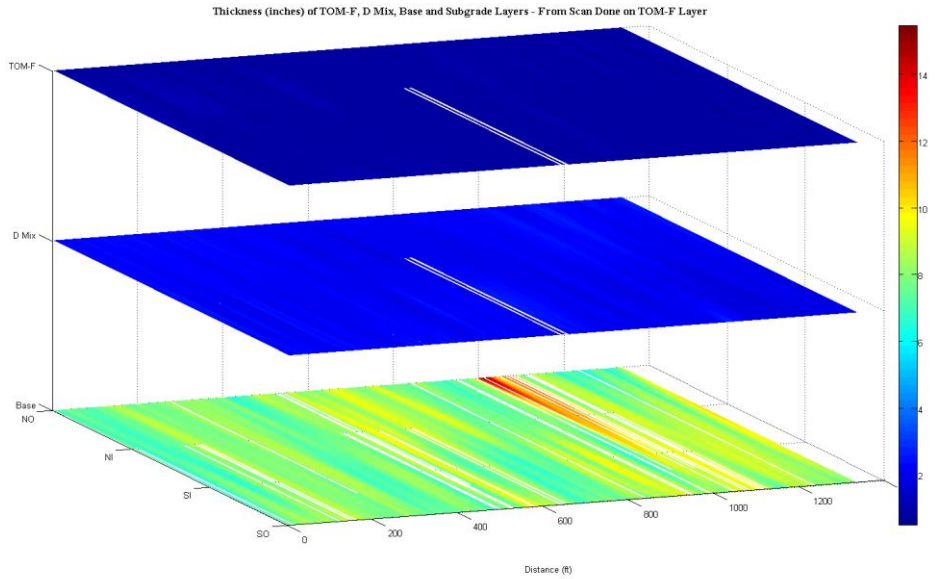

Figure 9.13 Thickness - TOM-F, D Mix and Base Layers – Flexible

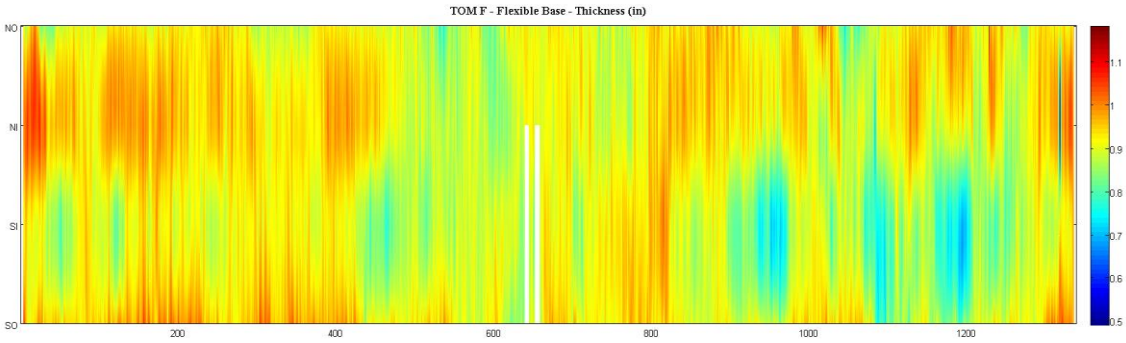

Figure 9.14 Thickness - TOM-F Layer – Flexible

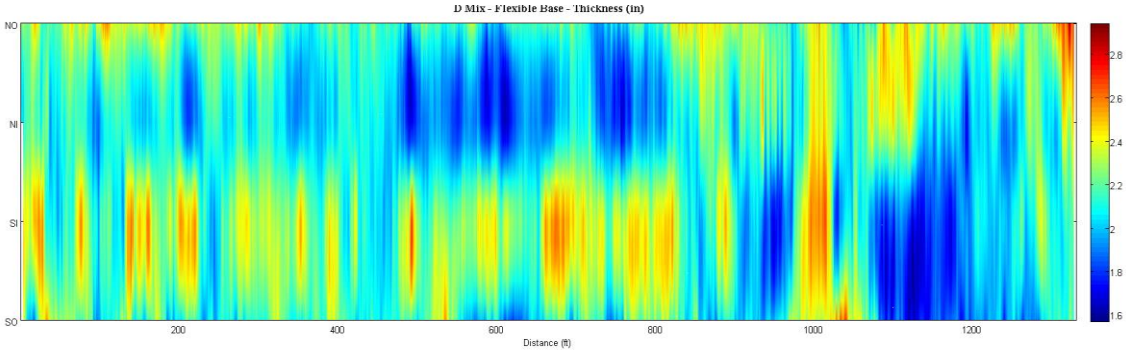

Figure 9.15 Thickness - D Mix Layer – Flexible

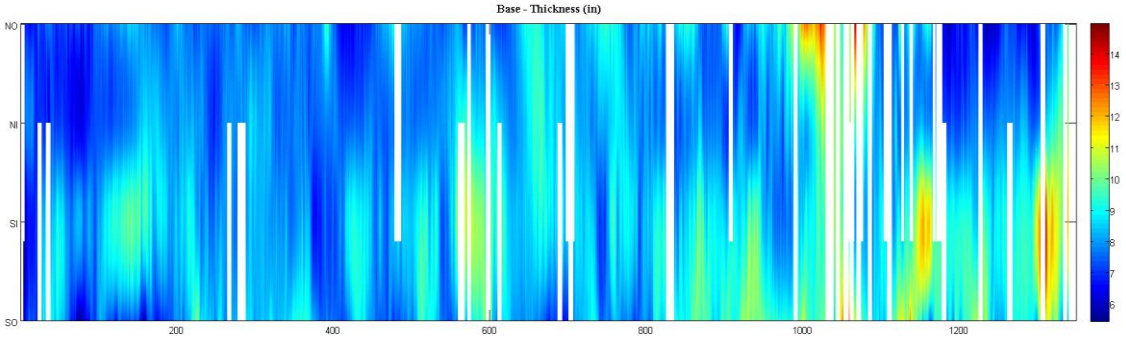

Figure 9.16 Thickness - Base Layer – Flexible

Using the laboratory characterization of base materials and putting the results in PaveSCM software the water content and the matric suction will be determined and therefore MR profile of the base layer will be plotted in the LayerMapp software with the help of dielectric constant and thickness scans.

10. CONCLUSIONS AND RECOMMENDATIONS

10.1. Conclusions

This study proposed several enhancements to the Pavement ME Design with the purpose of increasing the sensitivity of pavement performance to base layers and subgrade. These enhancements include: (a) ANN models to predict the SWCC by using the soil physical properties and climatic parameters; (b) a mechanistic-empirical model to predict the equilibrium soil moisture suction beneath pavement for each of the AASHTO soil classes of base course and subgrade soils (c) ANN models to predict the stress and moisture-dependent resilient modulus (M_R); (d) regression models to predict the coefficients of the suction dependent shear strength and permanent deformation model; (e) a modified modulus of subgrade reaction (k) model that considered the cross anisotropy of the base material and the shear interaction between the PCC slab and the base course.

In the later part of this study, the effect of the proposed models were evaluated on pavement performance. The sensitivity of moisture, degree of bonding and tire speed were quantified on the rutting, fatigue cracking (top-down and bottom-up) and faulting performance using the developed models and compared with the predicted performance using Pavement ME design models.

To improve the construction quality of pavement layers, a rapid non-destructive approach was also evaluated. Ground penetrating radar signals were utilized to generate the dielectric constant and electrical conductivity profiles of underlying layers and further used to estimate M_R and percent of stabilizer with the help of specific laboratory characterization.

10.1.1. Soil Water Characteristics Curve of Base and Subgrade soils

- Two three-layered neural network architectures consisting of one input layer, one hidden layer and one output layer were constructed for plastic and non-plastic soil, respectively. The input variables for plastic soil include the material percent passing the No.4 sieve, material percent passing the No.200 sieve, liquid limit(*LL*), plasticity index(*PI*), saturated volumetric water content and local mean annual air temperature (*MAAT*). The input variables for non-plastic soil are particle diameter corresponding to 30 percent, 60 percent and 90 percent passing of material (D_{30}, D_{60}, D_{90}), gradation scale parameters (Θ), gradation shape parameter (Ψ), saturated volumetric water content and local *MAAT*. The hidden layer assigns 20 neurons. A total of 3600 plastic soil and 250 non-plastic soil data collected from the NCHRP 9-23A project were used to develop the ANN models.
- Compared to the existing prediction models, such as the Zapata model, and the Perera model , the developed ANN models had the highest accuracy (e.g., smallest *RMSE* and highest R^2 values) to predict the SWCC fitting parameters in the Fredlund-Xing equation. The developed ANN models can accurately estimate the matric suction of soil at any given saturation level. The obtained R^2 values were 0.95 and 0.91 for plastic and non-plastic soils, respectively.
- The prediction accuracy of the developed ANN models were validated by two data sources, i.e., test data from the NCHRP 9-23A database and independent data from other literature sources. The comparison of model-predicted matric suction values to the measured ones validates that the developed ANN models are capable of accurately predicting the SWCCs for both plastic and non-plastic soils.

10.1.2. Equilibrium Suction Prediction Model for Subgrade Soil

- A GIS based TMI contour map of the continental United States was developed using precipitation and temperature data collected from the PRISM (Parameter-elevation Regressions on Independent Slopes Model) Climate Group. The contour map of TMI was validated by comparing the values for specific locations with the original TMI map.
- A mechanistic-empirical model to determine equilibrium suction was developed in this study based on Mitchell's steady state diffusivity equation and a functional relationship between TMI and mean annual moisture depth.
- A GIS based equilibrium suction contour map of the continental United States was generated by calculating the values for all map units using the mechanistic-empirical approach developed.
- A simplified regression model was developed to predict equilibrium suction from readily available and influential parameters such as TMI, plasticity index and the dry suction value.

10.1.3. Resilient Modulus Model of Base Materials

- Two three-layered ANN models were developed for plastic and non-plastic base materials respectively. Input variables for plastic and non-plastic soil included material percent passing 3/8" sieve, material percent passing no. 200 sieve, plastic limit, plasticity index, maximum dry density, optimum moisture content and test moisture content. The output variables are the three coefficients k_1, k_2 and k_3 of the resilient modulus model.
- The developed ANN models showed a higher prediction accuracy compared to the three

regression models selected from the existing literature. The ANN models can accurately estimate the resilient modulus of base materials at any stress level. The obtained R^2 values are 0.91 and 0.90 for plastic and non-plastic base materials, respectively.

- The ANN models do not provide any insight into the complex relationship between the M_R model coefficients and the base physical properties. Thus, it is not recommended to use as a prediction tool for the values that are out of the range of the training dataset. In this study, a large dataset of 779 base materials were collected from the LTPP database and hence provided a wide range of input properties.
- The developed ANN models were validated using the resilient modulus test data from different sources. The R^2 value between the measured and predicted validation resilient modulus values was 0.8.

10.1.4. Shear Strength and Permanent Deformation Prediction Model

- To improve the predictability of the mechanistic-empirical permanent deformation model, a new set of prediction models were developed for shear strength model coefficients (c' and φ') and permanent deformation model coefficients (ϵ0, ρ, β, m and n). In addition to the repeated and monotonic load triaxial test data, soil physical properties such as gradation, Atterberg limits, dry density and moisture content data were also collected for corresponding base and subgrade materials
- Two different sets of prediction models were developed for shear strength model coefficients of unbound base and subgrade respectively. Regression analysis was conducted to determine the relationships between the shear strength model parameters and the collected physical properties of unbound base materials. R^2 value of 0.81 and

0.87 for c' and φ' parameters respectively indicate that the regression equations had a good prediction accuracy. Similarly, an empirical correlation was used to define the φ' parameter and an ANN model was developed to predict the cohesion parameter from subgrade physical and strength properties. The obtained R^2 value 0.98 and 0.97 for training and validation dataset demonstrated the prediction accuracy of the c' parameter.

- Regression analysis was conducted to determine the prediction models of the permanent deformation model coefficients for unbound base materials. The predicted coefficients showed a good match with the measured values.

10.1.5. Modulus of Subgrade Reaction for Rigid Pavements

- A slab-base interface shear bonding submodel was developed based on the shear strength properties of the base course, c and ϕ . Depending on the degree of bonding in the slab-base interface, the equivalent section and the altered deflection basin, which further affected the modified *k*-value.
- The estimated degree of bonding values were compared with the previously developed "backcalculated best-fit (BBF)" approach bonding condition. In the BBF approach, the slab-base interface is only considered as a non-bonded or fully bonded condition. However, this study found that most of the treated base layers were either in a fully bonded or partially bonded condition and the unbound base layers were mostly partially bonded.
- Modified *k*-values were compared with the BBF *k*-values. Significant changes in the *k*-values were observed due to the base modulus and interface bonding corrections.

Modified k-values were compared with the BBF k-values. Significant changes in the k-values were observed due to the base modulus and interface bonding corrections. The BBF approach has higher k-value than the modified model due to the difference in interface bonding ratios. The BBF interface bonding between slab and base is considered fully bonded for most of the cases while the modified k-value model considered partially bonded conditions.

- A three-layered ANN model was constructed to predict the modified *k*-value, which included one input layer, one hidden layer and an output layer. The FWD deflection basins were computed using a finite element program. The developed ANN model was validated by comparing the prediction results with the calculated modified *k*-values from the LTPP pavement sections. The obtained R^2 value of 0.92 indicated that the developed models had a desirable accuracy in the prediction of the modified *k*-value. A sensitivity analysis was conducted to evaluate the effect of the degree of bonding on *k*-value. The results showed that, in general, a higher degree of bonding produces a higher modified *k*-value.

10.1.6. Prediction of Pavement Performance and Sensitivity Analysis

- As the moisture content increases in the base layer, the load repetitions to the fatigue cracking reduces. The rut depth in the base layer shows an increasing trend with the moisture content, while such trend is not as obvious as with the fatigue cracking.
- The ANN model for k-value was used to evaluate the sensitivity of moisture and degree of bonding using the proposed models. The sensitivity of the modified k-values to

moisture and degree of bonding was found to be improved significantly compared to the existing Pavement ME Design k-values. The sensitivity of moisture increased for all selected pavement sections due to the inclusion of the suction effect in the M_R model. However, the effect of the degree of bonding is same for the modified k-value and Pavement ME Design k-value when there is either fully bonded or no bond condition in slab-base interface. But the developed ANN model can predict the k-value for the partially bonded condition as well.

- To study the effect of moisture and degree of bonding on pavement performance, tensile stress at the top and bottom of the slab and differential deflection across the transverse joint were evaluated. The sensitivity of moisture and degree of bonding were calculated using the proposed M_R and modified k-value model and compared with the results from Pavement ME Design M_R and k-values. The M_R values using the proposed model and the corresponding modified k-values from the ANN model showed much higher sensitivity on calculated stress and deflections compared to the results from Pavement ME Design models.

10.1.7. Prediction of Percentage of Stabilizer in Base Layer

- A mechanistic-empirical correlation model was developed to predict the molar concentration in stabilized base pore water solution based on electrical conductivity and evaporable volumetric water content. Predicted molar concentration was compared with the basic concentration of cement ions in soil pore water solution collected from the literature and a reasonably good match was observed. A proportional relationship can be established further between molar concentration of salt ions and percentage of stabilizer

in the base material.

- An expression of electrical conductivity was derived from parallel and perpendicular polarization of GPR signal waves. Therefore, the stabilizer content in the base can be directly estimated in the field using the GPR signals and the laboratory based correlation model between electrical conductivity and the percentage of stabilizer.

10.1.8. Determination of Base Modulus using Ground Penetrating Radar wave

- A mechanistic based non-destructive (NDT) approach was established developed to determine the resilient modulus (M_R) profile of flexible base. The ground penetrating radar (GPR) signals were analyzed by the PaveSCM software to obtain the dielectric constant profile. The dielectric constant data was input into the LayerMAPP software in addition to the laboratory characterize soil-water characteristics curve (SWCC) and suction-dielectric characteristics curve (SDCC) and estimated the M_R of in-situ base.
- A new preprocessing approach of the raw GPR scans was undertaken before using dielectric constant readings in PaveSCM software. The preprocessing steps include filtering of radar signals, surface normalization, height variation correction of signal amplitude and thin-layer subtraction.

10.2. Recommendations for Future Research

There are several items of future work that emerge from the work that has been accomplished in this study including the following:

- Replace the models that are currently in the Pavement ME Design software by those that have been developed in this study.
- Incorporate the equilibrium suction contour map of the US that have been developed in

this study into the Pavement ME Design software.

- Develop new relationships to characterize the properties of stabilized base course materials as they are controlled and affected by the soil moisture suction.
- Validate the GPR based approach that has been proposed in this study to predict the base modulus and stabilizer content using in-situ field data.

REFERENCES

AASHTO. (2008). Mechanistic-empirical pavement design guide: A manual of practice. AASHTO Designation: MEPDG-1, Washington, D.C.

Adu-Osei, A., Little, D., and Lytton, R. L. (2001). Cross-anisotropic characterization of unbound granular materials. Transportation Research Record: Journal of the Transportation Research Board, 1757, 82-91.

Aitchison, G.D., Richards, B.G., (1965). A broad scale study of moisture conditions in pavement subgrades throughout Australia. In Moisture equilibria and moisture changes in soil beneath covered areas, Sydney, Butterworths, 184-232.

Al-Qadi, I. L., Elseifi, M. A., and Yoo, P. J. (2004). Pavement Damage due to Different Tire and Vehicle Configurations. Report to the Virginia Tech Transportation Institute, Virginia Polytechnic Institute and State University, Blacksburg, VA.

Al-Qadi, I. L., Wang, H., Yoo, P. J., Dessouky, S. H. (2008). Dynamic analysis and in situ validation of perpetual pavement response to vehicular loading. Transportation Research Record 2087, 29-39.

Al-Qadi, I.L., H. Wang, and E. Tutumluer. (2010). Dynamic Analysis of Thin Asphalt Pavements by Using Cross-Anisotropic Stress-Dependent Properties for Granular Layer. In *Transportation Research Record: Journal of the Transportation Research Board*, 2154(1), 156–163.

Annan, A.P. (2003). Ground Penetrating Radar: GPR Principles, Procedures & Applications. Sensors & Software Inc., Technical Paper, Mississauga, ON, Canada.

ARA, Inc. (2004). Guide for Mechanistic-Empirical Design of New and Rehabilitated Pavement Structure. Draft Final Report 1-37A, National Cooperative Highway Research Program, Transportation Research Board, Washington, DC.

AS2870-2011, Standards Australia, (2011). Residential slabs and footings. Sydney.

Asphalt Institute. (1981). Thickness design-asphalt pavements for highways and streets (No. 1). Asphalt Institute.

Aubertin, M., Mbonimpa, M., Bussière, B. and Chapuis, R.P. (2003). A model to predict the water retention curve from basic geotechnical properties. Canadian Geotechnical Journal, 40(6), 1104-1122.

Balanis, C. A. (2012). Advanced engineering electromagnetics. 2nd Edition, John Wiley & Sons, Inc.

Balmer, G. G. (1958). Shear strength and elastic properties of soil-cement mixtures under triaxial loading. Retrieved from Portland Cement Association Research and Development Laboratories.

Bari, M. E., Zollinger, D.G., and Jung, Y.S. (2013). Modeling and calibration of concrete slab interfacial effects. TRB 2013 Annual Meeting Compendium of Papers, Transportation Research Board, Washington, D.C.

Basile, A., and D'Urso, G. (1997). Experimental corrections of simplified methods for predicting water retention curves in clay-loamy soils from particle-size determination. Soil Technology, 10(3), 261 -272.

Basma, A.A., Al-Suleiman, T.I., (1991). Climatic Consideration in New AASHTO Flexible Pavement Design. Journal of Transportation Engineering. 117(2), 210–223.

Biot, M. (1922). Bending of an infinite beam on an elastic foundation. Journal of Applied Mathematics and Mechanics, 2(3), 165-184.

Boussinesq, J. (1885). Application des potentiels à l'étude de l'équilibre et du mouvement des solides élastiques: Gauthier-Villars.

Brown, S.F. (1996). Soil Mechanics in Pavement Engineering. *Geotechnique,* 46(3), 383–426.

Brunsell, N.A., Gillies, R.R., (2003). Scale issues in land–atmosphere interactions: A review, with implications for remote sensing of the surface energy balance. Agricultural and Forest Meteorology 117, 203–221.

Bulut, R., R. L. Lytton, and W. K. Wray. (2001). Soil Suction Measurement by Filter Paper. Geotechnical Special Publication 115. American Society of Civil Engineers, New York.

Bulut, R. and, Nevels, J., (2018). Influence of maximum water storage on thornthwaite moisture index. Proceedings of Second PanAm Unsaturated Soils, Dallas, Texas.

Cameron, D.A., (2001). The extent of soil desiccation near trees in a semi-arid environment. In: Toll DG (ed) Unsaturated soil concepts and their application in geotechnical practice, Dordrecht, Kluwer Academic, 357–370.

Carpenter, S.H., Lytton, R.L., Epps, J.A., (1974). Environmental factors related to pavement cracking in west Texas. Research Report No. 18-1, Texas Transportation Institute, College Station, Texas.

Cary, C., and C. Zapata. (2011). Resilient modulus for unsaturated unbound materials. Road Materials and Pavement Design, 12(3), 615-638.

Cetin, A., Kaya, Z., Cetin, B., and Aydilek, A. H. (2014a). Influence of compaction method on mechanical properties of unbound granular materials. Road Materials and Pavement Design, Vol. 15, No. 1, pp. 220–235.

Ceylan, H., Gopalakrishnan, K., and Lytton, R. (2011). Neural networks modeling of stress growth in asphalt overlays due to load and thermal effects during reflection cracking. Journal of Materials in Civil Engineering, ASCE, 23 (3), 221-229.

Chen, Y., and Lytton, R. (2019). Development of a new faulting model in jointed concrete pavement using LTPP data. Transportation Research Record: Journal of the Transportation research Board, 0361198119838988.

Chow, L.C., Mishra, D. and Turumluer, E. (2014). Aggregate base course material testing and rutting model development. Final Report NCDOT Project 2013-18, FHWA/NC/2013-18

Clough, G. W., Sitar, N., Bachus, R. C., & Rad, N. S. (1981). Cemented sands under static loading. Journal of Geotechnical and Geoenvironmental Engineering, ASCE, 107(GT6), 799-817.

Coleman, J.D., (1965). Geology, climate and vegetation as factors affecting soil moisture. Moisture equilibria and moisture changes in soils beneath covered areas, Sydney, Butterworths, 93-99.

Coleri, E., M. Guler, A. Gungor, and J. Harvey (2010). Prediction of subgrade resilient modulus using genetic algorithm and curve-shifting methodology: alternative to nonlinear constitutive models. Transportation Research Record: Journal of the Transportation Research Board, No. 2170, 64-73.

Croney, D. (1977). The design and performance of road pavements. Transport and road research laboratory, HMSO, U.K.

Daly, C., Gibson, W.P., Taylor, G.H., Johnson, G.L., Pasteris, P., (2002). A knowledge-based approach to the statistical mapping of climate. Climate Research 22, 99-113.

Daly, C., Halbleib, M., Smith, J.I., Gibson, W.P., Doggett, M.K., Taylor, G.H., Curtis, J., Pasteris, P.A., (2008). Physiographically-sensitive mapping of temperature and precipitation across the conterminous United States. International Journal of Climatology 28, 2031-2064.

Daly, C., Neilson, R.P., Phillips, D.L., (1994). A Statistical-Topographic Model for Mapping Climatological Precipitation over Mountanious Terrain. Journal of Appl. Meteorology 33, 140-158.

Delatte, N. J., Jr., Wade, D. M., and Fowler, D. W. (2000). Laboratory and field testing of concrete bond development for expedited bonded concrete overlays. ACI Materials Journal, 97(3), 272-280.

Edil, T., C. Benson, and A. Sawangsuriya. (2006). Interim Report to University of Minnesota: Resilient Behavior of Unsaturated Subgrade Soils. University of Wisconsin–Madison.

Edris, E.V., Lytton, R.L., (1976). Dynamic properties of subgrade soils including environmental effects. Research Report No. TTI-2-18-74-164-3, Texas Transportation Institute, College Station, Texas.

El-Keshky, M. (2011). Temperature Effect on the Soil Water Retention Characteristic. MS thesis, Arizona State University.

Epps, Jon A., S. Sebesta, B. Hewes, H. Sahin, R. Luo, J. W. Button, R. L. Lytton, C. A. Herrera, R. Hatcher, and F. Gu. (2014). Report No. FHWA/TX-13/0-6621: Development of a specification for flexible base construction. Texas A & M Transportation Institute.

Fang, H., Hand, A.J., Haddock, J.E., White, T.D. (2007). An object-oriented framework for finite element pavement analysis. Advances in Engineering Software 38, 763-771.

Farouk, H., and Farouk, M. (2014a). Calculation of subgrade reaction modulus considering the footing-soil system rigidity." Proc., 2nd Int. Conf. on Vulnerability and Risk Analysis and Management (ICVRAM)

Federal Highway Administration. (2001). Backcalculation of Layer Parameters for LTPP Test Sections- Slab on Elastic Solid and Slab on Dense-Liquid Foundation Analysis of Rigid Pavements. Publication No. FHWA-RD-00-086, Washington, D.C.

Fernando, E. G., J. Oh, D. Ryu, and S. Nazarian. (2008). Consideration of Regional Variations in Climatic and soil Conditions in the Modified Triaxial Design Method. Research Report 0-4519-2, Texas Transportation Institute, Texas A&M University System, College Station, Texas.

Filonenko-Borodich, M. (1940). Some approximate theories of elastic foundation. Uchenyie Zapiski Moskovkogo Gosudarstuennogo Universiteta Mekhanika, Moscow, 46, 3-18.

Findley, W. N., Lai, J. S., Onaran, K., and Christensen, R. M. (1977). Creep and Relaxation of Nonlinear Viscoelastic Materials with an Introduction to Linear Viscoelasticity. *Journal of Applied Mechanics*, 44, 364.

Fityus, S., Buzzi, O., (2008). On the use of the Thornthwaite Moisture Index to infer depths of seasonal moisture change, Australian Geomechanic 43, 69-76.

Flintsch, G. W. (2003). Ssoft computing applications in pavement and infrastructure management: state-of-the-art. CD-ROM Proceedings of the 82nd Annual Meeting of the Transportation Research Board, National Research Council. Washington D.C.

Flood, I., and Kartam, N. (1994). Neural networks in civil engineering. II: Systems and application. Journal of Computing in Civil Engineering, 2(8), 149-162.

FPA, (2017). Design procedure for drilled concrete piers in expansive soil. Document No. FPA-SC-16-0, Houston, Texas.

Fredlund, D. G., and Rahardjo, H. (1993). Soil mechanics for unsaturated soils. New York: John Wiley & Sons.

Fredlund, D. G., and Xing, A. (1994). Equations for the Soil–Water Characteristic Curve. Canadian Geotechnical Journal, 31(3), 521-532.

Fredlund, M., Fredlund, D., and Wilson, G. (1997). Prediction of the soil-water characteristic curve from grain-size distribution and volume-mass properties. Proceedings of the Third Brazilian Symposium on Unsaturated Soils.

Gay, D.A., (1994). Development of a predictive model for pavement roughness on expansive clay. PhD dissertation, Texas A&M University, College Station, Texas.

Glasser, F. P., and Marr, J. (1984). The effect of mineral additives on the composition of cement pore fluids. Proceedings of British Ceramic Society, 35:419.

Gruber, P., and Sharp, R. S. (2012). Shear forces in the contact patch of a braked-racing tyre. Vehicle System Dynamics, 50(12), 1761–1778

Gu, F., H. Sahin, X. Luo, R. Luo, and R. L. Lytton. (2014). Estimation of resilient modulus of unbound aggregates using performance-related base course properties. Journal of Materials in Civil Engineering, 27, (6), p. 04014188.

Gu, F., Zhang, Y.Q., Droddy, C.V., Luo, R. and Lytton, R.L. (2015). Development of a New Mechanistic-Empirical Rutting Model for Unbound Granular Material." Journal of Materials in Civil Engineering, 28(8).

Gu, F., Luo, X., Luo, R., Lytton, R., Hajj, E., and Siddharthan, R. (2016). Numerical modeling of geogrid-reinforced flexible pavement and corresponding validation using large-scale tank test. Construction and Building Materials, 122, 214-230.

Gu, F., Luo, X., Zhang, Y., Chen, Y., Luo, R., & Lytton, R. L. (2017). Prediction of geogrid-reinforced flexible pavement performance using artificial neural network approach. Road Materials and Pavement Design, 1-17.

Gu, F., Luo, X., Zhang, Y., Lytton, R. L., and Sahin, H. (2016a). Modeling of Unsaturated Granular Materials in Flexible Pavements. E3S Web of Conferences, 9, p. 20002.

Gupta, S. C., Ranaivoson, A., Edil, T. B., Benson, C. H., and Sawangsuriya, A. (2007). Pavement design using unsaturated soil technology. St. Paul: Minnesota Department of Transportation.

Gupta, S., and Larson, W. (1979). Estimating soil-water retention characteristics from particle size distribution, organic matter percent, and bulk density. Water Resources Research, 6 (15), 1633–1635.

Haghverdi, A., Cornelis, W.M. and Ghahraman, B. (2012). A pseudo-continuous neural network approach for developing water retention pedotransfer functions with limited data. Journal of Hydrology, 442, 46-54

Hall, K. T. (1991). Performance, Evaluation, and Rehabilitation of Asphalt-Overlaid Concrete Pavement, Ph.D. Dissertation, University of Illinois, Urbana, Illinois.

Han, Z., and Vanapalli, S. K. (2015). Model for predicting the resilient modulus of unsaturated subgrade soil using the soil-water characteristic curve. Canadian Geotechnical Journal, 10(52), 1605-1619.

Heath, A. C., J. M. Pestana, J. T. Harvey, and M. O. Bejerano. (2004). Normalizing behavior of unsaturated granular pavement materials. Journal of Geotechnical and Geoenvironmental Engineering, 130(9), 896–904.

Hernandez, J. (2010). Evaluation of the Response of Perpetual Pavement at Accelerated Pavement Loading Facility: Finite Element Analysis and Experimental Investigation.

Hetényi, M. (1971). Beams on elastic foundation: theory with applications in the fields of civil and mechanical engineering, University of Michigan, Ann Arbor.

Hoffman, M. S., and Thompson, M. R. (1981). Mechanistic Interpretation of Nondestruction Pavement Testing Deflection, Civil Engineering Studies, Transportation Engineering Series No. 32, Illinois Cooperative Highway and Transportation Research Series No. 190, University of Illinois, Urbana, Illinois.

Holtz, R.D., and Kovacs. W.D. (1981). An Introduction to Geotechnical Engineering. PrenticeHall, Englewood Cliffs, NJ.

Horvath, J. S. (1983). New subgrade model applied to mat foundations. Journal of Geotechnical Engineering, 109(12), 1567-1587.

Huang, Y. H. (1993). Pavement analysis and design. Prentice-Hall, Englewood Cliffs, NJ.

Hutson, J., and Cass, A. (1987). Soil Science Journal. A retentivity function for use in soil water simulation models, 1(38), 105-113.

Iancu-Bogdan, T. and Vasile, M. (2010). The Modified Vlasov Foundation Model: An Attractive Approach for Beams Resting on Elastic Supports. EJGE, Vol.15.

Islam, S., Sufian, A., Hossain, M., Miller, R., and Leibrock, C. (2018). Mechanistic-Empirical design of perpetual pavement. Road Materials and Pavement Design, 1-14.

Islam, S., Hossain, M., Jones, C. A., Bose, A., Barrett, R., Velasquez Jr, N. (2019). Implementation of AASHTOWare Pavement ME Design Software for Asphalt Pavements in Kansas. Transportation Research Record, 0361198119835540.

Jain, S.K., Singh, V.P. and Van Genuchten, M.T. (2004). Analysis of soil water retention data using artificial neural networks. Journal of Hydrologic Engineering, 9(5), 415-420.

Jana, R.B., Mohanty, B.P. and Springer, E.P. (2007). Multiscale pedotransfer functions for soil water retention. Vadose Zone Journal, 6(4), 868-878.

Jayatilaka, R., Gay, D.A., Lytton, R.L., Wray, W.K., (1992). Effectiveness of Controlling Pavement Roughness due to Expansive Clays with Vertical Moisture Barriers. Research Report No. FHWA/TX-92/1165-2F, Texas Transportation Institute, Texas A&M University, Texas Department of Transportation, Austin, TX.

Jeong, J., and Zollinger, D. G. (2001). Characterization of stiffness parameters in design of continuously reinforced and jointed pavements. Transportation Research Record: Journal of the Transportation Research Board, 1778, 54-63.

Ji, R., N. Siddiki, T. Nantung and D. Kim. (2014). Evaluation of resilient modulus of subgrade and base materials in Indiana and its implementation in MEPDG. The Scientific World Journal.

Johari, A., and Javadi, A. A. (2010). Prediction of soil-water characteristic curve using neural network. Proceedings of the Fifth International Conference on Unsaturated Soils, 1, pp. 461-466. Barcelona.

Juarez-Badillo, E., (1975). Constitutive relationships for soil. Proc. Symposium on recent developments in the analysis of soil behavior and their applications to geotechnical structures, The University of New South Wales, Kensington, Australia, 231-257.

Jung, Y. S., and Zollinger, D. G. (2011). New laboratory-based mechanistic-empirical model for faulting in jointed concrete pavement. Transportation Research Record: Journal of the Transportation Research Board, 2226(1), 60-70.

Kalcheff, I. V., and Hicks, R. G. 1973. A Test Procedure for Determining the Resilient Properties of Granular Materials. *Journal of Testing and Evaluation,* 1(6), 472-479.

Khavassefat, P., Jelagin, D., Birgisson, B. (2012). A computational framework for viscoelastic analysis of flexible pavements under moving loads. Materials and Structures 45, 1655-1671

Khoury, N.N., Zaman, M.M., (2004). Correlation between Resilient Modulus, Moisture Variation, and Soil Suction for Subgrade Soils. Transportation research record: Journal of the Transportation Research Board, No. 1874, 99-107.

Kim, S. H. (2004). Prediction of level of anisotropy of aggregates based on gradation, shape, form, and textural properties. Ph.D. dissertation, Texas A&M Univ., College Station, Texas.

Kim, S.H., J. Yang, and J. H. Jeong. (2014). Prediction of subgrade resilient modulus using artificial neural network. KSCE Journal of Civil Engineering, 18(5), 1372-1379.

Koekkoek, E., and Booltink, H. (1999). Neural network models to predict soil water retention. European Journal of Soil Science, 50, 489-495.

Lawrence, M., & Petterson, A. (1993). Brainmaker Professional: Neural Network Simulation Software User's Guide and Reference Manual: California Scientific Software.

Lekarp, F., U. Isacsson, and A. Dawson. (2000). State of the art. I: Resilient response of unbound aggregates. Journal of Transportation Engineering, 66(1), 66–75.

Liang, R. Y., S. Rabab'ah, and M. Khasawneh. (2008). Predicting moisture-dependent resilient modulus of cohesive soils using soil suction concept. Journal of Transportation Engineering, 134(1), 34–40.

Ling, M., X. Luo, S. Hu, F. Gu, and R. L. Lytton. (2017). Numerical modeling and artificial neural network for predicting J integral of top down cracking in asphalt pavement. Transportation Research Record: Journal of the Transportation Research Board, No. 2631, 83-95.

Ling, M., Luo, X., Chen, Y., Gu, F., and Lytton, R. L. (2018). Mechanistic-empirical models for top-down cracking initiation of asphalt pavements. International Journal of Pavement Engineering, 1-10

Liu, H., and Dane, J. (1993). Reconciliation between measured and theoretical temperature effects on soil water retention curves. Soil Sci Soc Am J, 57:1202-7.

Luo, X., Gu, F., Zhang, Y., Lytton, R. L. Zollinger, D. (2017). Mechanistic-Empirical Models for Better Consideration of Subgrade and Unbound Layers Influence on Pavement Performance. Transportation Geotechnics, 13, 52-68.

Lytton, R. L. (1995). Foundations and pavements on unsaturated soils. Proceedings of the 1st International Conference on Unsaturated Soils, International Society of Soil Mechanics and Foundation Engineering, Paris, 3, 1201–1220.

Lytton, R.L., Aubeny, C.P., Bulut, R., (2005). Design procedure for pavements on expansive soils. Research Report No. 0-4518-1, Vol. 1, Texas Transportation Institute, College Station, Texas.

Lytton, R.L., (1997). Engineering structures in expansive soils, Solos Nao Saturados, Rio de Janeiro, Brazil.

Malla, R. B., and S. Joshi. (2007). Resilient modulus prediction models based on analysis of LTPP data for subgrade soils and experimental verification. Journal of Transportation Engineering, 133(9), 491-504.

Maree, J. H. (1978). Ontwerpparameters vir klipslag in plaveisels.

Masad, S.A., and D.N. Little. (2004). Sensitivity Analysis of Flexible Pavement Response and AASHTO 2002 Design Guide to Properties of Unbound Layers. *Research Report ICAR 504-1*. International Center for Aggregates Research, Austin, TX.

Masad, S., Little, D. N., and Masad, E. (2006). Analysis of flexible pavement response and performance using isotropic and anisotropic material properties. Journal of Transportation Engineering, 132(4), 342-349.

McKeen, R. G., Johnson, L.D., 1990. Climate Controlled Soil Design Parameters for Mat Foundations. Journal of Geotechnical Engineering, 116(7), 1073-1094.

McKeen, R.G., (1981). Design of Airport Pavements for Expansive Soils. Report No. DOT/FAA/ RD-81/25. New Mexico Engineering Research Institute, University of New Mexico, Federal Aviation Administration, Washington, DC.

Mishra, S., Parker, L., and Singhal , N. (1989). Estimation of soil hydraulic properties and their uncertainty from particle size distribution data. Journal of Hydrology, 108, 1-18.

Mitchell, P. W., (1979). The structural analysis of footings on expansive soil. Research Report No. 1, Kenneth W. G. Smith and Associates, Adelaide, South Australia.

MnDoT Pavement Design Manual. (2007). Minnesota Department of Transport, Chapter 3.

Nazzal, M. D., and L. N. Mohammad. (2010). Estimation of resilient modulus of subgrade soils for design of pavement structures. Journal of Materials in Civil Engineering, 22(7), pp 726-734.

Nazzal, M. D., and O. Tatari. (2013). Evaluating the use of neural networks and genetic algorithms for prediction of subgrade resilient modulus. International Journal of Pavement Engineering, 14(4), 364-373.

NCHRP. (2003). Harmonized test methods for laboratory determination of resilient modulus for flexible pavement design. Report 1-28 A, Transportation Research Board, Washington, D.C.

Núñez, W.P., R. Malysz, J.A. Ceratti, and W.Y.Y. Gehling. (2004). Shear Strength of Permanent Deformation of Unbound Aggregates Used in Brazilian Pavements. In *Proc. Of the 6th International Symposium on Pavements Unbound*, 23–31

Oh, J.-H., Lytton, R. L., and Fernando, E. (2006). Modeling of pavement response using nonlinear cross-anisotropy approach. Journal of transportation engineering, 132(6), 458-468.

Olaiz, A.H., Singhar, S.H., Vann, J.D., Sandra, L., (2018). Comparison and Applications of the Thornthwaite Moisture Index Using GIS. Proceedings of Second Pan-American conference on Unsaturated Soils, Dallas, Texas.

Oloo, S.Y. (1994). A bearing capacity approach to the design of low-volume traffic roads. Ph.D. dissertation, University of Saskatchewan, Saskatoon, Canada.

Oloo, S.Y., Fredlund, D.G., (1998). The Application of Unsaturated Soil Mechanics Theory to the Design of Pavements. Proceedings of the 5th International Conference on the Bearing Capacity of Roads and Airfields, Trondheim, Norway, 1419–1428.

Pachepsky, Y.A., Timlin, D. and Varallyay, G.Y. (1996). Artificial neural networks to estimate soil water retention from easily measurable data. Soil Science Society of America Journal, 60(3), 727-733.

Park, S. W., and Lytton, R. L. (2004). Effect of stress-dependent modulus and Poisson's ratio on structural responses in thin asphalt pavements. Journal of Transportation Engineering, 130(3), 387-394.

Pasternak, P. (1954). On a new method of an elastic foundation by means of two foundation constants. Gosudarstvennoe Izdatelstvo Literaturi po Stroitelstuve i Arkhitekture, Moscow.

Penman, H. L., (1963). Vegetation and hudrology. Technical Communication 53, Commonwealth Bureau of Soils, Harpenden, England.

Perera, Y., Zapata, C., Houston, W.N., and Houston, S.L., (2004). Long-term moisture conditions under highway pavements. Proc., Geo-Trans, GSP No. 126, 1, ASCE, Reston, VA., 1132–1143.

Perera, Y. Y., Zapata, C. E., Houston, W. N., and Houston, S. L. (2005). Prediction of the soil water characteristic curve based on grain-size-distribution and index properties. Geotechnical Special Publication, 49-60.

Post Tensioning Institute (PTI), (2004). Design and construction of post-tensioned slabs on ground. 3rd Edition, Phoenix, Arizona.

Puppala, A. J. (2007). Estimating Stiffness of Subgrade and Unbound Materials for Pavement Design. NCHRP Synthesis 382. Transportation Research Board, National Research Council, Washington, DC.

Rahardjo, H., Satyanaga, A., D'Amorec, G.A.R., and Leong, E.C. (2012). Soil–water characteristic curves of gap-graded soils. Engineering Geology, 125(27), 102–107.

Rahman, M. M., Uddin, M. M., and Gassman, S. L. (2017). Pavement performance evaluation models for South Carolina. KSCE Journal of Civil Engineering, 21 (7), 2695-2706

Rahman, M. M., and Gassman, S. L. (2019a). Effect of resilient modulus of undisturbed subgrade soils on pavement rutting. International Journal of Geotechnical Engineering, 13 (2), 152-161.

Rahman, M. M., Islam, K.M., and Gassman, S. L. (2019b). Correlations of permanent strain and damping coefficients with resilient modulus for coarse-grained subgrade soils. International Journal of Geotechnical Engineering, 1-10.

Rao, K. (2000). Dynamic soil tests and applications. A. H. Wheeler & Co. Ltd, New Delhi, First Edition.

Reardon, E. J. (1992). Problems and approaches to the prediction of the chemical composition in cement/water systems. Waste Management, 12, 221-239.

Reddi, L., and Poduri, R. (1997). Use of liquid limit state to generalize water retention properties of fine-grained soils. Geotechnique, 47(5), 1043– 1049.

Roque, R., Zou, J., Kim, Y. R., Baek, C., Thirunavukkarasu, S., Underwood, B. S., and Guddati, M. N. (2010). Top-down cracking of hot-mix asphalt layers: Models for initiation and propagation. NCHRP Project No. 1-42A.

Russam, K., Coleman, J. D., (1961). The effect of climatic factors on subgrade moisture conditions. Geotechnique, 11(1), 22-28.

Ruttanaporamakul, P. (2012). Resilient moduli properties of compacted unsaturated subgrade materials. Arlington: The University of Texas at Arlington.

Saha, S. (2013). Mechanistic characterization of rubberized asphalt mixture and design using full scale tire-pavement finite element modeling. Clemson University, Clemson, SC.

Saha, S., F. Gu, X. Luo, and R. L. Lytton. (2017). Prediction of soil-water characteristic curve using artificial neural network approach. Proceedings of Second Pan-American Conference on Unsaturated Soils, 124-134. Dallas, TX.

Saha, S., F. Gu, X. Luo, and R. L. Lytton. (2018a). Prediction of soil-water characteristic curve for unbound material using artificial neural network approach. Journal of Materials in Civil Engineering, 30(5), 06018002.

Saha, S., Gu, F., Luo, X., and Lytton, R. L. (2018b). Use of an artificial neural network approach for the prediction of resilient modulus for unbound granular material. Transportation research record: Journal of the Transportation Research Board, 0361198118756881.

Saha, S., F. Gu, X. Luo, and R. L. Lytton. (2018c). Evaluation of artificial neural network model for predicting soil–water characteristic curve. Transportation Research Board 97th Annual Meeting, Washington DC.

Saha, S., Gu, F., Luo, X., and Lytton, R. L. (2019a). Development of a modulus of subgrade reaction model to improve slab-base interface bond sensitivity. International Journal of Pavement Engineering, 1-12.

Saha, S., Gu, F., Luo, X., and Lytton, R. L. (2019b). Parametric Study of Modified Subgrade Reaction Model Using Artificial Neural Network Approach. Proceedings of Eighth International Conference on Case Histories in Geotechnical Engineering, Philadelphia, Pennsylvania.

Saha, S., Narain, H., Gu, F., Luo, X., Little, D. N. and Lytton, R. L. (2019c). Development of a Mechanistic-Empirical Model to Predict Equilibrium Suction for Subgrade Soil. Under review in Journal of Hydrology.

Saha, S., Gu F., Luo X., and Lytton, R.L. (2019d). Use of an ANN based approach to improve moisture and interface bond sensitivity on rigid pavement performance. In preparation.

Saha, S., Gu F., Luo X., and Lytton, R.L. (2019e). Improved sensitivity of moisture on rutting and fatigue cracking performance of flexible pavement", 2019. In preparation.

Saha, S., Deng Y., Luo X., Little, D.N., and Lytton, R.L. (2019f) An electrical conductivity based approach to estimate the percentage of stabilizer in unbound base materials. In preparation.

Saha, S., Devadas A., Deng Y., Luo X., and Lytton, R.L. (2019g). A ground penetrating radar based non-destructive approach to determine resilient modulus of base layer. In preparation.

Sahin, H. (2014). Nondestructive test method for rapid assessment of flexible base performance in transportation infrastructures. PhD Dissertation, Texas A&M University, College Station, TX.

Sahin, H., Gu, F., & Lytton, R. L. (2015). Development of soil-water characteristic curve for flexible base materials using the methylene blue test. Journal of Materials in Civil Engineering, 27(5).

Salour, F., Erlingsson, S., and Zapata, C. (2014). Modelling Resilient Modulus Seasonal Variation of Silty Sand Subgrade Soils with Matric Suction Control. Canadian Geotechnical Journal, 51(12), 1413-1422.

Schaap, M.G., and Bouten, W. (1996). Modeling water retention curves of sandy soils using neural networks. Water Resources Research, 32(10), 3033-3040.

Schwartz, C.W., R. Li, S. Kim, H. Ceylan, and K. Gopalakrishnan. (2011). Sensitivity Evaluation of MEPDG Performance Prediction." *Final Report of NCHRP 1-47 Project*, University of Maryland and Iowa State University.

Shi, X., Fwa, T., & Tan, S. (1993). Warping stresses in concrete pavements on Pasternak foundation. Journal of transportation engineering, 119(6), 905-913.

Shi, X., Tan, S., & Fwa, T. (1994). Rectangular thick plate with free edges on Pasternak foundation. Journal of engineering mechanics, 120(5), 971-988.

Sillers, W.S., Fredlund, D.G., and Zakerzadeh, N. (2001). Mathematical attributes of some soil-water characteristic curve models. Geotechnical and Geological Engineering, 19(34), 243–283.

Smith, K. D., Burinsma, J. E., Wade, M. J., Chatti, K., Vandenbossche, J.M., and Yu, H. T. (2017). Using Falling Weight Deflectometer Data with Mechanistic-Empirical Design and Analysis. Volume 1: Final Report, Federal Highway Administration, Washington, DC.

Snethen, D.R., Johnson, L.D., Patrick, D.M., (1977). An Investigation of the Natural Microscale Mechanisms That Cause Volume Change in Expansive Clays. Report No. FHWA-RD-77-75. U.S. Army Engineer Waterways Experiment Station, Federal Highway Administration, Washington, DC.

Soil Eordibility. (2014). Retrieved March 2014, from http://web2.uwindsor.ca/courses/earth_science/hudec/nigeria/Erodibility.htm

Soliman, H., and Shalaby, A. (2015). "Permanent Deformation Behavior of Unbound Granular Base Materials with Varying Moisture and Fines Content." Transportation Geotechnics, Vol. 4, pp. 1–12.

Soliman, H. and A. Shalaby. (2016). Validation of Long-Term Pavement Performance Prediction Models for Resilient Modulus of Unbound Granular Materials. Transportation Research Record: Journal of the Transportation Research Board, No. 2578, 29-37.

Sun, X, Li, J. Zhou, A.N., (2017). Evaluation and comparison of methods for calculating Thornthwaite Moisture Index. Journal of Australian Geomechanics, 52(2), 61-75.

Tarr, S. M., Okamoto, P. A., Sheehan, M. J., and Packard, R. G. (1999). Bond interaction between concrete pavement and lean concrete base. Transportation Research Record: Journal of the Transportation Research Board, 1668, 9–17.

Teimoorinia, , H., Bluck, A., and Ellison, S. (2016). An artificial neural network approach for ranking quenching parameters in central galaxies. Monthly Notices of the Royal Astronomical Society, 457(2).

Terzaghi, K.V. (1955). Evaluation of coefficient of subgrade reaction. Geotechnique, 5, 297-326.

Theyse, H. L., De Beer, M., and Rust, F. C. (1996). Overview of South African mechanistic pavement design method. Transportation Research Record: Journal of the Transportation Research Board, 1539(1), 6-17.

Theyse, H. (2000). Laboratory design models for materials suited to labour-intensive construction. Pretoria: CSIR Transportek. Contract Report CR-99/038.

Thompson, M. R. (1966). Shear strength and elastic properties of lime-soil mixtures. Highway Research Record, Washington, D.C., 139, 1-14.

Thornthwaite, C.W., (1948). An Approach toward a Rational Classification of Climate. Geographical Review, 38(1), 55-94.

Titus-Glover, L., and E. G. Fernando. (1995). Evaluation of pavement base and subgrade material properties and test procedures.

Torres-Hernandez, G. (2011). Estimating the Soil–Water Characteristic Curve Using Grain Size Analysis and Plasticity Index. Tempe: Arizona State University.

Tseng, K.H., and R.L. Lytton. (1989). Prediction of Permanent Deformation in Flexible Pavement Materials. In *Implication of Aggregates in the Design, Construction, and Performance of Flexible Pavement, ASTHMA STP 1016, ASTM, Philadelphia, PA.*, pp. 154–172

Tutumluer, E., and Seyhan, U. (1999). Laboratory determination of anisotropic aggregate resilient moduli using an innovative test device. Transportation Research Record: Journal of the Transportation Research Board, 1687, 13-21.

Tutumluer, E., D. Mishra, and A. Butt. (2009). Final Report, Illinois Center for Transportation (ICT) R27-1 Project: Characterization of Illinois Aggregates for Subgrade Replacement and Subbase, University of Illinois Urbana-Champaign, Urbana, IL.

Tutumluer, E., Little, D. N., & Kim, S.-H. (2003). Validated model for predicting field performance of aggregate base courses. Transportation Research Record: Journal of the Transportation Research Board, 1837, 41-49.

Vallabhan, C. V. G., and Das, Y. C. (1988). An improved model for beams on elastic foundations. Proceedings of the ASME/PVP Conference, Pittsburgh, Pennsylvania,19-23.

Vallabhan, C.V.G., and Das, Y.C. (1989). A refined model for beams on elastic foundations. International Journal of Solids and Structures, 27, 629-637.

Van Genchten, M.T., (1980). A closed-form equation for predicting the hydraulic conductivity of unsaturated soils. Soil Science Society of American Journal. 44, 892-898.

Vesic, A. B. (1961). Beams on elastic subgrade and the Winkler's hypothesis. Proceedings of the 5th International Conference on Soil Mechanics and Foundation Engineering, 1, 845-850.

Vlasov, V. Z. and Leont'ev, N. N. (1966). Beams, plates and shells on elastic foundations. Israel Program for Scientific Translations, Jerusalem.

Wang, S. (2011). The effects of implements of husbandry farm equipment on rigid pavement performance, Iowa State University - Ames, Iowa.

Wang, H., and Al-Qadi, I. L. (2012). Importance of Nonlinear Anisotropic Modeling of Granular Base for Predicting Maximum Viscoelastic Pavement Responses under Moving Vehicular Loading. *Journal of Engineering Mechanics*, 139(1), 29-38.

Wang H., Al-qadi, I.L., and Stanciulescu, I. (2012). Simulation of tyre-pavement interaction for predicting contact stresses at static and various rolling conditions. International Journal of Pavement Engineering, 13(4), 310-321.

Wang, H., Al-Qadi, I., and Stanciulescu, I. (2014). Effect of surface friction on tire–pavement contact stresses during vehicle maneuvering. Journal of Engineering Mechanics, 140, 04014001

Williams, J., Prebble, R., Williams, W., and Hignett, C. (1983). The influence of texture, structure and clay mineralogy on the soil moisture characteristic. Australian Journal of Soil Research, 1(21), 15–32.

Wilm, H.G., Thornthwaite, C.W., Colman, E.A., Cummings, N.W., Croft, A.R., Gisborne, H.T., Harding, S.T., (1944). Report of the Committee on Transpiration and Evaporation 1943-44. Eos. Transactions American Geophysical Union, 683-693.

Winkler, E. (1867). Die lehre von der elastizität und festigkeit (The Theory of Elasticity and Stiffness). Dominicus, Prague.

Witczak, M. W. (2003). NCHRP Report 1-28A: Harmonized test methods for laboratory determination of resilient modulus for flexible pavement design. Transportation Research Board, Washington, D.C., 2003.

Witczak, M.W., Zapata, C.E., Houston, W.N., (2006). Models Incorporated into the Current Enhanced Integrated Climatic Model for Used in Version 1.0 of the MEPDG. NCHRP 9-23 Project Report, Arizona State University, Tempe, Arizona.

Wolfe, W., Butalia, T., (2004). Continued Monitoring of SHRP Pavement Instrumentation Including Soil Suction and Relationship with Resilient Modulus. Report No. FHWA/OH-2004/007, U.S. Department of Transportation, Federal Highway Administration, Washington, D.C.

Wray, W.K., (1989). Mitigation of Damage to Structures Supported on Expansive Soils, Vols. I, II, and III. Texas Tech University, National Science Foundation, Washington, DC.

Wu, W., Dandy, G. C., and Maier, H. R. (2014). Protocol for developing ann models and its application to the assessment of the quality of the ann model development process in drinking water quality modelling. Environmental Modelling & Software, 54, 108–127.

Yau, A., and H. L. Quintus. (2004). Predicting elastic response characteristics of unbound materials and soils. Transportation Research Record: Journal of the Transportation Research Board, No. 1874, 47-56.

Zapata, C. (1999). Uncertainty in Soil-Water Characteristic Curve and Impacts on Unsaturated Shear Strength Predictions. Tempe: Arizona State University.

Zapata, C. E. (2010). NCHRP Project 9-23A: A national database of subgrade soil-water characteristic curves and selected soil properties for use with the MEPDG. Transportation Research Board, Washington, D.C.

Zapata, C. E., Houston, W. N., and Walsh, K. D. (2003). Soil-water characteristic curve variability. Advances in Unsaturated Geotechnics, 99, 84-124.

Zhang, J., Li, J., Yao, Y., Zheng, J., and Gu, F. (2018a). Geometric anisotropy modeling and shear behavior evaluation of graded crushed rocks. Construction and Building Materials, 183, 346-355.

Zhang, J., Peng, J., Li, J., Zheng, J., and Yao, Y. (2018b). Characterisation of Stress and Moisture-Dependent Resilient Behavior for Compacted Clays in South China. Road Materials and Pavement Design, DOI:10.1080/14680629.2018.1481138.

Ziaie-Moayed, R., and Janbaz, M. (2009). Effective parameters on modulus of subgrade reaction in clayey soils. Journal of Applied Sciences, 9, 4006-4012.